SEVENTH EUROPEAN CONFERENCE ON CONTROLLED FUSION AND PLASMA PHYSICS

Volume II

Lausanne, 1-5 September 1975
Centre de Recherches en Physique des Plasmas (CRPP)
Ecole Polytechnique Fédérale de Lausanne, Switzerland

SEVENTH EUROPEAN CONFERENCE ON CONTROLLED FUSION AND PLASMA PHYSICS

VOLUME II

INVITED PAPERS

SUPPLEMENTARY PAPERS

POST-DEADLINE PAPERS

Lausanne, 1-5 September 1975

Centre de Recherches en Physique des Plasmas (CRPP)

Ecole Polytechnique Fédérale de Lausanne, Switzerland

These Proceedings (Vol. 1: Contributed Papers, Vol. 2: Invited, Supplementary and Post-Deadline Papers) will be distributed free of charge to all registered participants. They will also be sold at the price of 40 Swiss Francs after the Conference. Orders should be placed with the Conference Secretariat, during the meeting, or sent to the Centre de Recherches en Physique des Plasmas, Ecole Polytechnique Fédérale de Lausanne, Avenue des Bains 21, CH-1007 Lausanne, Switzerland, after the meeting.

C O N T E N T S

I N V I T E D P A P E R S

P R E F A C E

This volume contains the texts of the invited lectures, post-deadline contributions that were read at the Conference and the supplementary pages to papers already published in the first volume of the Proceedings.

The invited lectures were selected by the Paper Selection Committee from suggestions given by heads of leading plasma research groups in Europe and elsewhere. A last minute arrangement during the Conference permitted the presentation of an extended lecture by Dr. I.R. Gekker, as well as an invited lecture by Dr. F.A. Nikolaev. The texts of these lectures are included in this volume. To keep the same arrangement as in the first volume the invited papers are printed in a logical order, regrouping those pertaining to a same subject, rather than in their order of presentation.

Please note that the post-deadline papers have been given numbers (underlined) which are different from the page numbers, to avoid confusion in referencing with papers of the first volume.

Except for retyping of manuscripts not conforming to the format and minor editing corrections, the texts are photographic reproductions of the original papers, which means that the authors must bear responsibility for the content of their papers.

The Organizing Committee

COMMITTEES AND SUPPORTING ORGANIZATIONS

ORGANIZING COMMITTEE

E.S. Weibel, Chairman

K. Appert, Finances

A. Heym, Communication

F. Hofmann, Conference Secretary

F. Troyon, Scientific Secretary

PAPER SELECTION AND PROGRAMME COMMITTEE

H.A.B. Bodin, Culham, U.K.

B. Lehnert, Stockholm, Sweden

C. Mercier, Fontenay-aux-Roses, France

G. Wolf, Jülich, Federal Republic of Germany

FINANCIAL SUPPORT

The organizations listed below have contributed financially to the Conference. Their support is gratefully acknowledged:

Département Fédéral de l'Intérieur, Berne

Ecole Polytechnique Fédérale de Lausanne

Etat de Vaud

Ville de Lausanne

INVITED PAPERS

BEHAVIOUR OF DISCHARGES AND INTERNAL DISRUPTIONS IN T.F.R.

T.F.R. Group presented by D.Launois

ASSOCIATION EURATOM-CEA SUR LA FUSION
Département de Physique du Plasma et de la Fusion Contrôlée
Centre d'Etudes Nucléaires
Boîte Postale n° 6. 92260 FONTENAY-AUX-ROSES (FRANCE)

Abstract : In TFR discharges the current concentrates around the magnetic axis, forcing the safety factor to become less than unity in this region, where a turbulent process arises. For high current discharges, above 200 kA, the energy confinement time levels at about 25 ms. The electron energy balance may be explained either by this turbulence or by dissipative trapped electron instability. The ion behaviour is consistent with the neoclassical transport theory.

I- Introduction

At the time of the Tokyo conference we reported /Ref 1/ that TFR had been successfully operated at the maximum current and maximum toroidal field (I_p = 400 kA ; B_T = 60 kG). Experiments carried out for roughly similar values of the safety factor at the plasma edge ($q(a) \sim 4$), yielded the dependences of the main plasma parameters (n_e, T_e, T_i, Z_{eff}) on the plasma current. Steady state regimes were achieved of I_p =200 kA for about 0.5 s. An important feature appeared to be the "levelling-off" of the energy confinement time τ_E at a value around 15 ms, for large plasma current ($I_p \geqslant 200$ kA). This is shown again on fig.1, with τ_E defined by $\tau_E = \frac{W_e + W_i}{UI}$ U is the steady state loop voltage.

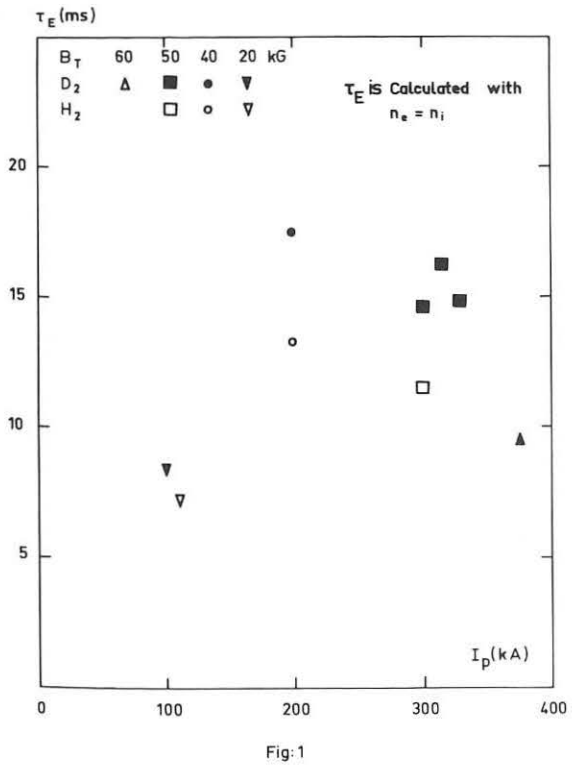

Fig: 1

Attempts were made to determine the plasma power balance. The ion ba-

lance could be explained by neoclassical diffusion, using the plateau regime coefficient . As to the electrons, which were responsible for most of the losses, we had to use anomalous transport coefficients. Our numerical simulation code could reproduce the actual experimental results (time evolution, radial profiles, energy balances) using, for the thermal conduction coefficient K_e, a pseudo classical type dependence ($\nu_{ei} \rho_\theta^2$) which did give rise to a shrinking of the current channel around the axis and to a related decrease in q . After q reached the value 1 on axis, we had to multiply K_e by a numerical factor over the region where $q<1$. However we could not get to a conclusion, as to what was the mechanism responsible for the enhanced losses (impurity radiation in the plasma core or anomalous thermal conduction coefficient).

Following this line, more experiments have been designed in order to

-follow the space time evolution of the impurities

-investigate the shrinking of the current channel and the enhanced internal heat transport

-bring out evidence of mechanisms that may govern the power balance .

To help in these experiments, the centering of the plasma column was improved with the installation of a new feed-back circuitry. The neutral gas injection can now be controlled during the course of a discharge enabling us to increase somewhat the plasma density.

The values of q(a) ranged from 2,7 to 15 for the various conditions we investigated.

II- Impurities

For the impurities the main conclusions reached by the vacuum UV spectroscopic study and given in /Ref 2/ are :

-The light impurity ions and heavy impurity of moderate charge (Mo^{12+}, Fe^{15+},..) have their maximum concentration at radii where T_e is equal or slightly smaller than their ionization potential.

-The highly charged ions (Mo^{30+}, Mo^{31+},..) are concentrated inside a diameter of about 10 cm.

-Inward diffusion velocities of the order of $2.10^3 cm.s^{-1}$ are cal-

culated for r ≃ 16 cm.

The power radiated by measured light impurity lines is about 35% of the input power but only a few per cent is due to Mo^{30+}-Mo^{31+}. The molybdenum central density is $\simeq 10^{11}$ cm^{-3}, the ratio $\frac{n_{Mo^{31+}}}{n_e}$ is roughly constant during the plateau current.

III- Shrinkage of the current channel and its consequence : internal disruptions for q ≲ 1 .

III-1. Experimental results .

III-1-1. Narrowing of T_e profiles as q(a) increases

The Thomson scattering profiles of T_e, measured under various current(Ip) and various toroidal field (B_T) conditions are shown on Fig.2.

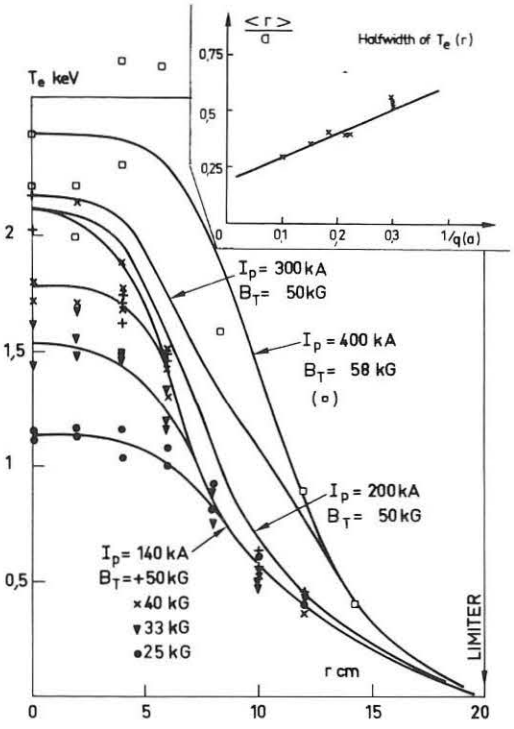

Fig: 2

The half maximum width of the profiles is an increasing function of $\frac{1}{q(a)}$ (see insert). In the central region ($r \lesssim 5$cm) the profile flattens out (for high current we may even observe a small dip on the axis) indicating a larger heat conduction.

III-1-2. Internal disruptions

We have measured the soft X-rays emission from the hot plasma core, in relation with the enhanced internal heat transport. Our experiments are similar to the ones that have already been carried out on S.T./Ref 3/

Our experimental set up is sketched on Fig.3.

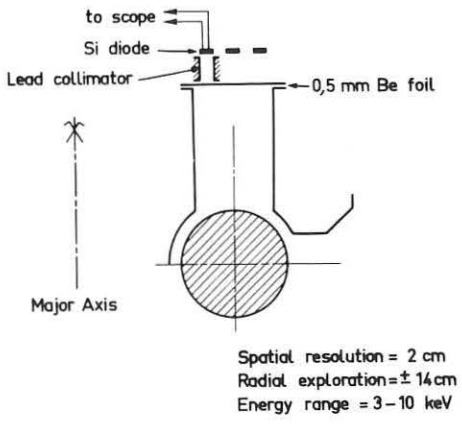

Fig 3: Soft X rays detector

The soft X-ray signal obtained under typical conditions is sketched on Fig.4 .

The signal amplitude A roughly follows the plasma current amplitude. A superimposed saw-tooth type oscillation (ΔA) appears when T_{eo} reaches its

maximum, at about 50 ms.

The saw-tooth oscillation exhibits a m=o, n =o mode structure with a period varying from 1 ms to 3 ms, at higher densities.

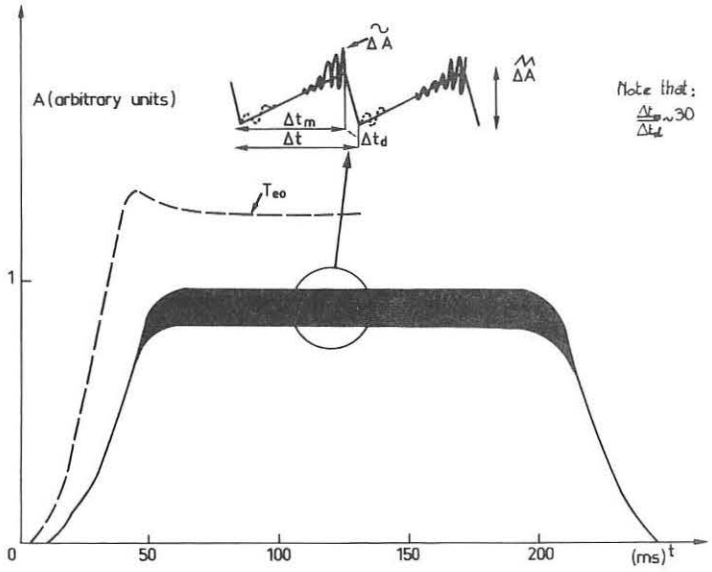

FIG 4

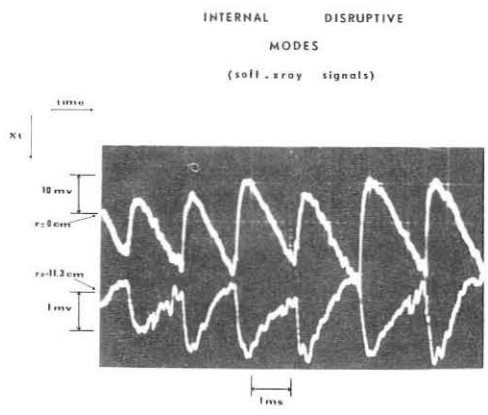

Fig 5

Fig.5 shows that, further away from the axis, the soft X-ray signal emitted is inverted, i.e. a decrease of the signal in the inner part of the plasma corresponds to an increase in the outer part. The start up time of the relaxation is fairly identical at any radius (the spread is less than 10 μs), but the rise time is longer at larger radius.

Quite generally a sine wave oscillation ($\tilde{\Delta A}$) with an m=1, n=1 mode structure is in turn superimposed to the saw-tooth mode. It appears during the slow rise of the saw-tooth and, quite often, survives its fast fall off. The rise time is of the order of $\sim 3.10^3 s^{-1}$ The frequency is close to 10 kHz but generally weaker after the fall off of the saw-tooth.

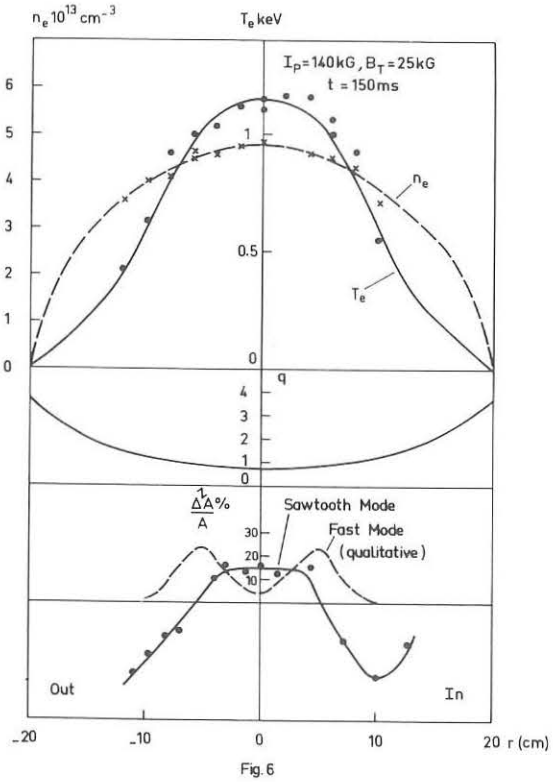

Fig. 6

Fig.6 shows that the radius at which $\frac{\hat{\Delta A}}{A} = o$ and the radius at which $\frac{\tilde{\Delta A}}{A}$ is maximum are close of the radius r_1 where q=1. Hereafter

we will identify r_1 with the point where $\frac{\widetilde{\Delta A}}{A} = 0$.(Considering local values rather than the actual chord averaged signal would yield a slightly larger r_1).

The functional dependences of the saw-tooth mode on I_p and B_T have been searched for. The results are summarized on fig.7. We observed the radius r_1 (as defined above) to vary approximately as $(I / B_T)^{1/2}$. The internal saw-tooth mode vanishes out whenever $q(a) \sim 12$.(For these low current conditions q(o) could not go below 1 even though the current channel become very narrow) .

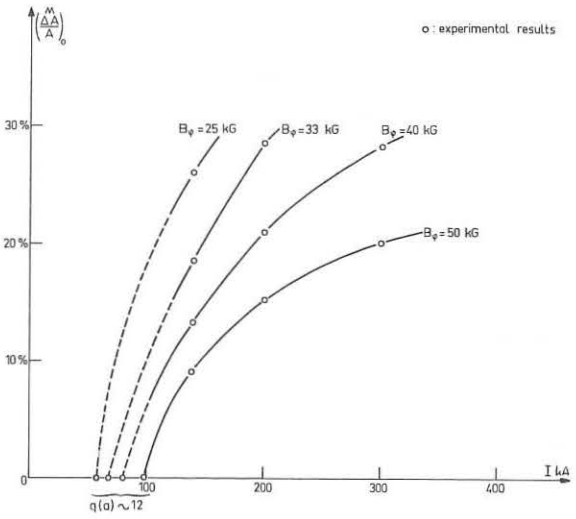

Fig: 7

III.1.3. Physical picture and consequences

The question now is what to attribute the variation of the soft X-ray flux to ? The X-ray emission depends on n_e, T_e and Z_{eff}. Concerning Z_{eff}, our first attempts to search for fluctuations have not yet produced reliable information. However the Thomson diffusion measurements yielded informations on T_e and n_e during the saw-tooth period as shown on fig.8. In spite of a large inaccuracy, the measurements support the conclusion that a temperature fluctuation is mostly influencing the soft X-ray emission ($\frac{\Delta T_e}{T_e} \sim 15\%$).The density fluctuation is in the range of only a few percent as evidenced also from 2 mm microwave interferometry. Consistently, the rise in T_e related to the saw-tooth rise can be explained on the basic of ohmic heating only (including Z_{eff} in the calculation), if it is assumed that the losses are negligible meanwhile. This implies that the losses would essentially occur

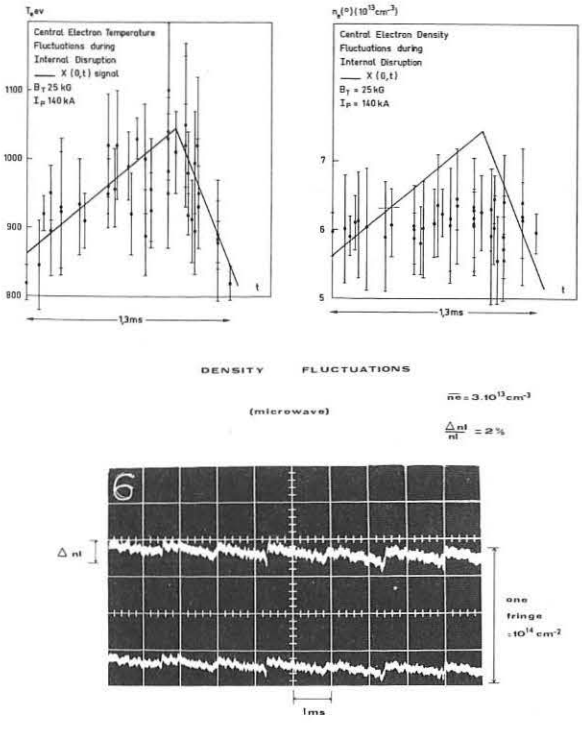

FIG:8

during the rapid fall off of the saw-tooth in the region where $q<1$, leading to a steady state on a time scale longer than the saw-tooth period. Tentative mechanisms responsible of the turbulent loss process will be considered and discussed later.

Since for this process, q(o) is always close to unity we are in a position to estimate a few physical quantities.

i) In particular, the knowledge of q(o) permits to determine $j(o)$ and, taking the electric field calculated from the loop voltage, the steady state $Z_{eff}(o)$. This reads $Z_{eff}(o) = \frac{102 \cdot q(o) \cdot U(\text{volts})\, T_e^{1.5}(\text{keV})}{B_T(\text{Wb/m}^2) \cdot \ln\Lambda} - 0.98$

Knowing T_e, U, B_T we then get an upper bound of $Z_{eff}(o)$ by taking q(o)=1.

ii) Conductivity measurements /Ref 4/ performed by inducing RF currents yield the conductivity profile $\sigma(r)$ in the outer region. The range of theoretical curves that may reasonably be fitted to the data can be greatly reduced if we constrain q(o) to be close to unity.

iii) If the central current profile is such that $j(r) \sim \frac{T_e^{3/2}(r)}{Z_{eff}(r)+1}$ one gets $Z_{eff} \sim C^{te}$ as r varies (for $r \leqslant 10$cm). Typical values obtained for Z_{eff} using $q(o) \sim 1$, are of order 5 to 7, for discharges with the large limiter (40 cm I.D.). With the smaller limiter (34cm I.D.) Z_{eff} decreases to 2 to 3 .

III-2. Interpretation of the data.

III-2-2. Shrinking of the current channel.

According to the observations described above we interpret this phenomenon as a thermal instability arising as a consequence of the ohmic heating process.

In order to study it analytically we write the thermal conduction coefficient as $K_e \sim n_e^2(r)\, T_e^{\alpha}(r)\, (\frac{B_\theta}{r})^{\beta}$ and solve for the electron temperature profiles choosing the density profile as $n_e = n_o \exp -\frac{\gamma}{2} r^2$ with α, β and γ as parameters. As shown of Fig.9, for some values of the parameters α, β no steady state equilibrium is reached. The current channel keeps skrinking down, whereas the maximum value goes up. However a steady state equilibrium is obtained over a parameter region which stretches out as the density profile gets narrower (increasing γ on fig.9)

If we compare with the numerical simulation where the functional dependence is $\sim \nu_{ei} \rho_T^2 (1+q^2)$ we always expect - for not too sharp density profile, at least - that the shrinking of the current causes q to become less

than unity on the axis. This results in an internal turbulence phenomenon. Here ρ_T is the Larmor radius in the total magnetic field. We note from Fig.9 that for very sharp density profiles even point A is in the equilibrium region. For these conditions q(o) is still greater than unity.

This situation is to be compared to the experiments with $q(a) \sim 12$, for which the density profile was very sharp ($\chi \sim 4$) ; q(o) was larger than 1 and no internal disruption appeared. A more detailed investigation of this model is given in Ref.5.

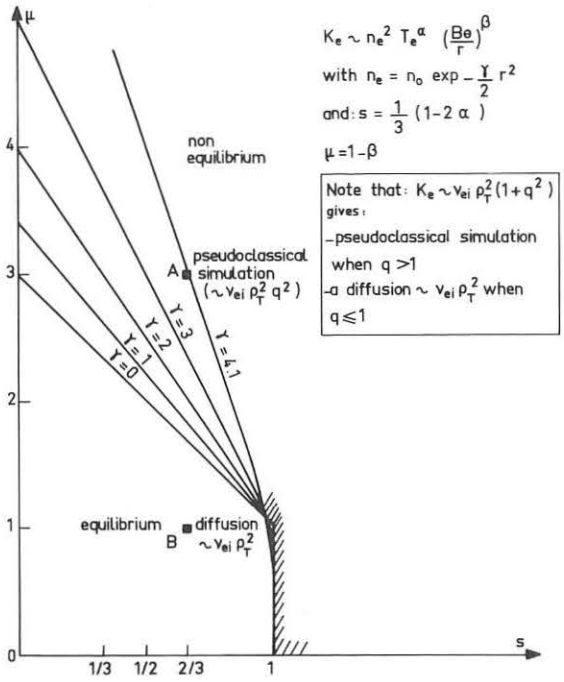

Fig: 9

In the interpretation above, it has not been necessary to modify the $Z_{eff}(r)$ in the resistivity term to account for the T_e profiles.

III-2-3 Internal disruptions.

i) The m=1, n=1 sinewave mode, f=10 kHz. This shrinking of the current channel causes q(o) to become less than 1 which in turn may give rise to various instabilities. The m=1, n=1 structure of the sinewave mode shows that this mode is of MHD origin ($q=\frac{m}{n}=1$). Among the linear theory predictions we may choose as candidates the internal kink mode and growing magnetic islands.

The internal kink mode theory in toroidal geometry /Ref.6/ shows that the stability of this mode depends on the q profile and on a parameter including the kinetic pressure term $\frac{R n(o) T(o)}{I B_T}$. For a given profile, the weaker the parameter, the lower the critical value of q(o) below which the instability would appear. This is indeed qualitatively observed as shown on Fig.10. However the critical value of q(o) seems to be larger than the one predicted by the theory. It has to be emphasized that the theory did not include a few non-basic phenomena which would however increase the critical value (magnetic shear, coupling with m=2 tearing mode). On the other hand experimental errors are introduced by some arbitrariness in the choice of the T_e profile and by uncertainties in the determination of n(o)

and $T_e(o)$.

However the similarity of the soft X-ray signals emitted near the q=1 surface with the signal emitted -in the case of negative voltage spikes /Ref.7/ near the q=2 surface-where the internal kink mode cannot occur, speaks in favor of magnetic islands /ref.8/. So far the study of the m=2 mode with the aid of soft X-ray detector has not been performed. Measurements with magnetic probes indicate that $\frac{\tilde{B}_\theta}{B_\theta} \sim 1\%$ for the m=2 mode in normal regimes. However before a complete disruption of the plasma channel this mode would grow ($\frac{\tilde{B}_\theta}{B_\theta} \sim 3\%$) and a coupling between the m=1 and m=2 modes would occur /Ref.9/.

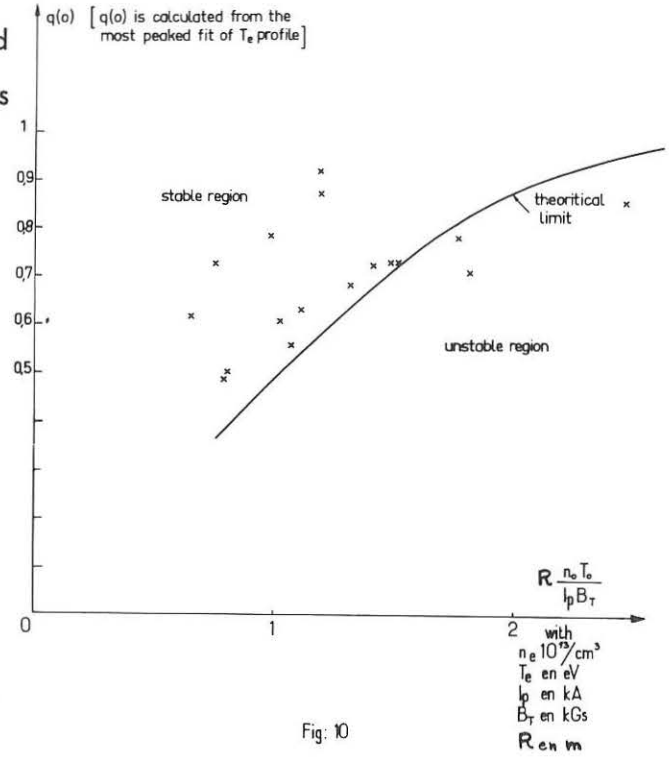

Fig: 10

ii) The m=o, n=o saw-tooth mode $f \sim 300 - 1000$Hz . The theoretical calculations that might provide an explanation for those modes are still in progress, and three different lines are being investigated:

- non linear evolution of internal kink modes /Ref.10/
- magnetic island instabilities /ref.8/
- non linear convexion cell /ref.11/

a detailed comparison between the non linear theories predictions and the experimental results is presently under way.

IV- Energy balance .

IV-1 . Experimental results.

A detailed study of energy balances as a function of q(a) has been carried out /ref.12/. We varied Ip from 100 to 400 kA and B_T from 25 to 60 kG. $T_e(o)$ appears to be mainly a function of B_T, and for a given B_T, the energy lifetime is a function of n_e, I_p and U i.e. of Z_{eff}. (So as to compared with our former results published in Tokyo we have assumed $n_e = n_i$).

Fig.11 shows the evolution of τ_E at 50 kG as a function of current. The lifetime is lower at lower B_T . Compared to our earlier results τ_E increased by 60%, that is roughly 9 ms. This is due on one hand to the increase in $\bar{n}_e$ resulting from the improved controlled injection of neutral gas, and on the other hand to the decrease in Z_{eff} likely resulting from the improved plasma positioning system. Here again we note a levelling off of $\tau_E = f(I_p)$. This is partly due to the difficulty of increasing the density without destroying the plasma.

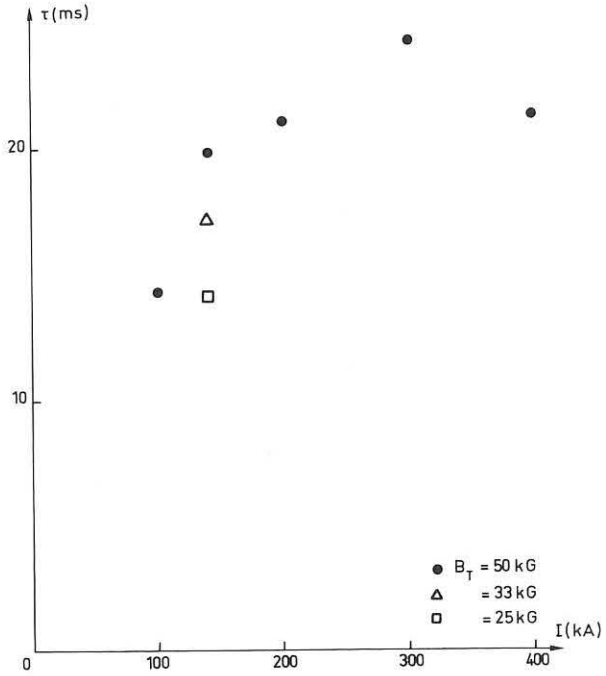

FIG 11

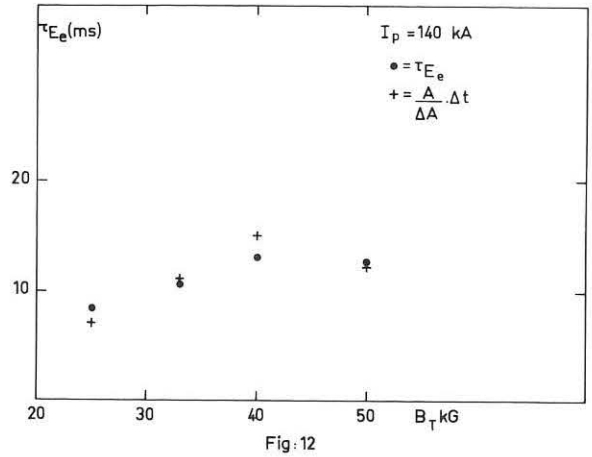

Fig: 12

If the energy loss of the electrons near the center is indeed governed by the saw-tooth induced turbulence, the energy lifetime is $\tau'_{Ee} = \frac{\Delta t}{\Delta(n_e T_e)/n_e T_e} \sim \frac{\Delta t}{\Delta A/A}$ where Δt is the saw-tooth period. Fig.12 shows the comparison between τ'_{Ee} and $\tau_{Ee} = \frac{W_e(0)}{E_j(0) - P_{ei}(0)}$ as a function of B_T for I_p = 140 kA. Here $P_{ei}(0)$ is the power going over from the electrons into the ions. The two quantities vary quite similarly. The good agreement between the absolute values is fortuitous since the soft X-ray flux is not merely proportional to the plasma pressure $n_o T_o$. At fixed B_T, too , the dependences of both quantities on I_p are in good agreement. This would suggest that, at least in the central region where $q < 1$, the electrons energy lifetime is determined by the internal disruption phenomenon.

IV-2. Experimental thermal conduction coefficient for the electrons.

An experimental heat conduction coefficient K_e can be derived from the steady state heat transport

equation. It takes on the form

$$K_e = \frac{\int_o^r (EJ - W_{ei} - W_{imp})\, r\, dr}{r\, n_e T_e \left[-\frac{d}{dr} \mathrm{Log}\, T_e - \frac{3}{2} \frac{d}{dr} \mathrm{Log}\, n_e \right]}$$

where W_{ei} is the power transferred from the electrons to the ions and W_{imp} is the power radiated by the impurities. The calculation performed by a computer code in which the data on n_e (r) , T_e (r) , T_i (r) and Z_{eff} is introduced, is obviously very sensitive to the gradients and we had to smooth out the data. Flatter smoothed profiles of T_e(r), increase K_e(r) in the central region. The shape of K_e(r) resulting from different values of $Q = \frac{q(a)}{q(0)}$ which is a parameter describing the shrinkage of the current channel, is given on fig.13. We note that K(r) is fairly constant up to $\frac{r}{a} = 0.7$. The rise of K_e(r) near the edge indicates losses induced by impurity radiation. The result above is obtained assuming that Z_{eff} is a constant as r varies, but the assumption that τ_{Ee}(r) is a constant as r varies leads to a very similar result. Since we have evidence that internal disruption is responsible for the energy loss, we are forced to conclude, from the constancy of τ_{Ee}(r) , that the influence of the internal disruption carries over into the outer region where $q > 1$. However, the experimental proof for such an interpretation has not yet entirely been obtained.

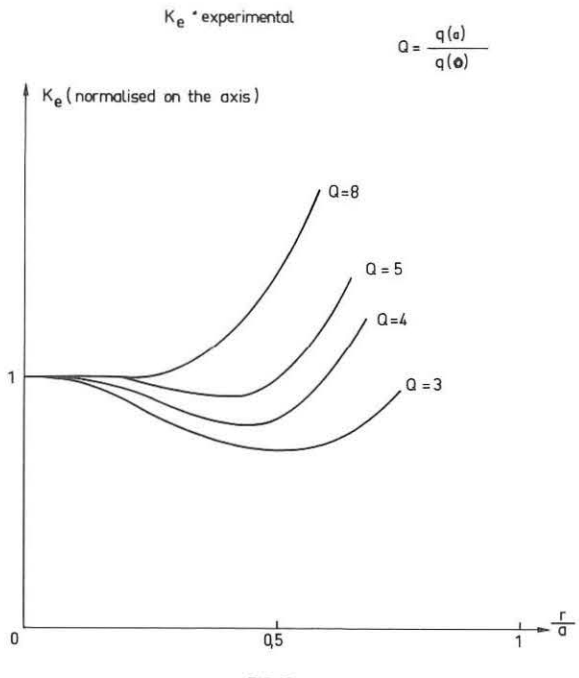

FIG 13

An analytical expression for Ke(r) that would fit to the various experimental Ke, calculated from the steady state data gathered over many discharges, can be expressed as /ref.5/.

$$K_{analit.} \sim Z_{eff} \left(n_e A_i q \right)^{-1/2} T_e^{-3/4} .$$

IV-3. Tentative comparison of the experimental K_e with various diffusion regimes.

If we want to simulate the discharge behaviour (profiles, particle and energy balances) with aid of a pseudoclassical K_e ($\nu_{ei} \rho_\theta^2$) using the measured values of Z_{eff}, we have a good agreement between the experimental τ_{Ee} and the pseudoclassical τ_{Ee} up to 200 kA. Beyond that point the disagreement becomes very important (fig.14).

We then consider two possibilities to account for the discharges

One possibility would be to consider that the heat conduction is governed by the trapped electron instability, the conditions for which- including shear criteria /Ref.13/ - are fulfilled in our case. Taking into account the experimental profiles, the energy balance is calculated at r =10cm where $\nu_{eff} < \omega_{bounce}$ - for the theoretical predicted K_e. Fig.15 shows the values predicted for $\overline{T}_e$ as a function of I_p, using this thermal conduction coefficient. Moreover such a coefficient accounts for the evolution of τ_E as a function of the parameters B_T, I_p, n_e . It should be noted however that the drift oscillations that should be responsible for the thermal losses have not yet been identified.

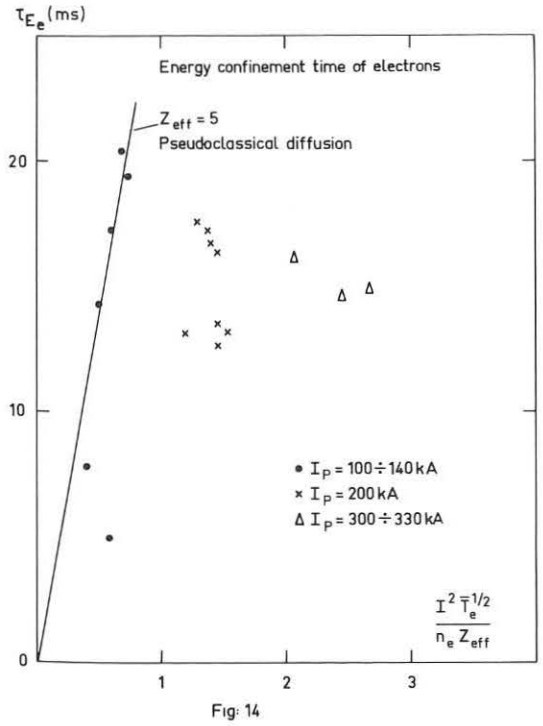

Fig. 14

The other possibility would be to call for the observed internal disruptions. Unfortunately at the present time no thermal coefficient related to this loss mechanism has been derived. However, we mentioned earlier the points arguing in favor of this turbulence (variation of τ_{Ee} with the plasma parameters, constancy of τ_{Ee} over r), making it a likely candidate.

These attempts to account for the balances show the present difficulty to choose among various mechanisms explaining the electron thermal conduction law.

The same applies to the ion thermal conduction the average values /Ref 14 / can be explained either by the neoclassical K_i, either by a K_i having the functional dependence of the trapped electron instability K_e.

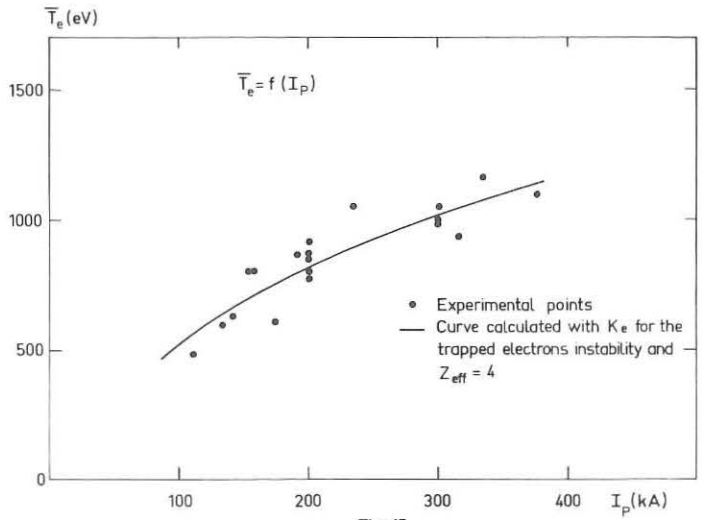

Fig: 15

V-Conclusion

In spite of uncertainties in the interpretation of our results, the conclusions that have been reached in TFR at the present time are the following.

- the ion behaviour may always be interpreted using the neoclassical diffusion coefficients.

- the impurity radiation at the center does not affect significantly the electron balance.

- the electrons behave anomalously. The internal turbulence associated with $q < 1$ could presently play the main role in the transport mechanism. However this anomalcus transport as well as the ion transport can alternately be explained by the dissipative trapped electron instability, using the transport coefficient theoretically derived for this instability.

References

/1/ Proceedings in Fifth Conference on Plasma Physics and Controlled Nuclear Fusion, Tokyo 11-15 November 1974- Papers A6-1 ; A6-2

/2/ T.F.R. Group presented by C.De Michelis at this conference

/3/ Von Goeler, W.Stodiek and N.Sauthoff, Phys.Rev.Letters, 33, n°20, 11 nov. 1974, pp.1201-1203.

/4/ T.F.R. Group presented by P.Plinate at this conference

/5/ C.Mercier, Soubbaramayer at this conference

/6/ M.N.Bussac, D.Edery, G.Laval, R.Pellat, J.L.Soulé at this conference

/7/ Von Goeler and all in ref.3 and private communication.

/8/ A.Samain, rapport EUR-CEA-FC-782, (submitted to Plasma Physics).

/9/ T.F.R. Group to be published

/10/ M.Cotsaftis to be published

/11/ R.Y.Dagazian, E.K.Maschke and R.B.Paris at this conference

/12/ T.F.R. Group presented by P.Platz at this conference

/13/ W.M.Tang, J.C.Adam and P.H.Rutherford : Proceedings of the Annual Meeting on theoretical aspects of controlled thermonuclear research (Sherwood Theory Meeting) - April 7-9, 1975 - Paper F-3.

/14/ T.F.R. Group presented by M.Chatelier at this conference

LOW AND HIGH DENSITY OPERATION OF ALCATOR

G.J. Boxman[o], B. Coppi[*], L.C.J.M. de Kock[o], B.J.H. Meddens[o], A.A.M. Oomens[o], L.Th.M. Ornstein[o], D.S. Pappas[*], R.R. Parker[*], L. Pieroni[†], S.E. Segre[†], F.C. Schüller[o], and R.J. Taylor[*].

[*]Massachusetts Institute of Technology, Cambridge, Massachusetts, U.S.A.
[o]Association Euratom-FOM, Rijnhuizen, Jutphaas, The Netherlands
[†]Association Euratom-CNEN, Frascati, Italy.

Abstract: Two main plasma regimes are identified in Alcator, depending on the value of the streaming parameter, $\xi \equiv \langle u_{\parallel}/v_{the} \rangle$, where $u_{\parallel}$ and v_{the} are the electron drift and thermal velocities. For high $\xi (\gtrsim 0.4$ in $H_2)$ two-component electron distribution functions are obtained, rf emission at frequencies greater than and equal to the ion plasma frequency, and strong ion heating up to temperatures of 1 keV occurs. For low values of ξ (generally obtained by pulsed gas injection), the distribution function is Maxwellian; nearly classical resistivity and rates of bremsstrahlung emission are observed. The energy replacement time τ_E is found to increase roughly in proportion to the density. In the extremes of the two regimes $T_i \approx T_e$. Preliminary results of ion heating by rf injection near the lower hybrid frequency are reported.

Introduction: In this paper, we report on results obtained in Alcator[1], a tokamak device with major radius R = 54 cm, limiter radius a = 9.5 cm, and maximum toroidal field of 100 kG. The results reported here were obtained with toroidal fields in the range of 35 kG to 55 kG, with the bulk of the measurements taken at 40 kG. The corresponding plasma current range was 50 to 150 kA, with discharge duration from 70 to 400 msec. The base pressure was between 3×10^{-9} and 1×10^{-8} Torr. Vigorous discharge cleaning, accomplished by audio-frequency excitation of the ohmic system, preceded each run. The majority of the measurements were performed in hydrogen or deuterium. Additional measurements were performed in He and other gases or with a controlled dose of contaminants. Normal filling pressure was about 1×10^{-4} Torr; initial plasma density corresponds closely to this pressure. For clean machine conditions, the density always decreases with time, with the predominant decrease occurring in the first 5 msec of the discharge. In order to vary the plasma density, and therefore the electron flow velocity, additional gas is injected after toroidal equilibrium is established. In this way plasmas with average densities in the range of 5×10^{12} cm^{-3} to 2×10^{14} cm^{-3} have been investigated.

Two main regimes of operation are encountered by varying the value of the streaming parameter, $\xi \equiv \langle u_{\parallel}/v_{the} \rangle$ where $u_{\parallel}(v_{the})$ is the local flow (thermal) velocity of the electrons; the average is over the minor toroidal cross section. In one, the classical or "Coulomb" regime which occurs for relatively high density and low values of ξ, the electron distribution function is nearly Maxwellian as measured by both laser and soft x-ray techniques. In the other, the anomalous or "slide-away" regime, characterized by relatively low density and high values of ξ, the electron distribution function inferred from these measurements is not Maxwellian. This regime is also characterized by strong heating of ions (up to $T_i \sim 1.2$ keV) accompanied by emission of rf radiation near ω_{pi}, lack of hard x-ray production (< 1 mR per shot near limiter), extremely low level of MHD instability and long stable discharges (up to 400 msec has been obtained). We believe that this is a new regime of tokamak operation.

Resistivity measurements: Examples of spectra obtained from pulse-height analysis of bremsstrahlung in the range 1-10 keV are shown in Fig. 1. We find the presence of an energetic tail in the slide-away regime, whereas we obtain a Maxwellian spectrum in the case of the Coulomb regime. An indication of similar effects is also obtained using laser scattering, and the results are documented elsewhere[2,3]. In the Coulomb regime, the peak temperature $T_e(0)$ determined from the soft x-ray measurement is systematically about 20% higher than that found from the laser, which may reflect a difference between transverse and longitudinal temperature. In the following we use the laser (transverse) temperature for evaluation of the classical resistivity.

We define

$$\xi \equiv \left\langle \frac{u_{\parallel}}{v_{the}} \right\rangle = \frac{2}{a_c^2} \int_0^{a_c} dr\, r \left[\frac{J_{\parallel}(r)}{en(r)}\right] \left[\frac{2T_e(r)}{m_e}\right]^{-\frac{1}{2}} \qquad (1)$$

where $J_{\parallel}(r)$, $n(r)$, and $T_e(r)$ are the current density, particle density, and electron temperature, and a_c is the effective radius of the current channel. We evaluate Eq. (1) by using the following radial profiles $T_e = T_e(0) \times \left[1 - (r/a_c)^{3/2}\right]$, $n = n(0)\left[1 - (r/a)^2\right]$ and $J_{\parallel}(r) \propto T_e^{3/2}(r)$ with $a_c = 8$ cm. These profiles are consistent with measurements made by the laser at 4 cm off centre. Using these profiles, we evaluate $\langle \eta/\eta_{cl} \rangle$, where $\eta = E_{\parallel}/J_{\parallel}$, η_{cl} is the Spitzer-Härm resistivity for hydrogenic plasma and $E_{\parallel}$ is the electric field (assumed to be constant over the cross section). In terms of the peak electron temperature $\hat{T}_{eo}$ (in units of keV)

$$\left\langle \frac{\eta}{\eta_{cl}} \right\rangle = 2.98 \frac{V}{\hat{I}} \hat{T}_{eo}^{3/2} S \,, \qquad (2)$$

where V is the loop voltage, $\hat{I}$ is the loop current in units of 100 kA, and S is a profile shape factor given by

$$S = \frac{2}{a_1^2} \int_0^{a_1} dr\, r \left[\frac{T_e(r)}{T_{eo}}\right]^{3/2} . \qquad (3)$$

(a_1 is the limiter radius).

Typical values of S found for other tokamaks range between 0.2 and 0.4. For the temperature profile used her S=0.23. Hence, the uncertainty in our temperature profile could lead to an underestimate of $\langle \eta/\eta_{cl} \rangle$ by a factor of 2.

Results for a variety of plasma densities, currents and filling gases are shown in Fig. 2. For each gas, a cross-hatched region is indicated which marks the transition region between Maxwellian and non-Maxwellian spectra. The data obtained for He was obtained by pulsed-gas injection into an initially hydrogenic discharge, with density about 5×10^{12} cm^{-3}. Since the density for the points obtained in Fig. 2c is greater than 2.5×10^{13} cm^{-3}, we believe that the majority of ions in these discharges are helium. We call attention to the fact that $\langle \eta/\eta_{cl} \rangle$ is never significantly greater than unity in H_2 and D_2, and approaches the classical value of 1.8 in He. There is also a systematic decrease in $\langle \eta/\eta_{cl} \rangle$ for $\xi > \xi_c$ for all gases.

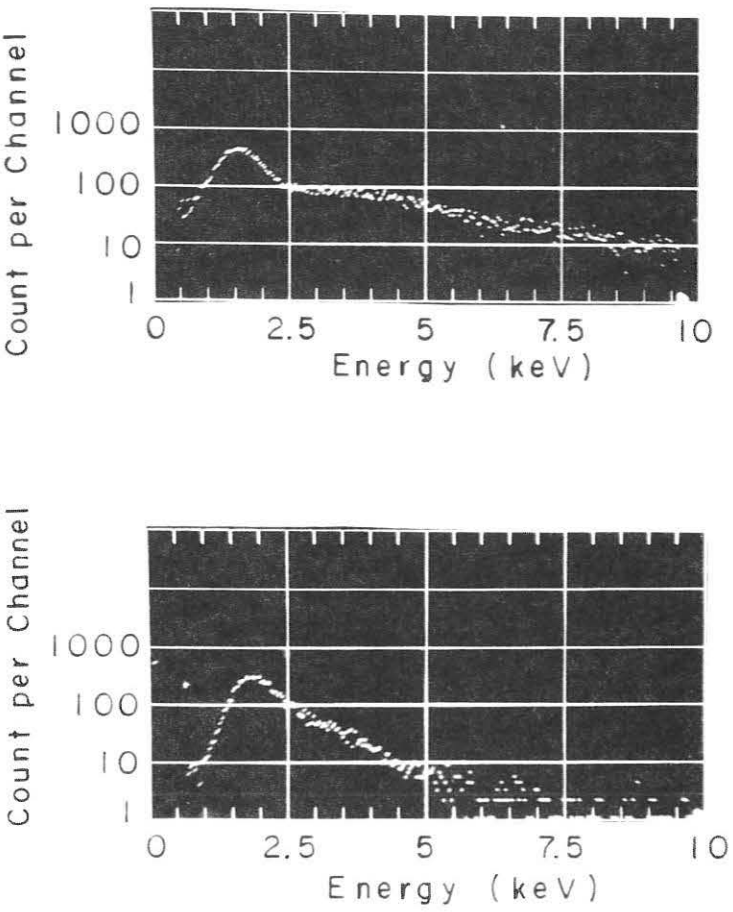

Fig. 1. Soft x-ray spectra obtained in slide-away (top) and Coulomb (bottom) regime.

We also report experiments concerned with effects of impurities on the resistivity measurements. Beginning with a well-conditioned machine, O_2 was injected into a hydrogenic discharge, and the partial pressure of O_2 was varied between 1 and 30×10^{-6} T. As a result, $\langle \eta/\eta_{cl} \rangle$ increased to about 2 and the electron temperature increased from 0.7 keV to 1 keV. The results

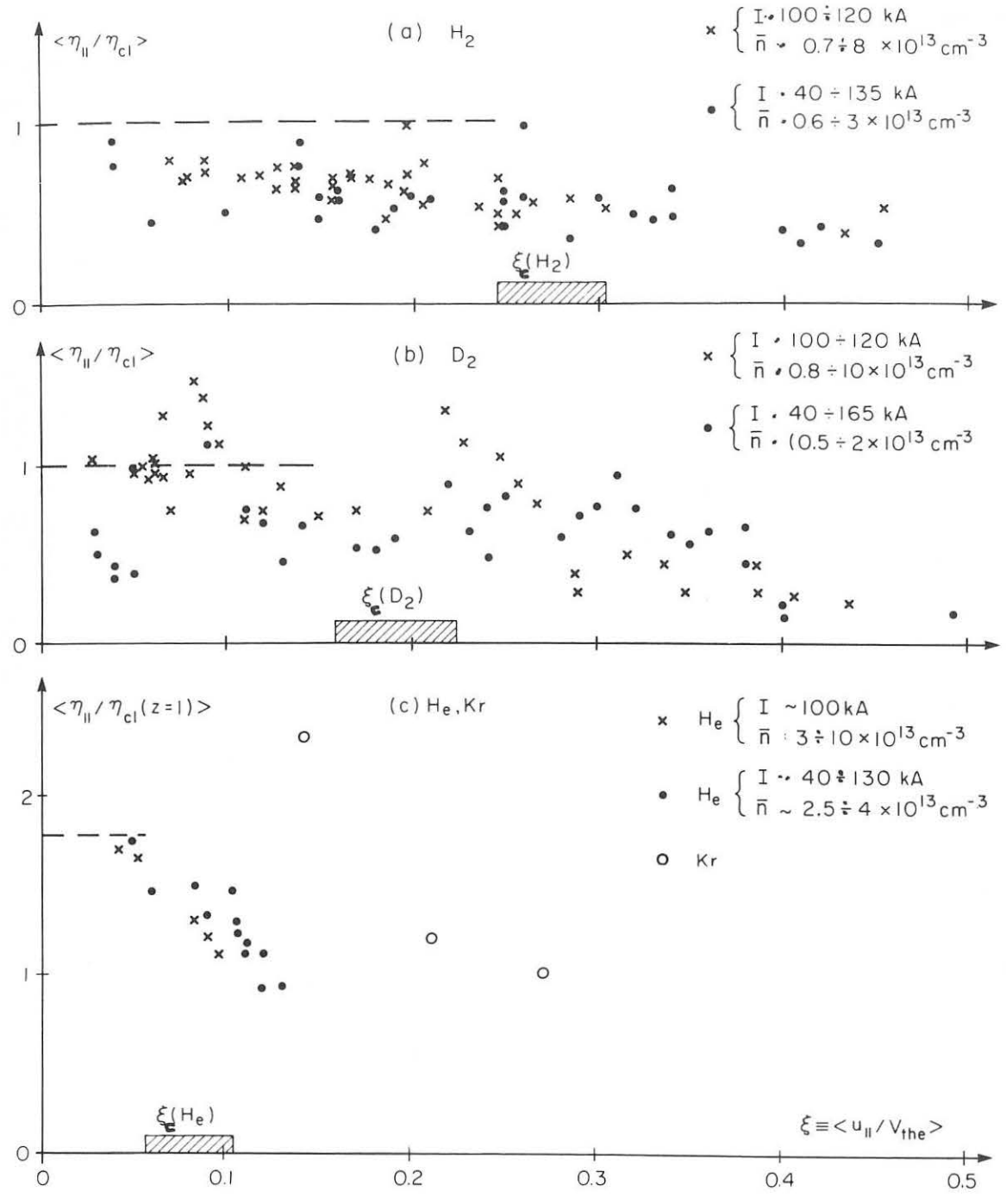

Fig. 2. Resistivity measurements in H_2 (a), D_2 (b), and He (c) as a function of the streaming parameter ξ.

are summarized in shots numbered 1-15 shown in Fig. 3. Then, normal tokamak operation ceased and the machine was discharge-cleaned in O_2 for about 30 min. Immediately, upon recommencing tokamak operation, $\langle \eta/\eta_{cl} \rangle$ increased to values of 3-5 and the electron temperature nearly doubled, as shown in shots 20-30 in Fig. 3. In addition to having higher voltage "anomaly" and electron temperature, these discharges differed in having an increasing rather than

the usual decreasing density with time, a much higher level of hard x-ray activity (100 mR/shot) and strong MHD instabilities[4]. Discharge cleaning in H_2 tended to reverse the process, but the normal duration of about 1 hr was not sufficient to reproduce the normal behaviour. Similar results were obtained by using N_2 rather than O_2 as the contaminating gas. We also note that values of ξ, obtainable for the contaminated machine, were generally in the range of 0.05-0.1. These results which show $\langle\eta/\eta_{cl}\rangle$ increasing to levels more typical of conventional tokamak operation give support to the credibility to results obtained under clean conditions.

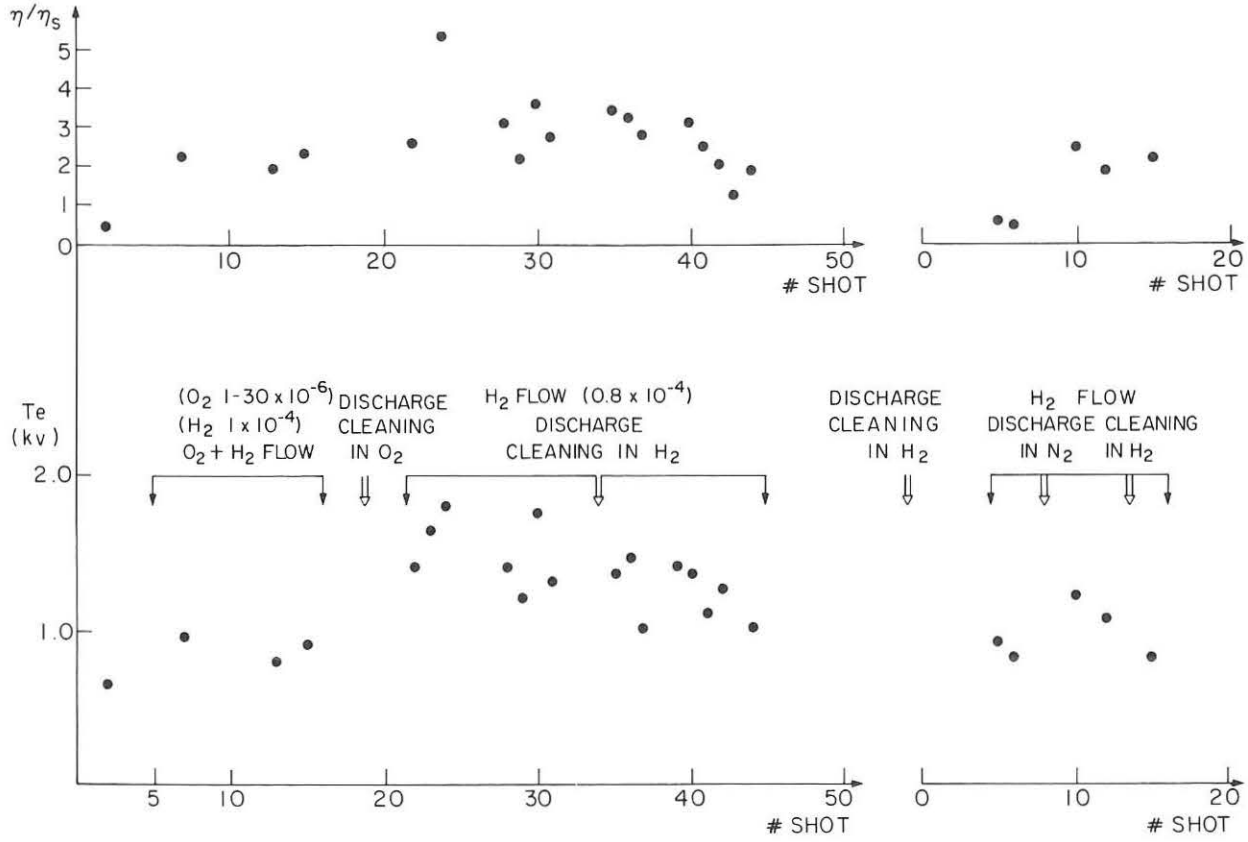

Fig. 3. Resistivity and temperature measurements in clean and contaminated conditions.

Below we will use a parameter α defined as $\alpha \equiv \langle\xi\rangle \langle\eta/\eta_{cl}\rangle$. In contaminated discharges the value of $\langle\eta/\eta_{cl}\rangle$ is increased, so that a higher value of α can be taken as an indication for a higher contamination level at the same value of ξ in different discharges.

Slide-away regime: Since plasmas with high ξ are known to be unstable in linear geometry (for example to ion-acoustic modes in the case $T_e > T_i$) we have been led to search for evidence of similar instabilities in the Alcator device. Additional motivation for this work was provided by the observation of high ion temperatures ($T_i \approx T_e \approx 1$ keV) even though the electron-ion equi-

libration time is much longer than the ion energy containment time. Here, we report the discovery of a band of strong rf emission in the vicinity of the ion plasma frequency ω_{pi}, extending from ω_{pi} to 5-10 ω_{pi}. The higher frequencies tend to occur first in time and correlate with the onset of hard x-ray emission (total dose $\sim$ 1 mR) and intense synchrotron radiation. The emission in the vicinity of ω_{pi} always occurs a few milliseconds later and correlates with the appearance of energetic ions (See Fig. 4). Thus, we identify the ω_{pi} radiation as being connected with the anomalous ion heating.

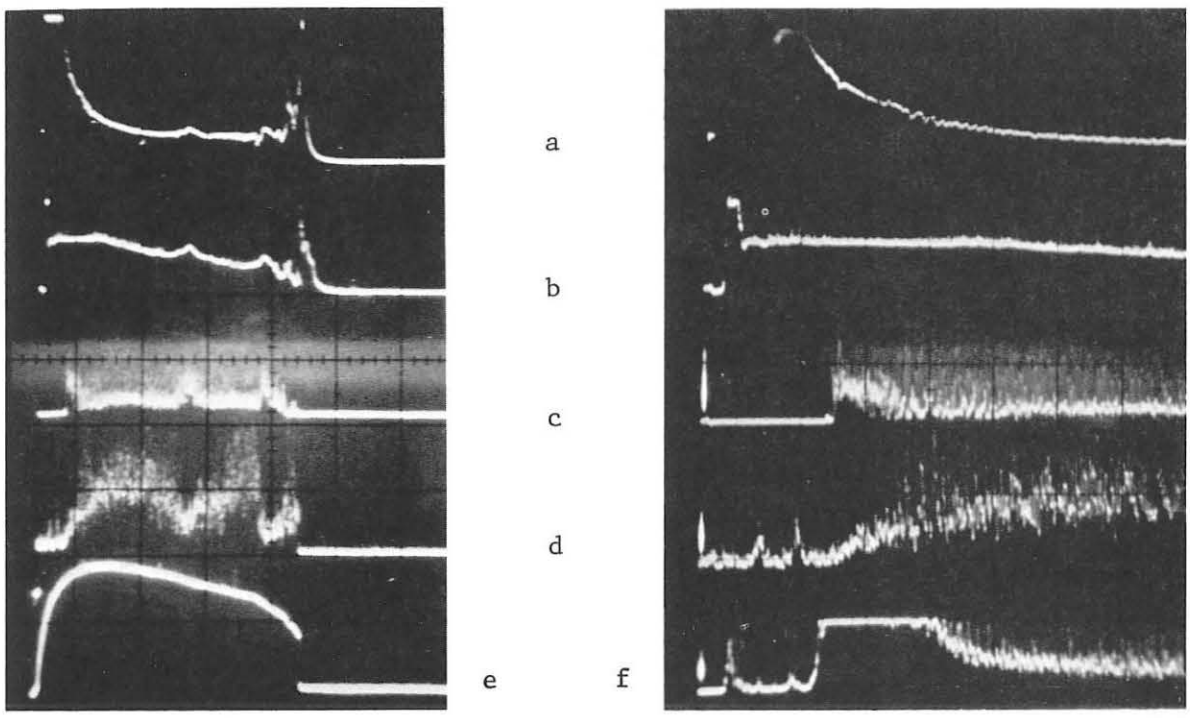

1. 2.

Fig. 4. Example of slide-away phenomena
a. loop voltage 1 V/div; b. electron density 1.2×10^{13} cm^{-3}/div; c. total rf-emission (arbitrary units); d. charge exchange neutrals: energy $\sim$ 2.5 keV; e. discharge current 65 kA/div; f. x-ray emission energy > 200 keV.
Sweep speed: 1. 50 msec/div; 2. 10 msec/div.

Measurements of the emission spectrum were taken with a small molybdenum-tipped probe, 0.6 mm in diameter. The probe is movable and can be positioned at any point within the 2.5 cm shadow of the limiter. Two spectrum analyzers were used to obtain the spectra in the ranges 300-2000 MHz and 1-20 GHz. The spectra were recorded by either repeated, fast (10 msec) sweeping of the analyzer, or by shot-to-shot scanning of the passband frequency.

In Fig. 5, we present the spectra obtained at three moments in time during the discharge. A strong peak at the lower end of the spectrum is found at frequencies corresponding to $f_{pi} = 210\sqrt{n_e/A}$, where A is the ion mass number. This dependence is displayed in Fig. 6, where we have plotted the density calculated by assuming the peak of the spectrum to correspond with f_{pi} vs

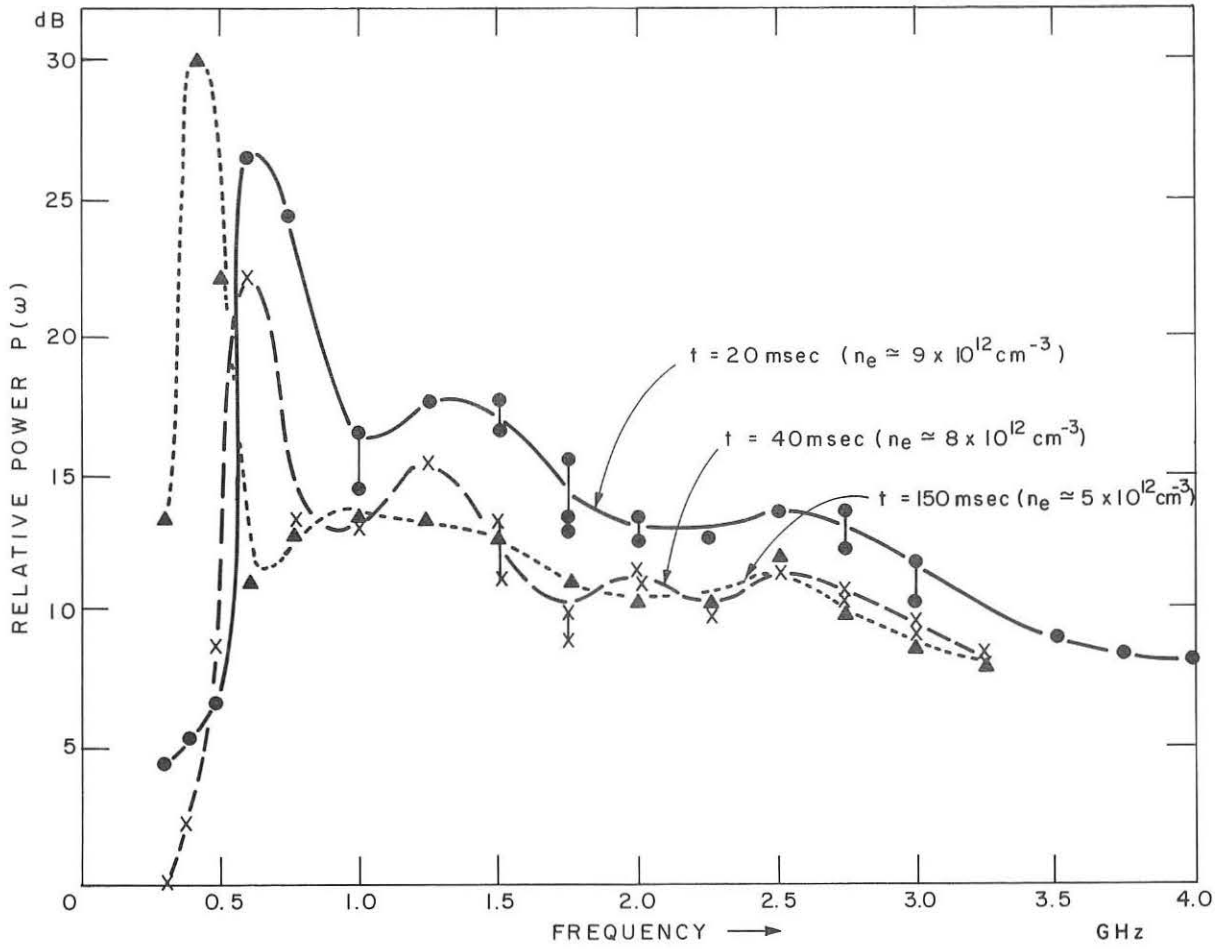

Fig. 5. Spectral emission from a slide-away discharge in hydrogen; shot-to-shot measurements were taken at B_ϕ = 40 kG, I = 100 kA.

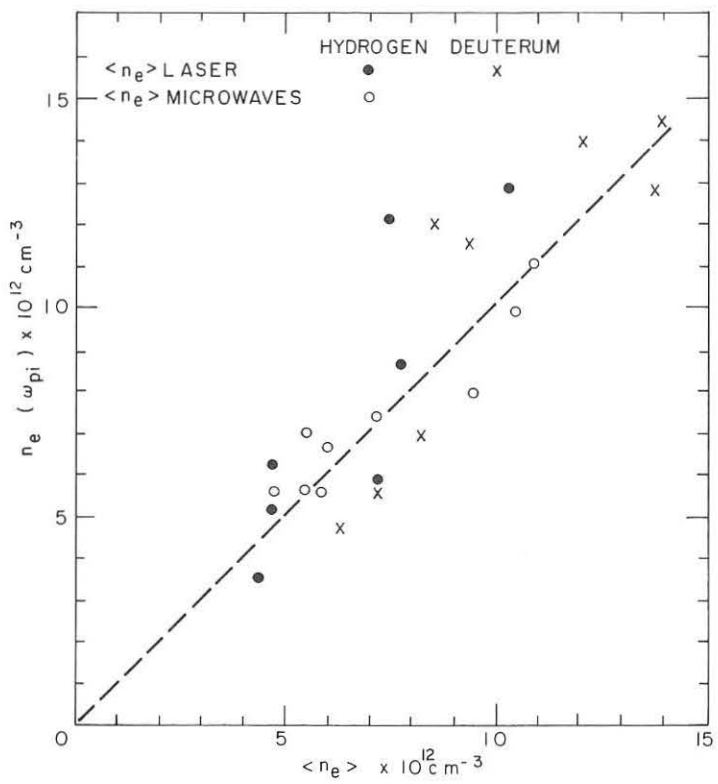

Fig. 6. The electron density $n_e(\omega_{pi})$ calculated when the measured peak frequency is interpreted as ω_{pi} vs the measured electron density $\langle n_e \rangle$.

the actual average density as measured by either 4 mm or 2 mm interferometers or by calibrated Thomson scattering. A 30 dB drop in the intensity is observed just below f_{pi}, and when the average density decreases during a discharge pulse, this cut-off moves

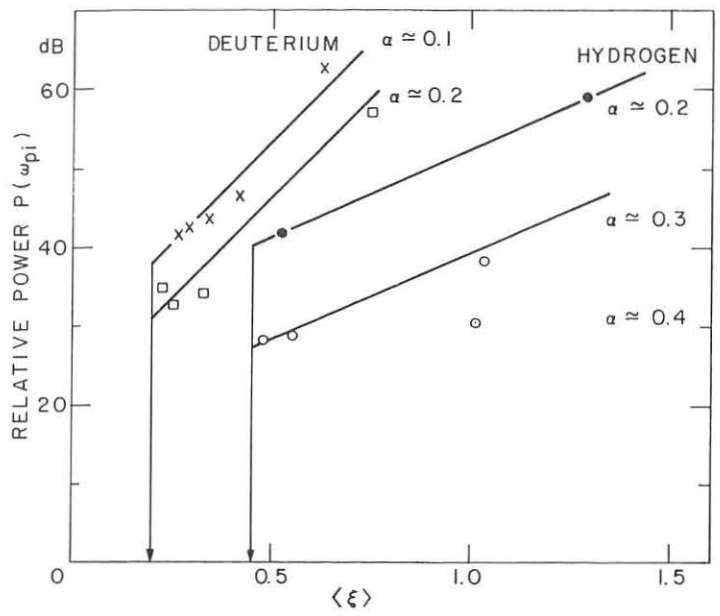

Fig. 7. Relative power level $P(\omega_{pi})$ of the radiation emitted at ω_{pi}.

accordingly. The spectrum extends to several GHz where the emission level becomes comparable to the sensitivity of the analyzer ($\sim$ 45 dB). The relative power $P(\omega_{pi})$ of the emitted radiation at f_{pi} as a function of ξ is found to have a distinct threshold at values of 0.45 for hydrogen and 0.2 for deuterium discharges as shown in Fig. 7. There are also indications that the presence of impurities leads to a decrease of the emitted power. Discharges with higher impurity content (α = 0.3 to 0.4) have $P(\omega_{pi})$ decreases by 15 to 20 dB.

The fact that the emission is cut off below ω_{pi} tends to rule out turbulence associated with classical current-driven ion-acoustic waves. In this regime of operation $\omega_{pe}^2 >> \omega_{ce}^2$ and the lower hybrid resonance frequency $\omega_{LH} \approx \omega_{pi}$. This suggests the excitation of lower hybrid modes which propagate for $\omega > \omega_{pi}$, whose mechanism has been investigated[5].

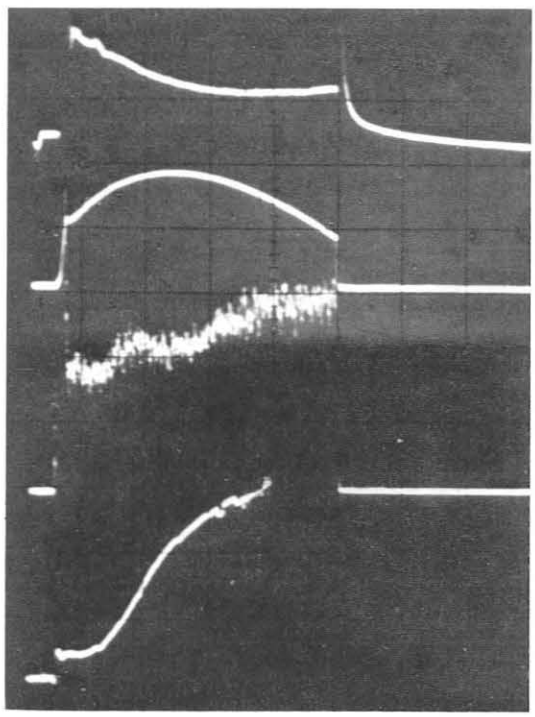

Sweep speed: 20 msec/div.

Fig. 8. Example of a discharge in the Coulomb regime: a loop voltage 2 V/div; b. discharge current 65 kA/div; c. O^{VI} emission at λ = 1032 Å, 6.8×10^{15} photons/sec/cm^2.sterad/div; d. electron density 4.6×10^{13} cm^3/div.

Coulomb regime: After formation of a discharge at normal filling pressure of 1×10^{-4} T, gas is injected by means of a pulsed gas valve. In this way, discharges with $\langle n_e \rangle$ up to 2×10^{14} cm^{-3} have been studied. Typical traces of voltage, current, and density for this mode of operation are shown in Fig. 8. In this mode, the electron and ion distribution functions are nearly

Maxwellian (c.f. Fig. 1.b), and the resistivity appears to be close to classical as evidenced by data presented in Fig. 2 for $\xi << \xi_c$. Both soft x-ray and visible bremsstrahlung measurements show that the effective Z (defined here as the ratio of measured to computed free-free hydrogenic bremsstrahlung decreases from 5-10 at low density ($\sim 1\times10^{13}$ cm^{-3}) to near unity at high density (1×10^{14} cm^{-3}). This implies that the relative impurity concentration in the centre of the plasma decreases as the density is increased, a conclusion which is also supported by the density dependence of the UV-lines of light impurities, for example, O^{VI} as shown in Fig. 8.

Poloidal beta $\beta_\theta \equiv \langle nk(T_e+T_i)\rangle/B_\theta^2(a_1)/2\mu_o$ and gross energy replacement time $\tau_E \equiv \frac{3}{2}\langle nk(T_e+T_i)\rangle$Volume/I.V. have been measured (see Fig.9). Here the profiles quoted above are used. The data points represent τ_E, neglecting the ion energy content, and the dashed line indicates the effect of including the ions. The energy replacement time is roughly proportional to n_e and has weak (if any) dependence on I and B_ϕ. The poloidal beta, consistent with the measurement of τ_E, scales as $\beta_\theta \propto n_e/I^p$, where $p \approx 1$. We also find the maximum density is proportional to the maximum value of I, which suggests a limiting value of β_θ.

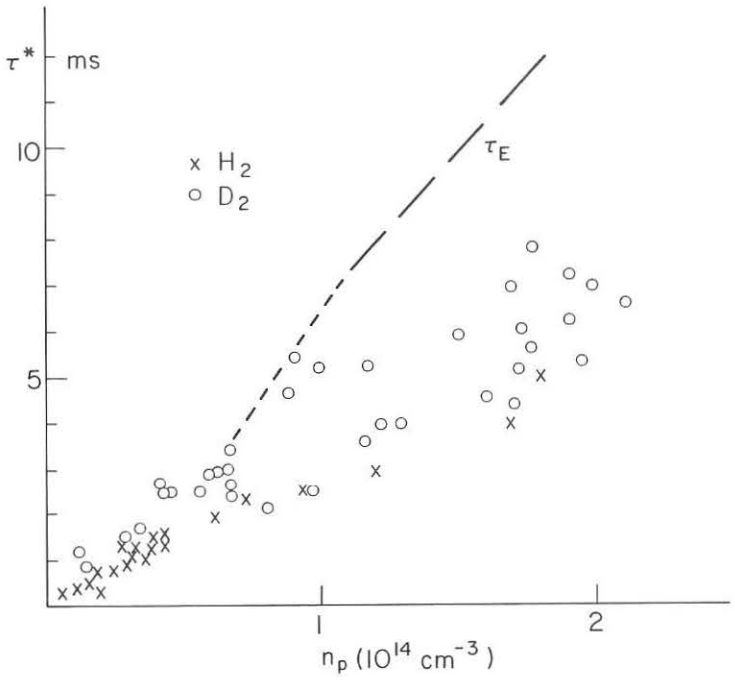

Fig. 9. Energy replacement time vs density.

R.F. heating: Ion heating by rf injection near lower hybrid frequency ω_{LH} has also been studied[6]. A pulse of rf power, frequency 2.45 GHz, peak power 70 kW and width variable up to 100 msec have been applied by means of an S-band waveguide flush-mounted in the vacuum chamber wall and oriented so that $\vec{E} \parallel \vec{B}$. The total absorption efficiency is high with 70-80% of the forward power absorbed. No deleterious effects (such as density rise or impurity increase) on the discharge are found. Typical ion temperature rise is on the order of 100 eV (see Fig. 10). Strong tail-heating is also observed; the effect is nonlinear in the applied power. For ion heating to occur, it is not necessary to satisfy $\omega = \omega_{LH}$ anywhere in the plasma.

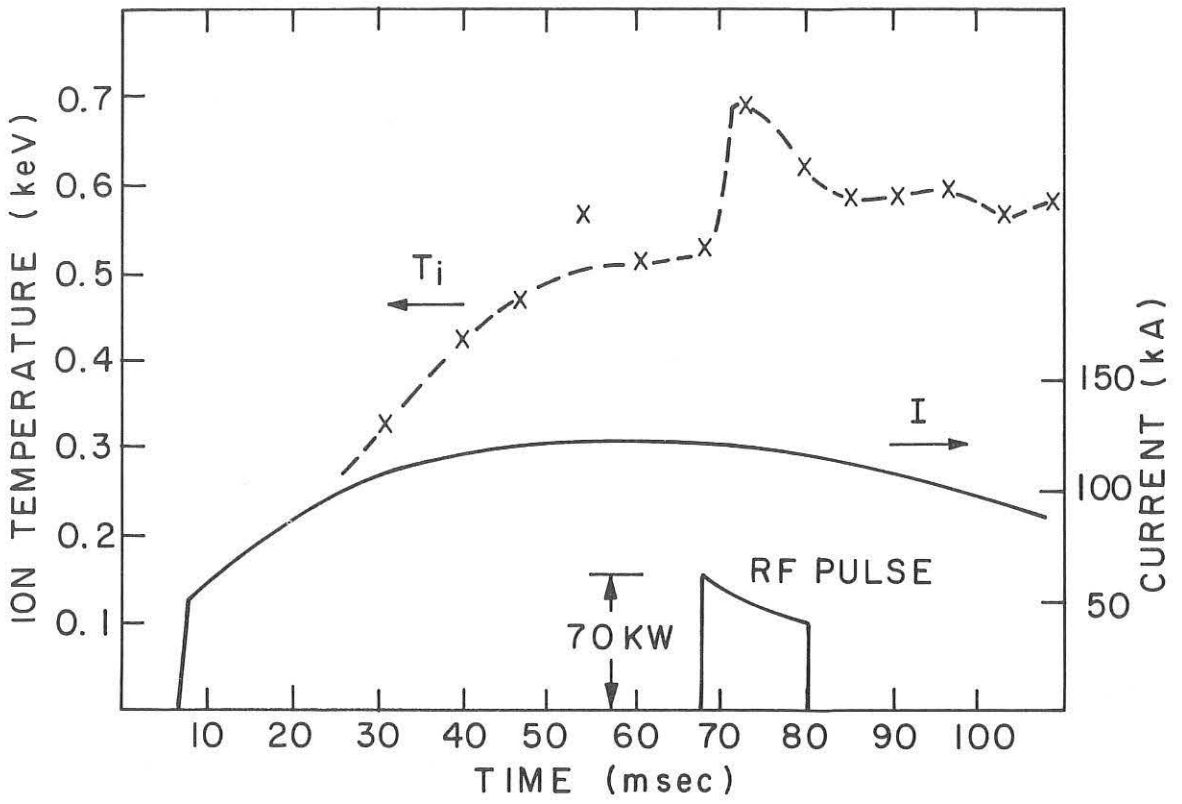

Fig. 10. Development of the ion temperature with rf heating applied.

Acknowledgements

Supported in part by the U.S. Energy Research and Development Administration, Contract E(11-1)3070, the Association Euratom-FOM, Rijnhuizen, Jutphaas, The Netherlands and the Association Euratom-CNEN, Frascati, Italy.

It is a pleasure to acknowledge the contributions of the staff and the use of the facilities of the Francis Bitter National Magnet Laboratory supported by the National Science Foundation.

References

[1] Ascoli-Bartoli, U. et al., Proc. Fifth Int. Conf. on Plasma Phys. and Contr. Nucl. Fusion Research, Tokyo, 1974, I, 191, P. IAEA-CN-33/A 8-4.

[2] Pieroni, L. and Segre, S.E., Phys. Rev. Letters 34 (1975) 928.

[3] Segre, S.E. and Pieroni, L., Phys. Letters 51A (1975) 25.

[4] De Kock, L.C.J.M., et al., Rijnhuizen Report 74-86 (1974).

[5] Coppi, B., et al., M.I.T.(Cambridge, Mass.) Report PRR 758 (1975) (Submitted to Nuclear Fusion).

[6] Parker, R.R., R.L.E.-M.I.T. (Cambridge, Mass.) Quarterly Progress Report 102 (July 1971).

CONFINEMENT AND NEUTRAL INJECTION EXPERIMENTS IN ORMAK*

The ORMAK Group
Presented by J. F. Lyon
Oak Ridge National Laboratory, Oak Ridge, Tennessee, U.S.A.

Abstract: The ORMAK operating regime has been extended to higher toroidal fields, discharge currents, and neutral injection power. Confinement studies have concentrated on anomalous electron energy transport (through scaling studies at constant q), and the effects of MHD instabilities (through soft x-ray fluctuations) and impurities (through $Z_{eff}(r)$ measurements). Ion heating increases linearly with coinjection power, and counterinjection heating efficiency increases with discharge current.

Machine Operation Improvements: Previous studies of confinement [1] and neutral beam injection [2] in ORMAK were conducted at toroidal fields $B_T \leq$ 18 kG, discharge currents $I \leq 130$ kA, and 25 kV neutral injection power $P_{inj} \leq 45$ kW per injection direction. Typical plasma parameters at I = 95 kA were $T_e(r=0) \sim 700$ eV and $T_i(r=0) \sim 220$ eV for $\bar{n}_e$ (central chord average) $\sim 2 \times 10^{13}$ cm^{-3}, and $T_i(r=0) \sim 275$ eV for coinjection. Since the Tokyo IAEA conference, confinement and neutral injection studies have used improved machine parameters ($B_T \leq 25$ kG, $I \leq 200$ kA, $P_{inj} \leq 180$ per injection direction at 30 kV) with feedback control of the vertical field and with oxygen rather than hydrogen discharge cleaning. Typical plasma parameters at 160 kA are now $T_e(0) \sim 1200$ eV and $T_i(0) \sim 360$ eV for $\bar{n}_e \sim 2 \times 10^{13}$ cm^{-3}, and $T_i(0) \sim 500$ eV with injection.

Confinement Studies Review: Transport properties have previously been discussed [1] with some emphasis on the differences in the discharge characteristics in the high density (large amplitude m=2 MHD oscillations in poloidal field B_θ, peaked (high) $T_e(r)$ type A discharge) and low density (small amplitude $m \geq 3$ oscillations, broad (low) $T_e(r)$ type B discharge) regimes. The electron energy transport was found to be anomalous, although the gross

energy confinement time τ_E was in reasonable agreement with pseudoclassical [3] scaling. Possible reasons for the electron anomaly are (1) impurities and (2) instabilities (especially MHD instabilities and dissipative trapped electron modes). The main theme of the confinement study was therefore to evaluate these effects through (1) scaling experiments (I varied) at a constant $q(a_\ell)$, the safety factor at the limiter (a_ℓ = 23 cm), and fixed filling pressure, (2) studies of spatially resolved soft x-ray fluctuations, and (3) estimates of $Z_{eff}(r)$ and $P_{radiation}(r)$ from different measurements.

Constant $q(a_\ell)$ Experiments: The central framework for the confinement study was chosen to be the variation of the discharge characteristics with I at constant $q(a_\ell)$. This allowed variation of the ohmic heating power from 120 kW to 550 kW without changing the gross magnetic configuration, and hence gross MHD stability. In this sequence of experiments $q(a_\ell)$ was held constant (q = 5) along with the hydrogen filling pressure (4.5 x 10^{-4} torr), and the ohmic heating current I was varied from 30 kA

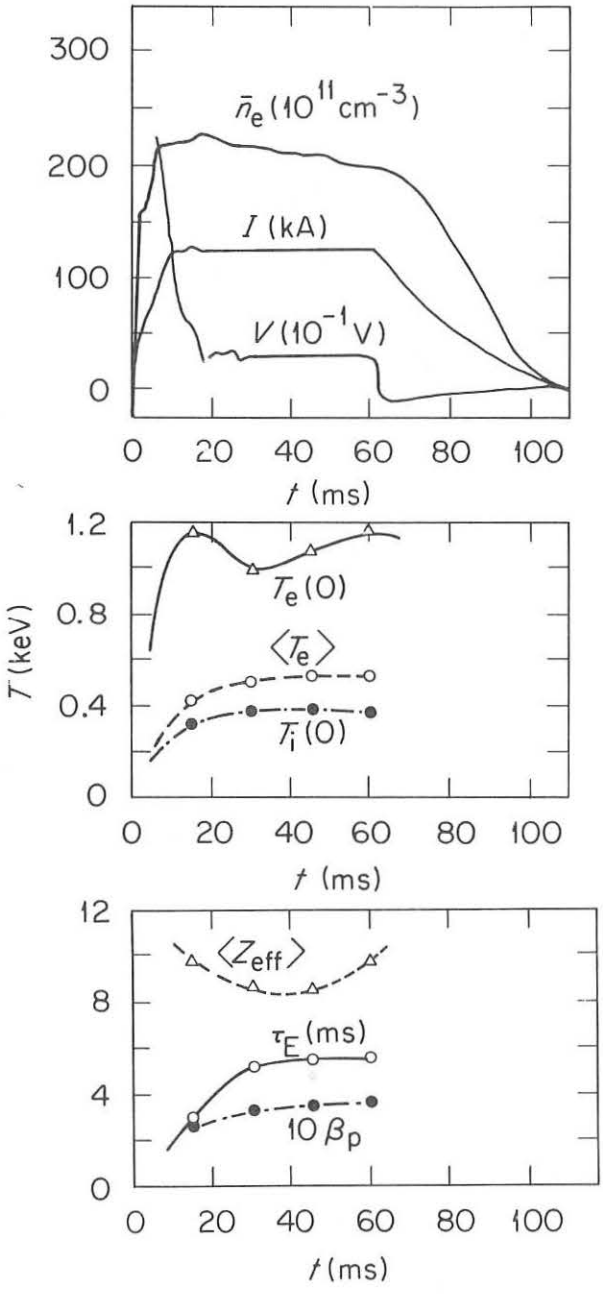

Fig. 1. Time behavior of typical 120 kA discharge in constant $q(a_\ell)$ sequence.

to 155 kA, corresponding to a toroidal field variation from 4.5 kG to 22.5 kG.

Figure 1 shows the time evolution of the principal parameters for a typical discharge (I = 120 kA, B_T = 19.0 kG) in this series. Here $\langle T_e \rangle$ is a particle average and $\langle Z_{eff} \rangle$ a volume average, with $\langle Z_{eff} \rangle$ estimated from

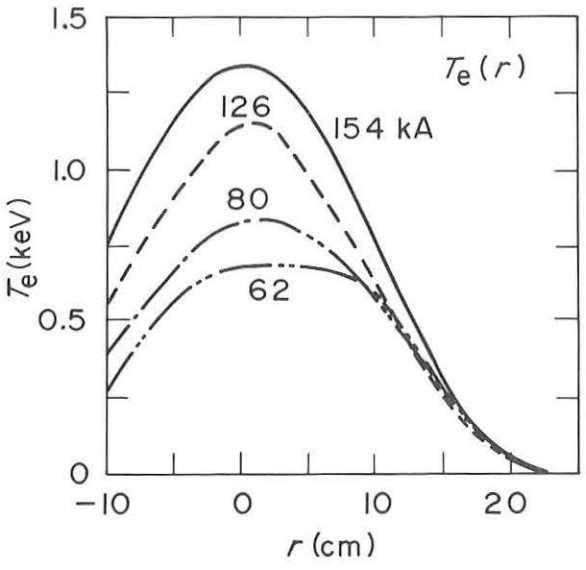

Fig. 2. Variation of electron temperature profiles with discharge current in the constant $q(a_\ell)$ sequence at 45 ms.

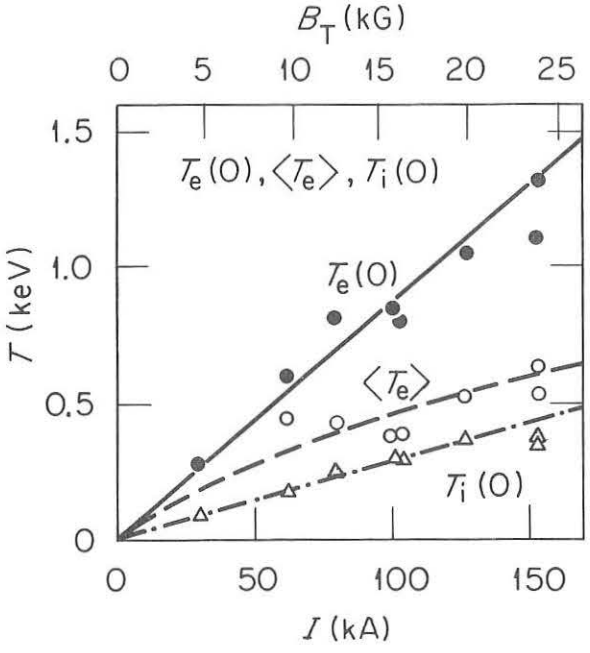

Fig. 3. Variation of plasma temperatures with I in constant $q(a_\ell)$ sequence at 45 ms.

the plasma resistance. Figure 2 shows the variation of $T_e(r)$, and Fig. 3 shows the variation of $T_i(0)$, $T_e(0)$, and $\langle T_e \rangle$ with discharge current at t = 45 ms. The central core temperature increases linearly with current, while there is little change in the outer (or edge) electron temperature. This is reflected in the slower increase ($\sim I^{2/3}$) of the average electron temperature $\langle T_e \rangle$ up to 0.65 keV. At low current (I $\leq$ 100 kA) the $T_e(r)$ profile is similar to the type B profile of the Tokyo paper [1]; while at high current the $T_e(r)$ profile is peaked, similar to a type A case.

There is no significant change in the electron density profile with increasing plasma current, with $n_e(r) \sim [1 - (r/a_\ell)^2]^2$. Both $n_e(0)$ and $\bar{n}_e$

increase linearly with current, with $\bar{n}_e \approx 1.6 \times 10^{11}$ I(kA) cm^{-3} and $n_e(0) \approx 1.6\ \bar{n}_e$. The calculated β_p is roughly constant ($\simeq 0.3$) as suggested by the previously observed scaling $\beta_p \sim n_e/I$ while the plasma resistance decreases inversely with increasing I. Therefore the gross energy confinement time τ_E is roughly linear with current (GMS scaling [4]), as shown in Fig. 4. Pseudoclassical scaling [3] agrees reasonably well with the experimental energy confinement times, but fails to predict the experimental dependence of the energy confinement time on electron density ($\tau_E \sim n_e^{\alpha}$, $\alpha \approx 1$) for other conditions fixed. Also, τ_E scaling expected for dissipative trapped electron modes is higher than the experimental scaling by a factor of 2 to 5.

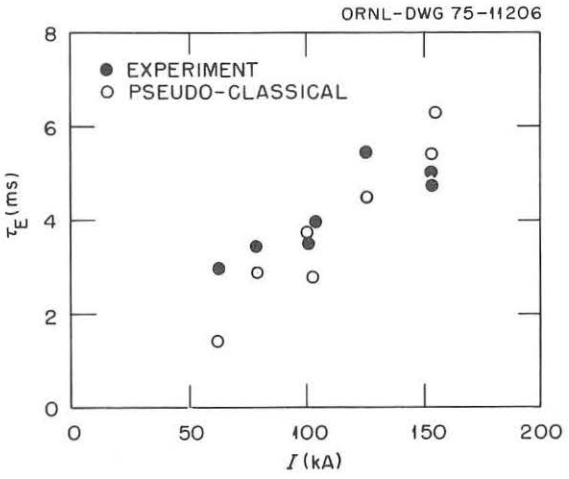

Fig. 4. Variation of measured and calculated energy confinement time with current for constant $q(a_\ell)$ at 45 ms.

The ion energy confinement still appears to be approximately neoclassical [1,5] in ORMAK. From Fig. 3 $T_i(0)$ is seen to increase almost linearly with I, except at the highest current. This linear dependence agrees with the Artsimovich plateau scaling [6], $T_i \sim (n_e I B_T)^{1/3}/\sqrt{A_i} \sim I$ for the constant $q(a_\ell)$ study. A more exact calculation including all the terms in the ion energy balance in a 1-D dynamic transport code and using Hinton-Hazeltine [5] values for ion thermal conductivity gives essentially the same answer, assuming $Z_{eff} = 10$. Charge-exchange measurements indicate that $T_i(r)$ is flatter than $n_e(r)$, $T_i \sim 1 - (r/a_\ell)^{\beta}$ where $\beta \approx 2.5$-3, although $T_i(r)/T_i(0) \sim n_e(r)/n_e(0)$ is assumed for plasma energy estimation.

Internal MHD Oscillations: Fluctuations in the soft x-ray emission from ORMAK were studied with an array of nine planar silicon (PIN) diode detectors collimated to view radial chords across a minor cross section. The chord minimum tangency points extended from -2 cm (inside) to +14 cm (outside) in 2-cm intervals, and the x-ray signals were assumed to be approximately representative of these points. This arrangement of detectors permitted distinguishing between odd and even poloidal mode numbers (m) only near the center of the plasma, and the investigations were confined to a single toroidal location. Fluctuations in the soft x-ray intensity studied during the sequence of constant $q(a_\ell)$ experiments show features similar to those obtained on the ST [7] and TFR [8] tokamaks.

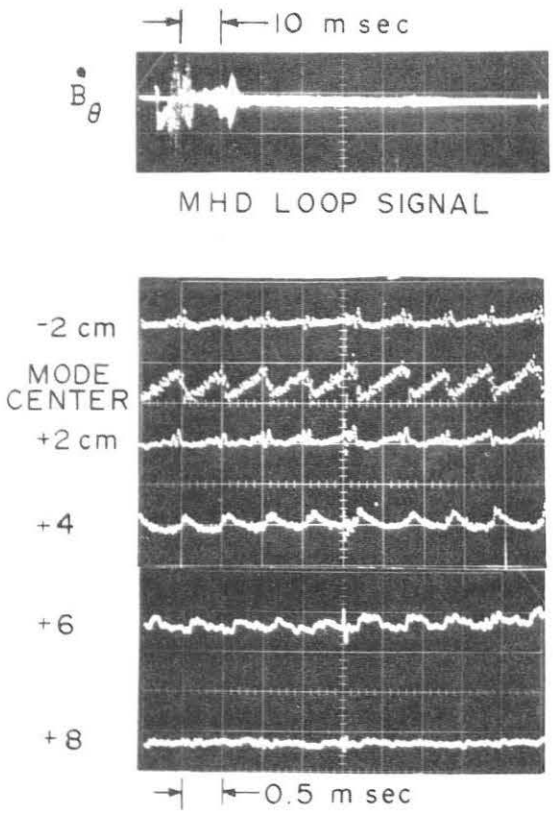

Fig. 5. Sawtooth waveforms from collimated soft x-ray diagnostic for type B discharges at 80 kA and $q(a_\ell) = 5$.

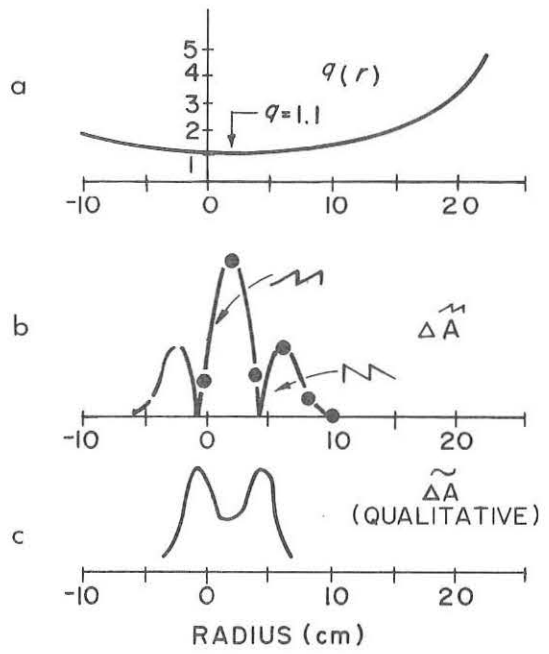

Fig. 6. Radial dependence of (a) safety factor q, (b) sawtooth amplitude, and (c) m=1 oscillation amplitude for 80 kA, q(a)=5 type B discharges.

For the low current, type B discharges, fluctuations were dominated by "sawtooth" oscillations (shown in Fig. 5), with m odd (assumed 0) and a period of $\sim$ 0.5 ms, and with the rapidly changing portion associated with a growing oscillation (m even, assumed 1) at the $\tilde{B}_\theta$ frequency. Figure 6 is for one type of such discharge in the constant $q(a_\ell)$ sequence and compares the radial dependence of the fluctuation with q(r) calculated from the laser $T_e(r)$ measurement assuming $j(r) \sim T_e^{3/2}$ (E fully penetrated, Z_{eff} constant).

Figure 7 shows a similar comparison for a higher current, type A discharge. In the interior the fluctuations are dominated by m=1 oscillations at the $\tilde{B}_\theta$ frequency. These oscillations are more continuous than for type B, and themselves are dominant compared with the sawtooth. The m number of the x-ray oscillations at larger radii ($\sim$ 10-14 cm), though not measured, is believed to be m = 2 by comparison with [7]. A phase reversal is noted between the last two points, and we assume q = 2 is nearby.

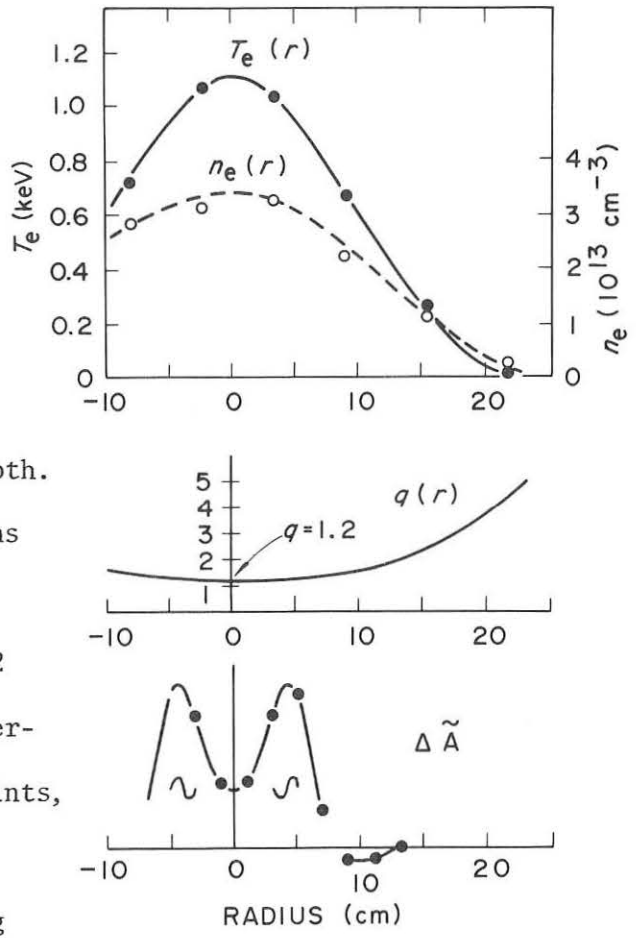

Fig. 7. Radial dependence of (a) electron temperature and density profiles, (b) safety factor q, and (c) x-ray oscillation amplitude for 120 kA, $q(a_\ell)$ = 5 type A discharges.

The locations of q = 2 resulting from $j \sim T_e^{3/2}$ modeling are generally in reasonable agreement with locations derived from the soft x-rays. Such agreement is sometimes found for the location of q = 1, but frequently q(0) from the $T_e(r)$ profile is higher than 1 for cases where sawtooth oscillations were consistently observed. This latter circumstance includes cases in which

the readjustment of $T_e(r)$ required to yield $q(0) = 1$ is outside the limits permitted by possible error in measuring T_e. We believe that these results indicate a nonuniform $Z_{eff}(r)$, and thus inaccuracies in the $j \sim T_e^{3/2}$ model.

Estimates of $Z_{eff}(r)$: Three different methods are used to estimate the effective ionic charge $Z_{eff}(r)$ in evaluating the effect of impurities on the radial electron power flow: (1) enhancement of hydrogenic bremsstrahlung from measurement of central, spatially collimated soft x-ray energy spectra; (2) charge-exchange measurement along two radial chords of 90° pitch-angle scattering of injected fast ions [2,9]; and (3) plasma resistance and $T_e(r)$ profiles. The present model used to calculate $Z_{eff}(r)$ from resistance assumed $j(r)$ to have the form $j_0[1 - (r/a)^{\alpha}]^{\beta}$ where the parameters j_0, α, β, are determined from the total plasma current, and the calculated positions of q=1 and q=2 are made to agree with the mode-rational surface positions determined from the internal MHD oscillations. Here we assume Spitzer resistivity and a fully penetrated electric field. Figure 8 shows these estimates of $Z_{eff}(r)$, along with $Z_{\eta}(r)$ model used in the Tokyo IAEA paper [1] which assumes that constant ratio of high Z impurity density to proton density required to make the calculated and measured resistance agree. This example is similar to the 126 kA case in the constant $q(a_\ell)$ sequence but at lower

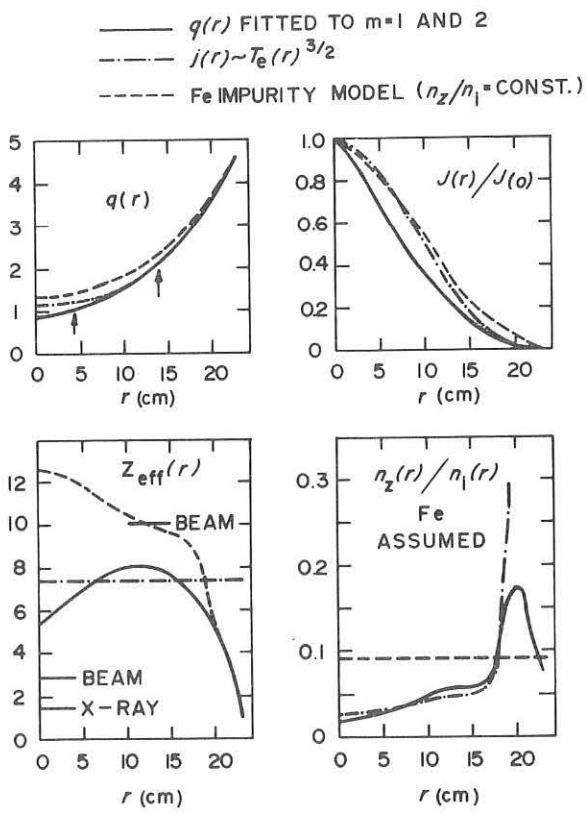

Fig. 8. Safety factor, current profile, $Z_{eff}(r)$, and relative impurity ion density calculated from (1) $q(r)$ fitted to $q = 1$ and 2 (solid curves), (2) $j(r) \sim T_e(r)^{3/2}$ (dashed-dot curves), and (3) from Fe impurity model assuming n_Z/n_i = constant (Z_η).

density ($\bar{n}_e \sim 1.4 \times 10^{13}$ cm^{-3}). Although the uncertainties of each measurement are too large to determine $Z_{eff}(r)$, the best consistency is obtained by discarding the $Z_{eff}(r)$ central peaking arising from the previous impurity model (Z_η). The $Z_{eff}(r)$ obtained from the calculated q(r) profile does not require any assumptions about impurity species. If we assume the dominant impurity is iron (the Fe XV and Fe XVI lines are now stronger than the carbon lines and second to the oxygen lines in intensity), then n_Z/n_i is as shown in Fig. 8. A significant peaking occurs near the plasma edge which becomes more exaggerated if a low Z impurity (such as oxygen) plays a significant role.

Electron Radial Power Flow: The results from the previous two sections can be combined to give a qualitative picture of the radial power flow in a typical discharge. First, near the axis the power flow due to internal disruptions is significant, but the energy involved is small. For example, this energy transport is estimated to be ~30% of the total power contained within the q=1 surface (but only ~2% of the total ohmic heating power) for the type B case shown in Fig. 6 and only ~10% for the higher density type A case shown in Fig. 7. The energy flow associated with internal m=1 disruptions ($\sim 3/2\ n\Delta T_e/\tau$) is calculated from the soft x-ray sawtooth amplitude (giving ΔT_e), period τ, and plasma density. Second, in the outer part of the plasma the radiation loss is dominant. Measurements of the radiated power with a pyroelectric detector indicate that an essentially constant fraction (~70%) of the ohmic heating power is lost via radiation over most of the discharge duration and for the entire current range of the constant $q(a_\ell)$ sequence of experiments. This fraction is in rough agreement with results from radially movable point limiter experiments and with measurements made using an array of liner thermocouples. Measurements obtained by varying the radial position of the pyroelectric radiometer indicate that the

radiation comes mainly from the outer part of the plasma, rather than from a central core. The biggest unknown with respect to the radial power flow mechanism is in the important middle region where the m=2 mode rational surface is located. This middle region controls the bulk of the radial power flow, and its mechanism is not well understood.

Neutral Beam Injection Studies: Injection experiments since the Tokyo IAEA conference have principally addressed two main themes: (1) ion temperature scaling with increasing injection power and (2) improvement of counterinjection heating efficiency and reduction of plasma deterioration with increasing toroidal current. Here coinjection indicates injection parallel to the discharge current and counterinjection antiparallel to I. Calorimetric measurements in ORMAK and test stand operation of ORMAK injectors have shown that the measured neutral power injected into ORMAK is a factor of 2 less (at 25 kV) than previously estimated, requiring an upward revision in the ion heating efficiency.

Figure 9 shows the variation of central ion temperature with coinjection neutral beam power. Over the range the ion temperature increases linearly with injected power. A similar linear scaling of ion temperature with injection power is also obtained at other plasma densities and discharge currents, as well as for D^0 injection into an H^+ plasma. In these experiments the possibility of beam perturbation of the normally dominant electron-ion heat transfer ($P_{ei} \sim n_e n_i / \sqrt{T_i}$) was minimized by adjusting the filling pressure and the fedback vertical field to keep the plasma density, plasma shift, and

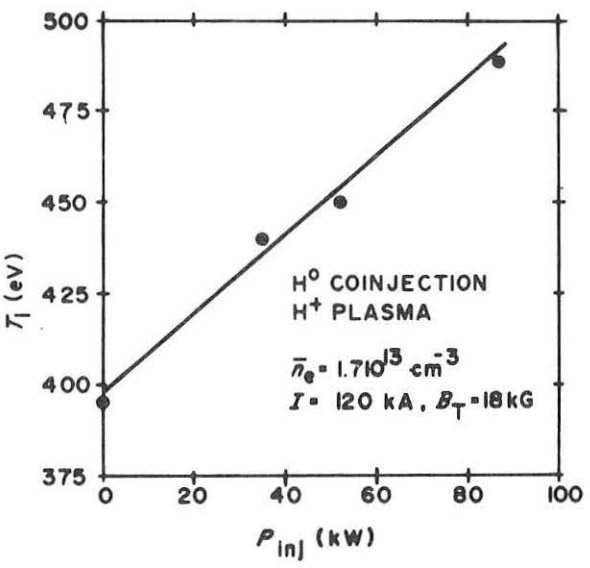

Fig. 9. Linear ion heating with H^0 coinjection power.

discharge current approximately constant while the number of injectors used was changed. The net ion heating rate ($\sim$ 1 eV/kW) at low currents ($\lesssim$ 100 kA) can be made to agree with that obtained from a perturbation calculation for a reasonable set of plasma parameters (principally Z_{eff}). In this calculation [9] the beam power input to the ions is calculated from a Fokker-Planck treatment of the fast (injected) ion distribution, including the effect of scattering into the "loss region." However, at higher plasma currents ($\sim$ 160 kA) the experimental ion heating rate is approximately unchanged whereas the calculated value [10] doubles because of the correspondingly higher T_e and consequently greater fraction of injected power transferred to the ions. At the higher current the loss region is not important (and hence the role of Z_{eff} is reduced) and there is also less uncertainty in the larger ion temperature increase obtained. Since the perturbation calculation [9] gives a net ion heating rate $\Delta T_i/P_{beam}$ which varies (approximately as $T_i^{3/2}\ \bar{G}_i\ /n_e^2(n_+/n_e)$, where $\bar{G}_i$ is the volume density-averaged fraction of beam power going to the ions, the largest remaining uncertainty in the apparent disagreement is the relatively uncertain proton deficiency n_+/n_e.

Figure 10 shows the effect of increasing coinjected power on the electron temperature profile. For 35 kW D^0 injection the central T_e rises, but the volume average T_e remains at 410 eV. For 95 kW D^0 coinjection the $T_e(r)$ distribution broadens, and the volume density-averaged T_e increases to 500 eV. There is consistent evidence for net electron heating that is typically $\sim$ 100 eV out of 800 eV for $T_e(0)$, in rough agreement with the perturbation calculation values.

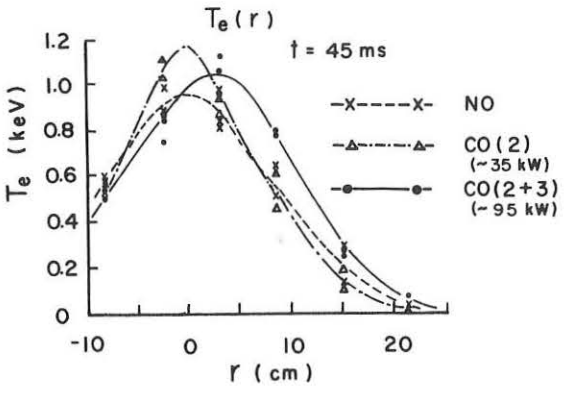

Fig. 10. Effect of increasing D^0 coinjection power on $T_e(r)$ for H^+ plasma. Here I = 110 kA, $\bar{n}_e$ = 1.9 x 10^{13} cm^{-3}, and B_T = 18 kG.

Counterinjection Improvement with Toroidal Current: At low discharge currents ($\leq$ 100 kA) counterinjection leads to little net ion heating in ORMAK. The relatively poor ion heating efficiency seems to be due primarily to the fact that counterinjected fast ions can pitch-angle scatter into the "loss region" [11] in phase space produced by the large radial excursions (to the limiter or wall) of the unconfined fast-ion "banana" drift orbits (for particular pitch angles) before they give up a significant part of their energy to plasma ions [9]. Direct evidence for the higher loss of counterinjected fast ion can be seen in Fig. 11 which shows the perpendicular fast ion energy distribution obtained for coinjection and for counterinjection at low discharge current (90 kA) with a hydrogen beam and plasma. The two perpendicular energy distributions are similar, although considerably fewer (by about a factor of 5) counterinjected beam ions scatter through 90°. In addition, counterinjection at low discharge currents ($\leq$ 100 kA) is accompanied by deleterious effects on the discharge: decreased plasma stability, poor discharge reproducibility, lowered central electron temperature, and a tendency toward a decrease in density.

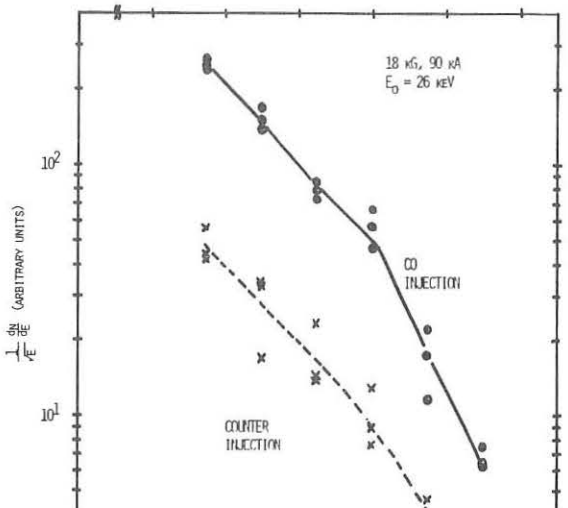

Fig. 11. Increase loss (relative to coinjection) for counter-injected fast ions scattered ~ 90° from the injected direction.

For higher currents, differences between coinjection and counterinjection due to loss region effects should decrease since the effect of the loss region scales as the ion gyroradius in the poloidal field, that is, the energy at which a fast ion orbit (characterized by an initial radius and

pitch angle) first hits the wall scales as I^2. Measurements on 155-kA discharges confirm the reduced singificance of the loss region at high currents in three ways. First, the perpendicular fast ion energy distributions obtained are similar to those shown in Fig. 11, but the counterinjection data now falls only a factor of 2 below the coinjected points. Second, counterinjection produces 45% to 60% as much ion heating as coinjection for similar discharges at 155 kA, as contrasted with a negligible amount at 95 kA. By comparison, Fokker-Planck calculations for the fast ion slowing down and pitch angle scattering give counterinjection/coinjection ratios for ion heating efficiency and fast ion containment of ~ 50% (due primarily to the electric field effect with the loss regions nearly negligible) at 155 kA and ~ 15% at 95 kA. Third, the deleterious effects of counterinjection are much weaker, when observed at all, than those obtained at lower plasma currents. For example, the central electron temperature is no longer lowered, and no appreciable adverse effect on plasma stability is observed. Figure 12 shows the improvement with toroidal current of the ratios (counterinjection)/(no injection) for several parameters (discharge voltage V, $T_e(0)$, and C III line intensity).

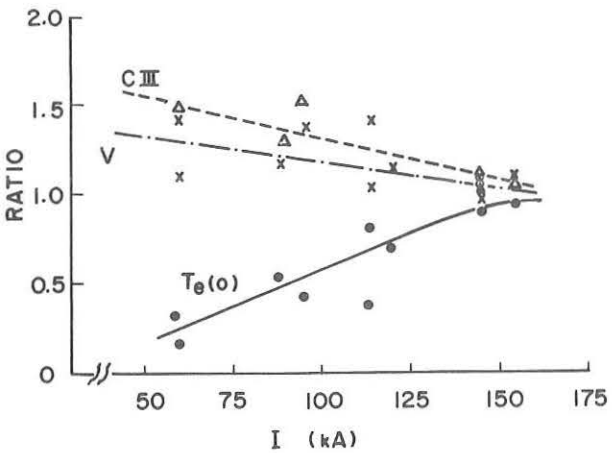

Fig. 12. Relative improvement (H^0 counterinjection/no injection) of various plasma parameters with toroidal current.

Conclusions: Confinement studies with $q(a_\ell) = 5$ and filling pressure held constant show that $n_e(0)$, $\bar{n}_e$, $T_e(0)$, and $T_i(0)$ vary linearly with I from 30 kA to 155 kA. The energy confinement time varies linearly with I and is in reasonable agreement with gross pseudo-classical scaling. Fluctuations on soft x-ray signals indicate that the

energy transport due to internal disruptions is small and that the q=1 and q=2 positions can be estimated. Comparisons between different estimates for $Z_{eff}(r)$ indicate that $Z_{eff}(r)$ is not peaked on the axis and that n_Z/n_i appears to be peaked near the outside. Radially movable radiometer measurements indicate that the bulk of the radiated power comes from the outer part of the plasma. Neutral beam injection studies indicate that the actual power injected is $\sim$ 1/2 that previously estimated. The ion temperature scales linearly with injection power, but at high I the heating rate is apparently less than that calculated. Counterinjection is more effective at high I. At 155 kA, the ΔT_i and fast ion fraction scattered through 90° are about half that obtained for coinjection, due primarily to the electric field effect, in agreement with Fokker-Planck calculations, and deleterious effects on the plasma behavior are absent.

Acknowledgments: This paper represents the work of the entire ORMAK group, but special credit for specific contributions should go to M. Murakami for electron confinement studies; J. F. Lyon for injection studies; J. L. Dunlap for soft x-ray fluctuation measurements; C. E. Bush for radiometer measurements; G. L. Jahns for soft x-ray spectra; G. H. Neilson for charge-exchange measurements; P. H. Edmonds for machine operation; E. C. Crume and D. L. Shaeffer for impurity modeling; W. R. Wing for data processing; R. V. Neidigh and R. Isler for spectroscopic measurements; L. A. Berry, J. D. Callen, and H. C. Howe for general discussions; and the Plasma Heating Department for the neutral beam installation and testing. The authors also wish to acknowledge the encouragement of J. F. Clarke and G. G. Kelley.

References

*Research sponsored by the Energy Research and Development Administration under contract with the Union Carbide Corporation.

[1] L. A. Berry et al., IAEA Tokyo Conf. Paper IAEA-CN-33/A 5-1 (1974).

[2] L. A. Berry et al., IAEA Tokyo Conf. Paper IAEA-CN-33/ A5-2 (1974); also Phys. Rev. Lett. 34, 1085 (1975).

[3] L. A. Artsimovich et al., JETP Lett. 13, 70 (1971); also see S. O. Dean et al., USAEC Report WASH-1295 (1974).

[4] E. P. Gorbunov, S. V. Mirnov, and V. S. Strelkov, Nucl. Fusion 10, 43 (1970).

[5] R. D. Hazeltine and F. L. Hinton, Phys. Fluids 16, 1883 (1973); also L. A. Berry, J. F. Clarke, and J. T. Hogan, Phys. Rev. Lett. 32, 362 (1974).

[6] L. A. Artsimovich, Nucl. Fusion 12, 243 (1972). L. A. Artsimovich, A. V. Glukhov, and M. P. Petrov, JETP Lett. 11, 304 (1970).

[7] S. von Goeler, W. Stodiek, and N. Sauthoff, Phys. Rev. Lett. 33, 1201 (1974).

[8] J. Tachon, Sherwood Theoretical Meeting, April 1975; J. P. Bussac, private communication.

[9] J. D. Callen et al., IAEA Tokyo Conf. Paper IAEA-CN-33/A 16-3.

[10] Private communication: H. C. Howe, J. D. Callen, R. J. Colchin, R. H. Fowler, and J. A. Rome.

[11] J. A. Rome, D. G. McAlees, J. D. Callen, and R. H. Fowler, submitted to Nucl. Fusion.

INVESTIGATIONS ON THE SOVIET TOKAMAKS

K.A.Razumova

I.V. Kurchatov Institute of Atomic Energy,Moscow, USSR

In recent years, the experimentalists working on the tokamak devices faced the problems which must be solved before starting the construction of the next tokamak generation.

The first problem is to find the scaling law for the confinement time and the mechanisms of the particle and energy losses. The second one is to estimate the minimum permissible value of q and the maximum value of $\beta = \frac{8\pi nT}{H_j^2}$. Further, the prospests for future devices are connected very essentially with the amount of impurities. The source of impurities and the main process of their desorption from the surrounding surfaces are not yet clear. The behaviour of the impurities inside the plasma is also unknown: do they concetrate inside the plasma column according to the Braginskii effect or they are stopped on its periphery? Finally, there are many problems relating to the additional heating, its possibilities and the processes in the plasma column attributed to it.

The experiments on the Soviet tokamaks were performed to answer these questions and I shall try to outline the present status of the experiments.

I

I shall begin with a discussion of the disruptive instability. After a set of experiments on T-6, the disruption may now be self-consistently explained as follows. Initially there are some surface

MHD-mode bursts, for example with m=2 or 3. The expression "surface" is, however, rather conditional because the mode m=2 appears to deform the whole column and fluctuations of the mean electron density are often observed. The disturbance then propagates to the neighbouring resonant surfaces (for instance with m=3 and 1 for the mode m=2). This disturbance seems to serve as a trigger for the neighbouring mode and may be a trigger for the higher ones. The original mode damps as a rule, but the energy is transfered to other modes. The distorted regions with the increased current density can overlap themselves and lead to broadening of the current channel , i.e. to the inductance decrease and to the other effects observed during the disruption. Undoubtedly, this description is hypotetical at this time. What is the reason for the the surface mode exitation? And why is the minimum permissible safety factor different in different experiments? One possible explanation is some local contact of the plasma with the limiter which leads to inhomogenity of the plasma parameters along the resonant toroidal surface and to the resonant oscillations. Indeed, if a rod is placed in the plasma column periphery, then the instability appears with the mode corresponding to the resonant surface touching the rod. The experiments on Tuman-2 show clearly that the plasma column is more stable when removed from the limiter by adiabatic compression whilst the q value is not changed during the compression. As the electron temperature increases more than predicted by the adiabatic compression law one can conclude that the interruption of the plasma -limiter contact leads to better plasma containment. The energy confinement time of the compressed plasma is significantly greater than for the usual toroidal plasma with the same parameters. So far it is difficult to say what is the reason for

additional insulation: the redistribution of density and tempera_ ture, the MHD-mode stabilization or the decrease of plasma con_ tamination. The improvement of plasma confinement is, however , very pleasant.

The internal mode with m=1 is now under study on T-4 in the joint Soviet-American experiment.

II

Another instability discovered some years ago caused many troubles on the TFR and seems to be observed on the Alcator at low density. This instability is connected with the existence of a considerable beam of runaway electrons. It has a fixed threshold which depends on the electron density and the averaged current density (Fig.1). Its appearance is accompanied by the appearance of saw-teeth on the longitudinal magnetic flux deriva_ tive oscillograms which correspond to the increase of the plas ma transverse energy (Fig. 2). The investigation of plasma HF-radiation at frequencies equal to or lower than the electron cyclotron frequency (Fig. 3) has shown that electrons of 50-150 keV are decelerated and their longitudinal velocity is transformed into transverse velocity. In this process a short burst of oscillations is generated in the wide range of frequen_ cies from several hundred kHz to 2000 MHz. As a result of this instability a considerable number of electrons of high transverse energy appears. These electrons move vertically in the toroidal drift direction, perhaps due to trapping in the field ripples. The fast ions also appear with equivalent temperatures up to 450 eV, which is a factor of 10 greater than under Ohmic heating. These ions drift in the toroidal drift direction too. The mecha_ nism of runaway electron velocity transformation has been sugges_

ted by B.B. Kadomtsev and O.P. Pogutse and was examined in more detail by O.P. Pogutse and V.V. Parail. When the velocity distribution function of electrons is considerably elongated in the $H_{||}$ direction, an intensive interaction of fast electrons with Langmuir oscillations occurs in the plasma at mean longitudinal velocity of the electrons more than v_{cr} ($\frac{W_{||} - W_{\perp}}{W_{||}} \lesssim 1$). This interaction results in the transformation of electron velocity due to the anomalous Doppler effect ($\omega - \omega_n = k v_{||n}$). The amplitude of oscillations increases. Under usual conditions Langmuir oscillations damp on the bulk electrons ($\omega \sim k v_{||T}$). However, when the Langmuir oscillation amplitude increases significantly due to the interaction with fast electrons, a plateau is formed on the electron distribution function and the oscillation decrement vanishes. Then a wide range of oscillations becomes unstable ($\frac{\omega_K}{K_z} = \frac{\omega_{pe}}{K} = v_z^o$) and practically the whole tail of the distribution becomes isotropic. The process will continue until the beam energy W_1 becomes of order of $W_{||}$. Then oscillations damp on the nonresonant electrons. The plateau disappears and the tail forms again. The theory describes the relaxation process well and agrees quantitatively with the experiment but it does not explain the appearance of a large number of locally trapped electrons, i.e. electrons with $W_{||}/W_1 \sim 1\text{-}2\ \%$ (a mirror ratio for ripples). And it is this aspect of the problem which is the most interesting in practice because it can lead, as experience shows, to the chamber destruction.

III

The recent experiments have shown that the existence of an anomalous resistivity in the tokamak plasma becomes less and less

possible. Earlier a significant discrepancy was observed at low density between the conductivity calculated according to Spitzer for hydrogen plasmas with the temperature measured by diamagnetic loops and that obtained from current - voltage characteristics. The first one was a factor of 50 - 100 greater than the latter. On TM-3 the measurements of bulk electron temperature by Thomson scattering and a transverse temperature of the fast electrons with energies more than 15 keV were carried out in the plasma of a low density. In Fig. 4 one can see that the electron temperature averaged over the cross section , as measured by diamagnetic loop is in some cases higher than that measured in the center by the scattering. In such a regime there is also a considerable fraction of runaway electrons with transverse energy about 20 - 30 keV.

IV

As is well known, in usual tokamaks it is impossible in principle to investigate the energy confinement time as a function of separate parameters, such as the electron temperature and the poloidal magnetic field. So far, we have obtained a rough but adequate estimate of this dependence by using additional HF-heating. It was shown that τ_ε grows with T_e.

V

The experiments on the finger-ring tokamak T-9 were performed to prove the theoretical expression for the safety factor

$$q = \frac{c H_\parallel a^2}{2\pi R} \cdot \frac{1+\kappa^2}{2} \qquad (1)$$

where K= b/a is the elongation of the plasma column cross-section. The q value was calculated from the poloidal probe measurements of the current distribution along the plasma radius.

This dependence is shown in Fig. 5 where are shown also the K-values measured by different techniques. In these experiments the magnetic probes registered also the mode of disturbance by comparing it with the model disturbance. The discharge current variation during the transition from one mode to other was also measured

$$J_m - J_{m-1} = \Delta J_m = \frac{J_m}{m-1} \qquad (2)$$

Thus one can say that the MHD-modes develop in the finger-ring tokamak in good agreement with the theory of V.D. Shafranov and L.E. Zacharov.

VI

The contamination of the plasma was investigated by mesurement both of spectral line intensity and of the X-ray intensity. In the latter case the continuum spectra and the line radiation were measured. It is easy to show that the spectral line intensity of slightly ionized impurity ions is proportional to the influx of neutral atoms of these impurities in a unit plasma volume. For the case of a stationary influx, if one neglects the loss of ions, one can write:

$$\Lambda_0 = n_0 S_0^i n_e + \frac{n_0}{\tau} \qquad (3)$$

$$n_0 S_0^i n_e = n_1 S_1^i n_e + \frac{n_1}{\tau}$$

where S_k^i is the rate coefficient of ionization. Then $\Lambda_0 = n_K S_K^i n_e$ and since the line intensity $J_K = n_K S_K^{ex} n_e$, $\Lambda_0 = J_K S_K^i / S_K^{ex}$ (the ratio S_K^i / S_K^{ex} is in principle a function of T_e only).

It was shown experimentally that the intensity of many lines of elements under investigation depends on n_e as shown in Figs. 6 and 7. One can see the linear increase of I_k with n_e (regime A). When the runaway electrons cause an anomalous outward shift

of the plasma column, there is no dependence of I_k on n_e (regime B).Finally, the line intensity increases when MHD-activity appears. Such a dependence takes place if n_e is varied either by the initial pressure variation or by the plasma current variation. The Figs. show that the line intensity $J_K = \Lambda_0 S_K^{ex}/S_K^i$ does not depend on T_e, since the latter was significantly different in both cases. Since a given ion should concentrate for the most part in the region where T_e is of order of the ionization potential, the ratio S_K^{ex}/S_K^i for a given ion should change rather slightly with discharge parameters. Thus the Λ_0-value appears to be a weak function of T_e. The line of neutral iron was detected in spite of the large distance between the diagnostic port and the limiter.Thus one can say that at least this element goes from the wall rather than from the limiter.

The results of spectral measurements on the TM-3 under conditions: I =40 kA, q (a) = 4.5, $\bar{n}_e = 1.8 \cdot 10^{13}$ cm^{-3}, $\bar{T}_e$= 350 eV, W_{in} = 150 kW , are as follows :

the radiation power measured by the bolometer - 25 kW;

the electron confinement time - 3.6 msec;

the same including impurity influx - 2.7 msec;

the absolute influx of neutral carbon - Λ_o (C)= 10^{14} 1/cm^{3}sec;

the same of neutral oxygen - Λ_o (O) = 1 ÷ 2. 10^{14} 1/cm^3.sec;

the carbon concentration provided that the ion lifetime is equal to that of electrons - η (C) = 1.5 %;

the same for oxygen - η (O) = 1.5 ÷ 3 % .

To find out the dependence of the low - Z impurity influx on wall contamination, an experiment was performed which added metha_

ne to hydrogen. It was found that the ratio of C IV ion line intensity to the electron density is proportional to the initial pressure of methane. The influx of carbon in methane discharge is a factor 5 more than the same in hydrogen one of the same density. The n_e-value does not change under these conditions during the stationary phase of the discharge. Thus it is possible to evaluate the lifetime of carbon ions in the TM-3 plasma : τ_ε (C) $\leq$ 5 msec. Earlier, it was found that in the hydrogen discharge where the impurity concentration is about 1 - 2 % the impurity concentrates at the axis, whereas at significant contamination of the plasma (in the methane discharge, for example, the carbon concentration was about 10 %) the lifetime of the impurity is of the order of the proton lifetime and the impurity does not accumulate. Thus the chamber wall seems to be the main source of impurities in the present-day tokamaks, and the impurity flux at low density is proportional to n_e. What is the mechanism of desorption ? Possible mechanisms are :

1. The desorption due to irradiation.

2 .The desorption due to neutral charge exchange atoms either from the center of the plasma, i.e. hot atoms, or from the periphery, i.e. cold ones.

3. The desorption due to charged particles.

1. The absence of any dependence of the impurity influx on T_e shows the insignificant role of the radiation losses in the energy range of 400 - 700 eV. The same is shown by the absence of unusual influx behaviour during the first milliseconds of the stationary phase of the discharge when an intensive irradiation of highly ionized impurity ions appears

At fixed impurity influx, the line intensity of slightly ionized ions does not change perceptibly when discharge parameters are varied and thus cannot lead to the influx variation due to photodesorption. Hence, the lines intensity variation of these ions cannot change the impurity influx and serves only as an indicator of its change.

2. In Fig. 8 are shown the fast charge exchange neutral atoms outfluxes as a function of n_e for two cases : the density is varied by the initial pressure variation and by the current variation. The fluxes differ significantly for these two cases and thus appear not to cause the observed impurity influx.

3. Two other mechanisms can be demonstrated as reasons for the impurity influx : the bombardment of the wall by the cold neutral atoms and by the discharged particles. In the latter case the size of the limiter shadow should influence strongly the impurity influx. For the present we have no data on this problem.

The analysis of X-ray spectra showed the appearance of elements of the stainless steel wall and of the limiter. As the TM-3 experiments show the value of $\sum_i n_i Z_i^2$ is up to $2.10^{14} cm^{-3}$ and metal ions' concentration is about 1-3 % at an electron density of about $2\text{-}5.10^{12}$ cm^{-3}. Unfortunately, these evaluations are so far too rough because both the continuum and the characteristic radiation are caused mainly by runaway electrons in the discharges under study. The accuracy of the absolute estimations depends strongly on the accuracy of the runaway electron fraction.

The contamination level plays the important role in impurity confinement under the very dirty conditions of present-day tokamaks. The low-Z impurity level rapidly reaches the stationary

state. This means that contradictory results on the impurity confinement may be obtained on machines with different pulse duration.

VII

During the recent year two methods of the additional heating were investigated on the Soviet tokamaks : ECRH and adiabatic compression. ECRH seems to have a very good outlook from the the physical point of view. It allows heating the plasma region or electron component, whichever one likes. Further, this method opens wide prospects for the plasma properties study, in particular the local transport coefficients measurements. On TM-3 the electron temperature distributions along the radius were studied by Thomson scattering before and after the ECRH-pulse. The results show the classical mechanism of heating.

The adiabatic compression follows the classical law, as experiments on Tuman-2 show. T_e increases more rapidly than by this law as mentioned above. The reason appears to be the improvement of plasma stability.

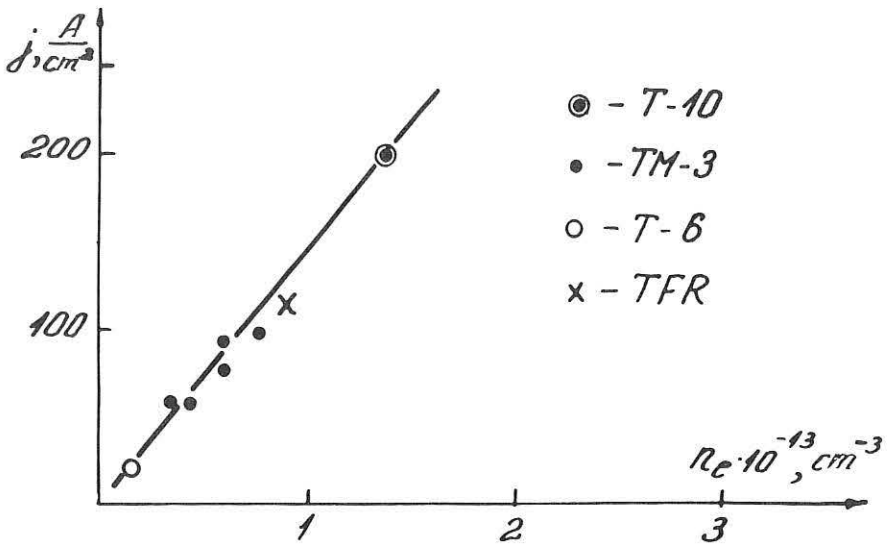

Fig. 1. Threshold of runaway electron instability appearance vs current density and average electron density.

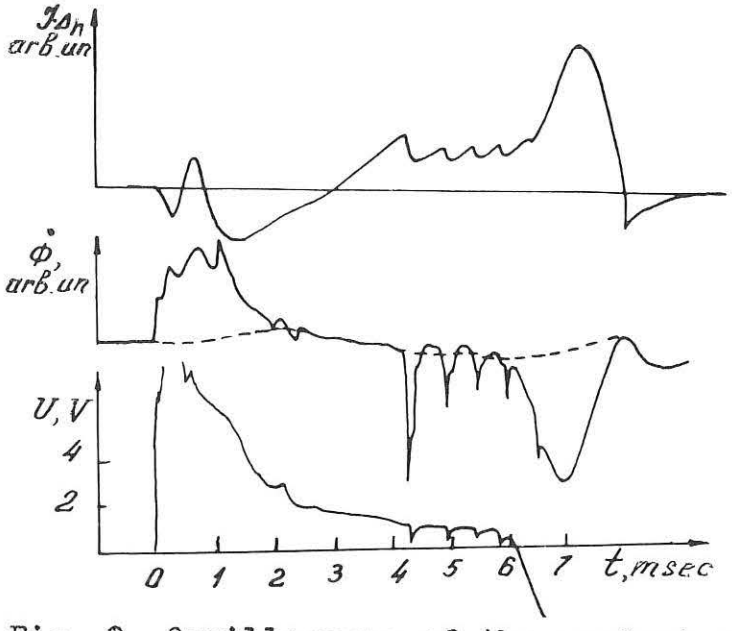

Fig. 2. Oscillograms of the product of plasma current and plasma column displacement $J \cdot \Delta_h$, magnetic flux derivative $\dot{\Phi}$ and voltage U in the case of instability.

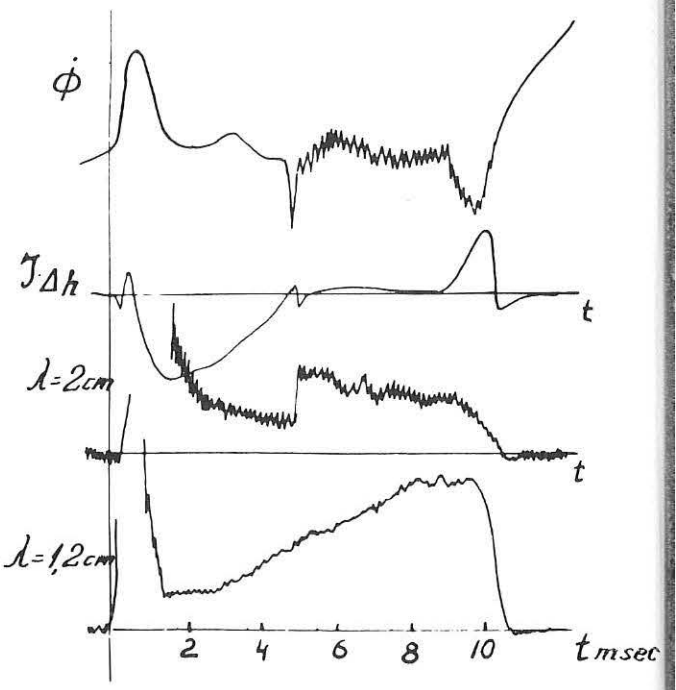

Fig. 3. Oscillograms of $\dot{\Phi}$, $J \cdot \Delta_h$ and HF-radiation intensity at λ = 2 cm and 1.2 cm.

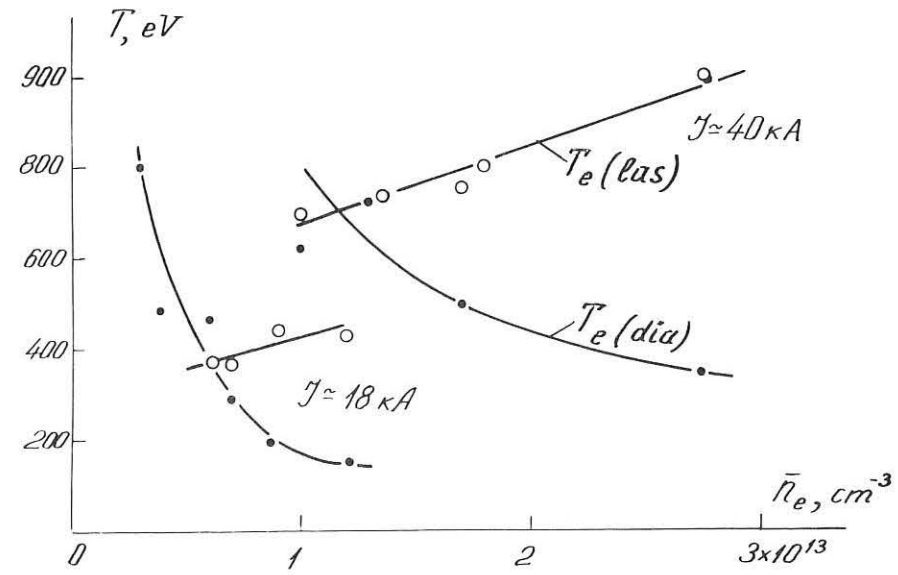

Fig. 4. The dependence of electron temperature measured by diamagnetic loop and that measured by laser scattering on $\bar{n}_e$.

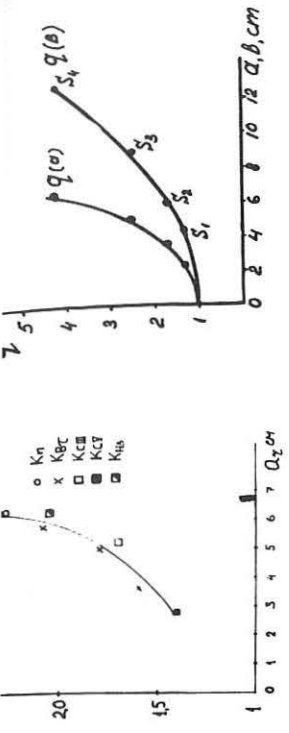

Fig. 5. Spatial distribution of elongation coefficient K = b/a and safety factor q for the finger-ring T-9 Tokamak.

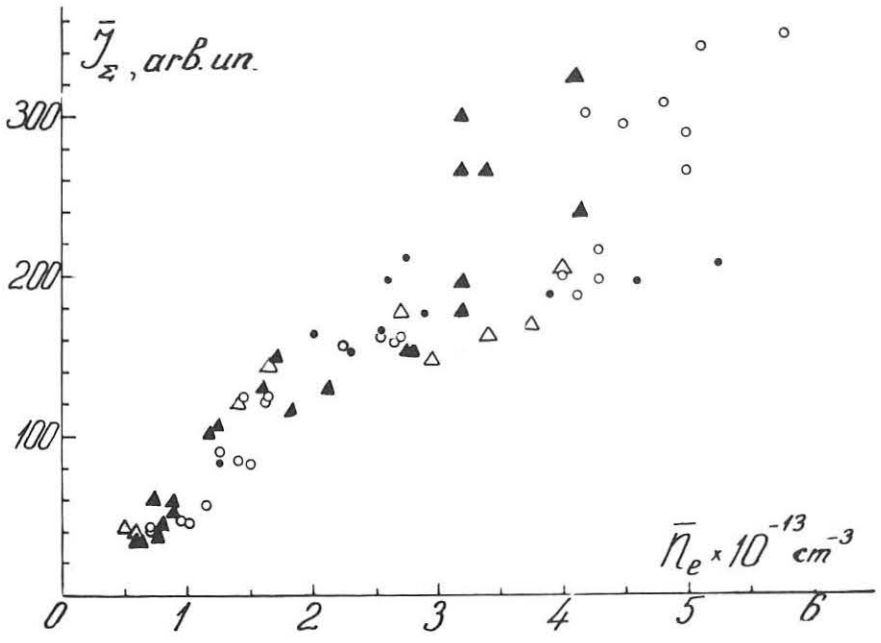

Fig. 6. Dependence of impurity spectral line intensity on $\bar{n}_e$ (the density is varied by the initial pressure variation).

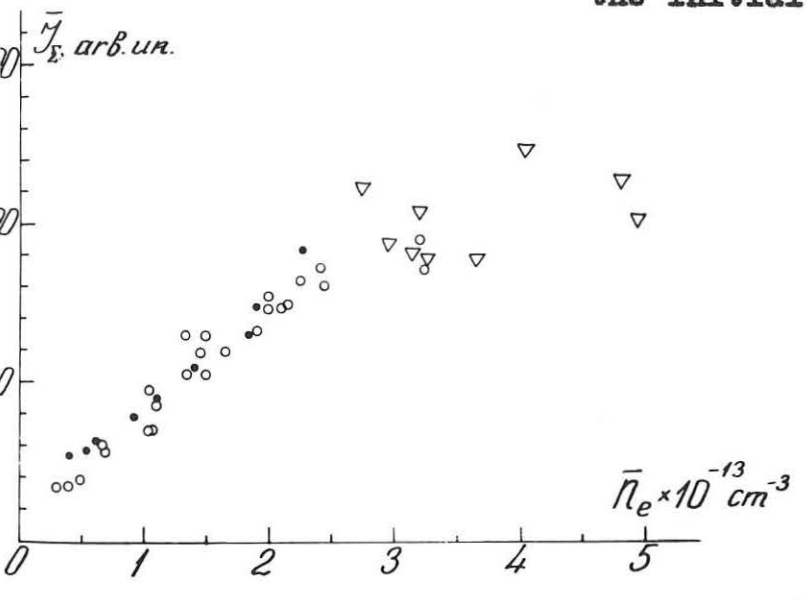

Fig. 7. The same as Fig. 6 but the density is varied by the discharge current variation

ig. 8. Dependence of fast charge xchange atoms flux on the electron ensity for the cases of Fig. 6 curve a) and Fig. 7 (curve b) he proton temperatures are pointed ut by the figures.

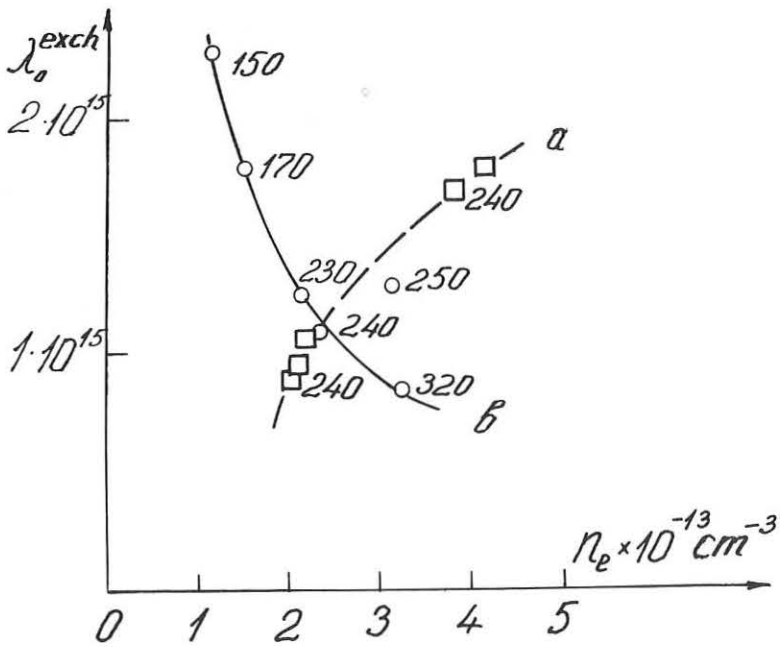

Investigation on the Disruptive Instability in Pulsator

O. Klüber

Max-Planck-Institut für Plasmaphysik, Garching,
Euratom-Association, Federal Republic of Germany.

It is well known that the economic efficiency of a fusion reactor depends on $\beta = 2\mu_o \bar{P}/B^2$ where $\bar{P}$ is the average pressure and B the magnetic field. In the case of a tokamak reactor the maximum attainable value of β is limited by equilibrium and stability conditions. Equilibrium exists only for $\beta_p = 2\mu_o \bar{p}/B_a^2 < R/a$, where B_a is the poloidal magnetic field at the plasma surface and R and a are the major and minor plasma radius respectively. Stability requires $q(a) = aB_\varphi/RB_a > 1$. Thus β is limited by the condition $\beta < a/q^2 R$.

Since a/R is typically 0,2 to 0,4, β is sufficiently large if q(a) is close to 1. This value, however, cannot be approached in actual tokamak devices because the so-called disruptive instability limits q to larger values. The nature of this instability is not understood as yet, but its phenomenology is well known: the disruptive instability manifests itself in a negative voltage spike, a sudden decrease in the major radius of the plasma column, loss of plasma energy and particles and a decrease of the current. This decrease may amount only to some percent, but it may also happen that the total discharge terminates within some ms. The instability is always preceeded by the occurrence of strong MHD modes in the outer regions of the plasma column, mostly of the type n = 1, m = 2, 3... where n and m are the toroidal and poloidal mode numbers. In general, the mode with m = q(a) predominates if q(a) is close to an integral number. Disruptions may happen at any integral q but they occur more frequently for smaller q values. Most tokamak discharges are operated with $q > 3$ or even $q > 4$ and almost all favourable results, e.g. large temperatures and confinement times have been achieved in this regime. Stable discharges with q values between 2 and 3 have also been produced; however

it has not been possible to enter the region $q < 2$ except in the case of the T6 tokamak. This device differs from all other tokamaks in having a copper shell very close to the plasma column.

Obviously, it is essential for the development of the tokamak towards a fusion reactor to decrease the q value for which safe operation is possible. It should be pointed out that even an occasional occurrence of the disruptive instability constitutes a serious danger for large tokamak devices because the sudden termination of the discharge current leads to large currents and forces in the vacuum vessel and the external circuits. For these reasons, the investigations on the disruptive instability are of particular importance in the field of tokamak research.

In the following, mainly the work done on the Pulsator device will be referred. Pulsator is a conventional tokamak of moderate size ($R = 70$ cm, $a = 12$ cm, $B_\varphi = 28$ kG maximum, $I = 95$ kA for $q = 3$ and $B_\varphi = 28$ kG) having a copper shell and an iron core transformer. It has, however, two features which turn out to be very suitable for investigations on the disruptive instability, namely a vertical field winding and a $\ell = 2$, $n = 1$ helical winding, both of which are located inside the copper shell and are fed with programable currents. Due to these windings, the ratio b/a between the inner radius b of the copper shell and the plasma radius a is unusually large; at the maximum attainable plasma radius $a = 12$ cm, $b/a = 1.63$. Hence, the plasmas produced in the Pulsator device are especially susceptible to the disruptive instability if the plasma column is not well centered. Nevertheless, it was possible to attain a minimum value $q(a) = 2.2$ by careful centering under very different conditions, i.e. at high and low currents and corresponding magnetic fields, and for electron densities between 10^{13} and 10^{14} cm^{-3}. An example for a discharge having small q(a) is shown in fig. 1. In this discharge the electron density was increased by pulsed gas input during the shot, thus allowing a maximum of $1.05 \cdot 10^{14}$ cm^{-3} to be attained at $t = 100$ ms.

The optimum current program leading to a well-centered plasma column could be found by trial and error. The difficulty to meet this requirement grew markedly with decreasing q(a). In the case of a disruption due to misprogramming it was quite easy to decide how the program must be changed since it turned out that the temporal evolution of the plasma current after the disruption was different for the cases of the plasma column displaced either too much outwards or inwards. When the plasma was displaced inwards before the onset of the instability, the disruption was hard, i.e. it resulted in a total termination of the discharge. In contrast, when the plasma was displaced outwards, the current increased again. The same behaviour has also been found for discharges operated in a d.c. vertical magnetic field and in cases when the programmed vertical field was used to trigger a disruption arbitrarily thereby de-centering the plasma column. /1/ In fig. 2 a sequence of shots is shown which differ in the time dependence of the vertical field B_z. Shot No. 1884 is a well centered, stable discharge. The decrease of B_z in shot No. 1886 and the accompanying outward displacement of the plasma causes a small decrease of the current, but no instability, whereas the stronger decrease in shot No. 1888 leads to a "soft" disruption: the current increases again. The inward displacement due to the increase of B_z in shot No. 1891 causes a "hard" disruption, i.e. it leads to current termination.

The observed difference between "hard" and "soft" disruptions can be ascribed to an enhanced interaction between the plasma and the limiter caused by the instability. The instability leads to an inward displacement (reduction of major radius) of the plasma column and to a decrease of the discharge current and hence to an increase of the inward directed force proportional to B_z/I. Therefore, if the plasma was displaced outwards before the onset of the disruption, the centering of the plasma column is improved by the occurrence of the instability; thus the interaction with the limiter is reduced and the current is able to recover. If, on the other hand, the plasma column was already displaced inwards before

disruption, the enhanced interaction is further increased and this leads to current termination. The interaction with the limiter manifest itself in an enhanced release of impurities. On Pulsator, the time dependence of the emission of various impurity lines, e.g. OIII, OVI, MoXIII has been observed during disruptions. The emission of all these lines increased rapidly, this increase starting with the appearance of the negative voltage spike.

The phenomena pointed out above refer to the more or less violent consequences of a disruption that has occurred, but not to the conditions leading to the onset of this instability. It is, however, conceivable, that some kind of enhanced interaction of the plasma with the limiter may be a starting mechanism for disruptions. This is suggested by the experimentally found sensitivity of a tokamak plasma to displacement. This view is reinforced by the results of the experiments using helical windings. /2/

The influence of a superimposed $\ell = 2$, $n = 1$ helical field on the stability behaviour of the Pulsator tokamak plasma is clearly not due to the change of the rotational transform. This follows from the experimental finding that helical currents corresponding to a vacuum rotational transform $\iota 2\pi$ of the order 10^{-5} to 10^{-4} are sufficient to produce effects and that these effects only occur if the helicities of the tokamak magnetic field and of the superimposed helical field are in the same sense. In this case, for given plasma parameters a certain well reproducible level I^{+}_{hel} of the current in the helical windings lead to a disruptive instability which exhibits all features characteristic of spontaneous disruptions such as negative voltage spike, decrease of current, losses etc. For helicities of opposite sense, even a helical current $I_{hel} > 30\ I^{+}_{hel}$ does not influence the stability. The effect is based upon geometric resonance of the tokamak magnetic field at the magnetic surface $q = 2$ and the superimposed $\ell = 2$, $n = 1$ helical field. This resonance leads to the formation of islands, as was shown by H. Wobig /2/.

Fig. 3 shows the island structure produced by superposition of the tokamak and the helical magnetic fields. The islands originate on the q = 2 surface; their width is proportional to $\sqrt{I_{hel}/B_\varphi}$. This linear superposition does not take into account the change of the tokamak plasma due to the presence of islands, but the experiments have shown that macroscopic plasma parameters change only slightly in the presence of superimposed helical fields. This has been observed in cases when the helical current was smaller than but very close to the critical value I^+_{hel}.

In order to explain this in more detail the time dependence of the relationship between $\sqrt{I^+_{hel}/B_\varphi}$ and q(a) must first be discussed. It was found that there is a characteristic time of about 1 ms. If the helical current or the plasma current and hence q(a) change on a time scale large compared to 1 ms, the critical value I^+_{hel} is independent of details of the temporal evolution. This means that the same value of I_{hel} leads to disruption whether I_{hel} is increased at constant q(a), or I_{hel} is held constant with decreasing q(a) due to increase of the plasma current.

A different behaviour is observed for time scales of the order of 1 ms. The quasi-steady state (d.c.) value I^+_{hel} can be exceeded without disruption using a current pulse having a duration of about 1 ms. Furthermore, stable a.c. operation above the d.c. value of I^+_{hel} is possible at frequencies of the order of 1 kc. This behaviour is clearly due to penetration effects, since 1 ms is roughly the skin time of the plasma.

In the cases of slowly increasing I_{hel} or slowly decreasing q(a) it was observed that the disruption is preceeded by a period of reduced MHD mode activity. An example is shown in fig. 4. In this case, I^+_{hel} was reached by a relatively fast increase of I_{hel}. The period of reduced mode amplitude can be extended by slower a increase of I_{hel} and for constant I_{hel} by an accordingly slower decrease of q(a). The period length corresponds to $I_{hel} \approx (0.6 - 0.95)\ I^+_{hel}$. This effect is not a transient phenomenon. If I_{hel} is held below I^+_{hel}, the period

of reduced mode amplitude can be extended arbitrarily. The decrease of the mode signal can either be due to a damping of the mode amplitude or to a sudden stopping of its rotational velocity. The experiments indicate that both phenomena occur. The stability of the plasma is improved by the superposition of resonant helical fields below the critical value. This means that a disruption which occurs reproducibly for given plasma parameters can be avoided by the superposition of a helical field, thus leading to an appreciable extension of the plasma current duration.

The nature of this stabilization is not yet clear, but very probably the rotation of the MHD modes and the growth of their amplitude are hindered by a fixed helical structure. In this connection it should be mentioned that the MHD modes themselves create islands, as has been shown by Chrisman et. al. /3/.

It is most noteworthy that the field perturbations created by the modes are typically of the order of 10^{-2} B_{ω}. Currents in the helical winding leading to disruptions cause field perturbations of the same order of magnitude. From this one may infer that magnetic islands of sufficient size are a necessary condition for the onset of the disruptive instability independent of whether one has rotating islands due to the MHD modes or fixed islands created by the superimposed resonant helical field.

The improvement of stability is the more pronounced the closer I_{hel} is to the critical value I^{+}_{hel}. Thus this effect cannot be used to extend the stable regime markedly. It provides, however, the possibility to investigate the influence of islands of appreciable size on a tokamak plasma. It has been seen that the change of the plasma parameters due to a stabilizing resonant helical field is surprisingly small. The most prominent effect that was observed is a decrease of the resistance of typically 15 %. An according increase of 10 % of the peak electron temperature was observed, but this increase is not clearly beyond the error bars as given by the shot-to-shot reproducibility. Thus, it can be stated that the

macroscopic plasma parameters are only slightly changed by the helical field. Since the effect of helical currents below the critical value is a suppression of the MHD modes, it can be statet that rotating islands have roughly the same influence on the plasma parameters as fixed islands. It is conceiveable, therefore, to determine the size of the islands created by the helical windings from the properties of the undisturbed plasma. The most important property is the shear in the region of the resonant surface which obviously determines the island width. The shear is given by the current density profile. For a given current density profile one can expect the real island size to be proportional to $\sqrt{I_{hel}/B_\varphi}$. The most interesting question is, of course, how the critical island size i.e. $\sqrt{I^+_{hel}/B_\varphi}$ depends on the plasma parameters. In order to investigate this, the toroidal magnetic field has been varied from 10 to 30 kG and the plasma currents from 10 to 120 kA, thus covering the range $2 < q(a) < 9$ under very different conditions. The result is plotted in fig. 5. It is clearly demonstrated that $\sqrt{I^+_{hel}/B_\varphi}$ is a monotonically increasing function of q(a). The solid curve plotted in fig. 5 represents an attempt to explain the experimentally found dependence of $\sqrt{I^+_{hel}/B_\varphi}$ on q(a). in accordance with the experimental results obtained using programmed vertical fields the hypothesis was made that disruption occurs if I^+_{hel} is such that the islands originating on the q = 2 surface touch the limiter. This means that for increasing q(a) the resonant q = 2 surface moves inward; thus the island size has to be increased in order to geto into contact with the limiter. The solid curve in fig. 5 was calculated using a current density profile representative for typical Pulsator plasmas and on the assumption that the island width is $\delta = C \cdot \sqrt{I^+_{hel}/B_\varphi}$ where the constant C was determined by adaption to the experimental points. Obviously, the variety of plasmas contributing to the experimental points of fig. 5 is not really represented by one current density profile. This appears to be the primary reason for the divergence of the points, since the current density profile governs the

distance from the q = 2 surface to the limiter and the shear. It is seen from fig. 5 that the points best fit one curve for q values close to 2. In this case in a approximation the total current is flowing within the q = 2 surface. Therefore, the distance of this surface to the plasma edge and the shear in the region between these surfaces are almost independent on the details of the current density distribution.

A change of direction of the current in the helical winding leads to a rotation of the islands by 90°. The critical value I^{+}_{hel} is not altered by such change if the limiter has a circular shape. If, in contrast, the limiter is non-circular I^{+}_{hel} is different for both current directions. This result has been obtained using a racetrack-like limiter, consisting of two half-circles having a radius of 8 cm and straight parts of 8 cm length, located such that the "major axis" is horizontal. If the current direction is such that the islands are located at the inside and the outside (i.e. the same position as is shown in fig. 3), I^{+}_{hel} is a factor 1.7 larger than in the case of islands located at the top and bottom. This result supports strongly the view that the contact between the islands and the limiter is the deciding factor for the onset of the disruptive instability.

Thus, all experiments carried out on Pulsator demonstrate that the creation of magnetic islands is an essential feature for the onset of the disruptive instability. Moreover, all results are consistent with the assumption that the disruption occurs when the islands come into contact with the limiter.

Figure captions:

Fig. 1 Pulsator discharge at low q.

Fig. 2 "Hard" and "soft" disruption due to inward and outward displacement of the plasma column.

Fig. 3 Island structure due to the superposition of a resonant helical field.

Fig. 4 Decrease of mode amplitude due to helical currents below the critical value.

Fig. 5 Dependence on the critical island size $\sqrt{I^{+}_{hel}/B_{\varphi}}$ on the safety factor q(a).

References:

/1/ O. Klüber et al, Proc. 5th Int. Conf., Tokyo, A8-2

/2/ F. Karger, H. Wobig et al, Proc. 5th Int. Conf., Tokyo, PD-2

/3/ P. Chrisman et al, ORNL-TM-4501

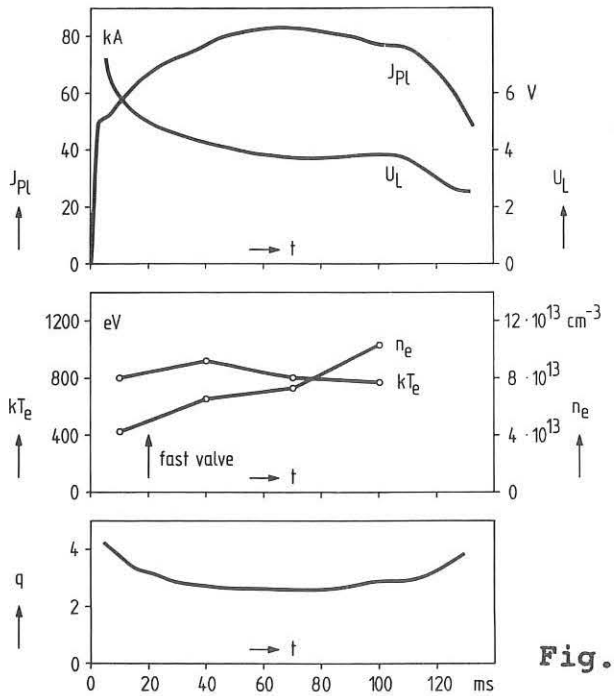

Fig.1

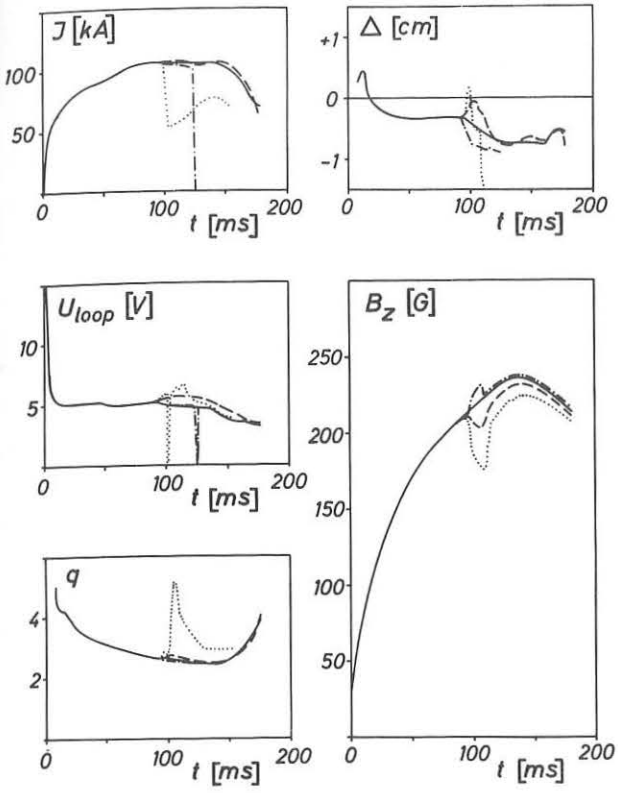

Fig.2

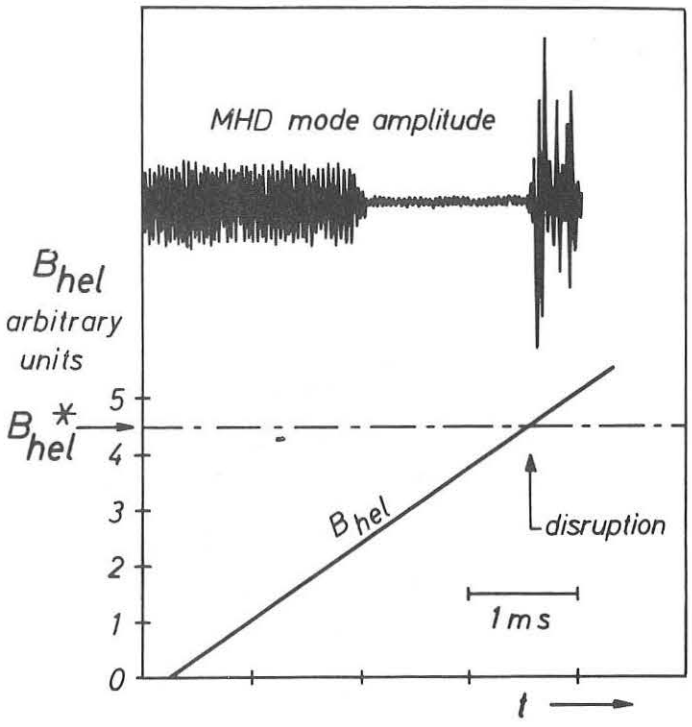

Fig.4

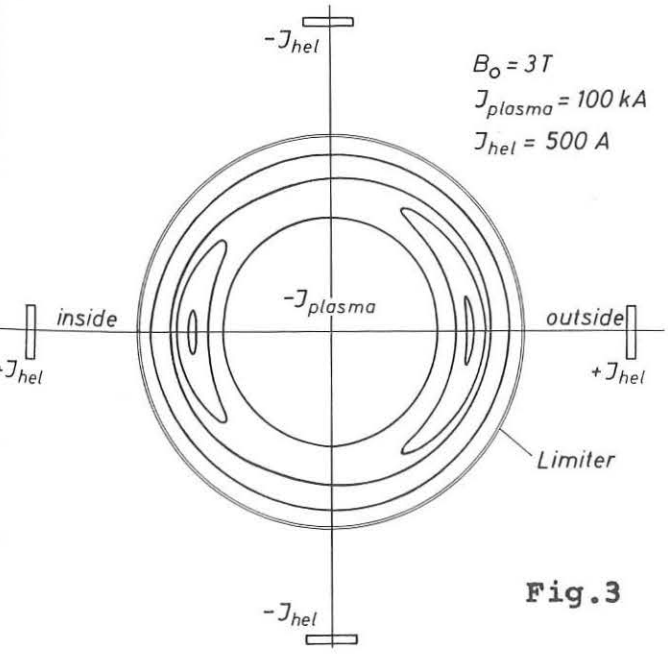

Fig.3

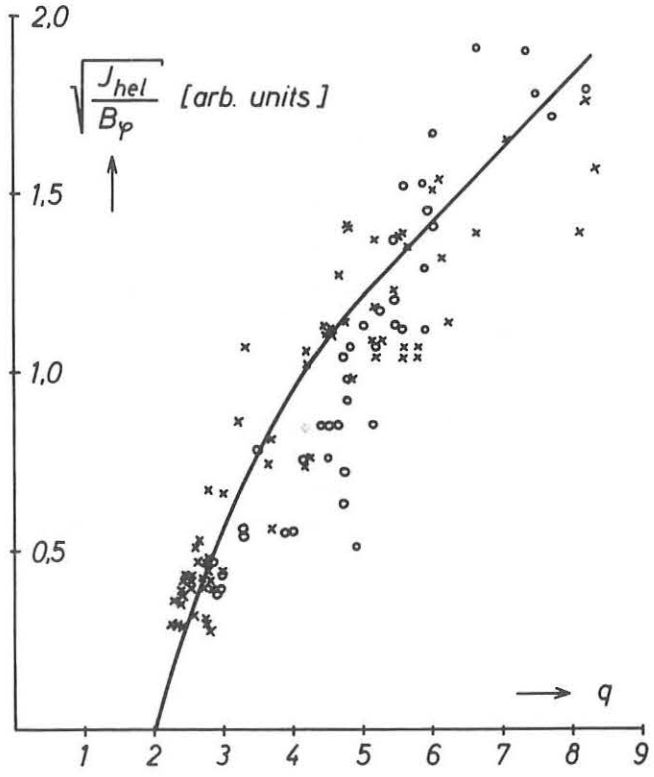

Fig.5

IMPURITY EVOLUTION IN T.F.R. PLASMAS

T.F.R. Group presented by C. De Michelis

ASSOCIATION EURATOM-CEA SUR LA FUSION
Département de Physique du Plasma et de la Fusion Contrôlée
Centre d'Etudes Nucléaires
Boîte Postale n° 6. 92260 FONTENAY-AUX-ROSES (FRANCE)

Abstract : Space and time resolved profiles of impurities have been obtained in TFR plasmas by a shot to shot scan. Light impurities are present at the very beginning of the discharge, resulting in $Z_{eff} \cong 4$ already at a time of 7 msec. On the current plateau, light impurity ions and heavy impurity ions of moderate charge are concentrated at radii where the electron temperature is equal or slightly smaller than their ionization potential, and radiate about 35 % of the input power. Inwards diffusion velocities of $\sim 2 \times 10^3$ cm/sec are deduced for a radius of $\sim$ 16 cm. Highly ionized molybdenum ions (Mo^{30+}, Mo^{31+}) are concentrated inside a radius of $\sim$ 10 cm, with a density of $\sim 10^{11}$ cm^{-3}.

In this paper we shall mainly describe a study of the visible and ultraviolet radiation in TFR deuterium discharges with a plasma current I_p = 140 kA and a toroidal magnetic field B_T = 26 kG (diaphragm diameter 40 cm). We shall not discuss here the coronal model used in the interpretation of the results ; details on this model can be found in /1/.

I- EXPERIMENTAL SET-UP

The diagnostics used are : a) a v.u.v. grazing incidence duochromator placed at φ = 45° (starting from the diaphragm and following the plasma current direction) equipped with a grazing incidence gold-coated mirror in order to obtain radial profiles (spatial resolution 8mm) ; b) two light guide multichannel systems, equipped with interference filters, at φ = 0° and φ = 180°, in order to spatially resolve the visible emission ; c) a normal incidence v.u.v. monochromator at φ = 225° ; d) a Thomson scattering system at φ = 180° for space and time resolved electron density and temperature measurements ; e) a soft x-ray detector at φ = 135° ; f) two bolometers, at φ = 270° and φ = 315°, and several thermocouples inbedded into the limiter. The two v.u.v. spectrometers are calibrated by means of the branching ratio method /2/ by using two visible monochromators placed in the same sections and viewing along the same chord ; the experimental errors on the measured absolute radiances are about a factor of two, and probably somewhat less

above 1000 Å.

II- RESULTS WITH 140 KA, 26 KG DISCHARGES

II-1. Time evolution. Figure 1 shows the time evolution of several

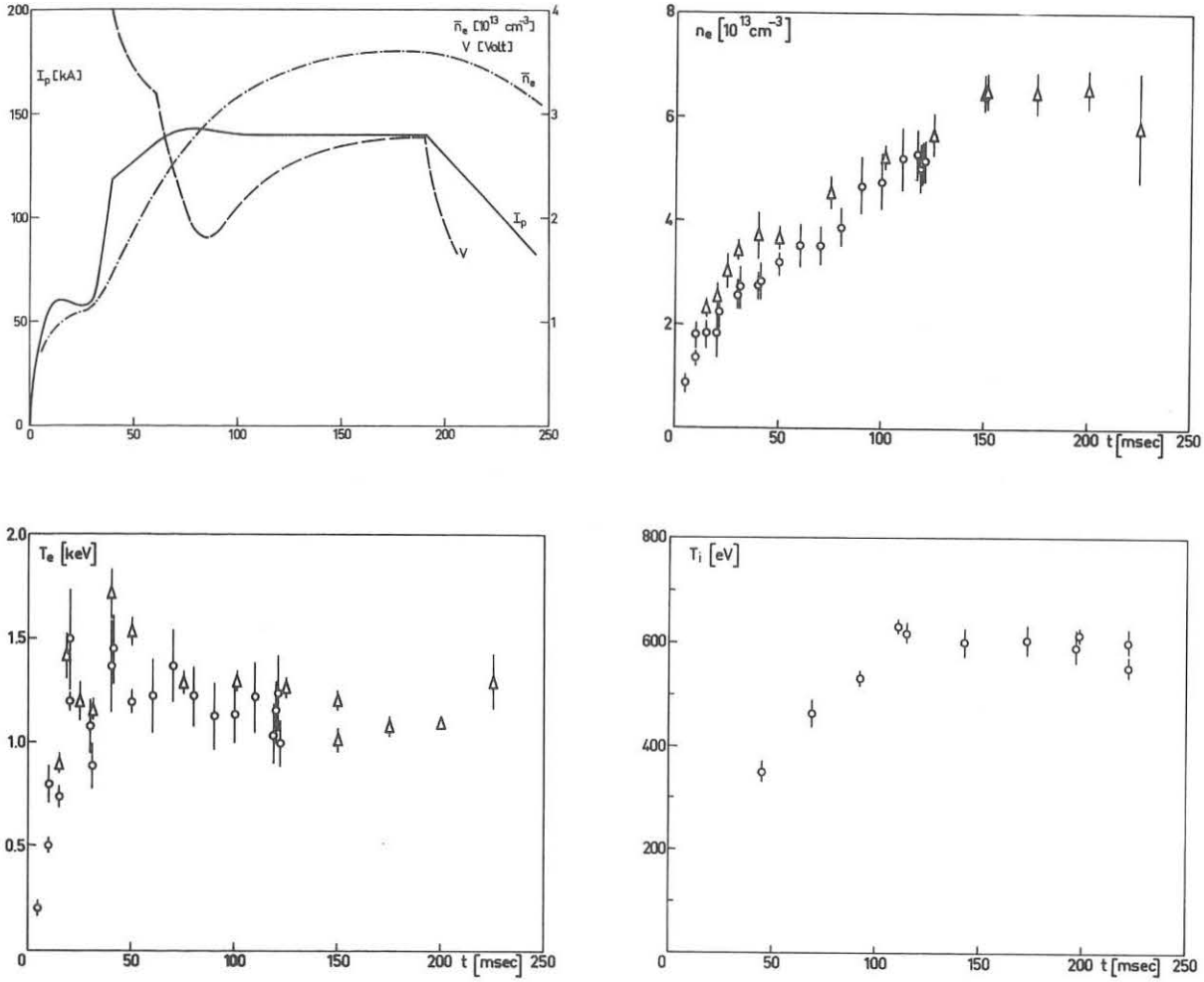

plasma parameters for the considered discharges : plasma current I_p, loop voltage V, average electron density $\bar{n}_e$ (as measured by a multichannel microwave interferometer placed at $\varphi = 0°$), central electron density n_e , central electron temperature T_e, and central ion temperature T_i (as measured by charge exchange neutrals). It will be noted that, whereas the electron density grows continuously until the current decrease, the electron and ion temperatures have approximately constant values during the current plateau. Figure 1 also shows typical signals from the v.u.v. duochromator ; in order to show the signal due to highly ionized molybdenum

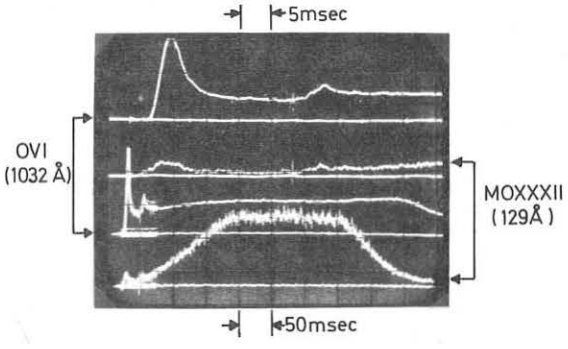

Figure 1.

these signals refer to a discharge with the same current but higher magnetic field and a longer plateau (see section III). The radiance due to low ionization ions (represented here by the OVI 1032 Å line) is characterized by an initial peak, followed by a second, less marked, peak corresponding to the firing of the second capacitor bank (at t = 30 msec), and then the signals are roughly proportional to the electron density. Highly ionized ions are characterized by a different behaviour ; the MOXXXII 129 Å line shown in figure 1 does not appear up to approximately 50 msec (since the background, due to light diffused in the monochromator, has to be subtracted from the signal shown), reaches a maximum at about 150 msec, and then remains constant until the current decrease.

II-2. Radial profiles : beginning of the discharge. The initial peaks clearly show that impurities appear early at the beginning of the discharge. Figure 2 shows the radial profiles of a few lines, at the time

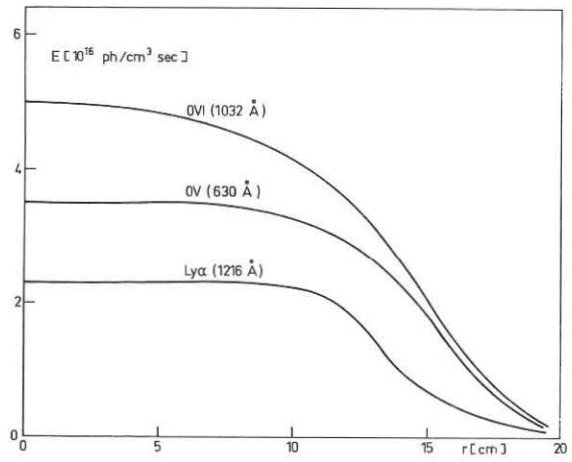

Figure 2.

of the initial peaks, demonstrating that we are in the presence of volume ionization and that a uniform plasma model can be used in order to interpret the experimental initial peaks. The lower half of figure 3 shows the temporal behaviour, at h = 0, of the radiance of Lyα and of several oxygen ions. The oxygen line peaks appear one after the other, according to their ionization potential. A one impurity, uniform deute-

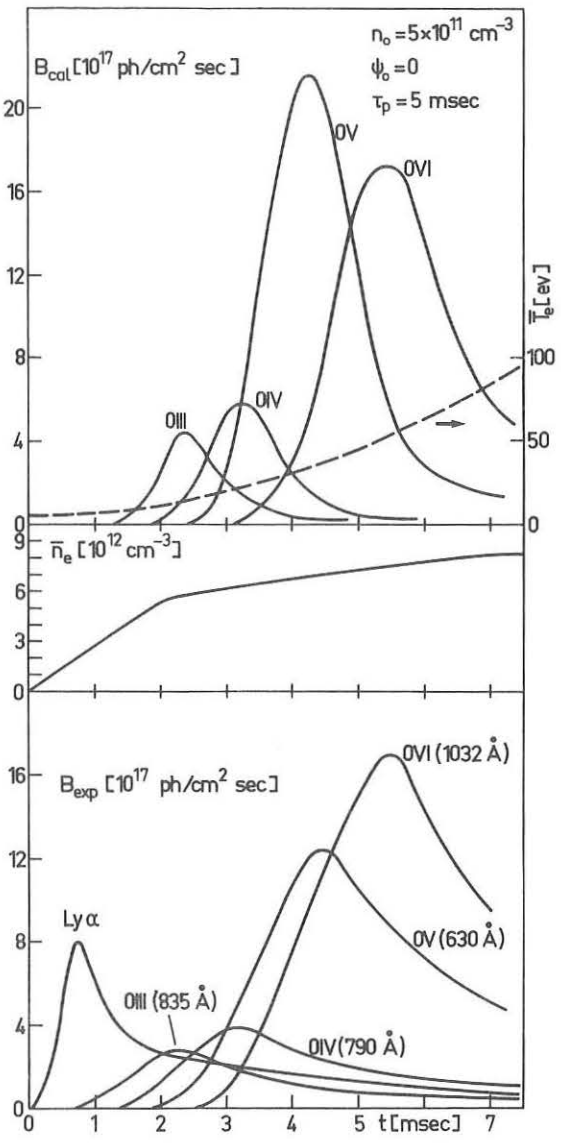

Figure 3.

rium plasma, coronal model has been used in order to deduce the amount of impurities initially present in the plasma. Taking the experimental average electron density $\bar{n}_e(t)$, the initial amount n_o of neutral oxygen and the average electron temperature $\bar{T}_e$ (t) have been adjusted in such a way that the peak times for the different lines and the intensity of the OVI peak coincide in the experimental and numerical case. The result of one of these calculations is shown on the upper half of figure 3, where on amount of 5×10^{11} cm^{-3} neutral oxygen initially present has been taken, there is no neutral oxygen flux, and the impurity confinement time τ_p has been taken equal to 5 msec.

Proceeding in this way for all the observed ions we were able to obtain the plasma "chemical" composition at a time of approximately 7 msec, when the average electron density is 0.8×10^{13} cm^{-3}. The results of this calculation are shown in Table I. Taking a limit ionization state corresponding to $T_e \leq 100$ eV, these impurity values show that, already at this early time $Z_{eff} \simeq 4$.

Element	Atoms/cm^3
O	5×10^{11}
N	10^{11}
C	4×10^{10}
Fe	$\leq 10^{10}$
Mo	$\leq 10^{10}$

TABLE I.
"CHEMICAL" COMPOSITION
OF THE PLASMA AT 7 MSEC
($\bar{n}_e = 8 \times 10^{12}$ cm^{-3})

However, since the electron density grows continuously, these impurity values are not sufficient to explain the independently calculated Z_{eff} value at the current plateau ($Z_{eff} \simeq 6$). Indeed, these values would then correspond only to $Z_{eff} \simeq 2.5$ (taking into account the increased electron temperature). This means that impurities must enter into the discharge after the initial phase, probably during the current increase due to the firing of the second capacitor bank, when a second peak appears on the impurity signals.

II-3. Radial profiles : current plateau. Figure 4 shows the space resolved profiles of electron density and temperature at the current plateau (150 msec), obtained by Thomson scattering. These data refer to a vertical scan of the lower half of the plasma. It must be noted that the plasma outer region has a very low electron temperature, reaching 100 eV only at a radius of $r \simeq 15$ cm. Figure 5 shows the experimental radiance $B_{D\beta}$ of the $D\beta$ line as a function of the chord height h, and the space resolved profile

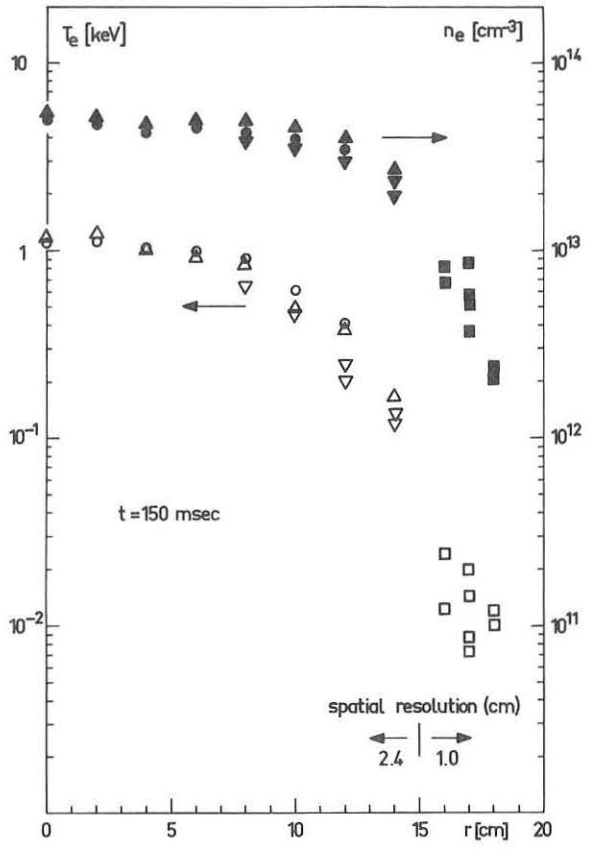

Figure 4.

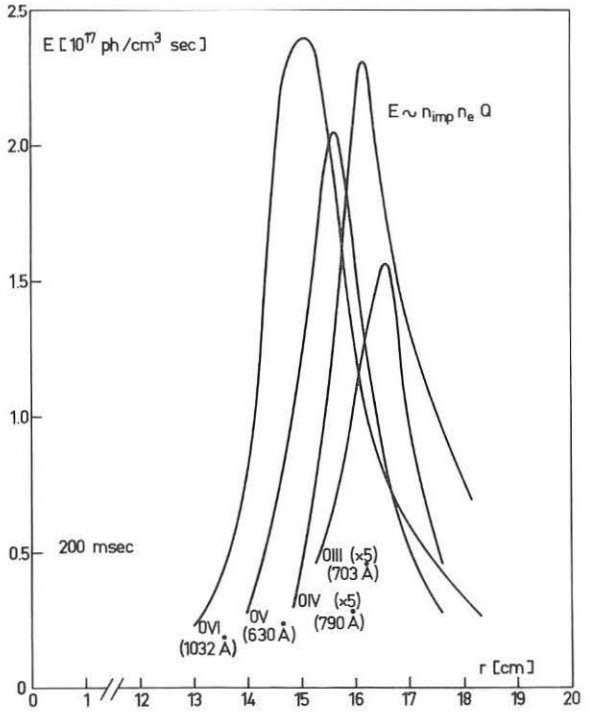

Figure 6.

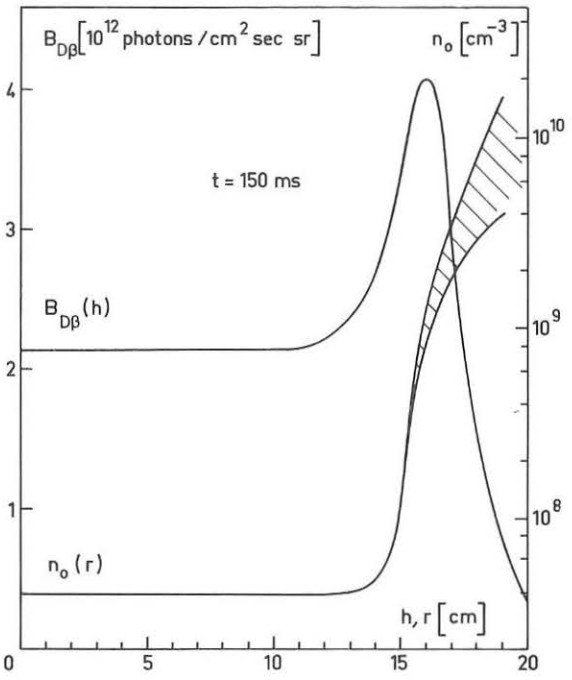

Figure 5.

of neutral deuterium density $n_o(r)$, obtained by Abel inversion. These data have been taken at φ = 180° at a time of 150 msec. For r $\geqslant$ 15 cm we have performed two calculations corresponding to two different fits of the electron temperature. The central neutral deuterium density has a value of 4 x 10^7 cm^{-3}, increasing to $\sim$ 10^{10} cm^{-3} at r = 19 cm. However, the central value must be taken as an order of magnitude indication, due to the difficulty of performing the Abel inversion procedure when the experimental, not inverted profile has a deep depression in the center. At φ = 0° (the diaphragm section) the shape of n_o (r) is approximately the same, but the absolute values are about one order of magnitude larger due to the plasma limiter interaction.

Figure 6 shows the radial (Abel inverted) profiles of the radiance of several oxygen ion lines at the current plateau. From these profiles one arrives to the conclusion that the maximum densities of the different oxygen ions are approximately the same, but the higher the ionization degree, the more the considered ion is inside the discharge. Moreover, experiments performed at two different locations have shown that the impurity distribution along the torus is, within the experimental errors, constant. The contribution of these oxygen ions to the electron density is (at r = 16 cm) of the order of 60 %.

II-4. Interpretation. Radial inwards diffusion. It is evident from the data presented above that the neutrals coming from the walls are ionized in a peripheral shell ; the observed signals are therefore interpreted in terms of an impurity flux. This flux is calculated starting from the equation describing the rate of growth of the density n_j of the ion j times ionized

$$\frac{\partial n_j}{\partial t} = S_{j-1}(T_e)\, n_e n_{j-1} - S_j(T_e)\, n_e n_j + \alpha_{j+1}(T_e)\, n_e n_{j+1} - \alpha_j(T_e)\, n_e n_j + \frac{1}{r}\frac{\partial}{\partial r}(r \vec{\psi}_j)$$

Here S_j and α_j are the ionization and recombination rate coefficients, and $\psi_j(r)$ is the local flux (cm^{-2} sec^{-1}) of the considered ion. All parameters are functions of the radius. However, experimentally it is found that $\partial n_j/\partial t = 0$ at the current plateau, and it can be easily shown that for the ions considered, at the electron temperature existing in the shell where they are produced, the two recombination terms can be neglected. Therefore, the knowledge of T_e (r), n_e (r), n_j(r), and n_{j-1} (r) is sufficient to calculate the flux term

$$\psi_j(r) = \frac{1}{r}\int_0^r r' [S_{j-1} n_e n_{j-1} - S_j n_e n_j]\, dr'$$

Figure 7 shows the quantity to be integrated, as a function of radius, for the couple of ions O^{4+} and O^{3+}. This quantity is calculated starting from the experimental data ; since they show that the ion O^{4+} is not present below a radius of 13.5 cm and the ion O^{3+} is not present above a radius of 17 cm, the two areas in the figure must be equal. Within the experimental errors this is indeed the case . One has therefore, for the ion O^{4+}, $(r\psi)_{max} = 2.5 \times 10^{16}$ cm^{-1} sec^{-1}, from which $\psi_{max} = 1.6 \times 10^{15}$ cm^{-2} sec^{-1}. Writing down the flux definition, i.e., $\psi_j = n_j v_j$, one finds that the diffusion velocity of the ion O^{4+} is $\sim 2 \times 10^3$ cm/sec at a radius of $\sim$15 cm. Similar values are found for the ions O^{5+}, O^{3+}, and N^{4+}. If one calculates the flux due to the friction between different ions /3,4/, assuming that the impurities are in the Pfirsch-Schlüter regime and neglecting

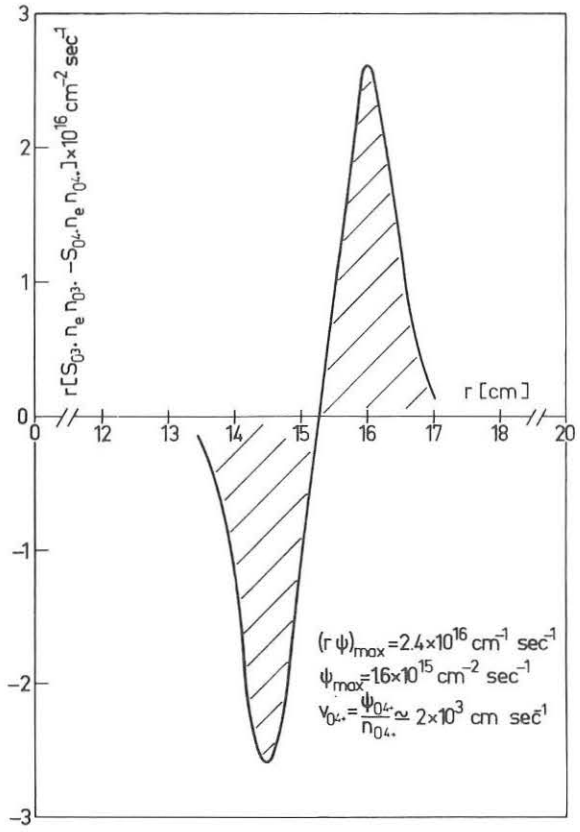

Figure 7.

temperature gradients, the value found for the inwards flux of O^{4+} (at the same radius) is $\sim 10^{15}$ cm^{-2} sec^{-1}, in good agreement with the value given above. In performing this calculation we have considered the effect on O^{4+} of the ions D^{+} (which contribute about 50 % to the flux), O^{5+}, and O^{3+}.

From the values on axis (chord height h = 0) of the experimental radiance we have calculated the atom flux ψ_c for all the observed ions (in this case $\psi_c = 2\pi\rho S_\lambda B_\lambda / \Gamma a Q$, where Γ is the branching ratio for the observed line, ρ the radius at which the observed ion is produced, Q the excitation rate coefficient, and B_λ the experimental radiance). The fluxes obtained in this way are given in Table II (note that, within the experimental errors, O^{2+}, O^{3+}, O^{4+}, and O^{5+} give the same atom flux).

TABLE II - ATOM FLUXES AT t = 150 MSEC

Ion	Observed line (Å)	B (cm^{-2}sec^{-1}sr^{-1}) on axis	ψ_c (cm^{-2} sec^{-1})
D	4860	3×10^{12}	3×10^{15}
OVI	1032	1.5×10^{17}	3×10^{15}
NV	1238	3×10^{16}	5×10^{14}
CIII	977	1.5×10^{16}	3×10^{14}
FEXV	284	1.5×10^{14}	2×10^{12}
MOXIV	374	5×10^{14}	5×10^{12}

The problem is now to know how deep into the discharge these impurities go. Calculations of the power necessary to ionize the incoming flux up to a limit ionization state determined by the electron temperature and

of the power necessary to heat the produced electrons to the measured electron temperature have shown that these impurities cannot all enter into the central hot plasma core and must, therefore, mainly recycle in a peripheral shell with a recycling time that can be estimated to be of the order of 10 msec. For example, oxygen (which is the dominant impurity) enters into the discharge and is progressively ionized up to the ion O^{6+} (for which we do not have a radial profile), and at this point should go mainly out to the walls, probably without recombining (at least for $r \leq 18$ cm). The mechanism responsible for this is, at this time, not clear.

We must stress out at this point that the radiation power loss in this peripheral shell (obtained by adding the contribution of all the observed lines) is quite important and corresponds to ~ 35 % of the input ohmic power. In this context, bolometric measurements have shown that most of the power goes to the walls (30 to 70 % depending on the location of the bolometer), whereas only ~ 4 % of the input ohmic power is found on the limiter. Although these measurements fail to account for the entire energy balance, their indication is in agreement with the fact that a large part of the input power is lost by radiation.

On the basis of what we have discussed up to now, the plasma should be composed of two well separated regions : a hot central plasma, with properties which can be varied by changing I_p and B_T, and a peripheral shell, interacting strongly with the walls and limiter, characterized by a large flux of impurities mainly recycling to the walls.

III- RESULTS WITH OTHER DISCHARGES.

Up to now nothing has been said about the central hot plasma. A search for the 117 Å line of MoXXXI (ionization potential $\sim$ 1800 eV), and the 129 Å, 178 Å doublet of MoXXXII (ionization potential $\sim$ 1870 eV) /5/ did not reveal any line emission in the 140 kA, 26 kG discharges. However, in a series of experiments the magnetic field was increased to 50 kG in several steps, at constant current, resulting in an increase of the central electron temperature /6/. The mentioned lines appeared when the central electron temperature reached a value of 1.5 keV, thus confirming the fact that they belong to highly ionized ions present in the central hot plasma. Figure 8 shows their time evolution, obtained in a series of experiments in which B_T = 40 kG, along with the plasma current I_p and the radiance of the 374 Å line of MoXIV. The intensity of the highly ionized molybdenum lines arrives to a maximum at approximately 170 msec and then remains constant until the current decrease. A coronal steady state model has been used in

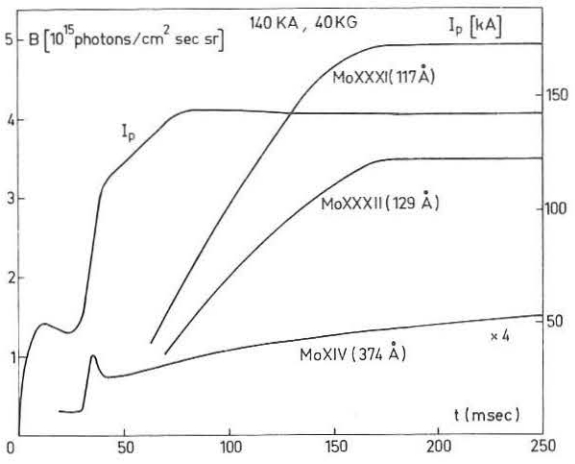

Figure 8.

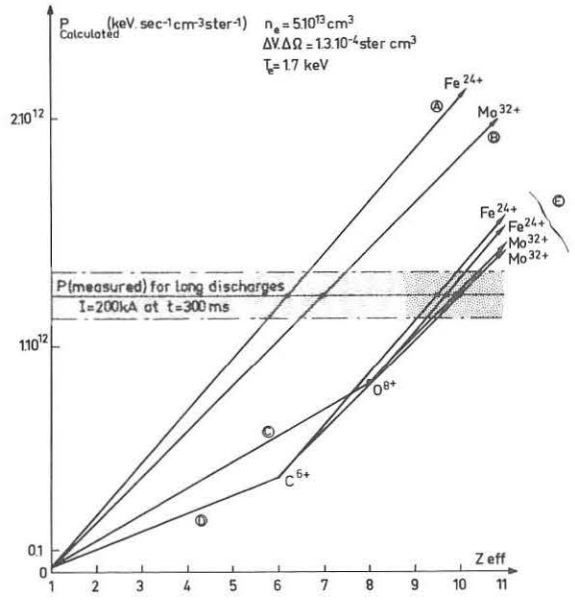

Figure 9.

order to deduce, from the lines emission, the quantity of molybdenum present in the center at the current plateau /1/. The result is 10^{11} cm^{-3}. A comparison with Table I shows that molybdenum must enter into the discharge after the initial period. Moreover, in order to account for the temporal behaviour shown in figure 8, the incoming flux of molybdenum must last of the order of 100 msec, starting from the firing of the second capacito bank. The power loss due to the radiation of these two lines represents only a few % of the input ohmic power. Finally, since the value of Z_{eff} for these discharges is $\sim$ 6, the contribution of the molybdenum ions to Z_{eff} is of the order of 25 %. Figure 9 shows how the Z_{eff} value is obtained starting from the absolute measurement of the soft x-ray power emitted by the plasma. For a given electron temperature a set of curves is calculated, corresponding to the x-ray power emitted using different assumptions on the nature of the impurity ions. The experimental value is then used in order to obtain from this set of curves a range of values for Z_{eff}. In the example of figure 9 corresponding to a 200 kA, 40 kG discharge, one finds in this way $7 \leq Z_{eff} \leq 10$ at the current plateau which gives a quantity of molybdenum between 4×10^{11} and 1.7×10^{11} cm^{-3} (the first value is obtained considering that the only impurity present is molybdenum, the second one considering molybdenum plus completely stripped oxygen). Note that the lower of these two values is in good agreement with the value obtained from the u.v. measurements ($\sim 10^{11}$ cm^{-3}), expecially since in this calculation we have neglected the presence of highly ionized iron. The value of Z_{eff} in the center, calculated starting from the q (r = 0) = 1 assumption,

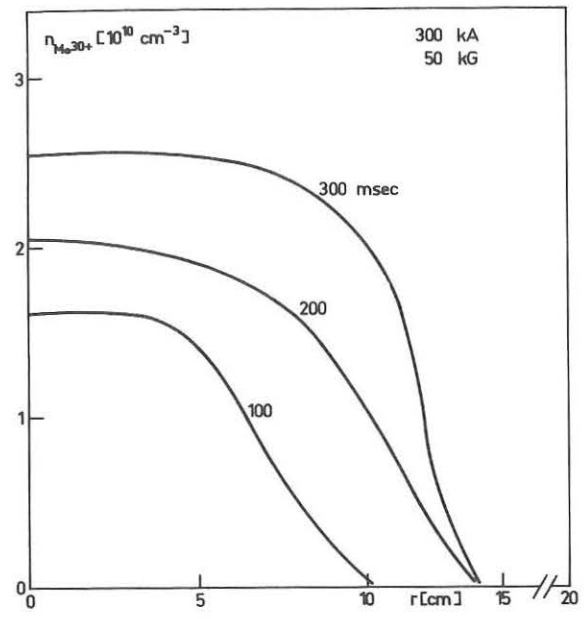

Figure 10

is in this case 8, well within the x-ray evalution, thus showing that the resistivity enhancement is due mainly to the presence of impurities and not to turbulence.

Figure 10 shows the radial (Abel-inverted) profiles of the density of Mo^{30+}, obtained with 300 kA, 50 kG discharges. This series of shocks had a longer duration, and in particular the electron density increased up to 350 msec, in such a way that (between 100 and 300 msec) the ratio $n_e / n_{Mo^{30+}}$ remained constant. The results of figure 10 can be used, if the coronal steady state is rapidly attained, to calculate the flux of the ion Mo^{30+}, using the equation

$$\frac{\partial n_{Mo^{30+}}}{\partial t} = \frac{1}{r}\frac{\partial}{\partial r}\left(r \vec{\Psi}_{Mo^{30+}}\right)$$

In this way we obtain $\Psi_{Mo^{30+}}(r = 5\ \text{cm}) = 3 \times 10^{11}\ \text{cm}^{-2}\ \text{sec}^{-1}$. With the usual flux definition, and assuming that the impurity confinement time is of the order or larger than 100 msec, one deduces an inwards diffusion velocity of the order of 10 cm/sec.

IV- CONCLUSIONS

The main conclusions of this paper are the following :

- Impurities appear very early at the beginning of the discharge and have a uniform distribution during the ionization phase. The main impurity is oxygen ($\sim$ 5 % as compared to the electron density), and the value of Z_{eff} is $\sim$ 4 already at this early stage.
- During the current plateau an approximatly stationary state is reached ; the impurity ions are radially distributed following their ionization potential. The ions O^{3+}, O^{4+}, O^{5+}, and N^{4+} have an inwards diffusion velocity of the order of 2×10^3 cm/sec at a radius of 15-16 cm in good agreement with the theoretical value. The total flux of oxygen is $3 \times 10^{15}\ \text{cm}^{-2}\ \text{sec}^{-1}$.
- Energy and particle balance considerations show that only a small portion of the incident impurities can reach the central hot plasma.
- The plasma is composed of two separated regions : a central hot plasma with properties depending on I_p and B_T, and a peripheral shell (width 5-7 cm) interacting strongly with the walls and limiter, characterized by a large flux of impurities mainly recycling to the walls.

- An important fraction of the input ohmic power is lost as line radiation in this external shell ($\sim$ 35 % in the discharge considered) ; on the contrary, radiation from the two observed lines due to highly ionized molybdenum ions present in the center contributes only a few % to the losses.
- The values of Z_{eff} obtained from absolute measurements of the soft x-ray emission are in agreement with the values obtained from the conductivity.
- Highly ionized molybdenum ions ($\sim 10^{11}$ cm^{-3}) are present in the central hot region and contribute about 25 % to Z_{eff}. The inwards diffusion velocity of the ions Mo^{30+} is $\sim$ 10 cm/sec at r = 5 cm.

REFERENCES.

/1/ - Equipe T.F.R., EURATOM-CEA Association Fontenay-Aux-Roses, Report EUR-CEA-FC 777 (July 1975) ; submitted for publication to Nuclear Fusion.

/2/ - HINNOV E., HOFMANN F.W., J. Opt. Soc. Am. 53, 1259 (1963).

/3/ - RUTHERFORD P.H., Phys. Fluids 17, 1782 (1974).

/4/ - TUDA T., TANAKA M., J. Phys. Soc. Japan 38, 1228 (1975).

/5/ - HINNOV E., IV Internat'l Conf. on u.v. and x-ray spectroscopy on astrophysical and laboraty plasmas, IAU Colloquium 27, Harvard (1974).

/6/ - Equipe T.F.R., contributed paper presented at this conference by P. Platz.

X-RAY MEASUREMENTS ON THE ST TOKAMAK

S. von Goeler
Plasma Physics Laboratory, Princeton University,
Princeton, New Jersey 08540, USA

With rising electron temperature, the x-ray emission has become an increasingly prominent feature of tokamak plasmas. The exact origin of the observed radiation is still a matter of debate. In the first part of the paper we try to summarize our present thinking on this topic with special emphasis on the role played by dielectronic recombination. This question is of relevance for the interpretation of impurity data. In the second part, we review the main results of our investigation of the fluctuations in the x-ray emission and their relation to the MHD-stability of the tokamak. We discuss the observation of $m=1$ oscillations accompanied by internal disruptions, and the observation of magnetic islands for the $m=2$ instability.

I. The X-Ray Spectrum

A typical x-ray spectrum from the tokamak (Fig. 1a) consists of a continuum and several impurity lines [1]. A comparison with a hypothetical bremsstrahlung spectrum calculated for a hydrogen plasma from the laser temperature and density profile shows that, although the slopes of the two spectra are in good agreement, the intensity of the measured spectrum is usually by a factor 5 to 100 larger than calculated for hydrogen bremsstrahlung (Fig. 1b). Obviously the main contribution to the spectrum comes from impurities.

If low-Z impurities like oxygen are dominant the analysis is relatively uncomplicated, because the low-Z atoms are completely stripped in the hot regions of the discharge. The continuum then consists of recombination radiation (I_{fb}) and bremsstrahlung (I_{ff}), the intensity ratio depending on temperature (e.g., for oxygen $I_{fb}/I_{ff}=4.3$ at $T_e=1$ keV and $I_{fb}/I_{ff}=1.5$ at 2 keV). The impurity concentration or Z_{eff} can be determined very accurately in this case. Unfortunately, the fact that discharges occur in which Z_{eff} is larger than 8 (Fig. 1c), shows that also high-Z impurities like iron or molybdenum have to be taken into consideration.

The presence of high-Z impurities complicates the analysis considerably, because we have to cope with several elements, and because the recombination radiation depends sensitively on the charge state of the ion, which in turn depends on an interplay of dielectronic recombination, radiative recombination, and confinement. Only recently are accurate predictions for

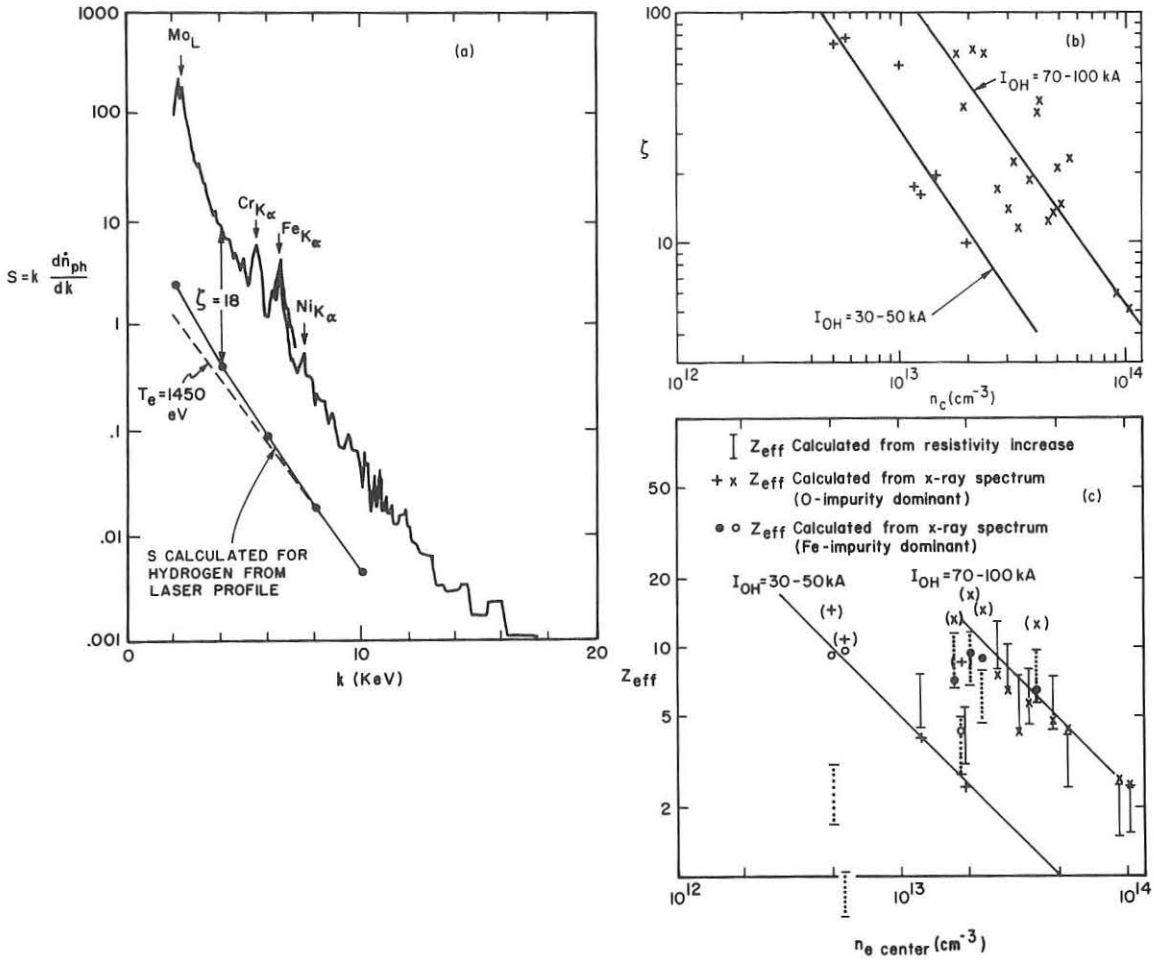

Fig. 1. (a) Comparison of measured x-ray spectrum with hydrogen spectrum computed from laser data. Central laser temperature is $T_e = 1450$ eV. (b) Enhancement factor ζ vs central electron density n_c. (c) Z_{eff} determined from continuum x-ray intensity and plasma resistivity vs n_c. (PPPL 753692)

the dielectronic recombination for tokamak plasmas [2] emerging. Figure 2 shows the radiative power loss calculated by Merts et al. [2] for iron impurities in corona equilibrium. At low electron temperatures ($T_e \lesssim 1.5$ keV), for which iron is not ionized to the helium-like state, dielectronic recombination is the dominant recombination process; for high electron temperatures ($T_e \gtrsim 1.5$ keV), for which iron is in the helium-like state, dielectronic recombination is of lesser importance. The effects of finite confinement, i.e., the transport of ions between cold and hot regions, lead to deviations from local corona equilibrium. These effects are difficult to predict, since the transport of the high-Z impurities is not well understood. If this transport is comparable to the energy transport, its effect is small at low temperatures where dielectronic recombination is large, but should be an important factor at high temperatures.

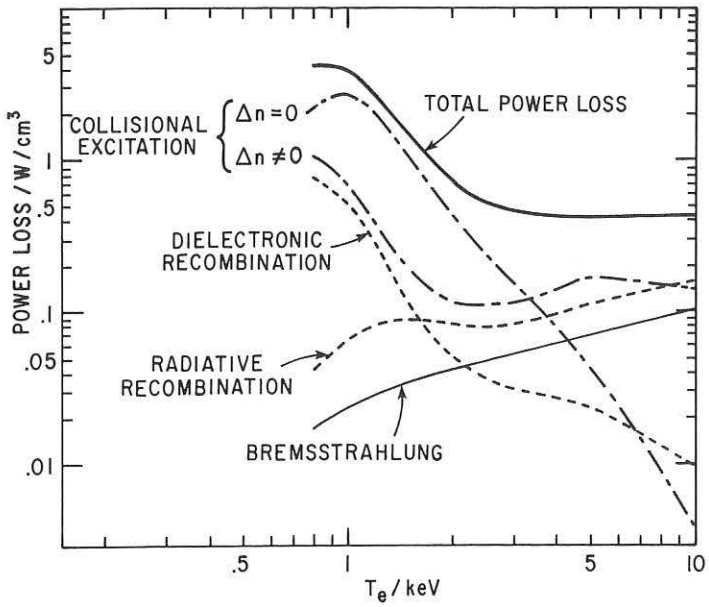

Fig. 2. Radiation power loss of iron impurities calculated by Merts, et al. [2], for $n_e = 10^{14} cm^{-3}$ and $n_{Fe} = 10^{12} cm^{-3}$. (PPPL 753684)

reflect the effect of a deviation from corona equilibrium due to finite confinement. Characteristically we observed the largest deviation from Cowan's [2] calculated curves for $T_e = 2000$ eV. These impurity lines are of great interest because they seem to be produced by dielectronic recombination, as predicted by Gabriel [4], rather than by direct collisional excitation.

II. X-Ray Fluctuations

Instabilities in the tokamak plasma have been studied by investigating fluctuations in the continuous, thermal x-ray emission. This method has revealed:

(a) The existence of $m = 0$, $n = 0$ internal disruptions preceded by $m = 1$, $n = 1$ oscillations [5]. This feature was observed at high filling pressures, near the high pressure instability limit and at low densities, near the runaway regime (Fig. 4).

These considerations were surprisingly well reflected in some crude measurements [3] of the K_α-line of iron which were performed on the ST Tokamak with a crystal spectrometer (Fig. 3). The fact that the measured spectrum fits better to the theoretical curve [2] for 1000 eV than for 1200 eV, the peak temperature measured by the laser, may perhaps

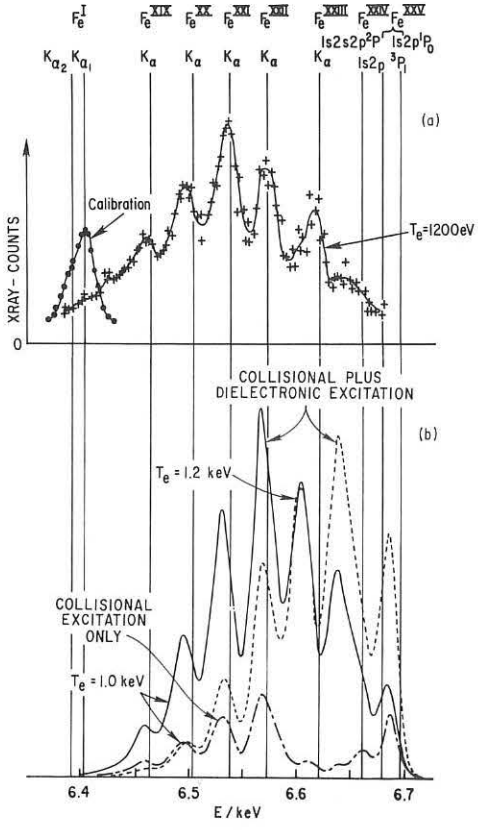

Fig. 3. K_α-line structure of iron: (a) Spectrum measured on ST at central temperature T_e = 1200 eV. The calibration is the K_α-line of neutral iron. (b) Computations of the K_α-line by Cowan [2] for T_e = 1200 and 1000 eV ($n_e = 10^{14} cm^{-3}$, $n_{Fe} = 10^{12} cm^{-3}$). For T_e = 1000 eV the contribution of direct collisional excitation is also shown. (PPPL 753691)

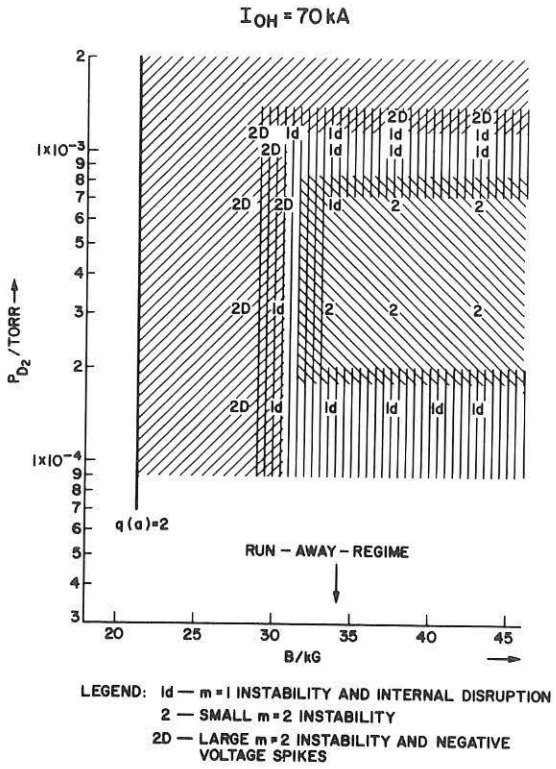

Fig. 4. Instability regimes in ST at ohmic heating current $I_{OH} = 70$ kA. Ordinate is filling pressure (D_2) and abscissa toroidal field. Approximate regions in which instabilities occur are shown by shading and lettering. (PPPL 743297)

(b) The existence of small $m = 2$, $n = 1$ oscillations. These oscillations were observed at intermediate filling pressures (Fig. 4), concurrent with and phase-locked to simultaneous $m = 3$ signals on the B_θ-loops.

(c) Evidence of the magnetic island structure of the large $m = 2$ oscillations preceding major disruptions with negative voltage spikes.

Typical measurements for the internal disruptions and $m = 1$ oscillations are shown in Fig. 5. (Similar data have been reproduced on the ATC and the TFR tokamaks [6]). When looking through the center ($r = 0$) of the column the x-ray intensity slowly increases by 3 to 30% for a time interval 0.5 to 5 msec, and than abruptly decreases. This sawtooth structure is evidence of the internal disruption. A little bit farther out ($r = 1.2$ cm) the sawtooth amplitude becomes smaller; at the same time small sinusoidally growing precursor oscillations appear. These have mode numbers $m = 1$, $n = 1$, as deduced from the phase relation between signals from different detectors looking at different radii and locations around the torus. At $r = 1.6$ cm the sawtooth amplitude becomes zero and the precursor oscillation begins to disappear. At still larger radii ($r = 2$ cm) the sawtooth appears again but is inverted until it finally vanishes at 2.8 cm. The node of the sawtooth (in Fig. 5 the point $r = 1.6$ cm) corresponds to the radius r_s where the $m = 1$ oscillations becomes abruptly smaller. It probably represents the $q = 1$ surface in the plasma, since it agrees with the $q = 1$ surface calculated from the laser temperature profile under the assumption $Z_{eff}(r) = \text{constant}$. This identification is, however, not absolutely certain. For instance, on ATC the $q = 1$ surface from the laser data was located at a larger radius than the node of the sawtooth, due, perhaps, to peaking of the impurities in the center of the discharge.

The exact physical nature of the $m = 1$ oscillations is still not satisfactorily explained. It is unlikely that the oscillations represent the

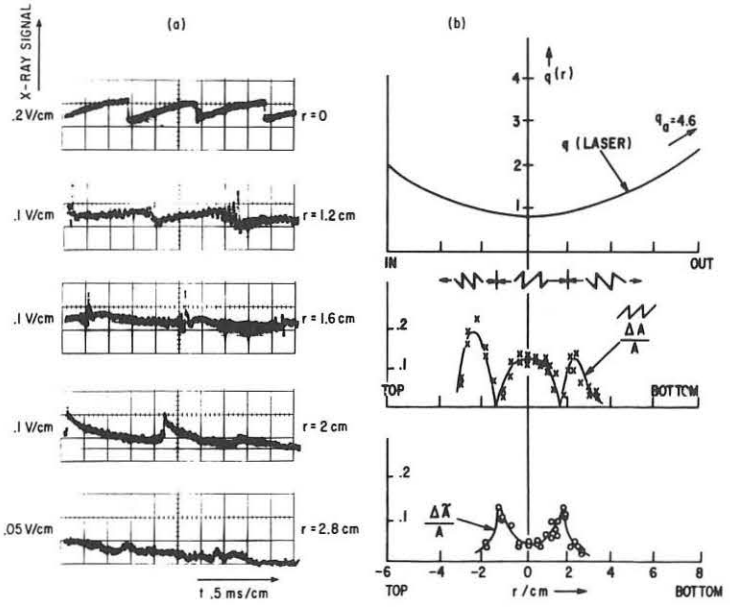

Fig. 5. Internal disruptions and $m = 1$ oscillations: (A) Typical scope traces of the x-ray intensity varying the distance r from the center of the discharge to the line of sight. (b) Radial profiles of the safety factor q from laser data, the sawtooth amplitude $\tilde{\Delta}A/A$ and the amplitude $\check{\Delta}A/A$ of the sinusoidal $m = 1$ oscillation shortly before the step. (PPPL 753793)

internal kink mode, predicted by Shafranov and Rosenbluth [7]. Toroidal terms [8] have a stabilizing effect on this mode and, moreover, the experimentally determined amplitude of the waves is much larger than nonlinear theory predicts. The arguments leading to this conclusion are summarized in Fig. 6. According to the predictions for the internal kink mode the displacement ξ is constant for $r < r_s$ and $\xi = 0$ for $r > r_s$. The unperturbed x-ray emission profile $\varepsilon_o(r)$ is assumed parabolic

$$\varepsilon_o(r) = \varepsilon_o(0)\,(1 - r^2/b^2) \quad .$$

Inserting such a profile in Abel's equation, we obtain for the line integral

$$I_o(r) = \frac{4}{3}\,\varepsilon_o(0)\,b\,(1 - r^2/b^2)^{3/2} \quad .$$

The parameters $\varepsilon_o(0)$ and b are determined by a fit to the measured I_o. An $m = 1$ perturbation to $\varepsilon_o(r)$ then yields the oscillation amplitude $\varepsilon_1(r)$ in terms of the displacement ξ

$$2\varepsilon_1(r) = \varepsilon_o(r - \xi) - \varepsilon_o(r + \xi) = 4\varepsilon_o(0)\,\xi\, r/b^2 \quad \text{for} \quad 0 < r < r_s \quad .$$

Inserting this into an Abel equation, modified for m-mode symmetry, yields

$$I_1(r) = 2\int_r^{r_s} \varepsilon_1(r_o)\, r\, dr_o/(r_o^2 - r^2)^{1/2} = 4\varepsilon_o(0)\,\xi b^{-2} r (r_o^2 - r^2)^{1/2} \quad .$$

The experimental points (+) for I_1 in Fig. 6 scatter appreciably, due to the lack of shot-to-shot reproducibility; it can therefore only be stated that the shape of the measured curve is not in disagreement with the predicted one. However, the absolute value of the displacement ξ can be

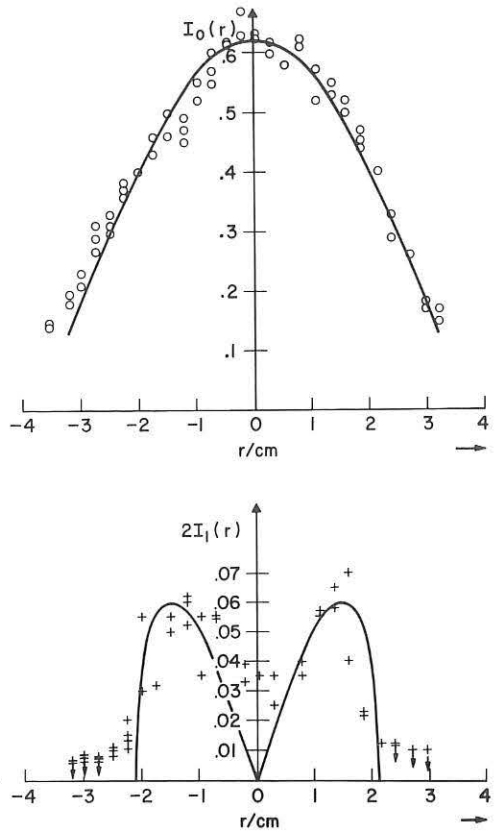

Fig. 6. Comparison of $m = 1$ with MHD-theory. (a) Measured average x-ray intensity I_o vs radius. The line is a best fit for an assumed parabolic profile of the unperturbed x-ray source. (b) Measured oscillation amplitude vs chord radius. The line is calculated, assuming a contant displacement $\xi = 0.46$ cm out to $r = r_s = 2.1$ cm and $\xi = 0$ for $r > r_s$. (PPPL 753690)

derived with better accuracy. We find $\xi/r_s \approx 0.2$ which is much larger than one would expect from the nonlinear theory of the internal kink mode.

Recently Rutherford [9] has included resistivity in the theory, showing that an $m = 1$ tearing mode exists with an island structure. Nonlinear calculations of this mode are not available, and it is therefore unclear whether the large amplitudes can be explained in this way.

The physical causes behind the internal disruptions are still unknown. The internal disruptions are, on the other hand, very important for the energy transport in the central core of the plasma. The energy loss due to the internal disruption can be estimated by measuring the decrease in electron temperature during a disruption. The resulting loss is of the same magnitude as the energy input due to ohmic heating into the plasma volume inside the $q = 1$ surface.

The small $m = 2$, $n = 1$ oscillations are observed at intermediate pressures. The x-ray traces (Fig. 7) exhibit small (10%) sinusoidal oscillations, which seem to have reached a nonlinear stationary state. The m- and n-numbers are again assigned by using phase measurements between various detectors, sampling at different radii and locations around the torus. Simultaneously, $m = 3$ oscillations, occurring presumably around the $q = 3$ surface, are picked up with B_θ-loops. The frequency of $m = 3$ and $m = 2$ oscillations is in the ratio 3:2, i.e., the plasma rotates like a solid body. Propagation is in the direction of the electron diamagnetic drift and the frequency is of the order ν^*, the diamagnetic drift frequency.

A comparison of the radial profiles of the small $m = 2$ oscillations with predictions for the tearing mode [10] is shown in Fig. 8. Polynomials are fitted to the unperturbed and to the oscillating x-ray line intensity, $I_o(r)$ and $I_2(r)$. These profiles are Abel inverted to obtain local x-ray

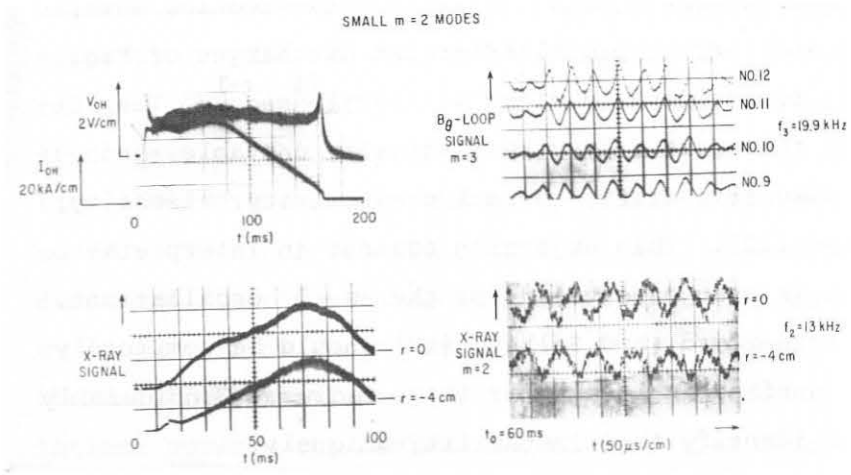

Fig. 7. Typical current, voltage and x-ray traces for the small m = 2 oscillations. The x-ray signals have a kind of "grassy" appearance, which is due to small sinusoidal m = 2 oscillations. B_θ-loops and the voltage traces exhibit m = 3 oscillations. (PPPL 753794)

emissions $\varepsilon_o(r)$ and $\varepsilon_2(r)$. Assuming that changes in x-ray emission result only from a displacement — a reasonable assumption if the plasma behaves like an incompressible fluid — we obtain the curve for the measured displacement $\xi = \varepsilon_2/2(d\varepsilon_o/dr)$. Also shown is a theoretical curve, the displacement from the linear analysis of Furth, Rutherford, and Selberg [10], which is also used in the nonlinear analysis of Rutherford [11]. Linear theory predicts a pole at the singular surface, which is smoothed out by island formation. The width of the island, under the so-called "constant ψ" approximation is indicated in Fig. 8. At this point the concept of ξ based on linear perturbation breaks down. For small m=2, as well as for the m=1 oscillations, the island structure could not be identified because the signals were too small and too close to the noise level.

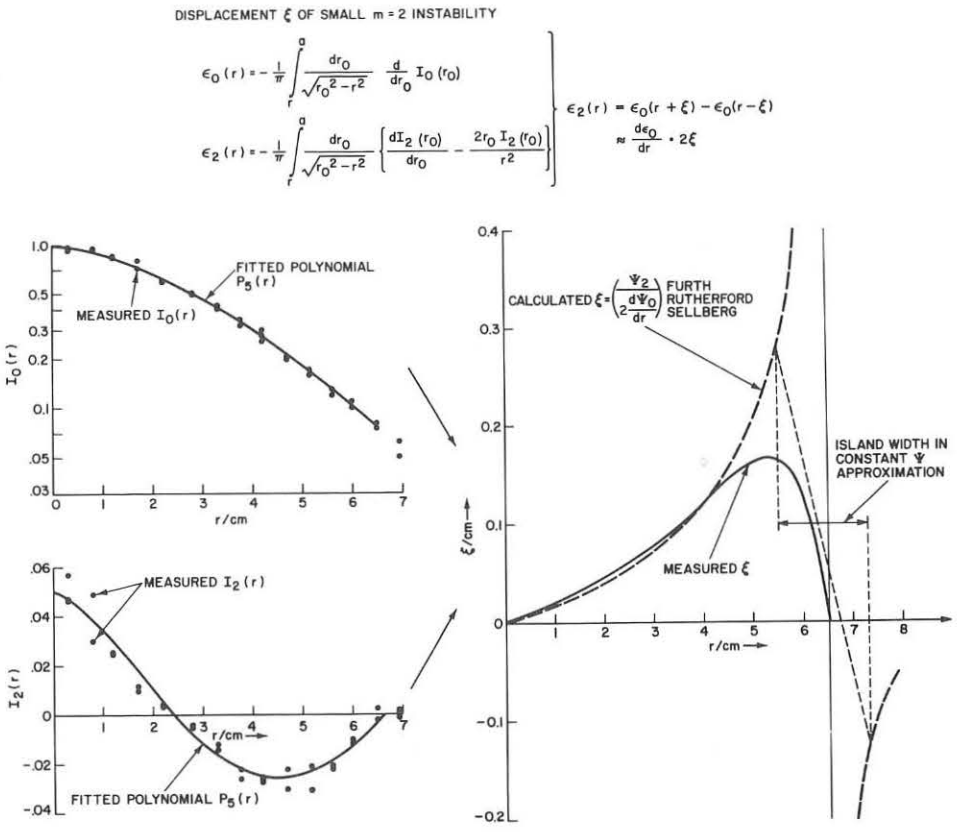

Fig. 8. Comparison of the radial profile of the small m = 2 oscillations with tearing mode theory. (PPPL 743890)

A calculation of the linear growth rate γ_T [10] of the tearing mode, based on laser temperature and current profiles for the discharges of Fig. 8, gives $\gamma_T \approx 6 \cdot 10^3 \text{sec}^{-1}$, to be compared with $\omega^* \approx 8 \cdot 10^4 \text{sec}^{-1}$. The pure $m = 2$ tearing mode is therefore only very marginally unstable, and probably the effects of diamagnetic drift, thermal conductivity, viscosity, etc. have to be incorporated [12]. This objection against an interpretation as a pure tearing mode is even more valid for the $m = 3$ oscillations, which according to Furth, Rutherford, and Selberg [10] should be completely stable, because the $q = 3$ surface is located at large radius. Considerably more work has to be done to identify this instability uniquely.

The large $m = 2$ oscillation followed by large scale disruptions has been studied already with B_θ-loops [13, 14], the ion-beam probe [15] and framing cameras [16]. The x-ray technique has yielded, as new information, some evidence for the island structure. In Fig. 9a is shown a radial plot of the maximum and minimum of these oscillations just before the disruption. Typical oscilloscope traces are inserted at serval radii. The positions of the crossovers at $r = 4$ and 8.5 cm represent points of phase reversal relative to a fixed monitor. In the region between $r = 6$ and 8.5 cm the

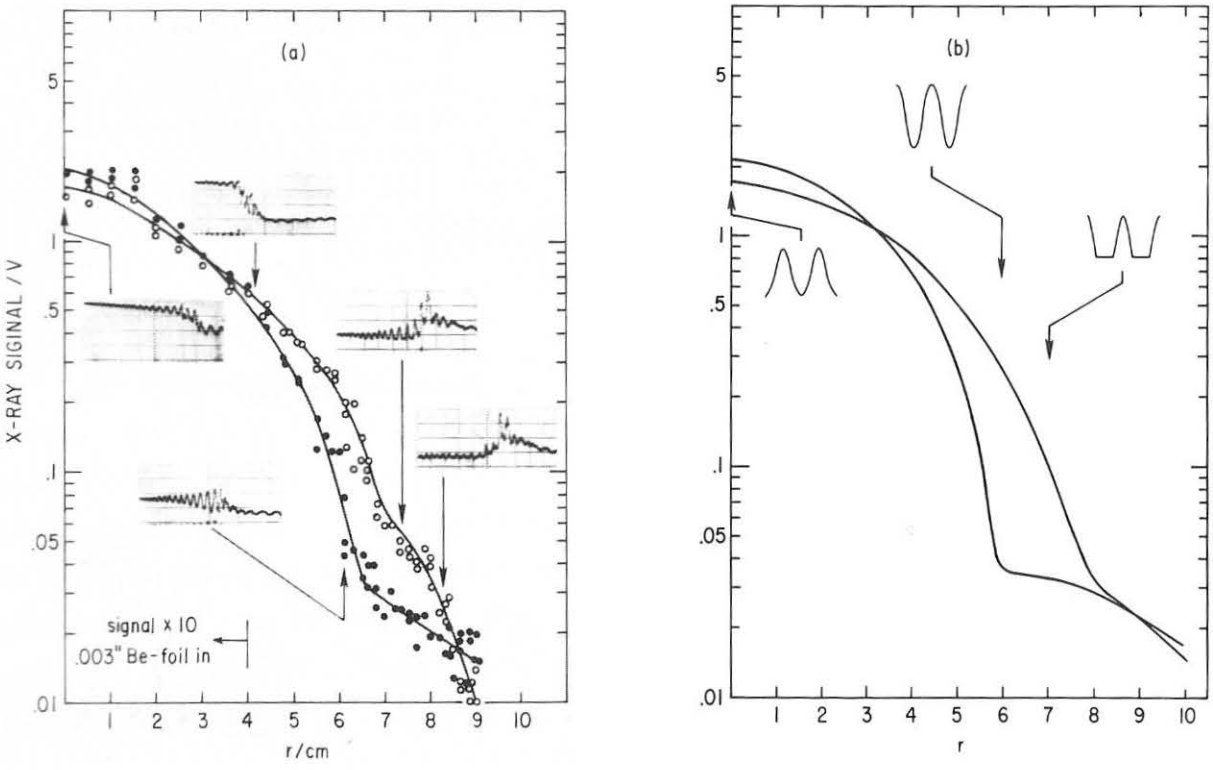

Fig. 9. Large $m = 2$ oscillations and disruptions. (a) Measured x-ray intensity vs radius: Dots (•) represent peak intensity and circles (o) valley intensity of the oscillation just before disruption; in the range 4 cm $< r <$ 8.5 cm the phase with respect to a fixed monitor changes and the dots become minima and the circles maxima. Scope traces exhibit truncation in the range 6 cm $< r <$ 8.5 cm. (b) Computer simulation of this measurement based on the tearing mode theory [10]. (PPPL 753795)

oscillations are truncated for part of the oscillation period — the scope trace at $r = 7.3$ cm is a good example. The truncation time increases with radius. The truncation is the feature that seems to be caused by the island structure, as the computer simulation of Fig. 9b suggests. In the computation it is assumed that the x-ray emission ε is constant on a magnetic surface ψ, i.e., $\varepsilon = \varepsilon(\psi)$. A functional dependence is chosen, so that ε decreases steeply with radius and is flat (ε = constant) within the island. ψ is taken from Furth, Rutherford, and Selberg [10]. Integration along chords of observation and rotation of the island pattern produces oscillations between the maximum and minimum lines with time shapes at different radii as shown. These calculations qualitatively reproduce the features observed in Fig. 10. The truncation seems to be associated with the fact that the electron temperature and consequently x-ray emission are relatively flat across the island.

The oscilloscope traces of Fig. 9 demonstrate also the effect of the large scale disruption on the x-ray traces. The x-ray intensity decreases in the central hot region of the plasma and increases in the outer region of the island: i.e., the large scale disruption exhibits the same sawtooth-like feature as the the internal disruption. Figure 10 shows the time development of the x-ray profiles during the disruption. The profile is flattened out and there is some indication that the disruption is a process that begins close to the island and propagates on a time scale of a few 100 μsec toward the inside as well as toward the outside. The latter conclusion is drawn from the observation that the negative voltage spike appears 200 μsec after the sudden break in the sawtooth of the x-ray data. The velocity of propagation is in agreement with Jacobsen's [16] measurements. Practically nothing is known about the physical causes behind the disruption.

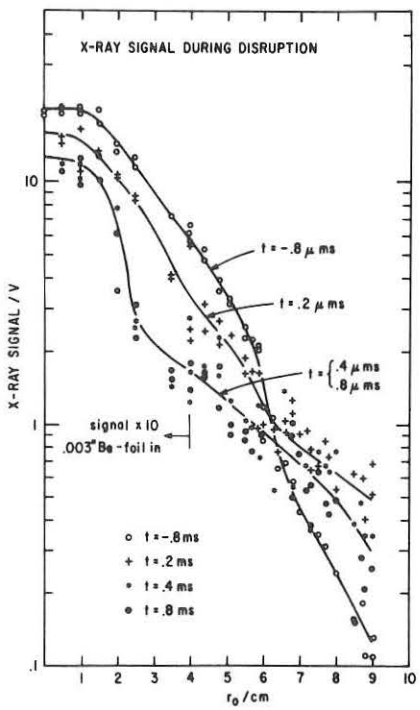

Fig. 10. Average x-ray intensity at different times during the disruption. (PPPL 753796)

In summary it seems that the stability of the ST tokamak was governed by the tearing mode or closely related instabilities. The safety factor $q(0)$ in the center

was always close to one and the $q = 2$ point was located at sufficiently large radius, so that the $m = 2$ instability was either stable or only marginally unstable, as discussed in Ref. [10]. If $q(0) \lesssim 1$, we observed $m = 1$ oscillations and internal disruptions, which were not too harmful because they involved only a small plasma volume in the center of the discharge. If $q(0) \gtrsim 1$ we observed $m = 2$ oscillations, which were stationary and of small amplitude at intermediate densities, while at high densities they had large amplitudes and led into disruptions. It is unclear at present whether the small $m = 2$ oscillations are fundamentally different from the large precursor oscillations of the disruption, or whether at the lower densities, higher temperature or small changes of the current profile lead to a nonlinear state without disruption.

The support of Dr. M. B. Gottlieb and Dr. H. P. Furth and many discussions with members of the theoretical division, in particular, with Dr. P. H. Rutherford, and the ST staff, especially W. Stodiek, are gratefully acknowledged. We thank W. Mycock, M. Perron and his crew for the technical assistance. We are grateful to Drs. R. Cowan and A. Merts of Los Alamos for making their computer calculations available.

This work was supported by USERDA Contract E(11-1)-3073.

---

[1] S. von Goeler, et al., Nuc. Fus. 15 (1975) 301.
[2] A. L. Merts, R. D. Cowan, private communication.
[3] N. I, Bretz, et al., in Plasma Physics and Controlled Nuclear Fusion Research (Proc. 5th Int. Conf. Japan, 1974) Paper A3-1, to be pub- by IAEA.
[4] A. H. Gabriel and T. M. Paget, J. Phys. B 5 (1972) 673; A. H. Gabriel, Mon. Not. Roy. Astron. Soc. 160 (1972) 99.
[5] S. von Goeler, et al., Phys. Rev. Lett. 33 (1974) 1201.
[6] R. Smith, Princeton Plasma Physics Laboratory Report MATT-1150 (1975); J. Tachon, et al., Proceedings of Annual Meeting on Theoretical Aspects of Controlled Thermonuclear Research (Sherwood Meeting), Apr 7-9, 1975, Arlington, Virginia.
[7] V. D. Shafranov, Sov. Tech. Phys. 15 (1970) 175; M. N. Rosenbluth, et al., Phys. Fluids 16 (1973) 1894.
[8] A. Ware, Phys. Rev. Lett. 26 (1971) 1304.
[9] P. H. Rutherford, private communication.
[10] H. P. Furth, P. H. Rutherford and H. Selberg, Phys. Fluids 16 (1973) 1054.
[11] P. H. Rutherford, Phys. Fluids 16 (1973) 1903.
[12] P. H. Rutherford and H. P. Furth, Princeton Plasma Physics Laboratory Report MATT-872 (1971).
[13] S. V. Mirnov, I. B. Semenov, in Plasma Physics and Controlled Nuclear Fusion Research (Proc. 4th Int. Conf. Madison, 1971) II, IAEA (1971) 401.
[14] J. C. Hosea, et al., in Plasma Physics and Controlled Nuclear Fusion Research (Proc. 4th Int. Conf. Madison, 1971) II, IAEA (1971) 77.
[15] J. C. Hosea, et al., Phys. Rev. Lett. 30 (1973) 839.
[16] R. Jacobsen, Princeton Plasma Physics Laboratory Report MATT-1038 (1974).

Experimental Results on JAERI Tokamaks

Y. Shimomura
Japan Atomic Energy Research Institute, Tokai, Ibaraki, Japan

This paper describes recent experimental results on JFT-2a and JFT-2. In JFT-2a, a separatrix magnetic surface is stably obtained, and heat and particle fluxes to the divertor are investigated. In JFT-2, plasma densities in hydrogen and helium discharges are investigated.

1. Introduction

This paper describes recent results on JFT-2a and JFT-2 experiments. Their machine parameters are summarized in Table 1.

Table 1. Machine Parameters of JFT-2a and JFT-2

	JFT-2a	JFT-2
Major Rarius	0.6 m	0.9 m
Minor Radius	0.1 m	0.25 m
Toroidal Magnetic Field	1.0 T	0.9/1.8 T
Remarks	Divertor Non Circular	Dynamic Limiter Fat Tokamak

JFT-2a shown in Fig. 1 is a Tokamak device with an axisymmetric magnetic limiter and/or divertor. Detailed description of the machine and preliminary experimental results were given in refs. 1) and 2). The following sections describes the characteristics of a separatrix magnetic surface and the plasma behavior in the divertor region.

JFT-2 is a fat Tokamak device. Machine parameters and experimental results with a toroidal field of 0.9 T were reported in ref. 3). In a number of tokamak devices a steady increase in the plasma density during discharges has been observed[4]. In JFT-2 tokamak, however, the electron density in a hydrogen discharge decays with time shortly after the ionization of the filling gas is completed. In section 3, the

time behavior of densities, their dependencies on the filling pressure are investigated in the hydrogen and helium discharges.

2. JFT-2a

2.1 Operation Conditions and Plasma Parameters

The experimental results described below were mainly obtained under the following conditions. The movable shell is at the open position, protection plates extend 5 mm from the shell, and no titanium is flushed (Fig.1). The base pressure is 1×10^{-7} torr. Hydrogen gas of 1.5×10^{18} atoms is admitted by four fast acting valves. Plasma current $I_p \approx 15$ kA and divertor hoop current $I_D \approx 1.1 \times I_p$.

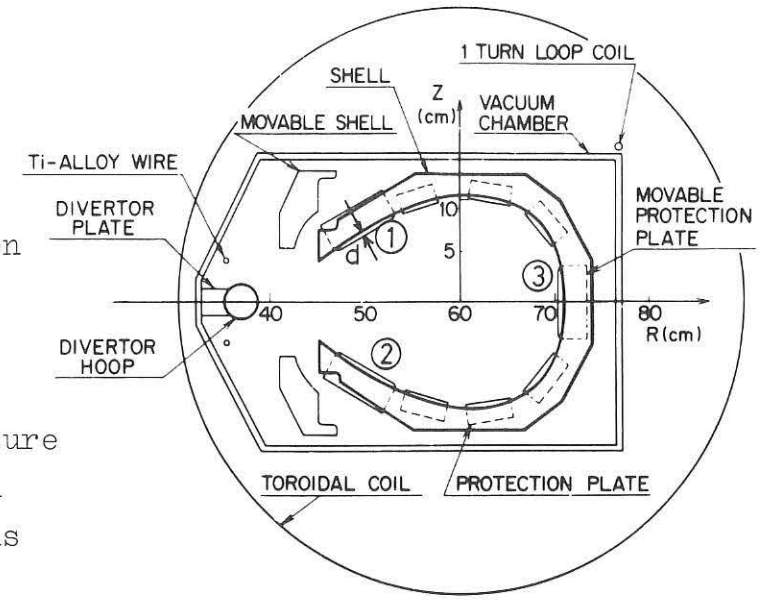

Fig.1 Cross section of JFT-2a

Figure 2 shows the time behavior of the plasma enclosed in a separatrix magnetic surface which will be described in

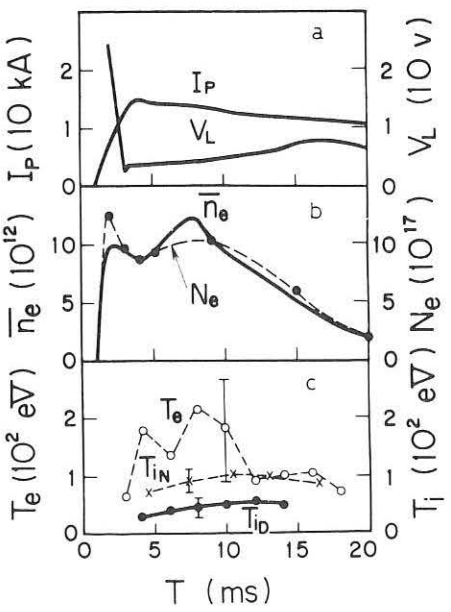

Fig.2 Time variations of plasma parameters.
(a) plasma current, I_p, and loop voltage, V_L; (b) total number of electron, N_e, and mean electron density, $\bar{n}_e$ at R = 60 cm; and (c) electron temperature, T_e at R = 62 cm and Z = -1 cm, and ion temperature, T_{iN} and T_{iD}, obtained by neutral particle energy analysis and doppler broadening of H_α line, respectively.

more detail in the next subsection. The peak current is 15 kA, the loop voltage is 4 V at 4 ms and no negative spikes are observed. The electron temperature near the centre measured by Thomson scattering is about 200 eV, and the ion temperature is 50 eV by doppler broadening of H_α line and 100 eV from neutral particle energy analysis. Energy confinement time and β_p are calculated to be 0.7 ms and 0.35, respectively, by assuming parabolic profiles of the temperature and density. These parameters are consistent with those expected from a conventional Tokamak and no adverse effects of a separatrix magnetic surface are observed.

2.2 Magnetic Configuration with a Separatrix Magnetic Surface

The field configuration with a separatrix magnetic surface is investigated by measuring the plasma in the scrape-off layer and by tracing runaway electrons.

Figure 3 shows the time variations of the electron density and temperature in the divertor region which are about ten times lower than the values at the centre of the main plasma column. Density and temperature at 1 mm from the surface of protection plates ② and ③ (Fig.1) are also measured and are similar to those in the divertor region shown in Fig. 3. In the case of $I_D = 0$ or $I_D = 0.45 \times I_p$, ion saturation current in the divertor region is about 10^3 or 10^2 times less than in the case of $I_D \approx 1.1 \times I_p$ (Fig.3). The plasma observed in the divertor region clearly originates from the main plasma column.

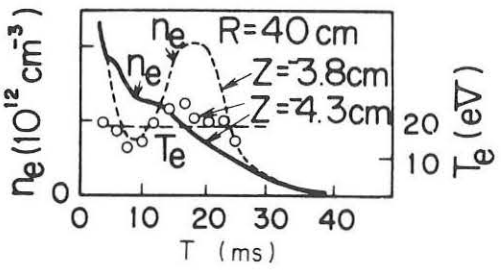

Fig.3 Time variations of electron density and temperature measured by double probes in the divertor region.

Figure 4 shows X-ray intensity from a target placed in the divertor region with various discharge condensions including ustable discharges where negative spikes preceded by growing or saturated m = 2 precursor fluctuations of poloidal field

are observed. X-ray from the target increases but X-ray from the protection plate decreases as the protection plate is extracted. It is noted that runaway electrons pass at a distance about 12 mm from the inner surface of the shell and reach the divertor region even in the unstable discharges and the separatrix magnetic surface is located well inside of the shell and the protection plates.

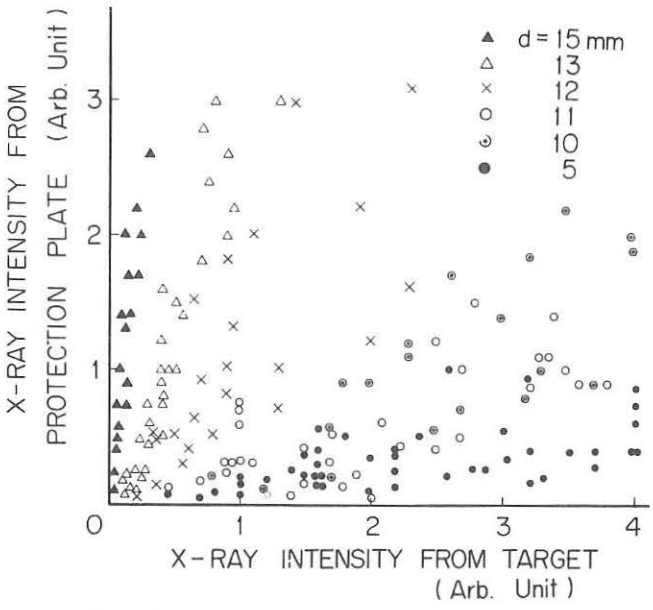

Fig.4 X-ray from a target placed at R = 42 cm and the protection plate ① during 15-20 ms. "d" is shown in Fig. 1.

2.3 Plasma Behavior in the Divertor Region

Characteristics of a plasma in the divertor region is investigated by scanning magnetic probes, double probes, directional electrostatic probes, thermocouple probes and X-ray probes at R = 40 cm.

In Fig.5, profiles of ion saturation current density i_s at 7.5 ms, time integrated heat flux density q_H during 0 - 10 ms (—●—) and 20 - 40 ms (--o--), and X-ray intensity I_x at 16 ms are shown. These profiles are shown to be axisymmetric within 10 %. Energy conversion efficiency of the thermocouple probe is assumed 100 %. It is noted that X-ray intensity I_x from a target (X-ray probe of 4 mmϕ) is undetectable during the first 15 ms of the discharge.

It is seen that these profiles, especially I_x- and q_H-profiles at 20 - 40 ms, are asymmetric with respect to median plane. Larger peaks of q_H and I_x, and also a smaller peak of i_s are located towards the direction of ion ∇B drift or the direction along which electrons flow out from the main plasma along a magnetic surface under the acceleration of the toroidal electric field. This is confirmed by changing the direction of

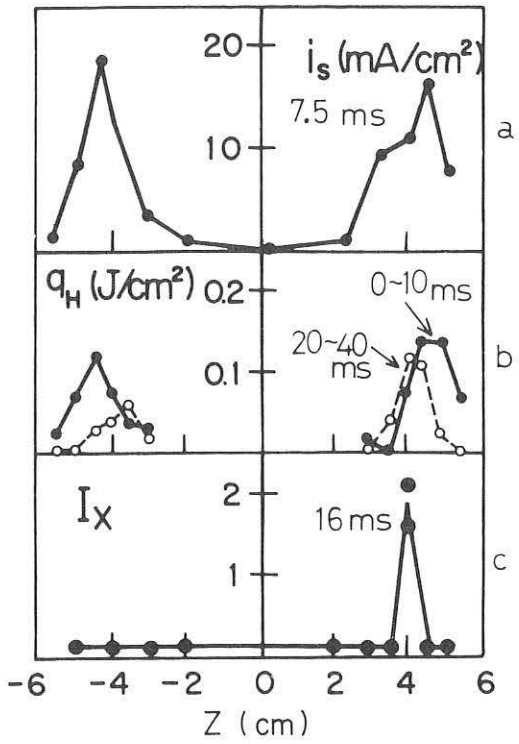

Fig.5 Characteristics of a plasma in the divertor region at R = 40 cm.
(a) ion saturation current density, i_s; (b) time integrated heat flux density, q_H; and (c) X-ray intensity, I_z, from a target of 4 mmϕ.

the toroidal magnetic field and the plasma current. The correlation between the time integrated heat flux density q_H and X-ray intensity I_x during 15 - 20 ms with various discharge currentsis shown in Fig. 6. It is seen that heat flux increases with X-ray intensity. It is clear that runaway electrons causes this asymmetry during the later phase of the discharge.

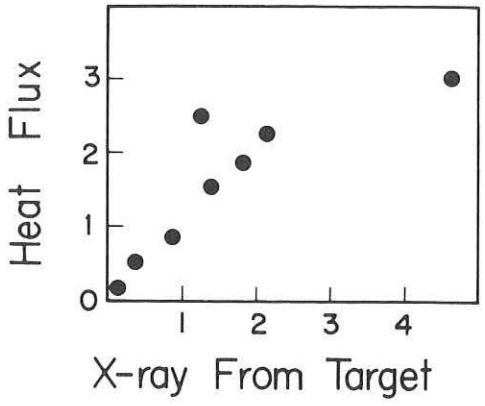

Fig.6 Correlation between heat flux to the divertor region and X-ray from a target in the divertor region at R = 40 cm during 15 - 20 ms.

The particle flux to the divertor region calculated from the ion saturation current at 7.5 - 20 ms is $0.6\text{-}2 \times 10^{17}$ particles/ms which amounts several times less than the particle loss flux from the main plasma column estimated from the total electron number in the column and H_α intensity. The total energy to the divertor is 13 - 20 % of total joule input.

Diffusion constant in the divertor region at R = 40 cm is roughly estimated from the profiles of ion saturation current at different major radii

and is less than 1×10^3 cm^2/sec at 7.5 ms which is about 10 times less than the Bohm diffusion coefficient.

2.4 Conclusions

A plasma enclosed in a separatrix magnetic surface and in the divertor region is investigated. The main results are as follows: 1) A separatrix magnetic surface is stably located inside material surfaces. 2) Plasma parameters of a main column are consistent with those expected from a conventional Tokamak and no adverse effects of a separatrix magnetic surface are observed. 3) Heat and particle fluxes to the divertor are axisymmetric. 4) These fluxes are several times less than the total loss fluxes from the main plasms column. 5) Heat flux to the divertor region is asymmetric with respect to the median plane, which is due to runaway electrons from the main plasma column.

The result 4) is due to the small dimension and weak toroidal magnetic field of JFT-2a. The results of 1), 2) and 3) encourage us to make an attempt to reduce impurity content in a plasma by an axisymmetric divertor in a future large Tokamak.

3. JFT-2*

3.1 Experimental Conditions

The vacuum vessel is stainless steel without an insulating break, pumped by a turbo molecular pump with a speed of 1000 l/s to a base pressure of $1 - 2 \times 10^{-7}$ torr. Usually, after opening the torus to air, we make about 2000 shots of discharges for the purpose of cleaning the vacuum wall. Furthermore, before the start of experiments the discharge cleaning of about 500 shots is made to obtain reproducible discharges.

In the plasma experiments described here, the torus is filled with steady gas flow. In some experiments we use a pulsed valve. The intervals between discharges are 1.5-10 min, which are limited by the cooling of the toroidal coils.

---

*This section was prepared by N. Fujisawa et al (JFT-2 group).

3.2 Characteristics of Plasma Densities

The typical time behavior of the plasma densities in hydrogen and helium discharges is shown in Fig. 7(a). The maximum plasma current I_P^{Max} is 100 kA and the filling pressures are $P_f=3.5\times10^{-4}$ torr in hydrogen discharge and $P_f=2.5\times10^{-4}$ torr in helium one. The mean line-of-sight density is measured with a 4 mm microwave interferometer. Figure 7(b) presents the time behaviors of the plasma current and the electron temperatures measured from soft X-ray energy spectra.

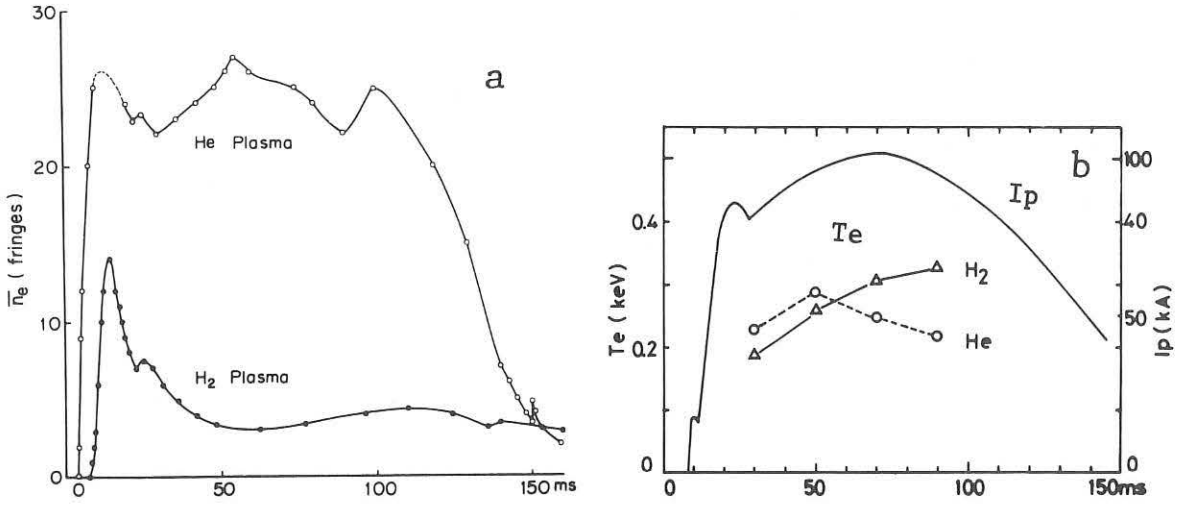

Fig.7 Typical time behavior of plasma densities, current and electron temperature in hydrogen and helium discharges with $I_p^{Max}=100$ kA, $P_f=3.5\times10^{-4}$ in hydrogen and $P_f=2.5\times10^{-4}$ torr in helium.

The line density reaches its maximum value at about 7 ms after the start of the discharge. While helium discharges almost keep their maximum line densities during discharges, in hydrogen discharges the line density decays with a time constant of 10-25 ms, and after 25-30 ms, reaches a nearly steady value.

The dependences of the line densities on the filling pressures are shown in Fig.8. The maximum line densities in helium discharges are in direct proportion to the filling pressure. Considering that the density profile is nearly flat at about 7 ms after the start of the discharge, the density in helium discharges corresponds to the complete ionization of the filling gas. The total electron number in helium discharges decreases, because the density profile is peaked with time.

The maximum density in hydrogen discharges are about 20-25 % of the electrons in the filling gas, and the steady densities are less than 10 %.

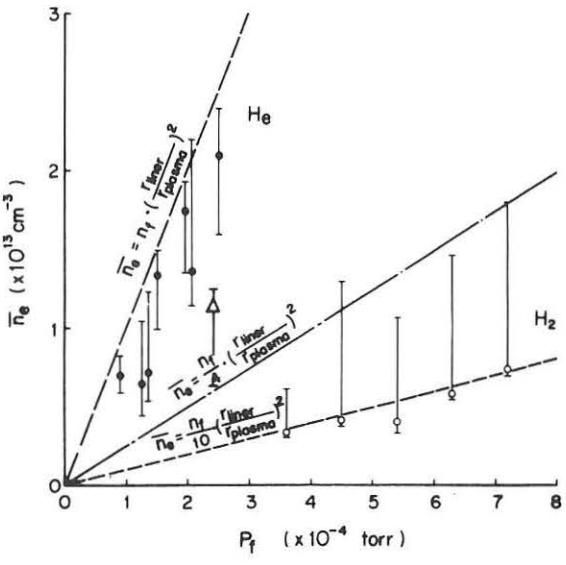

Fig.8 Dependencies of densities on filling pressures in hydrogen (⊕) and helium (●). Density(⊼) at initial stage of discharge cleaning. Upper value is one at $\frac{1}{2}I_p^{Max}$, marked one is steady value.

3.3 Characteristics of Densities before Discharge Cleaning

Figure 9 shows the time behavior of the density at the initial stage of the discharge cleaning, namely after only 50 shots of discharges after opening the torus to air. It should be emphasized that the maximum density is about 50 % of the filling gas, and that the density does not decay with time. The mark (⊼) in Fig.8 evidently indicates the difference between the densities before and after the discharge cleaning. This may be due to the reduced adsorption on the surfaces and/or the influx of the impurities.

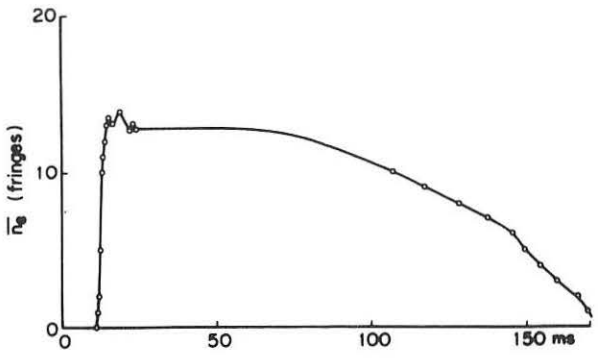

Fig.9 Time behavior of density at initial stage of discharge cleaning with I_p^{Max}=90 kA, P_f= 2.4×10^{-4} torr in hydrogen.

3.4 Gas Analysis Measurement

The working gas pressures after discharges have been measured with a mass spectrometer with a response time of 1 s. Figure 10 shows the time behaviors of the partial pressures corresponding to the mass 2 and 4, which are hydrogen and helium, respectively. The torus with no evacuation is filled via a pulsed gas valve at 3 s before the start of the discharge. In both hydrogen and helium discharges, it is reasonable that gas pressures drop shortly after the discharges. The hydrogen and helium particles adsorbed on surface are gradually desorbed over a long period of time.

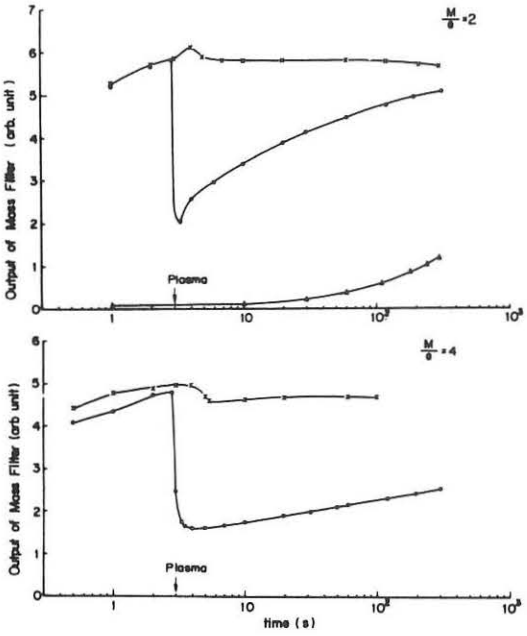

Fig.10 Time behavior of partial pressures of hydrogen and helium.
× ..... without discharge
○ ..... with discharge
△ ..... back ground

3.5 Conclusions

The density in hydrogen and helium discharges on the JFT-2 tokamak is investigated. The main results are as follows: 1) The line density in hydrogen discharges decays with time, and reaches a steady low value less than 10 % of the filling gas. 2) Helium discharges are observed to keep the maximum line density throughout the duration of discharges. 3) At the initial stage of the discharge cleaning the line density in hydrogen discharges does not decay. 4) Hydrogen and helium particles adsorbed on the wall are gradually desorbed over a long period of time.

Reference

1) Yoshikawa, M. et al, Fifth Conference on Plasma Physics and Controlled Nuclear Fusion Research (Tokyo, 1974) Paper CN-33/A1-2.
2) Shimomura, Y. et al, JAERI-M 6102 (1975).
3) Fujisawa, N. et al, Fifth Conference on Plasma Physics and Controlled Nuclear Fusion Research (Tokyo, 1974) Paper CN-33/A1-1.
4) TFR Group, Fifth Conference on Plasma Physics and Controlled Nuclear Fusion Research (Tokyo, 1974) Paper CN-33/A6-1.
5) P.E. Scott, et al, MATT-1111 (1975).

OBJECTIVES OF THE JET EXPERIMENTS

presented by P. Noll, JET Design Team, Culham Laboratory;

permanent address: KFA, Jülich, Germany

1. Introduction

The various national laboratories studying controlled nuclear fusion within the European Community have recently initiated the joint prepartion of a large Tokamak experiment. This experiment is known as Joint European Torus (JET). It is expected to yield the information required to decide whether or not to proceed to the experimental reactor stage in the Tokamak system.

The present design proposal has been worked out by the JET Design Team which has been assembled at the Culham Laboratory since 1973. It includes many contributions from the Commission and from the Associated Laboratories. Preparatory studies were performed by the former JET Working Group which recommended the construction of a 3 MA Tokamak.

In the following we outline the objectives, the experimental programme, the design and the main physics problems of JET.

2. Objectives and areas of work

The essential objective of JET is to obtain and study a plasma in conditions and dimensions approaching those needed in a thermonuclear reactor. The achievement of temperatures $T_e \sim T_i \geq 5$keV at densities $n \geq 3 \cdot 10^{13}$ cm^{-3} and of $n\tau_E > 10^{13}$ cm^{-3}s will be attempted (τ_E = energy replacement time). These studies will be aimed at defining the parameters, the size and the operating conditions of a Tokamak reactor.

A large plasma current, large dimensions, additional heating and an adequate control of the plasma-wall interaction are required

to reach these conditions. The plasma current (∿4 MA) is within a factor 3 to 6 of that envisaged in a reactor. In the most favourable case ignition may be possible in JET. Flexibility is essential to permit reliable estimates of $n\tau_E$ to be expected for reactor parameters. The proposed project will permit variation of the aspect ratio, the plasma cross section from circular to D-shaped, the discharge duration and of the build-up phase (using compression or moving limiter techniques).

The areas of research on JET may be divided as follows:

(1) Scaling of plasma behaviour

This includes studies of

- transport processes over a wide range of parameters including the "collisionless regime" appropriate to a reactor;
- β_{crit}, the maximum possible ratio of plasma to magnetic field pressure, and q_{min}, the minimum "safety factor" value - (β_{crit} and q_{min} determine the economics of a reactor);
- long-time equilibrium, stability and impurity behaviour;
- diffusion and injection driven currents.

(2) Plasma-wall interaction, impurities

The plasma-wall interaction may strongly limit the performance of JET. Studies are envisaged of

- the choice of limiter and wall materials, in particular materials of low Z;
- the role of plasma-limiter interaction, possibly using limiter detachment experiments;
- the control of the outer plasma layer by injection of gases and by control of the energy deposition;
- the effect of a poloidal field divertor, probably in a later phase of the experiment.

(3) Additional heating

The following methods will be tested and studied

- fast (adiabatic) major radius compression;

- injection of fast neutrals ($\leq$ 80 keV for H^0, $\leq$ 160keV for D^0);
- high-frequency heating at the low hybrid resonance (~1 GHz) and in the magneto-acoustic and ion cyclotron range (5 - 1oo MHz).

(4) α-particle effects

Studies of α-particle production, confinement and subsequent α-heating are foreseen. The α-particles may be produced by direct reactions from an energetic beam of D^0 injected into a T plasma or by thermonuclear reactions in a D-T plasma. The activation due to the large neutron flux (up to 10^{20}/ discharge) will prevent maintenance after a few hundred discharges so that the total number of D-T discharges will probably be limited to a few thousand.

Significant fusion yields may also be obtained by injecting D^0 into a ^3He plasma, without complications caused by activation.

3. Experimental programme

The studies above will best be realised by a programme of phased exploitation.

Phase I: Exploratory studies

This phase will start 1980 (provided the construction can be performed as scheduled) and may well last 2 to 3 years in order to (a) establish a range of operating conditions, (b) perform scaling studies, (c) work up to the maximum plasma current for the installed power supplies including the use of D-shaped cross section, (d) examine additional heating without internal structures, (e) investigate impurity effects, (f) establish the limits of operation, (g) decide on future power supplies, and (h) decide whether the divertor is needed.

Phase II: Improvement of plasma performance

This phase starts 1982 or later. If the results from phase I are extremely favourable, it will be possible to go directly to phase III. If the results are less favourable, some of the following will be attempted: enhance power supplies, examine heating

methods using internal structures, increase heating power, fit divertor if necessary.

Phase III: Fusion studies

The earliest starting date is 1983 (conveivably 1982 if results from Phase I are extremely favourable). Fusion experiments will be attempted using non Maxwellian beam-plasma methods (maybe with compression) and D-T plasmas.

Within this broad outline of Phases I - III, the experimental strategy will also be determined by the developments in the world-wide field of Tokamak research.

4. The apparatus

The Jet apparatus, shown in fig. 1, consists of 8 modules. A complete octant can be replaced by remote handling techniques under active conditions. The all-metal chamber (1) has two walls and consists of a series of bellows and rigid sections. The movable limiters (2) are arranged in an axisymmetric fashion. The 32 D-shaped coils (4) are supported by steel ring reinforced transformer coils (7) and, against tilting, by the shell structure (5). During the discharge, the poloidal field coils (6,7) are essentially switched in parallel. The plasma equilibrium is controlled by feedback via 4 thyristor bridges. The magnetic circuit consists of an iron core (normally highly saturated) and of 8 unsaturated external limbs (8) which reduce stray magnetic fields in the neutral particle injector regions. 8 horizontal ports (9) (0.96 x 0.46m), 16 narrower ports (10) and 32 small ports (11) provide access for quasi-tangential neutral injection, RF-heating and diagnostics. The toroidal field coils are supplied by a static system and a flywheel-generator set; the poloidal field coils are supplied by a flywheel-generator set.

Table I presents several JET parameters. Flexibility of operation and high performance with respect to different loss processes at relatively low cost are achieved by the choice of a tight aspect ratio $R_o/a = 2.37$ and of an elongated cross section. With $b \approx 1.7a$ it should be possible to obtain an increase of the current and of the toroidal beta, $\beta_{TOR} = 2\mu_o \int pds / \int B^2_{TOR} ds$

(s = cross section area), by a factor 1.5-2 compared with the case b = a and the same values of R_o, a, q(o) and $\beta_I = 8\pi\int p ds/\mu_o I_p^2$, provided the current does not peak too much in the centre.

5. Indication of the plasma behaviour in JET

5.1 MHD stability

The MHD stability of the plasma in JET with elongated cross section has been studied numerically. Flat and peaked current profiles were investigated. The poloidal field coils were simulated by a perfect metal shell of similar dimensions. Part of this work is presented in [1].

Results are: (i) Unstable internal modes do not appear if, essentially, $q(o) > 1$. (ii) No instability was found for surface modes if, for the case of interest $q(o) > 1$, the current density j_{TOR} decreases strongly enough towards the plasma boundary (for instance parabolic with $j_{TOR}(a) = o$). (iii) The tight aspect ratio yields an improved stability of surface modes as compared with cases with large aspect ratio; this may partly be ascribed to an increase of the $q(a)/q(o)$ - ratio by toridicity effects. (iv) No instability of axisymmetric modes was found for the investigated peaked current profile.

The main conclusion is that JET carries a larger stable current than large aspect ratio Tokamaks with the same values of q(o) and of the total current in the toroidal field coils and that stable configurations with average beta $\bar{\beta}_{TOR} \approx 3\%$ (corresponding to $\beta_{TOR}(o) \approx 10\%$) appear to be possible.

Unstable current profiles are not expected because they should relax to marginally stable profiles except in the case of large amplitude disruptive modes which can lead to a current termination. It is desirable to control the current profile in such a way that such relaxation processes and the associated enhancement of energy losses are avoided. This is of particular importance during the current rise where unstable skin profiles tend to develop. In JET it is foreseen to use an expanding limiter with expansion time $\approx$ 1s or to increase the minor radius monotonously with the current

by control of the vertical magnetic field. Various studies undertaken for JET indicate that reasonable current profiles can then be obtained and that the thermal conduction loss to the limiter can be kept small (of the order of the steady state loss).

It is important to avoid in JET the abrupt current termination observed occasionally in Tokamaks. This large amplitude disruptive instability is presumably initiated by a thermal instability which leads to a slow peaking of the current profile and subsequently to internal instabilities. In JET, the central part of the plasma is presumably less affected by the boundary zone than in smaller tokamaks because the penetration distance of fast charge exchange neutrals is only a fraction (~ 10%) of the plasma radius. Moreover, the power deposition profile is mainly determined by the additional heating and not by Ohmic heating. The resulting current profiles may therefore be qualitatively different and less susceptible to peaking.

5.2 Plasma Parameters in JET

It is not possible to give definitive estimates of the plasma parameters in JET [2]. New instabilities are expected in the low collisional regime. Extrapolations from present experiments are therefore doubtful. On the other hand theoretical estimates of instability loss are unreliable in absence of experimental verification. The purpose of JET is to remove this uncertainty.

The JET parameters have been estimated in several ways. Some results are indicated in the fig. 2 together with observed data from existing experiments. The parameters assumed for JET are $I_p = 3MA$, $B_{TOR} = 3T$, $a = 1.2m$.

(a) Simulation code predictions

The points (1) show the effect of 4 MW of additional heating on an Ohmic initial state using thermal transport coefficients κ_i given by neo-classical theory and

$$\kappa_e = \kappa_s \equiv 400\ (1 + 1.6\ q^2)\ \rho_e^{\,2} \nu_e Z_{eff}\ ;$$

ρ_e is the electron gyro radius, ν_e is the classical electron collision frequency for $Z_{eff} = 1$. These coefficients, taken with $Z_{eff} = 5$, were found by Mercier and Soubbaramayer to fit best the evolution of temperature and density profiles in TFR, and also in

ST and T-3 [3]. These extrapolations yield $n(o)\tau_E \approx 4 \cdot 10^{13} cm^{-3} s$, $\hat{T}_i \approx 3$ keV with Ohmic heating alone ($\sim$ 1MW) and $\hat{T}_i \approx$ 10keV with 4 MW additional power. When "plateau-like" ion losses are present also in the low collisional regime (points (2)), even 16 MW are insufficient to reach $\hat{T}_i \approx 5$ keV.

The points (3) and (4) illustrate the effects of sputtering and (neoclassical) diffusion of wall material (Fe) for the cases of pseudoclassical loss and of taking $K_e = K_s$. Details of these calculations are given in [4]. In the case (4) cold gas is admitted. A cold plasma blanket is then maintained which reduces sputtering and inhibits the penetration of impurities into the plasma core. This promising method of impurity control has the disadvantage that the contaminated and relatively dense blanket imposes restrictions to the heating of the plasma core by neutral particle injection. The problems of neutral injection are discussed in [5].

(b) Global estimates [6]

The points (5) show the additional power required to reach break-even (injected power = fusion power) by injecting D-atoms into a T-plasma in the presence of impurities and additional losses caused by the collisional trapped ion mode. The density profiles of ions and impurities are taken as parabolic. A favourable power deposition profile is assumed. These estimates suggest that the envisaged power for neutral injection heating may be sufficient to reach the break-even condition. Modest amounts of impurities reduce the required power by reducing the trapped-ion loss.

Studies of self consistent density and temperature profiles indicate that the trapped ion loss may be much reduced for some profiles and that break-even may be achieved in JET with additional power $\leq$ 5 MW.

(c) Major radius compression

Major radius compression may be advantageous in cases when losses by the trapped-ion mode or by impurities are serious [7]. In JET it is possible to compress the plasma in a time $\tau_c \approx 40$ ms. The compression geometry is indicated in fig. 1 The point (6) of fig 2 represents the condition achieved by major radius compression

of an initial state maintained by 10 MW of additional heating against the trapped-ion mode loss. Even for a pessimistic assumption for this loss (which yields $\tau_E \approx 0.1$s in the final state) it is possible to achieve $\hat{T}_i \approx 6$ keV and appreciable α - power for a short time.

6. Conclusions

Experiments of the size of JET are necessary to define the operating conditions of a future test reactor. Present estimates indicate that the achievement of $\hat{T}_i > 5$keV and $n(o) \cdot \tau_E > 10^{13}$ cm^{-3}s should become possible in JET.

The areas of main concern are: (a) behaviour of impurities, (b) control of the current density profile, (c) uncertainty about the present electron energy loss and about the transport behaviour in future low collisional regimes, (d) uncertainty about heating methods in future Tokamaks.

New information relevant to JET will come from the presently approved Tokamak programmes within the next 5 years. The flexibility of JET will permit response to this information without major changes of the design. Some loss of performance will perhaps have to be accepted.

References

[1] J A Wesson; this conference, invited lecture

[2] J Hugill, this conference, paper 7

[3] (a) Report Equipe TFR, EUR-CEA-FC-703

(b) C Mercier, Soubbaramayer, 5th European Conference on Controlled Fusion and Plasma Physics, Proceedings Vol 2(73)157

[4] M H Hughes, this conference, paper 140

[5] J Sheffield, this conference , paper 21

[6] D A Marty, C Pellegrini, private communication

[7] B Green, P Noll, J Sheffield, to be published in Plasma Physics

Acknowledgements

The JET Design Team is especially indebted to the members of the Associated Laboratories for their contribution to the project. The team is grateful for the encouragement and help from the Directorates of the Associations and the Commission. It finally thanks all the members of the Culham Laboratory for their warm hospitality.

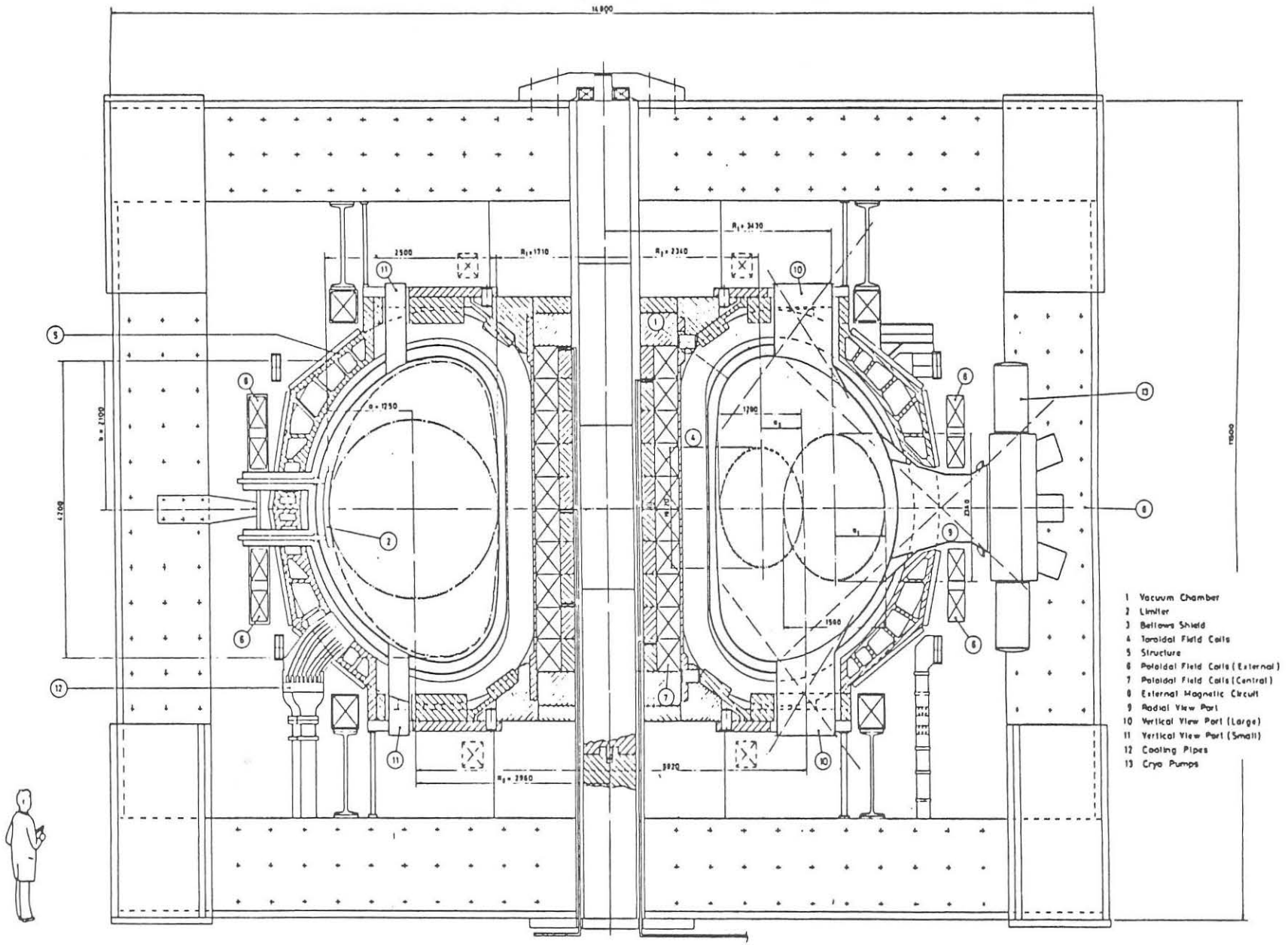

Fig. I. The JET Apparatus - Elevation

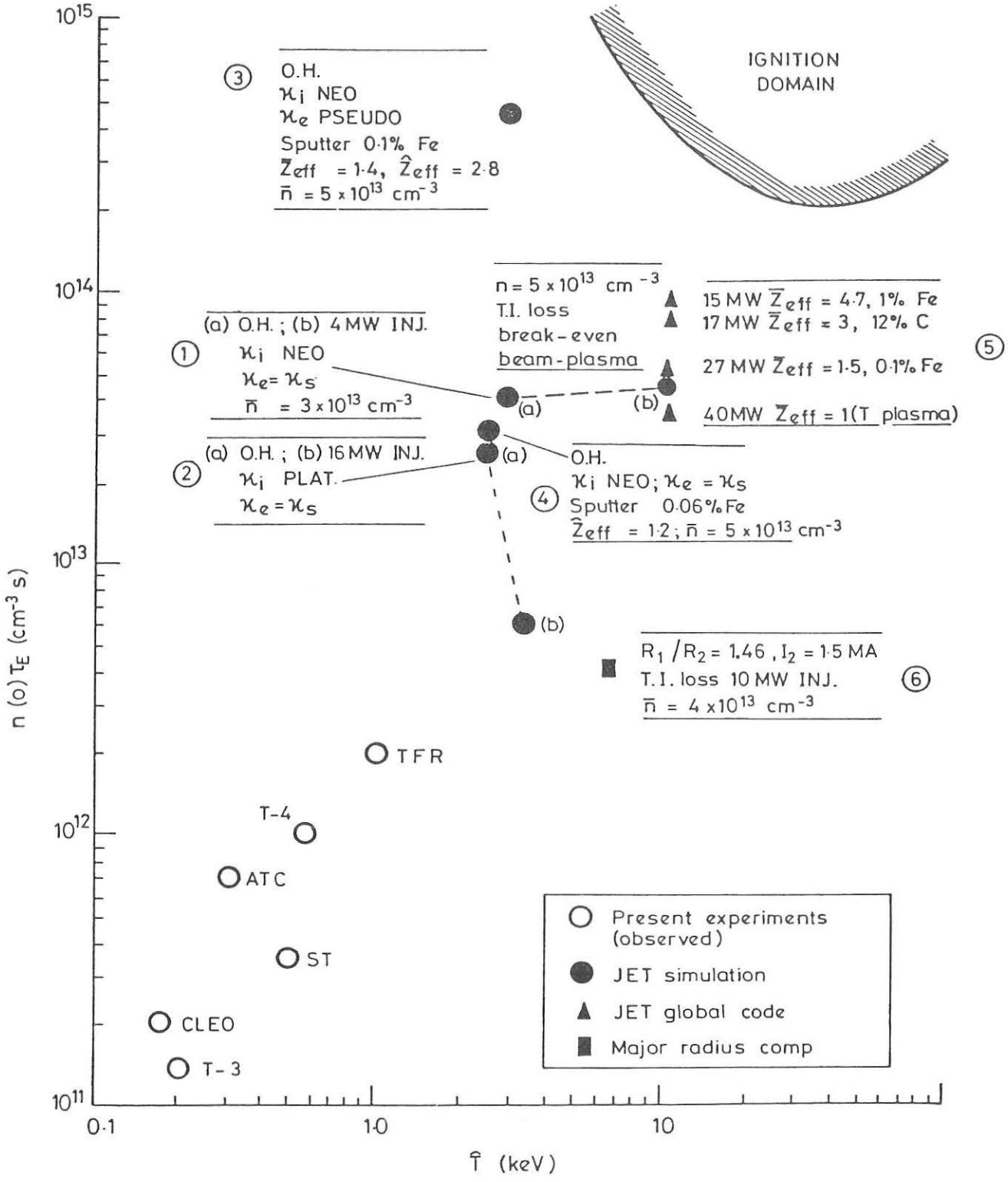

Fig. 2 Various Predictions for JET are compared with observed Results for some existing Experiments. The product of the central density and mean energy replacement time $n(o)\tau_E$ is plotted against the peak ion temperature ($\hat{T}_i$).

Table I JET Parameters

Plasma minor radius (max)	a	m	1.25
Plasma half height (max)	b	m	2.10
Plasma mean major radius	R_o	m	2.96
Toroidal field at $R = R_o$	B_o	T	2.77 (3.45)
Field ripple at $R = R_o + a$		%	±1.8
Flat top time of B_o	τ_{FT}	s	20 (15)
Plasma current (D-shape)	I_p	MA	3.85 (4.8)
Safety factor at surface / on axis	q(a)/q(o)	-	6/1
Current rise time	τ_I	s	~ 1
Maximum loop voltage	V_1	V	125
Volt-seconds required for current rise	Φ_{Rise}	Vs	18 (23)
Volt-seconds required during one ohmic replacement time at $\beta_I = 1$	Φ_{FT}	Vs	5 (7)
Volt-seconds available	$\Delta\Phi$	Vs	25 (34)
Mean ion density (typical)	$\bar{n}$	cm^{-3}	$5 \cdot 10^{13}$
Mean temperature for case $\beta_I = 0.9$	$\bar{T}$	keV	5 (8)
Heating power for $\beta_I = 0.9$, when $\tau_E = 1s$	P_H	MW	18 (29)
Neutral injection power foreseen	P_{inj}	MW	3-10 (≤25)
Peak power from grid and generators	$\hat{P}_{total}$	MW	~350 (~550)
Estimated cost of construction phase including commissioning, buildings and staff + 30% contingency (March 1975 prices)		MUC MØ	135 - ~180 -
Expected date of approval			Dec 1975
Expected date of operation			1980

Notes to table I

Values in ( ) are for extended performance (increased power supplies and additional heating; experimental phases II and III). I_p values are given for a particular peaked current profile with q(o) = 1 and poloidal currents = 0, which yields $\beta_I \equiv 8\pi \int pds/\mu_o I_p^2 = 0.9$ (poloidal beta). The Volt-seconds are given for this case and include resistive Vs loss during the skin phase. $\Phi_{FT} = \frac{3}{8}\beta_I . \mu_o R_o I_p$. The $\bar{n}$ and $\bar{T}$ values illustrate the $\beta_I = 0.9$ case: they are not computed from the power balance. $\hat{P}_{total}$ excludes peaks from inductive storage.

HYDROMAGNETIC STABILITY OF TOKAMAKS

J.A. Wesson

Culham Laboratory, Abingdon, Oxon, UK
(Euratom/UKAEA Fusion Association)

Abstract:

The first part of this paper presents an analysis of the stability of large aspect ratio Tokamaks having a circular cross-section. The various types of instability are considered in turn and the results are used to find the region of parameter space which is stable to all modes.

The second part of the paper deals with the more complicated problem of determining the constraints imposed by stability requirements in the optimisation of Tokamak configurations.

I. INTRODUCTION

The theory of stability of Tokamaks has two main purposes. The first is to help to elucidate the behaviour of present experiments. The second is to provide a set of constraints in determining the optimum design of future Tokamak experiments and reactors. The fact that the stability properties of present experiments are not well understood in any but the most superficial sense means that, for the present, we must regard the predictions for future experiments with caution. In this lecture we shall leave these uncertainties aside and attempt to provide an overall theoretical view of the stability of Tokamak configurations.

We shall first consider the stability of large aspect ratio, circular cross-section Tokamaks. We shall then investigate the departures from this case which seem necessary to achieve optimum designs. The results obtained for the proposed JET experiment[1] will be used to illustrate the stability properties of such configurations.

II LARGE ASPECT RATIO, CIRCULAR CROSS-SECTION TOKAMAKS

There are two basic types of instability for this case[2]:

Kink modes - which are generally the strongest instability, having growth rates $\gamma \sim \epsilon\,(V_A/a)$, where ϵ is the inverse aspect ratio, a/R, and $V_A^2 = B_\varphi^2/\rho$. These modes have a resonant surface in the vacuum region.

Interchange modes - having growth rates $\gamma \sim \beta^{\frac{1}{2}}\epsilon(V_A/a)$. These modes have a resonant surface within the plasma.

Each of these modes has a resistive counterpart:

Resistive kink, or tearing modes - which have a resonant surface inside the plasma and are therefore complementary to the ideal kink modes.

Resistive interchange modes - which are similar to the ideal interchange modes but only occur in the presence of resistivity.

We shall consider each of these modes separately and then combine the resulting stability criteria to find the region of parameter space which is stable to all modes.

KINK INSTABILITIES

It will be instructive to look at the physics of the kink instability. The potential energy change arising from a pertubation may be written

$$\delta W = \pi^2 R \int \underline{B}'^2 + \frac{B_\theta}{m} (m - nq) \frac{dj_{\varphi o}}{dr} \xi_r^2 .rdr$$

where $\underline{B}'$ is the perturbed magnetic field. It is clear that only the second term can provide a destabilising effect. The physical origin of this term may be seen as follows. The unstable kink perturbations are essentially incompressible and it is necessary, therefore, that the driving force provides a torque. Thus we take the curl of the force on the plasma and obtain

$$\underline{T} = \underline{\nabla} \times (- \underline{\nabla} p + \underline{j} \times \underline{B}) = \underline{B}.\underline{\nabla}\underline{j} - \underline{j}.\underline{\nabla}\underline{B} \qquad (1)$$

In the large aspect ratio ordering the second term is small and the φ component of the linearised form of equation (1) gives

$$T_\varphi' = (B.\nabla j)'_\varphi = - \frac{B_\theta}{mr^2} (m - nq) \left[\frac{d}{dr} \left(r \frac{d}{dr} (r B_r') \right) - m^2 B_r' \right] + \frac{dj_\varphi}{dr} B_r' . \qquad (2)$$

It is the torque arising from the dj_φ/dr term in this equation which drives the instability.

Assuming that a high current density is not tolerable on the conducting wall, there is no way of avoiding this destabilising current density gradient since j_φ must fall from its central value to a zero or small value at the wall. Fortunately the current density gradient also provides a strong stabilising effect, namely shear of the magnetic field. This is apparent from the expression

$$\frac{d\mu}{dr} = \frac{R}{r^3 B_\varphi} \int_o^r r^2 \frac{dj_\varphi}{dr} dr$$

where $\mu = q^{-1}$.

Let us now ask under what conditions the destabilising force results in

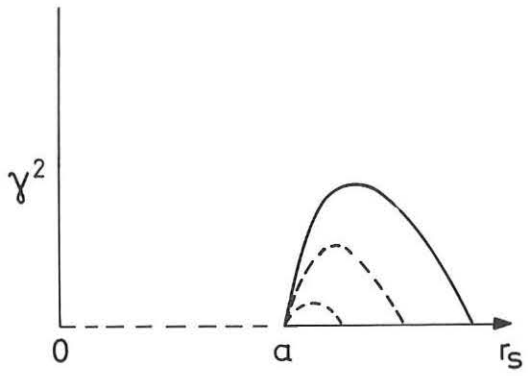

Figure 1a

Graph of the square of the growth rate against the position of the resonant surface, on which $m = nq$. (a is the plasma radius)

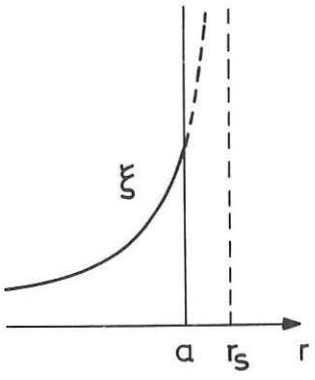

Figure 1b

Graph of the radial displacement ξ as a function of r

instability. Figure 1a gives a typical plot of growth rate (for a given m) against the radius r_s of the resonant surface $m = nq$. If a stabilising effect (shear for example) is increased, the growth rate is reduced as shown successively by lines 1, 2 and 3. We see then that marginal stability is reached when

$$\left(\frac{d\gamma^2}{dr_s}\right)_{r_s = a} = 0$$

In the limit $r_s \to a$ the eigenfunction becomes localised at the surface taking the form

$$\xi = \xi_a \frac{m - nq_a}{m - n_q}$$

as illustrated in figure 1b. In this limit the potential energy charge is given by

$$\delta W = - (2\pi B_{\theta a} \xi_a)^2 \frac{r_s - a}{a} \frac{j_{\varphi a}}{\langle j_\varphi \rangle}$$

where $j_{\varphi a}$ is the current density of the plasma surface and $\langle j_\varphi \rangle$ is the average current density in the plasma. We see then that a condition for stability is that

$$j_{\varphi a} \not> 0 . \qquad (3)$$

It has been implicitly assumed above that it is possible to take the limit $r_s \to a$. This is, in fact, always possible for sufficiently large m so that condition (3) is a necessary condition for stability for $m \to \infty$. This stability criterion for kink modes is therefore the analogue of the Mercier criterion for interchange modes.

Further analysis shows that, if $j_{\varphi a} = 0$, it is also necessary for large m that

$$\left(\frac{dj_\varphi}{dr} \right)_a = 0 .$$

For smaller m there are further requirements for stability. Expanding the current density at the plasma surface we have

$$j_\varphi = (a - r)^\nu \left(\alpha_0 + \alpha_1 (a - r) + .. \right) .$$

The stability conditions given above correspond to the requirement $\nu \geq 1$ for stability. It can be shown that for lower m numbers a larger value of ν is required for stability. However, for $\nu > 2$ the eigenfunctions are no longer localised at the surface at marginal stability and it is necessary to take account of the complete current distribution $j_\varphi(r)$.

We will now obtain a more general view of the limits placed on the current carrying capacity by the kink stability requirement. We assume that the possible current distributions are represented by the set

$$j_\varphi = j_{\varphi o} \left(1 - \frac{r^2}{a^2} \right)^\nu$$

for which the total current is given by

$$I = \frac{1}{\nu + 1} \pi a^2 j_{\varphi o} ,$$

and $q_a/q_o = \nu + 1$. A set of typical current profiles is shown in figure 2. The stability problem has been solved numerically and the resulting stability diagram is given in figure 3.

The horizontal axis gives the total current and also q_a. The vertical axis gives q_a/q_o and the current carrying capacity as measured by ν. We see that, as shown by analysis, $\nu > 1$ is necessary for stability and also that $\nu > 2.5$ gives stability to kink modes for all $q_a > 1$.

It is important to notice that complete stability against kink modes may be obtained for $q_a > 1$ through the peaking of the current distribution alone, there being no need for a large q_a except in so far as this is

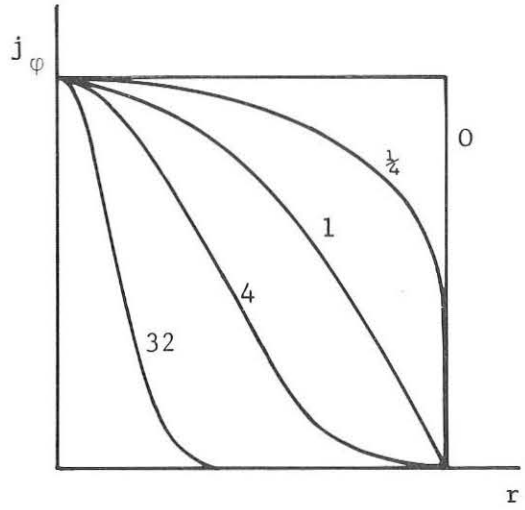

Figure 2

Current profiles of the type $j_\varphi = j_{\varphi o}(1 - r^2/a^2)^\nu$ for a set of values of ν

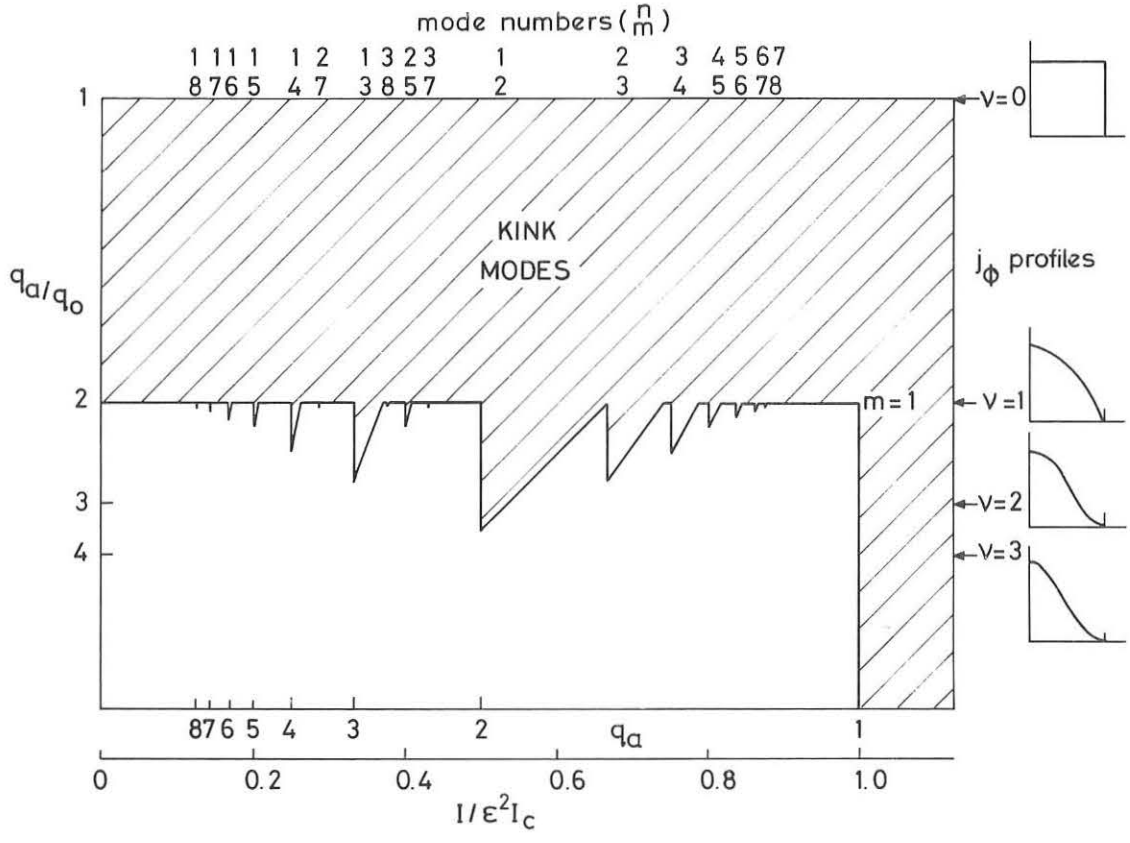

Figure 3

Stability diagram for kink modes. The shaded region is unstable. ($\epsilon \equiv a/R$ and I_c is the current in the coil producing the toroidal magnetic field)

implied by the peaked current together with an independent limit on q_o. Whatever advantage there is from higher q_a derives from the removal of modes $m < q_a$ and the consequent reduction in the amount of current peaking which may be required.

We see then that the current carrying capacity is such that

$$0.5 > \frac{I}{\pi a^2 j_{\varphi o}} > 0.27$$

depending on the value of q_a.

Thus, the shape of the current profile having been determined by the requirement of kink stability, the total current will now be determined by the amplitude of the profile. This is proportional to $j_{\varphi o}$, which is related to the safety factor q_o by the relation

$$j_{\varphi o} = \left(\frac{2B_\varphi}{R}\right)\frac{1}{q_o}.$$

The maximum current will therefore be obtained for the lowest value of q_o. We shall now investigate the limitation placed on q_o by other instabilities.

INTERCHANGE INSTABILITIES

Large m, ideal mhd, interchange modes

For circular, large aspect ratio Tokamaks the requirement for the stability of high m-number modes is that[3]

$$(-p')(q^2-1) + \frac{r B_\varphi^2}{8}\left(\frac{q'}{q}\right)^2 > 0. \qquad (4)$$

If, as $r \to 0$, p' and q' are proportional to r then the first term in (4) is proportional to r and the second to r^3. This leads to the much quoted $q_o > 1$ requirement. However, criterion (4) imposes no constraint on q_o since, even for $q_o < 1$, the magnitude of the first term is less than the second for radii greater than a small radius $r = 0\left(\sqrt{\beta(1-q_o^2)}\right)a$ and inside this radius the pressure term can be made zero by making $p' = 0$ as illustrated in figure 4.

Large m, resistive interchange modes

When the effect of resistivity is included the large shear stabilising term in the criterion (4) is removed and the stability criterion becomes[4,5]

$$(-p')\left[(q^2-1) + \left(\frac{q}{r}\right)^3 q' \int_o^r \left(\frac{r^3}{q^2} - \frac{2R^2}{B_\varphi^2} r^2 \frac{dp}{dr}\right) dr\right] > 0.$$

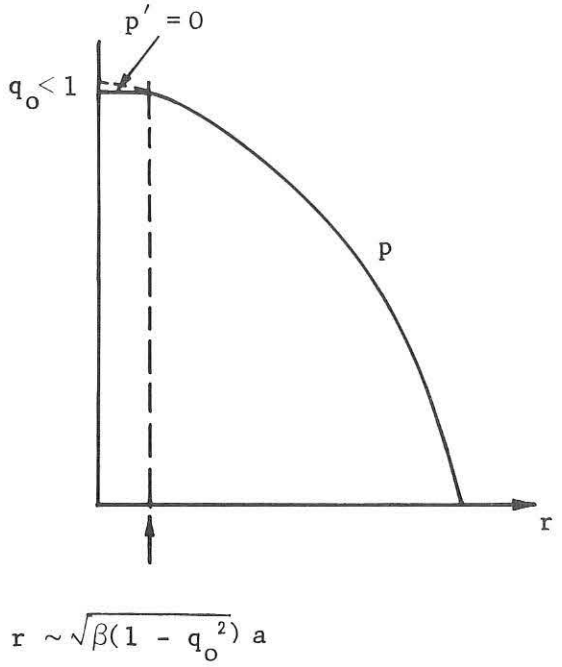

Figure 4

Graph of pressure against radius showing that the Mercier criterion imposes no limit on q_o (provided there is sufficient shear)

With this criterion it is no longer possible to obtain values of q_o much lower than unity without substantially impairing the pressure obtained. The criterion for these modes is therefore essentially $q_o > 1$.

Low m, ideal mhd, internal modes

The evidence on lower number modes is not complete but the analytic[6] and numerical results[7] available indicate that the criterion for low m modes is $q_o \gtrsim 1$.

TEARING MODES

The driving force for the tearing mode is the same as that for the kink instability. In the low β, large aspect ratio case the question of stability is decided as follows. Equation (2) is solved with $T_\varphi = 0$, that is

$$\frac{\partial}{\partial r}\left(r \frac{\partial}{\partial r}(r\psi)\right) - m^2\psi - \frac{\dfrac{dj_\varphi}{dr}}{\left(\dfrac{B_\theta}{mr^2}\right)(m - nq)}\psi = 0$$

subject to the appropriate boundary conditions. The solution is singular at the radius r_s at which $m = nq$ and the quantity Δ is computed where

$$\Delta = \frac{r}{\psi}\frac{d\psi}{dr}\bigg|_{r_s - \epsilon}^{r_s + \epsilon} \qquad \epsilon \to 0 .$$

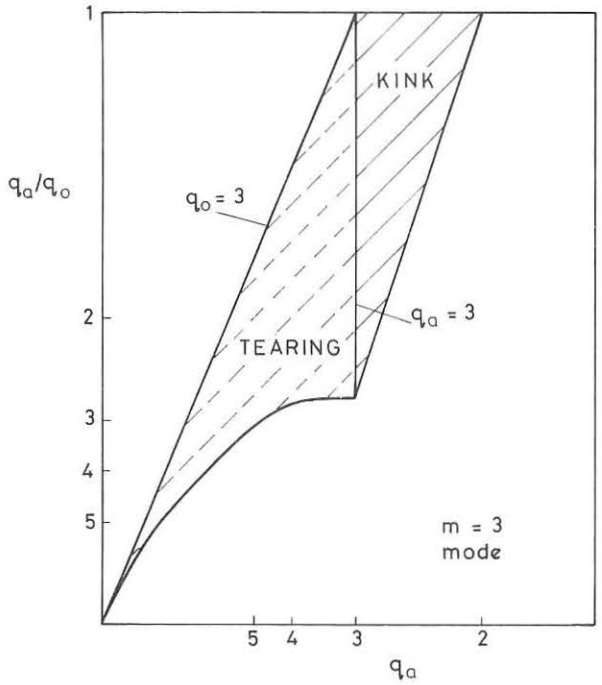

Figure 5

Stability diagram for the m = 3 kink and tearing modes

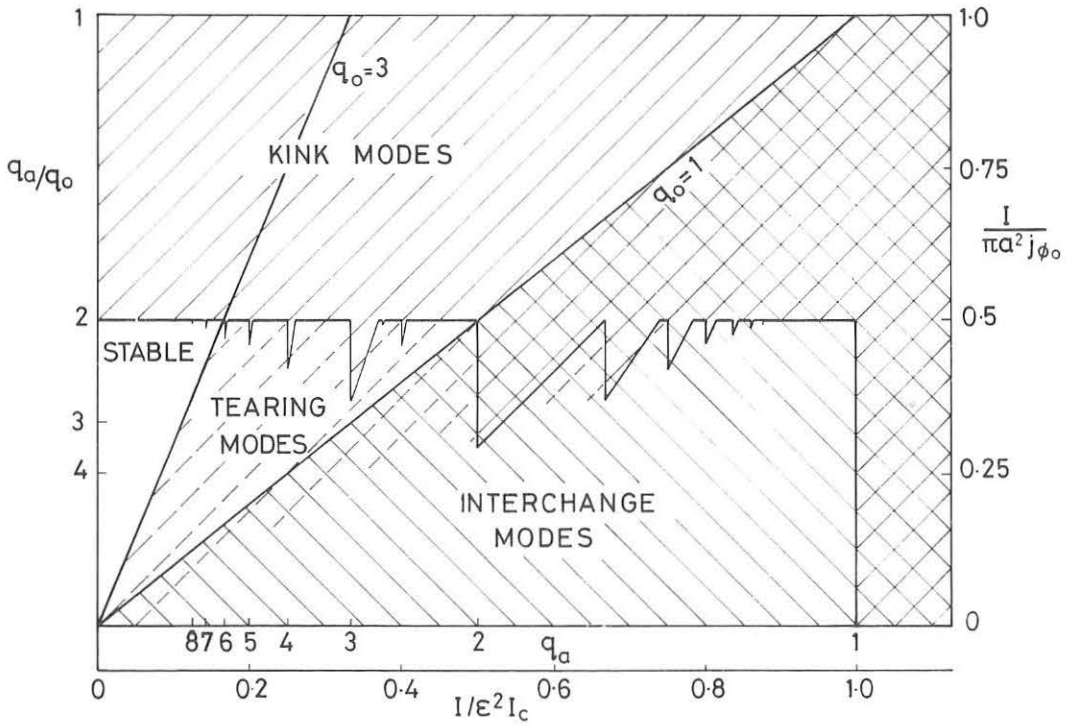

Figure 6

Complete stability diagram for the large aspect ratio case

The stability condition is then $\Delta < 0$. It is found that, although the higher modes can be stabilised for a sufficiently peaked current profile, the modes $m = 2$ and 3 remain unstable. In order to obtain stability against these modes it is necessary to avoid having a resonant surface in the plasma by requiring $q_o > m$. This, therefore, leads to the requirement $q_o > 3$ and this represents the principal limit on q_o. A stability diagram for the $m = 3$, $n = 1$ mode is given as an example in figure 5. The singular behaviour of the kink mode as $r_s \to a$ in the vacuum region is now removed and instability persists as the resonant surface passes into the plasma.

The tearing mode and interchange instabilities have been added to the kink stability diagram to obtain figure 6. We see that the maximum stable current is obtained for $q_o = 3$ and $q_a = 6$, the current carrying capacity now being only 0.17 of that for a constant current density with $q_o = 1$.

In the above description of the stability of the large aspect ratio, circular cross-section Tokamak, we took the geometry as given and searched for the best plasma configuration within that geometry. We shall now consider the optimisation of the geometry itself. This problem has not been fully explored but the general arguments will be summarised and the results obtained for a typical "optimised" Tokamak, namely JET, will be used as an illustration.

III OPTIMISED TOKAMAKS

The optimisation of Tokamak design requires the application of chosen criteria with appropriate constraints of which the most demanding are probably the stability requirements. This procedure is complex and is subject to considerable uncertainty. From the point of view of stability there are two important factors, in addition to those already discussed, which must be taken into account. These are the aspect ratio and the shape of the plasma.

Aspect Ratio

Two crucial requirements for a Tokamak are (i) a large plasma current (for good confinement) for a given current in the toroidal field coil and (ii) a high value of β. For a large aspect ratio these are related to the safety factor and the aspect ratio by the following approximate expressions

$$\frac{I}{I_c} = \left(\frac{a}{R}\right)^2 \left(\frac{I}{\pi a^2 j_{\varphi o}}\right) \frac{1}{q_o}$$

and

$$\langle\beta\rangle = \left(\frac{a}{R}\right)^2 \left(\frac{I}{\pi a^2 j_{\varphi o}}\right)^2 \frac{1}{q_o^2}\, \beta_p$$

Thus, for given $I/\pi a^2 j_{\varphi o}$ (for kink stability), given q_o (for stability against internal modes) and given β_p the above requirements lead to the choice of the smallest aspect ratio compatible with the other constraints. A more complete analysis leads to an aspect ratio between 2 and 3[8].

Plasma Shape

The question of optimum shape is not yet resolved. The difficulty is that, although non-circular cross-sections offer certain theoretical advantages[9], the actual behaviour of such configurations cannot be predicted with confidence. Furthermore the problem is intimately related to engineering constraints.

The principal advantage of an elliptic cross-section is that a higher equilibrium value of β can be achieved. Furthermore, by adding a triangular component to the shape, the value of $j_{\varphi o}$ which remains stable to localised interchange modes can be increased. For a circular cross-section the limiting value of $j_{\varphi o} R/2B_\varphi$ is unity ($q_o = 1$) but a stable value of 3 has been demonstrated for a horizontal ellipse and a value of 1.4 for a vertical ellipse[10],[11]. However it is not known whether this improvement also occurs for low m-modes.

JET

We will now analyse the stability properties of a design which has, in so far as it is possible with our present knowledge, been optimised. The example we shall take is the JET configuration which has a small aspect ratio ~ 2.5 and an elongated cross-section $\sim b/a = 1.6$. A diagram is given in figure 7. The surrounding conducting wall is included as an approximate representation of the position of the actual conductors.

(i) Kink modes

One clear change which occurs in going to a small aspect ratio equilibrium is that, for a given type of current distribution, the ratio q_a/q_o is enhanced and consequently the shear is increased. For example the flat current distribution having $q_a/q_o = 1$ for a large aspect ratio has $q_a/q_o = 1.7$ for JET. The current distribution $j_\varphi = j_{\varphi o} J_o(2.4\, r/a)$ has $q_a/q_o = 2.3$ for a large aspect ratio but the corresponding ("Bessel") distribution for JET has $q_a/q_o \simeq 4.8$. This has the effect, for $q_o = 1$, of making q_a large. As a result the lowest resonant mode has a high m number. For example in the JET case this is $m = 5$ for the "Bessel" current distribution. However, despite this, a necessary condition for stability is still that $j_{\varphi a} \not> 0$[12]. Numerical calculations for the "Bessel", ($j_{\varphi a} = 0$) case[13] were unable to detect any kink instability

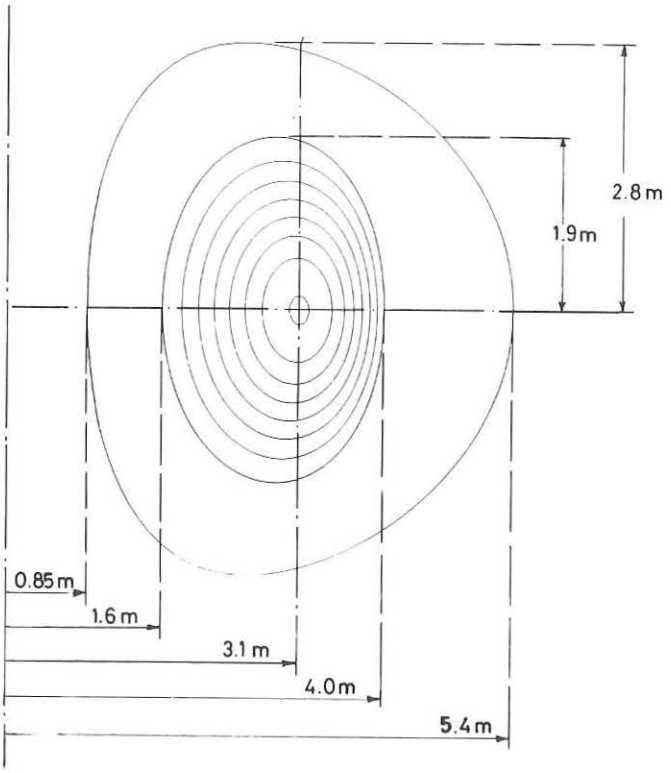

Figure 7

Diagram showing the geometry of JET configuration used in the stability calculations

for currents for which the internal modes were stable. This may be due to the fact that the m numbers involved are large ($m \geq 5$) and that, if unstable, the growth rates would be very small. If, in this case, as in the large aspect ratio case considered earlier, the $j_{\varphi a} \not> 0$ condition is essentially necessary and sufficient for large m-numbers a current distribution close to the "Bessel" distribution will probably be stable for kink modes.

An interesting result which the numerical calculations have brought out is that for unstable configurations the growth rate and the eigenfunctions vary continuously with q_a and do not have the banded structure found in the large aspect ratio case.

(ii) Internal modes

In the above discussion of kink modes there is the implicit assumption that the stability condition for internal modes remains $q_o \gtrsim 1$. A calculation for large m-numbers, using the Mercier criterion, has shown that (assuming an unflattened pressure profile) the requirement is quite close to $q_o > 1$[14]. Numerical calculations[13] for low m-numbers (m = 1, 2 and 3)

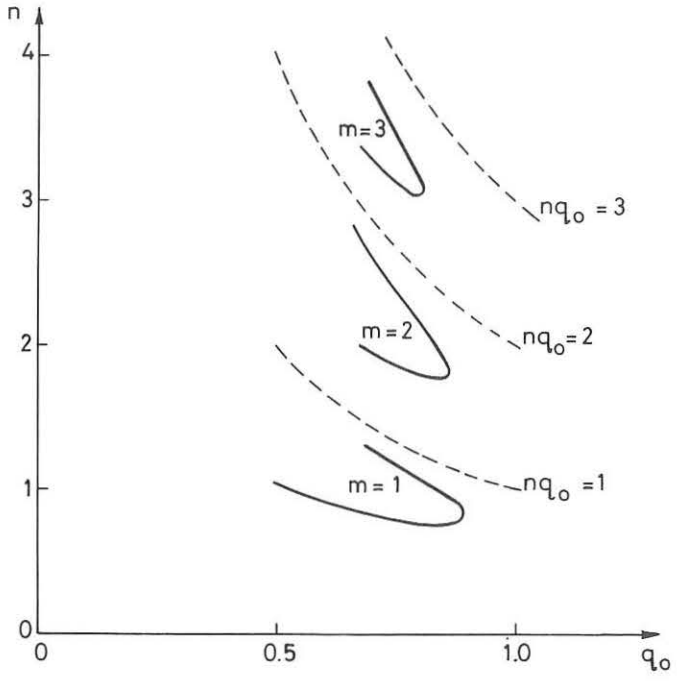

Figure 8

Stability diagram for low m-number internal modes for the JET configuration. n is the toroidal mode number, only integral values having physical meaning. (See paper CN 33/A 12-3 of the Tokyo Conference 1974)

found that the required value of q_o is approximately 0.9. These results are given in figure 8.

The above results indicate that for stability against interchange and kink modes the JET configuration would require a current distribution peaked approximately as the Bessel function, that is roughly parabolic, and having $q_o \simeq 1$. This would lead to a value of $q_a \approx 5$ and a current

$$I \approx 140\ B_\varphi$$

giving approximately 4 MA for $B_\varphi = 30$ kg.

n = 0 modes

Calculations for the JET configuration have shown that it is unstable to n = 0 modes unless a conducting wall is placed sufficiently close to the plasma. The instability results in vertical motion of the plasma. The general character of this instability is similar to the corresponding instability of an elliptical cylinder.

The destabilising force comes from the negative gradient of the magnetic field energy density outward from the plasma surface. The stabilising effect is the magnetic energy arising from the perturbed magnetic field in

the vacuum region. For a circular cylinder with no conducting wall these two effects are equal and the plasma is marginally stable. For an elliptical plasma a displacement in the direction of elongation is unstable. The instability can be stabilised by a suitably placed perfectly conducting wall. There is some dependence on the current distribution but the essential features are represented by the result for the constant current case. The stability criterion is[15]

$$D > 0 \quad \text{where} \quad D = \frac{\frac{b}{a}+1}{\frac{b}{a}-1}\left(\frac{b+a}{b_1+a_1}\right)^2 - 1$$

b and a being the major and minor axes of the ellipse and b_1 and a_1 being the corresponding axes of the elliptical conducting wall. The most unstable displacement in this case is an almost rigid shift. (Calculations of stability are often carried out assuming a rigid displacement but care must be taken in interpreting these results because in general this displacement is not the worst and only a finding of instability is conclusive).

If the plasma would be stabilised by a perfectly conducting wall, it is necessary to determine the effect of the finite conductivity of the wall. The result will depend upon the detailed configuration but the essential behaviour can be derived using the constant current model. With a finitely conducting wall the plasma is always unstable. Configurations which would have been stable with an infinitely conducting wall, have a growth rate γ given by

$$\gamma \tau_W = \frac{1}{D}$$

where τ_W is the magnetic field diffusion time characterising the conducting wall. The infinite value of γ as $D \to 0$ signifies the transition to hydromagnetic growth times. Since D is of order unity, growth times may be less than the time of the experiment. In this case feedback techniques will be necessary to stabilise this mode.

SMALL ASPECT RATIO - RESISTIVE MODES

We must now return to the question of resistive modes and ask what their stability properties are for small aspect ratio Tokamaks. In particular it is important to determine whether tearing modes impose the same limitations as in the large aspect ratio case.

(i) Resistive interchange modes

The criterion for resistive interchange modes has been applied to JET[16] and, as in the large aspect ratio case, it is still most stringent on the

magnetic axis and leads essentially to the stability criterion that q_o must be greater than unity.

(ii) Tearing modes

The procedure for determining stability in the large aspect ratio case was described earlier and led to the requirement $\Delta < 0$. The more complete criterion is that[17]

$$\Delta < \Delta_c$$

where Δ_c is a rather complicated function of the equilibrium quantities but which increases with β and therefore with a/R. The precise condition for a given configuration requires a numerical calculation, especially since the resonant surface, at $q = m/n$, defines a particular radius at which the condition $\Delta < \Delta_c$ must be applied. However, as illustrated in figure 9, Δ_c has a minimum value as a function of r_s and, for current profiles of interest, the largest value of Δ occurs at $r_s = 0$. It is possible therefore to obtain a sufficient condition for stability by requiring that

$$\Delta(r_s = 0) < \Delta_{c\,min}.$$

For q_o close to unity the resulting criterion for a circular cross-section is

$$\Delta(r_s = 0) < 2.9\,\beta_o \left(\frac{V_A\,\tau_R}{a}\right)^{\frac{1}{3}} \left(q_o^2 - 1\right)^{\frac{2}{3}}$$

where β_o is the value of β on axis, $V_A^2 = B_\varphi^2/\rho$ and $\tau_R = \sigma_o\, a^2$. The precise numerical coefficient depends on the particular configuration but the value given is a typical one. The most unstable mode is $m = 2$ and the value of $\Delta(r_s = 0)$ for this mode is of order 10. Taking typical parameters gives the stability condition

$$q_o^2 - 1 > \frac{N}{(\%\beta)^{3/2}}$$

where $\%\beta$ is the value of β_o expressed as a percentage and the factor N is typically of order unity for present Tokamaks and of order 1 to 0.1 for next generation Tokamaks such as JET. It is seen then that if β_o is a few per cent then a value of q_o slightly greater than unity gives stability. The predicted value of β_o for JET is of the order of 10%.

Assuming $\beta \propto (a/R)^2$, the required value of $q_o^2 - 1$ is proportional to $(R/a)^3$ and this factor provides the main improvement between large aspect ratio Tokamaks and the projected optimised Tokamaks. However, further analysis is required on this problem to determine the regime of validity of the calculation.

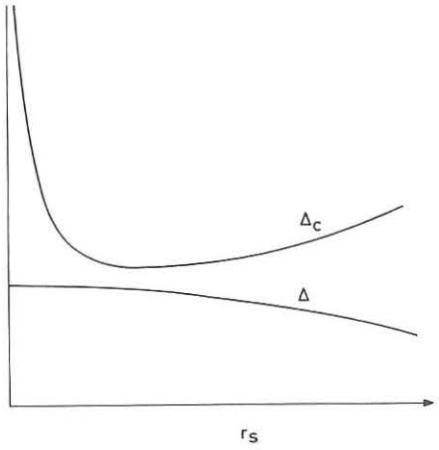

Figure 9

Typical graphs of Δ and Δ_c against the radius of the resonant surface

CONCLUSIONS

A large aspect ratio, circular cross-section Tokamak is stable to ideal hydromagnetic modes provided $q_o \gtrsim 1$, $j_{\varphi a} \not> 0$ and the current distribution is sufficiently peaked. The maximum stable current is then approximately

$$I = (2.5 \frac{a}{R}) a B_\varphi \qquad (5)$$

where I is in megamps, a in metres and B_φ in teslas. Assuming the poloidal currents play a negligible role in the pressure balance, the corresponding $\langle\beta\rangle$ value is

$$\langle\beta\rangle \equiv \cdot \frac{\int P ds}{\int \frac{B_\varphi^2}{2} ds} = 0.21 \left(\frac{a}{R}\right)^2 . \qquad (6)$$

There is no direct support for these results from present experiments. The best confinement is obtained for values of q_a from 3 to 10. It may be that the operative requirement is $q_o > 1$ and that the experimental current distributions then imply these high values of q_a. On the other hand it may be that tearing modes which are predicted for the large aspect ratio case are responsible for the lack of confinement at lower q_a.

Optimisation of the properties of a Tokamak leads to a small aspect ratio of 2 to 3. The results obtained so far indicate that the requirements for a circular cross-section are similar to those for the large aspect ratio in that stability against ideal hydromagnetic modes requires $q_o \gtrsim 1$ and $j_{\varphi a} \not> 0$.

Shaped cross-sections offer the possibility of stability to interchange modes down to a lower value of q_o. However a decision as to the usefulness of ellipticity or the optimum degree of ellipticity depends upon an assessment of a number of advantages and disadvantages. Regarding stability one important consideration is the acceptability of the axisymmetric mode which, it appears, will probably require feedback stabilisation.

Calculations for the small aspect ratio JET configuration show that a given q_o implies a larger q_a for the same current distribution because of toroidal effects. This means that the possible kink modes are limited to higher m values. It seems likely that the current distribution for stability will be similar to that for the large aspect ratio case. Numerical calculations for localised and low m-number internal modes indicate a required value of q_o close to unity. In this case the expressions (5) and (6), for I and β, apply quite accurately for JET and imply a current of 4 megamps and a β of 3% for β_φ = 30 kg .

In the limit of large aspect ratio the tearing mode appears to be unavoidable for $q_o < 3$. However, at small aspect ratio, toroidal effects become important and theory indicates that in the small aspect ratio Tokamaks of the next generation these modes may be stable for $q_o \gtrsim 1$.

Acknowledgments

The author would like to thank Alan Sykes, who carried out most of the numerical calculations described in this paper, and Jim Hastie for discussions on many aspects of the work.

References

1. P. Noll. Objectives of the JET experiment. This conference.
2. V.D. Shafranov, Sov. Phys., Tech. Phys. 15, 175 (1970).
3. V.D. Shafranov, E.I. Yurchenko, Zh. Eksp. Teor. Fiz. 53, 1157 (1967). Sov. Phys. JETP 26, 682 (1968).
4. A.B. Mikhailovskii, Nucl. Fus. 15, 95 (1975).
5. A.H. Glasser. Proceedings of this conference, Vol. I, p.113.
6. M.N. Bussac, D. Edery, G. Laval, R. Pellat, J.L. Soulé. Proceedings of this conference, Vol. I, p.100.
7. A. Sykes, J.A. Wesson, Nucl. Fusion 14, 645 (1974).
8. J. Sheffield, A. Gibson. To be published in Nuclear Fusion.
9. G. Laval, R. Pellat. 6th European Conference on Controlled Fusion and Plasma Physics, Moscow 1973, Vol. 2, p.64.
10. L.S. Solovev, V.D. Shafranov, E.I. Yurchenko. Proc. 3rd. Int. Conf. on Plasma Physics and Controlled Nuclear Fusion Research, Novosibirsk, 1968. (Nuc. Fus. Suppl. 25 (1969)).
11. G. Laval, H. Luc, E.K. Maschke, C. Mercier, R. Pellat. Proc. 4th. Int. Conf. on Plasma Physics and Controlled Nuclear Fusion Research, Madison 1971, Vol. II, p.507.
12. J. Hastie. Private communication.
13. J.A. Wesson, A. Sykes. Proc. 5th. Int. Conf. on Plasma Physics and Controlled Nuclear Fusion Research, Tokyo, 1974 (CN 33/A 12-3).
14. J. Jacquinot. Private communication.
15. G. Laval, R. Pellat, J.S. Soulé, Phys. Fluids 17, 835 (1974).
16. B. Green, H.P. Zehrfeld. Private communication.
17. A.H. Glasser, J.M. Greene, J.L. Johnson. Phys. Fluids 18, 875 (1975).

REVIEW
ON THE IAEA WORKSHOP ON LARGE FUSION TOKAMAK PROJECTS

E.I. Kuznetsov, V.S. Strelkov

The Kurchatov Institute of Atomic Energy
Moscow, U.S.S.R.

An international workshop on large tokamaks was held in Dubna, USSR July 4-11, 1975. The workshop was sponsored by the International Atomic Energy Agency with the assistance of the USSR State Committee for Utilization of Atomic Energy. More than 100 representatives from Belgium, the Federal Republic of Germany, France, the Netherlands, Sweden, the United Kingdom, the USA, the USSR and Japan participated in the workshop.

The main objective of the meeting was to consider four large tokamak devices, namely: JET, designed by scientists of the European Community countries; TFTR (TCT) designed in the USA; DFTR (T-20) designed in the USSR and JT-60 designed in Japan.

During the first two days of the workshop these four projects were subjected to general consideration. The three following days were devoted to a more detailed comparison of different systems in the devices. Conceptual designs of fusion reactors and future fusion power plants were discussed on the last day. There was also a general discussion on CTR research programs and on perspectives of developing a fusion power plant system.

The general purpose of all four designs is to develop a device which, in fact, is close to a test fusion reactor. It is considered to be a

system in which a controlled thermonuclear reaction of D-T plasma proceeds with energy release comparable to the input energy.

At the same time, problems to be solved on each of the four devices are different. This is due to the different engineering and constructional solutions accepted for the above designs. The main characteristics of these devices and the expected plasma parameters are given in Table 1.

The JT-60 project aims at solving mainly physical problems which will arise in the course of construction of a fusion reactor. Unlike the other three devices operation with tritium is not envisaged in it. Since the device has large dimensions it can be used to carry out a wide range of research including a poloidal diverter (magnetic limiter) and a removable limiter. Studies on plasma confinement and heating under conditions close to reactor-like ones as well as plasma-wall interaction, impurity behaviour and non-ohmic plasma heating are supposed to be carried out.

The power supply system utilizes both fly wheel generators and direct connection to the main lines. Longitudinal magnetic field coils have a circular cross-section. The vacuum chamber consists of two shells made of an alloy with a high nickel content.

In the American TFTR (TCT) device there should be achieved a high fusion temperature and conditions under which the total energy release in D-T reactions (neutrons and α-particles) are comparable to plasma energy losses.

Achievement of these conditions is substantially facilitated in a so-called two-component tokamak regime, when a fusion reaction proceeds between nuclei of a preliminarily produced plasma and fast particles injected into it. In this case, in order to get the ratio of the released energy to the input one equal to unity ($Q = 1$), it is sufficient to have the value of $n\tau$ or the order of 10^{13} cm^{-3} sec. For a rapid heating of the

plasma with neutral injection, high power injectors producing 60 and 120 kev particles (with a power of 40 MW) will be used. The current pulse length in the plasma equals 1 sec (flattop), and correspondingly, the injection pulse length is relatively small (0.1 sec). Injection of 60 kev particles heats the plasma and with injection of 120 kev particles a two-component tokamak regime can be achieved. For this device the impurity problem has not been considered in detail because it is thought that the short plasma life time should not allow impurities to accumulate and influence the ion heating conditions.

In the TFTR device, the longitudinal magnetic field coils and the vacuum chamber have a circular cross-section. In the first stage of studies with discharge currents of 1 MA an iron core will not be used. The vacuum chamber is made of one shell of 20 mm thick stainless steel. It is possible to form a plasma column by cutting it off by means of a limiter and to adiabatic compress in major radius with the use of a transverse magnetic field.

The Joint European Tokamak Project (JET) is far more advanced than the others. The objective of JET is to obtain and study a plasma with parameters approaching those needed for a self-sustaining thermonuclear reaction ($n\tau \sim 10^{14}$ cm^{-3} sec). The plasma column cross-section can be either circular or elongated. The possibility of getting an elliptical cross-section is considered as a means of providing an additional increase of the extreme value of $n\tau$. Along with ohmic heating as the main heating system, injection of neutral particles of 80 and 160 kev energy at 25 MW total power is envisaged. Besides, a RF lower hybrid resonance heating at a frequency of 800 Mhz and 20 MW is supposed to be used. The longitudinal magnetic field coils and the vacuum chamber are D-shaped. The chamber consists of two shells made of an alloy with a high nickel content. A closed magnetic circuit is used in the poloidal magnetic field system.

The power supply system provides for combined use of both the main lines and the motor-generator-fly-wheel sets.

A wide scope of physical and engineering studies is to be carried out on the T-20 device. Together with achieving plasma parameters needed for a self-sustaining reaction ($n\tau \sim 10^{14}$ cm^{-3} sec) the device is designed for long term D-T plasma operation with better than 90 % α-particle confinement. The plasma parameters in T-20 practically coincide with those of a hybrid power reactor. It is planned to carry out neutron physics investigations and to measure a tritium conversion ratio for different blanket modules as well as to study first wall sputtering under α-particle bombardment under frequently repeated pulse conditions. The cross-section of a longitudinal magnetic field coil is intermediate between a circular and D-shape one; the chamber cross-section is close to circular. The vacuum chamber consists of two shells made of stainless steel. In parallel with an air-core version, possibilities of using an iron core or a closed magnetic circuit in a system of poloidal magnetic field coils have been considered. However a final decision on the matter will be made later. Auxiliary plasma heating with 80 and 160 kev neutral particle injection and with RF plasma heating at 60 MW each are to be done.

Vivid discussions on physical problems of large devices connected with a possibility to achieve design parameters and chosen optimum solutions took place during the whole workshop and at the additional session. The problem of impurities and ways of reducing their content in plasma have attracted great attention. It should be pointed out that in spite of the fact that the role of impurities seems to be relatively smaller in large devices, the impurity problem has not yet been positively solved. Problems of vacuum chamber construction, wall and limiter material choice, elimination of local energy release in different parts of the chamber seem to be rather complicated and not finally solved. Evidently these problems should be studied, taking into consideration such factors as material strength and ability to be welded, embrittlement under neutron bombardment and sputtering under plasma charged particle irradiation.

The choice of an optimal cross-section for a plasma column and for a vacuum chamber depends on definite problems which must be solved. For example, the elongated plasma column cross-section in the JET device is designed for the maximum value of $n\tau$ at the lowest longitudinal magnetic field and, correspondingly, at the lowest device cost. At the same time, as calculations indicated, to obtain the extreme temperature in TFTR device, a circular cross-section with the minimum plasma volume at a given neutral injection power turns out to be preferable.

The problem whether an iron core or a closed magnetic circuit should be used in a poloidal magnetic field system cannot be solved in one way only. Discussions of this problem drew the attention of the participants to such an important problem as the modulation of the guiding field around the torus to be used because of the absence of a copper shell in all devices under consideration. This modulation takes place in case of a closed magnetic circuit and also without it. In the latter case it is connected to the necessity of using large iron masses for shielding the diagnostic apparatus, injectors and so on. The modulation leads to an additional magnetic field corrugation to the one appearing due to the finite number of coils. The rippling influences plasma confinement and it should be taken into consideration when both analysing physical conditions and designing fusion devices.

As mentioned above, in all the devices, auxiliary methods of plasma heating up to fusion temperatures are envisaged. During the discussions the main attention was paid to neutral beam injection, adiabatic compression and RF plasma heating. At present it is difficult to make a choice between these methods because none of them has been verified yet. Concentration of high Z impurities will have an important effect on neutral injection for it can lead to a beam absorption in the plasma column periphery. The problem of absorption in the column periphery as well as the development of input devices and of generators producing the necessary power are not yet clear for RF methods. For all the auxiliary heating methods the effect of the

auxiliary heating on the plasma confinement has not yet been cleared up. This is why large scale experiments must be carried out before a final choice of a reactor plasma heating technique can be made.

Taking into account the importance of obtaining data on plasma behaviour in large devices, as well as the low frequency of pulse repetition and rather high irradiation level, it becomes clear that plasma diagnostic problems are very important. At one of the sessions the diagnostics complexes for JET and T-20 were discussed. It was emphasised that it is necessary to have diagnostic means providing simultaneous measurement of the local distribution of the different plasma parameters and to analyse the effect of stray magnetic fields and of neutron irradiation on the apparatus.

All the devices are to be put into operation in the early 1980's. After conducting experiments it is planned to construct experimental fusion power reactors. Programs of power reactor development and conceptual design of different fusion reactors and plants were discussed at a special session. Concepts of hybrid and conventional tokamak reactors including those for materials studies designed in the USSR, the USA (UWMAK, TCT, DOUBLET) and Japan were discussed. Economical aspects of fusion reactors were also considered.

Future commercial reactors do not vary much in size. The major radius for instance is 10 to 15 m and the minor one is 2.5 to 5 m. In most cases the net electrical power is chosen to be between 2000 and 2500 MW(e).

The most important problems facing utilization of fusion reactors for power production and ways of solving them were considered in detail. Evidently, all these questions are closely connected to and depend on results which will be obtained on demonstrational and other facilities, i.e. which depend on achieving a self-sustaining reaction and on solving other physical problems. Nevertheless the discussion showed that it is already necessary

to carry out a wide scope of technological and engineering studies to provide development of commercial fusion reactors and power plants.

A general discussion on perspectives and on programs of CTR research in different countries was held and a summary of the four projects was made in the final session.

According to the opinion of the workshop participants the discussions were quite useful. It will make it possible to introduce into the projects a number of improvements during their further development and implementation. The problems pursued in the different projects are very real for achieving the common objective, i.e. the creation of demonstrational fusion reactors, and they complement each other. In his final remarks the chairman of the workshop B. Kadomtsev pointed out that each project corresponds to the problems posed, the objectives of the project and the laboratories where the projects will be put into reality.

The first experience of an international cooperation in studying large tokamak projects proved to be undoubtedly successful. It is desirable that such international workshops, with the help of IAEA, be made traditional.

LIST OF LARGE TOKAMAK PARAMETERS (June, 1975)

Parameter, Symbol, Unit	JET	TFTR(TCT)	DFTR(T-20)	JT-60
Major Radius R, m	2.96	2.48	5	3
Plasma Minor Radius a,m	1.25	0.85	2	1
Plasma Half Height b, m	2.1	0.85	2	1
Maximum Magnetic Field B, T	3.4	5.2	3.5	5
Plasma Current I, MA	4.8	2.5/1.0	6	3.3
Mean Ion Temperature T_i, kev	5	6/6	7-10	5-10
Mean Ion Density N_e, cm^{-3}	5.10^{13}	$4.10^{13}/8.10^{13}$	$(0.5-5).10^{13}$	$(2-10).10^{13}$
Value of β	1	1/2.5	1	1
Energy Confinement Time τ_E, sec	1	0.2	2	0.2-1
Type of Divertor	Limiter	None	None	Magnetic limiter Radially Outside
Total Peak Power, MW	550	700	1600	-
Auxiliary Heating Power, MW				
a) Neutral Injection	3-25	12/40	60	10-20
b) HF Heating	3-20	None	60	10
Neutral Injection Energy, kev	80,160	150/120,60	80,160	50,100

Table I

MICROINSTABILITIES AND BEAM HEATING EXPERIMENTS IN THE CULHAM SUPERCONDUCTING LEVITRON

N R Ainsworth, M W Alcock, R E Bradford, P R Collins, J G Cordey, T Edlington, W H W Fletcher, E M Jones, B E Keen, M F Payne, A C Riviere, D F H Start, C A Steed and D R Sweetman.

Culham Laboratory, Abingdon, Oxon. OX14 3DB, UK.
(Euratom/UKAEA Fusion Association)

ABSTRACT: The properties of fluctuations in a high shear axisymmetric torus with a strong poloidal field were investigated during a current driven discharge with $u/v_e < 0.1$ and during the collisional afterglow. The results showed that drift instabilities were present; during the discharge the scaling of amplitude with driving current and shear as $(I/\Theta)^{\frac{1}{2}}$ suggested the current driven mode whereas in the afterglow the scaling with shear as Θ^{-1} indicated the collisional mode.

Neutral beam injection was used to heat the plasma in the afterglow giving a temperature increase in agreement with classical processes. By modulating the intensity of the beam preliminary evidence was obtained for a plasma current driven by the injected fast ions - an effect first proposed by Okhawa [1].

1. INTRODUCTION: Multipole containment experiments have all shown MHD stability and as a consequence they have been used successfully for the study of microinstabilities and diffusion processes. Classical, neo-classical and Bohm scaling of diffusion have been observed in the G.A. Octopole [2] and both pseudo-classical and Bohm scaling of diffusion losses with electron temperature have been measured in the FM 1 experiments at Princeton [3]. The FM 1 experimental results illustrate the degree of containment to be expected in a high shear, axisymmetric torus with strong poloidal field - properties which should provide ideal conditions for containment. The Culham Levitron has the same favourable properties with ring currents up to 325 KAT in use, but, as in FM1, classical containment is not observed.

From the experiments we have done so far we report here observation of the collisional drift instability during the plasma decay and of the current driven drift instability during ohmic heating. Both of these affect the plasma containment. It is interesting to examine the operating regimes of our experiment in terms of the drift velocity u due to the current and the collision frequency of the electrons. This is illustrated in Figure 1. On the abscissa we have the ratio of the electron mean free path, λ_e, to the connection length, L_c, and on the ordinate we have the ratio $\alpha = u/v_e$, where v_e is the electron thermal velocity. The hatched area represents the region covered by our ohmic heating experiments and in addition we can have $\alpha = 0$ by use of electron

cyclotron resonance or neutral beam heating. Corresponding conditions met in some existing Tokamak experiments are shown based on data given in the IAEA Conference Proceedings in Tokyo in 1974, as well as those for ZETA [4]. The JET experiment [5] is expected to have rather low current density and to be well into the collisionless regime. It can be seen that the range of values of α studied here overlaps the values commonly used in Tokamaks. Although values of λ_e/L_c up to ~ 5 were reached in the present experiment, for most of this range neo-classical effects were estimated to be small.

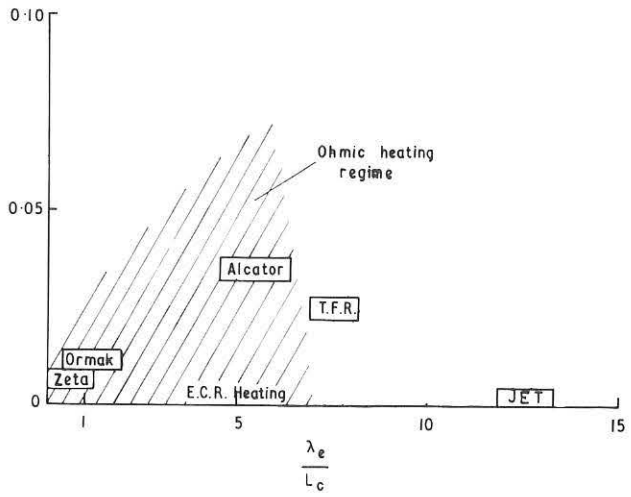

Fig. 1 A comparison of current driven drift velocities and collisionality conditions met in the present (hatched area) and other experiments.

In addition to the study of microinstabilities we report experiments on neutral beam heating of the plasma and, by modulating the neutral beam, preliminary evidence has been obtained for a beam induced current in the plasma whose existence was first suggested by Okhawa [1].

2. EXPERIMENTAL DETAILS

A detailed description of the Superconducting Levitron has been given elsewhere [6,7,8]. Figure 2 shows a section of the machine at the plasma region. The ring has a major radius of 30 cm, minor radius of 4.5 cm and floats inside an aluminium safety cage for periods of several minutes before re-cooling is required. The ring current I_R was normally 300 kAT but values down to 100 kAT were also used. The toroidal field B_T was operated at selected d.c. values up to 2 kilogauss giving a minimum shear length of 30 cm.

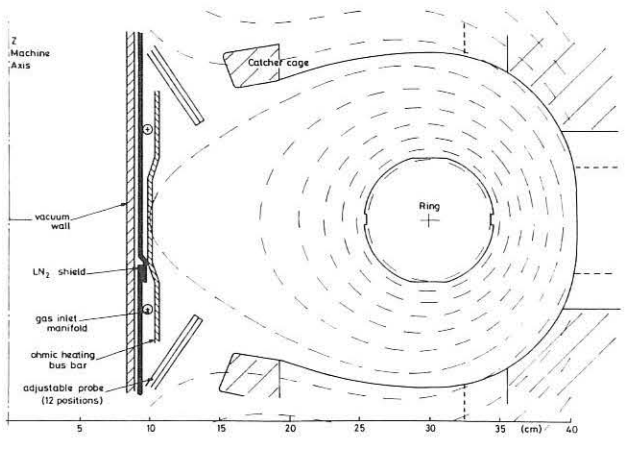

Fig. 2 Machine section in the r, z plane at the plasma region.

The plasma line density was measured with two separate μ-wave interferometers operating at 4 mm wavelength. The electron temperature was

obtained by measuring the absolute intensity of the 5876 Å Helium I line. Both density and temperature were also measured with a double probe when the effect of the probe on containment was acceptable.

Most of the experiments were carried out in plasmas produced by ohmic heating by adding a small 50 Hz component to the d.c. toroidal field. This gave a poloidal electric field E_p at the plasma of up to 0.15 volt/turn. Since the poloidal field B_p was much stronger than the toroidal field, E_p was essentially parallel to B.

The gases used were H_2, He and Neon and these were introduced through the symmetric set of holes around the centre column. The base pressure was 2.10^{-9} torr and the operating pressure for plasma production was normally of the order of 10^{-6} torr. In this pressure range no difficulty was experienced in producing plasma even at electric field values of less than 2 mV/cm. The plasma density reached with the ohmic heating was $\leqslant 2.10^{11}\,cm^{-3}$ and the electron temperature was $\leqslant$ 10 eV.

The high energy neutral injection system supplied a beam power through the plasma of 1.5 kW with pulses up to 2 sec long. The acceleration potential was 15 kV but three species were present so the beam consisted of 15, 7.5 and 5 keV components with the largest fraction in the 5 keV component [9]. The centre line of the beam lay at an angle of 37.5^{o} to the horizontal and passed through the plasma on the inner side of the ring at a distance from the axis of 20.6 cm in the midplane.

3. POWER AND PARTICLE BALANCE

With the electron density $n_e << 3.10^{12}\,cm^{-3}$ the plasmas were transparent to cold gas molecules so that the equilibrium electron temperature $\overline{T}_e$ was determined by particle balance requirements [6]

$$n_e\, N\, \langle \sigma\, v \rangle = \frac{n_e}{\tau_p} \qquad \ldots (1)$$

where N is the gas density, $\langle \sigma\, v \rangle$ the rate coefficient for ionization of the gas, which is strongly dependent on T_e, and τ_p the particle confinement time. Given N and τ_p the value of $\overline{T}_e$ is fixed and related to the ionization potential of the gas. The observed $\overline{T}_e$ for H_2, He and Neon were typically 5.5, 10 and 8 eV respectively.

When the heating power is switched off the electrons cool rapidly by ionization energy loss, $\tau_E \approx 2$ msec, and when $T_e \leqslant 2$ eV cooling occurs through collisions with the cold ions and thence the gas resulting in a τ_E of several tens of milliseconds. In the afterglow both T_e and T_i probably reach the temperature of the walls in times of the order of 200 msec.

With plasma production by ohmic heating the equilibrium n_e is determined by the power balance which in simplified form can be written as [6]

$$\frac{E_{\parallel}^2}{n_e\,(1+f)\,\eta_{\parallel}} = \frac{W_i + 3\,T_e}{\tau_p} \qquad \ldots (2)$$

where $E_{\parallel}$ is the RMS electric field along the field lines, $T_i \approx T_e$, and $\eta_{\parallel}$ is the Spitzer-Härm resistivity. The factor $(1 + f)$ where f is related to the fraction of trapped electrons, takes into account the neo-classical enhancement of resistivity and W_i is the energy required to produce an ion pair. If τ_p is independent of n_e, and T_e is kept constant by the requirements of equation (1) the relation (2) indicates that $n_e \propto I_\Omega^2$, where I_Ω is the ohmic heating current. The linear variation of n_e with I_Ω^2 was observed at low I_Ω [6] but it changes to $n_e \propto I_\Omega$ at high I_Ω as shown in Figure 3, indicating an additional loss process at high plasma current.

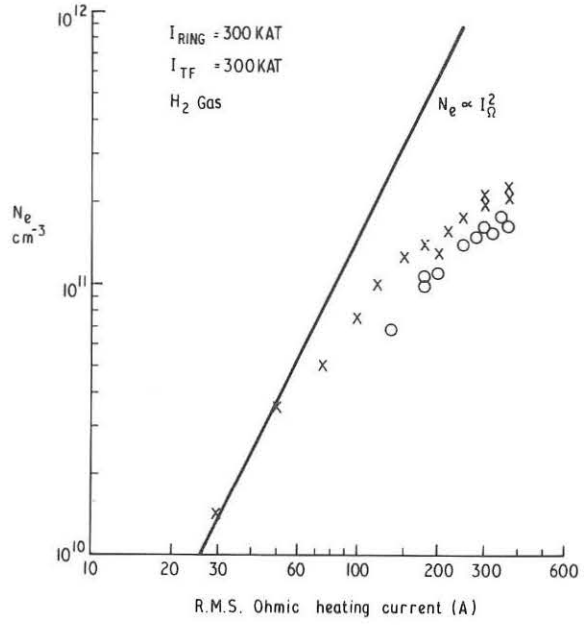

Fig. 3 Average electron density as a function of ohmic heating current.

4. FLUCTUATION MEASUREMENTS DURING OHMIC HEATING

Fluctuations in the plasma were measured by means of Langmuir probes biased to collect the saturated ion current, I_{SAT}. Figure 4 shows a radial profile of both I_{SAT} and the amplitude of its fluctuations $\tilde{I}_{SAT}$ on the outer side of the ring at $z = 0$. Sharp maxima in $\tilde{I}_{SAT}$ can be seen on both the inner and outer density gradients. Although the fluctuations have a larger amplitude on the outer side, the amplitude is still significant on the inner side nearer the ring where the field strength is greater and the curvature is favourable. At a fixed I_R the radial width of the $\tilde{I}_{SAT}$ signal was independent of B_T. The amplitude of $\tilde{I}_{SAT}$ increased and decreased at 100 Hz in phase with the applied ohmic heating current maxima.

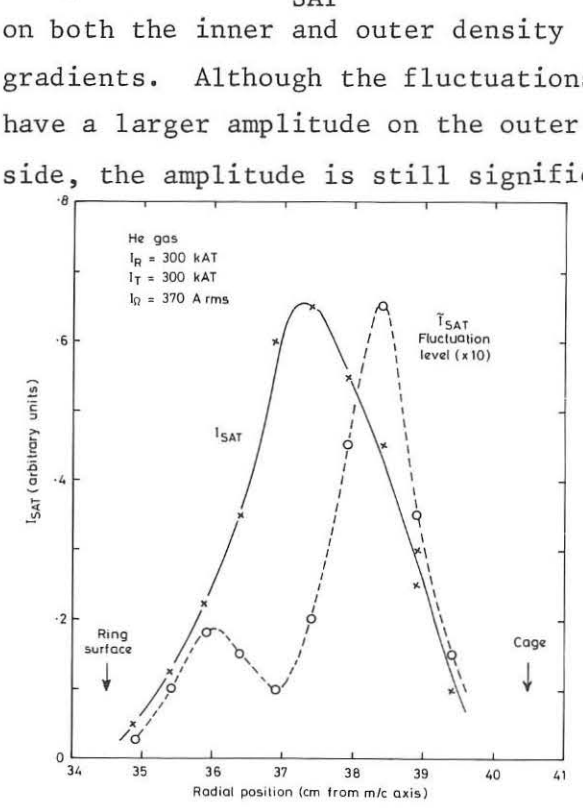

Fig. 4 Saturated ion current to probe as a function of radius on large major radius side of ring.

The wavelength, λ_T, in the toroidal direction was obtained from the correlation between two separate probes up to 5 cm apart on the same flux surface. Figure 5 shows the variation of the frequency $f (= \omega/2\pi)$ and λ_T with toroidal field stength. For the

dominant mode, $f\lambda_T$ is of the order of v_D (the diamagnetic drift velocity) and with the localisation in space and time outlined above it seems probable that the instability was a low frequency drift instability driven by the current induced in the plasma [10]. The results of Figure 5 show that as the toroidal field was increased the instability tended to occur with an integer number of wavelengths, p, between field lines, such that $p\,\lambda_T \approx 2\pi R/\iota$, where ι is the rotational transform and R the major radius at the point of measurement. This effect is understood to be due to a change in instability mode number in order to maximise the growth rate as the toroidal field was changed.

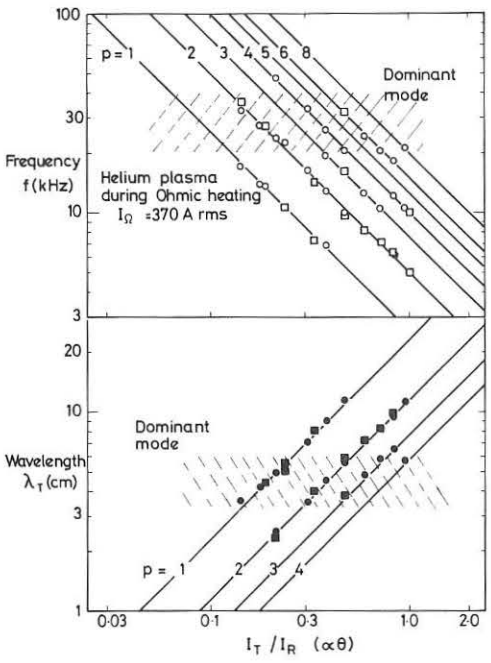

Fig. 5 Fluctuation frequency and wavelength in toroidal direction during ohmic heating as a function of the ratio of toroidal field current to ring current.

Theoretical expressions for ω and the linear growth rate γ are [10,11]

$$\omega = \omega^*/(1 + k_\perp^2 a^2) ,$$

$$\gamma = \frac{\nu_e c_s^2}{v_e^2}\left\{\frac{7}{4}\frac{k_\perp^2}{k_\parallel^2}\frac{\omega^{*2}}{\Omega_i^2} + \frac{\omega^* u}{k_\parallel c_s^2} - 1\right\} - \frac{k_x^2 a^2 \omega^*}{\sqrt{2}(1 + k_\perp^2 a^2)}$$

where $k_\perp^2 = k_x^2 + k_y^2$, $\omega^* = k_y v_D$, $v_D = c\,kT_e\,\kappa/eB$, $\kappa = d(\ell n\, n_o)/dx$, $c_s^2 = kT_e/M_i$ and $a^2 = c_s^2/\Omega_i^2$. If the slab model approximation for the introduction of shear is used, $k_\parallel = x_o\, k_y/L_s$ where L_s is the shear length, and x_o is the radial width of the instability given by $x_o^2 = 2/k_x^2$ then

$$\gamma = \frac{\nu_e m}{M}\left\{\frac{7\, k_\perp^2\, k_x^2\, a^4}{8\,\Theta^2} + \frac{k_x u}{\sqrt{2}\,\Theta\,\Omega_i} - 1\right\} - \frac{k_x^2\, k_y\, a^2\, v_D}{\sqrt{2}} \qquad \ldots (3)$$

Here $\Theta = 1/\kappa L_s$. For the current driven drift instability, and conditions well above threshold, the dominant term is

$$\gamma = \frac{k_x u \nu_e}{\sqrt{2}\,\Theta\,\Omega_e} \qquad \left(\propto \frac{I_\Omega}{\Theta}\right).$$

The linear growth rate γ can be related to the amplitude of the fluctuation n'/n_o by using non-linear theory which for drift waves [12,13] yields $\gamma \propto (n'/n_o)^2$ [14]. Hence from the theory we have $\omega \approx \omega^*$ as observed and $n'/n_o \propto (I_\Omega/\Theta)^{\frac{1}{2}}$.

Measurements of n'/n_o were made in He and Ne plasmas with I_R = 300, 200, and 100 kAT and varying both I_Ω and Θ. The values obtained are plotted as a function of I_Ω/Θ in Figure 6 and clearly the dependence of n'/n_o on $(I_\Omega/\Theta)^{\frac{1}{2}}$ is confirmed. If the plasma diffusion coefficient $D \propto (n'/n_o)^2$ then the variation of n_e with I_Ω in Figure 3 at high I_Ω can be explained by these fluctuations.

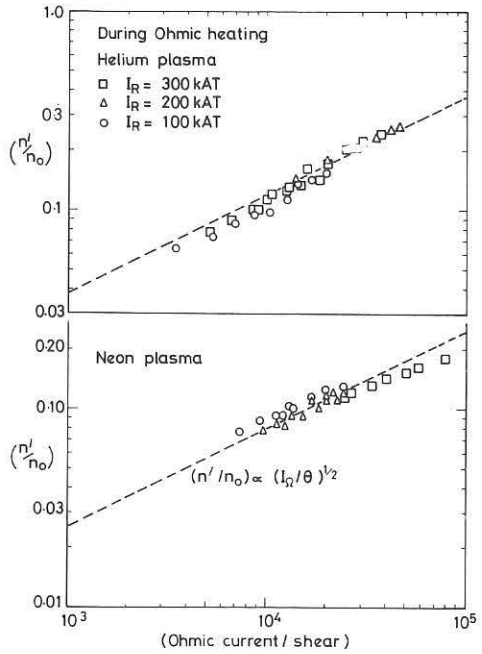

Fig. 6 Fluctuation amplitude during ohmic heating as a function of the ratio of driving current to shear strength.

5. FLUCTUATIONS IN THE AFTERGLOW

Fluctuation measurements made 25 to 30 msec after the ohmic heating driving current was switched off indicated the presence of a low frequency instability in the collisional afterglow when $I_\Omega = 0$. The radial profiles were similar to those measured during the discharge, Figure 4, with maximum fluctuation amplitude at the maximum density gradient but with smaller amplitude. The frequency and wavelength is shown in Figure 7 as a function of toroidal field strength. The values of λ_T were the same as those measured during the discharge but ω was lower corresponding to the lower temperature to be expected with no heating. From equation (3) with u = 0 and conditions well above threshold we have $\omega = \omega^*$ and

$$\gamma = \frac{7\, k_\perp^2\, k_x^2\, a^4\, \nu_e\, m}{8\, M\, \Theta^2}$$

giving $n'/n_o \propto \Theta^{-1}$. Values of n'/n_o for He are plotted in Figure 8 as a function of toroidal field strength ($\propto \Theta$) and these clearly show the Θ^{-1} dependence. In addition the decay times observed in the afterglow varied as Θ^2 as would be expected for $D \propto (n'/n_o)^2$ We conclude that it was the collisional drift instability which was observed and there were strong indications that the fluctuations determined the loss rate of the plasma in the afterglow. This instability was reported [15] as determining the containment time at $T_e < 1$ eV in FM 1.

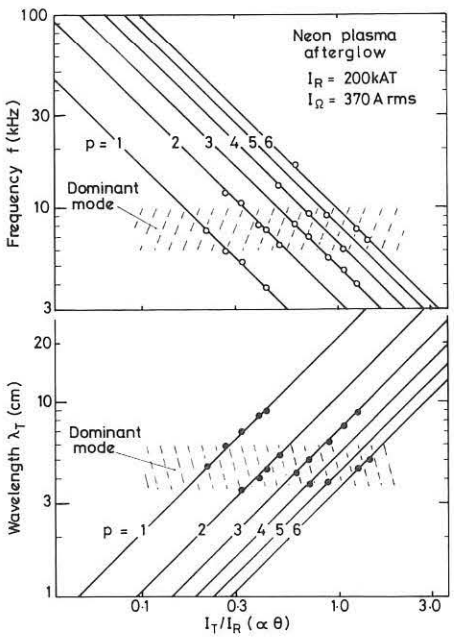

Fig. 7 Fluctuation frequency and wavelength in toroidal direction in the afterglow as a function of the ratio of toroidal field current to ring current.

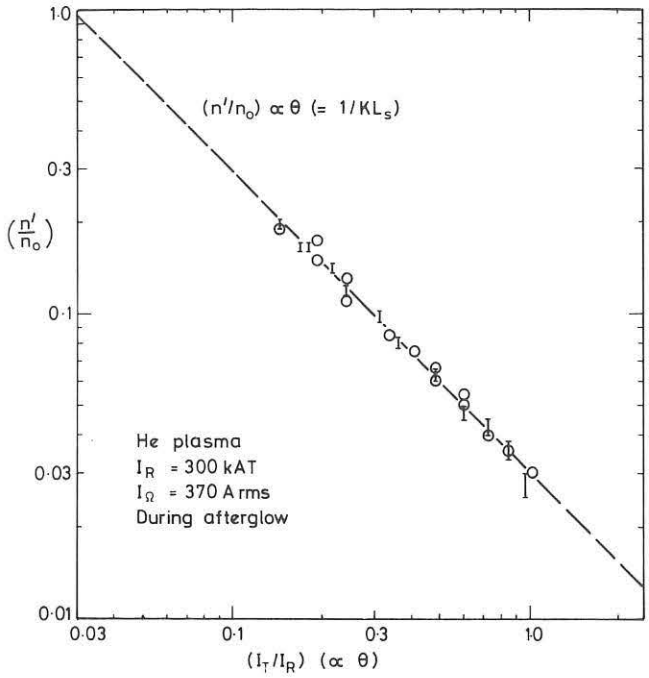

Fig. 8 Fluctuation amplitude in the afterglow as a function of shear strength.

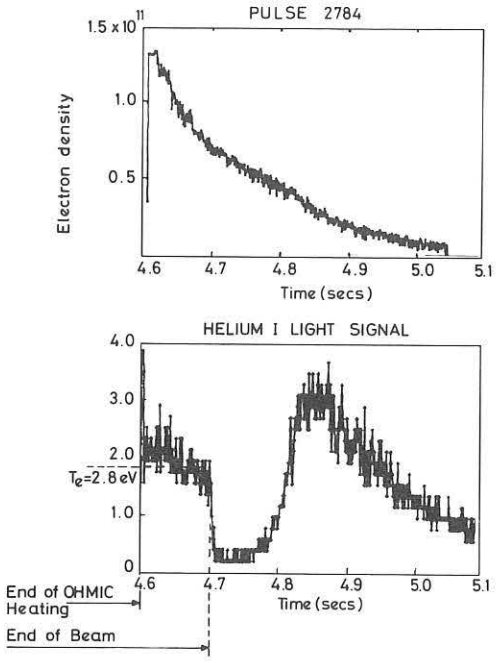

Fig. 9 Average electron density and He I light signal as a function of time in the afterglow. The He I signal shows the effect of beam heating followed later by recombination light.

6. HEATING OF THE PLASMA BY NEUTRAL INJECTION

Heating of the plasma by an injected beam was observed in the afterglow to give an increase in T_e from < .1 eV up to 2.5 eV. The effect is illustrated in Figure 9 where the observed He I light intensity, used to measure T_e, and the electron density are shown at the time that the neutral beam was switched off. The He I light falls abruptly as the electrons are cooled and recombination light appears ~ 100 msec later. The total fast ion population was measured by means of a foil covered Faraday cup immersed in the machine field close to the plasma. The absence of correlation between the signal to this detector and the He I light intensity as the gas pressure was varied indicated that the light signal was due to excitation by electrons rather than by hot ions.

The fast neutral energy spectrum for the 15 keV component is shown in Figure 10 in comparison with predicted spectra [16] for two ratios of slowing down time τ_s to charge exchange time τ_{cx} of 60 and 80. These values of τ_s/τ_{cx} were consistent with the measured values of n_e, T_e and N.

By using the measured electron density, H_2 and He pressures and the neutral beam power the electron temperature could be predicted from the equilibrium equations for hot ion density, cold ion density, T_e and T_i [6]. Comparison of predicted and measured T_e is shown in Figure 11, where the agreement is seen to be reasonable. The rate of density decay was reduced by the beam heating through additional ionization by the hot ions and by the electrons. The predicted ionization however was less by a factor of 10 than that required to explain the results but this quantity is sensitive to the

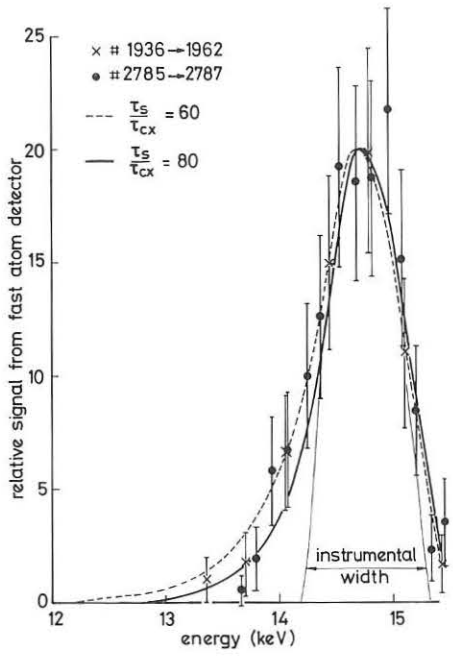

Fig.10 Fast neutral energy spectrum during injection into ohmic heating discharge.

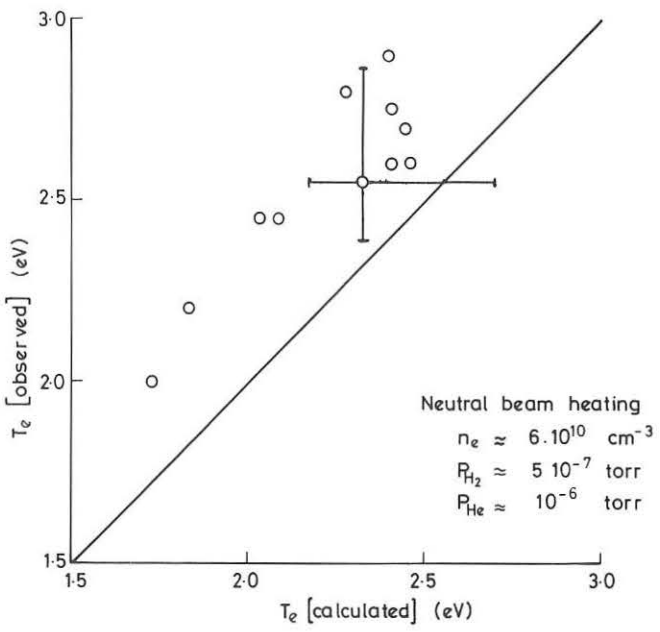

Fig.11 Comparison of observed and predicted electron temperatures during beam heating in the afterglow.

exact value of T_e and to the ionization rate coefficient in this low temperature regime. Under the present conditions the short charge exchange time prevents sufficient power transfer to occur for build-up of the plasma density.

7. BEAM INDUCED PLASMA CURRENT

The possible existence of a beam induced plasma current was first suggested by Okhawa [1]. The effect on the current of neo-classical corrections was considered by Connor and Cordey [17] and the correction to the Ohm's law by Callen et al. [18]. Evidence for this current was obtained here by modulating the beam at 120 Hz and detecting the modulated plasma current through the voltage induced in the cage circuit, which loops the plasma in the poloidal direction. The beam current can be defined as $I_{BEAM} = I_o\ (1 + \cos \omega t)$ and the net plasma current in the poloidal direction is then given by

$$I_p(t) = I_o \left(n_e \sigma_{cx} + N \sigma_{gi} \right) \ell \cdot \frac{B_p}{B} \cos \phi \cdot \frac{\tau_L}{\tau_c} \cdot \left[1 - \frac{Z_{fast\ ion}}{Z_{eff}} \cdot \frac{\tau_s(0)}{\tau_s \left(\frac{E}{T_e}\right)} \cdot \frac{1}{(1 + f)} \right] \cdot \left[1 + \frac{\cos(\omega t - \tan^{-1}(\omega \tau_L))}{(1 + \omega^2 \tau_L^2)^{\frac{1}{2}}} \right] \quad \ldots (4)$$

where $I_o(n_e \sigma_{cx} + N \sigma_{gi})\ell$ is the intensity of the trapped ion current, $\frac{B_p}{B} \cos \phi$ is a geometrical factor to allow for the angle of injection and field pitch angle, $\tau_L = (\frac{1}{\tau_{cx}} + \frac{1}{\tau_s})^{-1}$ is the momentum loss time for fast ions, τ_c is the time for a fast ion to pass around the minor azimuth so that $\frac{\tau_L}{\tau_c}$

is the amplification factor due to circulation. E is the fast ion energy. The correction factor

$$\left[1 - \frac{Z_{\text{fast ions}}}{Z_{\text{eff}}} \cdot \frac{\tau_s(0)}{\tau_s(E/T_e)} \cdot \frac{1}{(1+f)} \right]$$

allows for the back electron current which tends to cancel the current due to fast ion motion. Here a correction is made to τ_s since $v_e \approx v_{\text{fast ion}}$ and for 5 keV ions under the present conditions $\tau_s(0)/\tau_s(E/T_e) \approx 0.8$. The neoclassical factor, (1 + f) is about 1.1 when allowance is made for the effective λ_e so that the back electron current is expected to cancel the hot ion contribution by 70 percent. The last factor in equation (4) is the time dependence of the plasma current due to the modulation of the beam. The voltage induced on the cage is given by

$$V_{\text{CAGE}} = - \frac{\partial}{\partial t} \iint \mu_o \, I_p(t) \, \frac{dA}{R} \quad .$$

In the present case $\omega\tau_L \ll 1$ and the overall phase shift expected was close to 90^o. The predicted $V_{\text{cage}} \approx 10^{-6}$ volt. To reduce the effect of noise the signal was passed through a narrow band filter and then averaged in blocks of approximately 5 cycles in synchronism with the beam modulation by means of a multi-channel analyser. Figure 12 shows the signal amplitude with and without the plasma as a function of the number of records. Both the amplitude and phase of the observed signals were close to those expected. Measurements are continuing so as to establish the scaling of this signal with plasma density, gas pressure, beam current and parallel velocity of the ions.

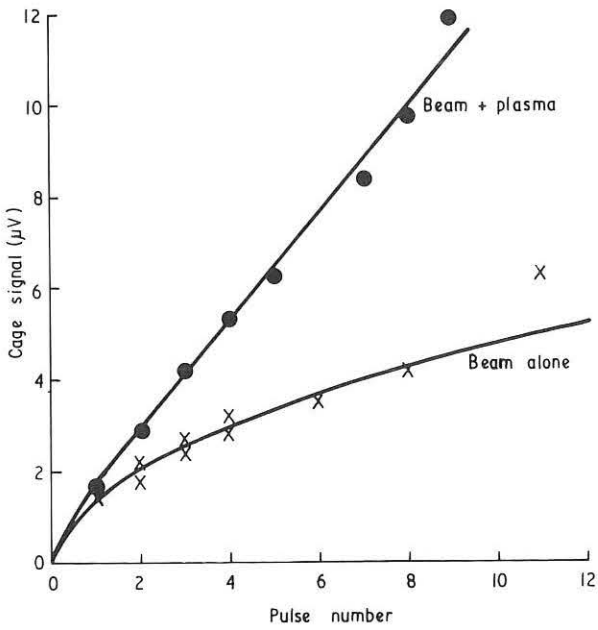

Fig.12 Integrated cage signal due to modulated plasma current and background noise as a function of the number of pulses recorded.

8. CONCLUSIONS

Fluctuations were observed in a current driven discharge with low values of u/v_e ($\leqslant 0.1$). The frequency, location and scaling with shear and current strongly indicated that these were due to the current driven drift instability. At the higher driving currents the plasma loss rate appeared to be dominated by these fluctuations and this may be relevant to other machines which use plasma currents to produce the confining field.

In the afterglow the measurements indicated the presence of the collisional drift instability. The scaling of decay rate with shear was consistent with the loss rate being determined by the fluctuations.

Heating of the plasma in the afterglow by means of neutral injection was in agreement with classical predictions.

By modulating the neutral beam preliminary evidence was obtained for a plasma current driven by the fast ions.

REFERENCES

[1] T. Okhawa, Nuclear Fusion 10 185 (1970).

[2] T. Tamano, Y. Hamada, C. Moeller, T. Okhawa and R. Prater, B4-3, Vth IAEA Conf. Plasma Phys. and Contr. Nucl. Fus. Res., Tokyo, Nov. (1974).

[3] K. Ando, S.Ejima, S. Davis, R. Hawryluk, H. Hsuan, D. Meade, M. Okabayashi, N. Sauthoff, J. Schmidt and J. Sinnis, B4-4, Vth IAEA Conf. Plasma Phys. and Contr. Nucl. Fus. Res., Tokyo Nov (1974).

[4] D.C. Robinson and R.E. King, B-8, IIIrd IAEA Conf. Plasma Phys. and Contr. Nucl. Fus. Res., Novosibirsk, August (1968).

[5] P. Noll, Invited paper on JET at this Conference.

[6] M.W. Alcock, R.E. Bradford, R. Freeman, D.P. Hammond, E.M. Jones, E. W. Laing, F.B. Marcus, A.C. Riviere, D.R. Sweetman and W.P.S. Tan, B4-1, Vth IAEA Conf. Plasma Phys. and Contr. Nucl. Fus. Res., Tokyo, Nov. (1974).

[7] D N Cornish, R.E. Bradford and A.J. Steel, Advances in Cryogenic Engineering 19 231-238 (1974).

[8] S. Skellett, VIIth Symp. on Fus. Tech. Grenoble, p.251 (1972).

[9] J.R. Coupland and E. Thompson, 2nd Symp. on Ion Sources and Formation of Ion Beams, Berkeley, Calif., October (1974).

[10] R.F. Ellis and R.W. Motley, Phys. Fluids 17 582 (1974).

[11] C.W. Horton and R.K. Varma, Phys. Fluids 15 620 (1972).

[12] T.H. Stix, Phys. Fluids 12 627 (1969).

[13] F.L. Hinton and C.W. Horton, Phys. Fluids, 14 116 (1971).

[14] B.E. Keen and M.W. Alcock (1975) - to be published.

[15] D.M. Meade, J.A. Schmidt and M. Okabayashi, 5B8, Bull.Am. Phys. Soc. Series II, 18, 1324 (1973).

[16] J.G. Cordey, A16-1, Vth IAEA Conf. Plasma Phys. and Contr. Nucl. Res. Tokyo, Nov. (1974).

[17] J.W. Connor and J.G. Cordey, Nucl. Fusion 14 185 (1974).

[18] J.D. Callen, R.J. Colchin, R.H. Fowler, D.G. McAlees and J.A. Rome, A16-3, Vth IAEA Conf. Plasma Phys. and Contr. Nucl. Fus. Res., Tokyo, Nov (1974).

BELT PINCH EXPERIMENTS

F. Hofmann, L. Bighel and J.M. Peiry

Ecole Polytechnique Fédérale de Lausanne, Switzerland
Centre de Recherches en Physique des Plasmas

Abstract: This paper consists of two parts: In the first part, a brief survey is given of the major belt pinch facilities around the world, whereas in the second part, the Lausanne Belt Pinch experiment is discussed and the results of recent measurements are presented.

1. Introduction

As is well known, the basic idea of the belt pinch [1] is to extend the stability domain of toroidal confinement devices to higher beta values by increasing the minor circumference of the plasma, without increasing its major radius. This can be done by elongating the minor cross section in the direction of the major axis of the torus. The belt pinch configuration is shown schematically in Fig. 1. It may be regarded as a toroidal screw pinch with non-circular cross section or, equivalently, as a straight hard-core screw pinch with closed ends. The pinch is produced by helical currents flowing on the inner and outer cylindrical surfaces of the torus, as indicated by the little arrows (Fig. 1). The induced currents in the plasma are also helical; they can be considered as a superposition of two closed current loops: a toroidal and a poloidal one. The poloidal plasma current usually decays more rapidly than the toroidal current because its L/R

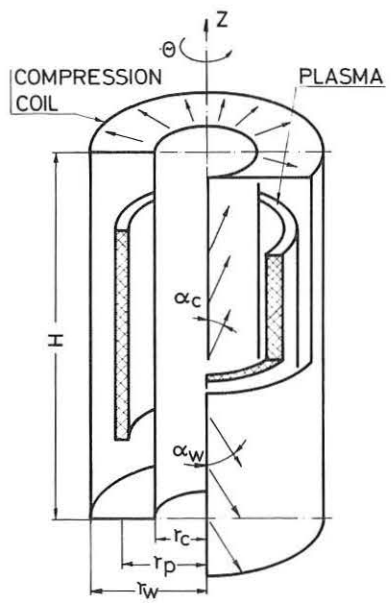

Fig. 1: Belt Pinch Geometry

time is smaller. When the poloidal current disappears, the diamagnetic dip in the toroidal field is filled in, and the pinch switches from the high-beta to the low-beta phase. In the low-beta phase, the configuration is identical with that of the Doublet or the elongated Tokamak.

Here, we are mainly interested in the high-beta phase and its stability. Obviously, the high-beta phase can only be studied when the plasma is relatively hot, such that resistive diffusion does not destroy the configuration.

2. Survey of World Effort in Belt Pinch Research

Table 1 is a list of the major belt pinch devices, whose results have been published in the literature.

Table 1

Device	Major Plasma Radius	Axial Height	Toroidal Plasma Current	$n_{e_{max}}$	$T_{e_{max}}$	High-Beta Confinement Time
	(cm)	(cm)	(kA)	(10^{15} cm^{-3})	(eV)	(μs)
1. NRL Pharos	3.5	180	1200	18	40	5
2. Jülich TESI	6	34	30	13	20	8
3. Jülich TENQ	46	108	200	3	30	60
4. Garching ISAR IV	24	100	200	10	20	10
5. Garching 1MJ	57	250	200	1.5	40	50
6. Lausanne	16	70	200	10	55	30

2.1. The NRL device [2], on top of the list, is actually a hard-core theta pinch, rather than a belt pinch. When it is operated with a reverse bias field, however, it produces a magnetic field configuration which is practically identical with that of the belt pinch. The experiment was first operated about 7 years ago, and the results were rather discouraging:

Confinement was lost after 5 μs. This was associated with an instability originating at the outer plasma boundary where the Suydam criterion is violated. The instability was first thought [2] to consist of rotating flutes, but it was later identified [3] as a spiral structure, moving along with the axial contraction of the plasma.

2.2. In the TESI device [4,5] at Jülich, plasmas with relatively modest elongation were studied. The high-beta phase originally lasted for about 2 μs only. It was later increased to 8 μs by increasing the voltage, i.e., the $\dot{B}$ at time t=0. It was found that, when the filling pressure was lowered below about 50 mTorr, the high-beta confinement time and the temperature were reduced, rather than increased as one would normally expect. This behaviour was attributed to the presence of impurities in the plasma.

2.3. The TENQ machine [6,7] is a much larger version of the same basic design. It uses a toroidal bias field to reduce beta, and thus improve the stability. Beta is about 0.3 and lasts for over 60 μs. The elongation of the minor cross section can be controlled within certain limits, the maximum elongation being about 4. At high filling densities, the plasma contracts axially until it reaches an equilibrium length. At low filling densities, however, the ends of the plasma seem to become unstable, and the confinement is lost after a few μs.

2.4. In the Garching ISAR IV belt pinch [1,8,9] stable confinement of up to 100 μs has been observed. However, for most of this time, the plasma was in the low-beta state, and the temperature was between 3 and 5 eV [9]. The high-beta phase lasted for about 10 μs. In some cases, helical flutes were observed on the outer plasma boundary, but these were not serious, i.e., they did not destroy the confinement. The flutes usually disappeared during the axial contraction. Experiments were performed at various q-values, and the pinch was found to become grossly unstable below about q=2.4.

2.5. The Garching 1MJ device [10,11] is by far the largest of all belt pinches. The high-beta phase was seen to last for about 50 μs and the maximum electron temperature was 40 eV [11]. This experiment has recently been modified, and is now being run at higher voltage [12].

2.6. The Lausanne Belt Pinch [13], the last item in Table 1, will be discussed in detail in section 3 of the present paper.

In addition to the six experiments mentioned above, there are several new belt pinches, presently under construction or just starting operation. Two of these machines have recently produced initial results: The TERP experiment at the University of Maryland [14] and the High Voltage Belt Pinch at Garching [15]. The latter is being used to study the fast implosion in belt geometry.

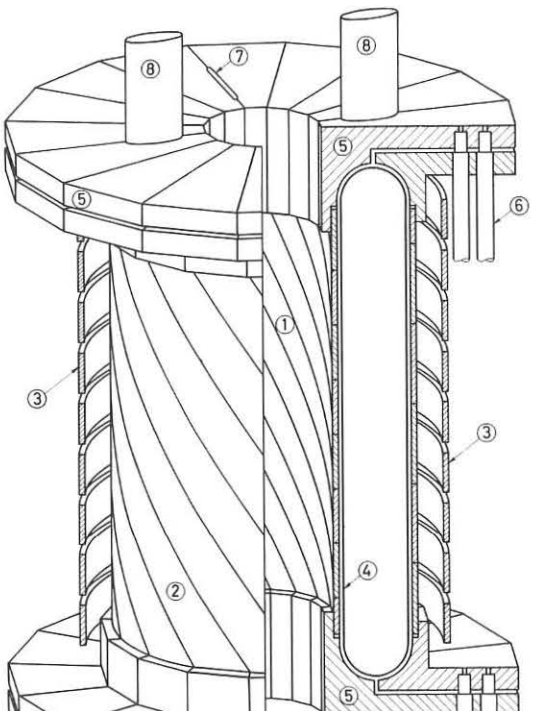

Fig. 2: Schematic of the Lausanne Belt Pinch: 1) inner helical coil, 2) outer helical coil, 3) conducting shell, 4) vacuum vessel, 5) connecting pieces, 6) feed cables, 7) slit for streak photography, 8) pumping ports.

In summary, we note that the results obtained to date in belt pinches are very encouraging, but in general, temperatures are still quite low, and one does not know whether the high-beta phase is stable at higher temperature. To produce a high temperature belt pinch is difficult, mainly because of technological problems associated with high-voltage insultation and reduction of impurities.

3. The Lausanne Belt Pinch

3.1. Experimental Apparatus

The main components of the experiment are (1) a fast capacitor bank with 120 kJ stored energy, (2) a metal-to-metal crowbar switch and (3) a helically wound, toroidal compression coil (Fig. 2). It should be noted that the coil is fed on both ends, in order to reduce its inductance, and thus increase $\dot{B}$. Important experimental parameters are listed in Table 2. The toroidal discharge tube consists of a single piece of Pyrex. Pre-ionization

of the deuterium gas is achieved by a high-frequency (4-MHz) electrostatic excitation, followed by a fast (1.2 μs FWHM) current pulse through the main coil. The pre-ionization discharge is damped by non-linear resistors. The main bank is triggered 1 μs after the end of the pre-ionization current, and the crowbar switch is normally fired at zero voltage (maximum current). The device is surrounded by a conducting shell (see Fig. 2) whose diameter can be changed in order to control the radial equilibrium. Extreme care has been taken to reduce the impurity content in the plasma to an absolute minimum. A turbomolecular pump is used and the entire vacuum system is made exclusively of metal and glass.

Table 2: Experimental parameters of the Lausanne Belt Pinch

Diameter of inner helical coil ($2r_c$)	20.4 cm
Diameter of outer helical coil ($2r_w$)	43.4 cm
Height of coil (H)	80.0 cm
Main bank capacitance	150.0 μF
Maximum charging voltage	40.0 kV
Coil inductance, without plasma	40.3 nH
Quarter period ($\tau/4$), without plasma	5.2 μs
L/R time of crowbarred current	400 μs
Maximum coil current	1.8 MA
Maximum toroidal field (at $r=r_c$)	17.0 kG
Maximum $\dot{B}$ at t=0	5.1×10^9 G/s
Maximum E-field on plasma surface, at t=0	250 V/cm

3.2. Streak Photography

Fig. 3 shows typical streak pictures, taken at 30 mTorr D_2 filling pressure and 30 kV charging voltage on the main bank.

The picture at the top was taken end-on, through a radial slit in the coil. It shows the radial motion of the plasma between the inner and outer walls of the torus. Four different phases can be distinguished: (1) a fast implosion which takes about 0.7 μs, (2) a slow radial oscillation of the plasma as a whole, around its equilibrium position, (3) a stable equilibrium phase, and (4) a disintegration phase, characterized by the appearance of light at the inner and outer walls of the glass torus. The disintegration is probably due to a deformation of the plasma minor cross section, followed by plasma-wall contact and rapid cooling. In the middle (Fig. 3), there is the corresponding streak picture taken side-on. It shows that there is practically no axial contraction. During the disintegration phase, however, one notices a certain asymmetry: Additional light appears first on one side ($z < 0$). Finally, the curve at the bottom of Fig. 3 is the toroidal plasma current as a function of time. The current rises rapidly and reaches its maximum value of about 200 kA at 5 μs. It then stays roughly constant for some time and finally drops off abruptly. The decay of the toroidal plasma current is obviously correlated to the disintegration of the pinch, as seen on the streak pictures.

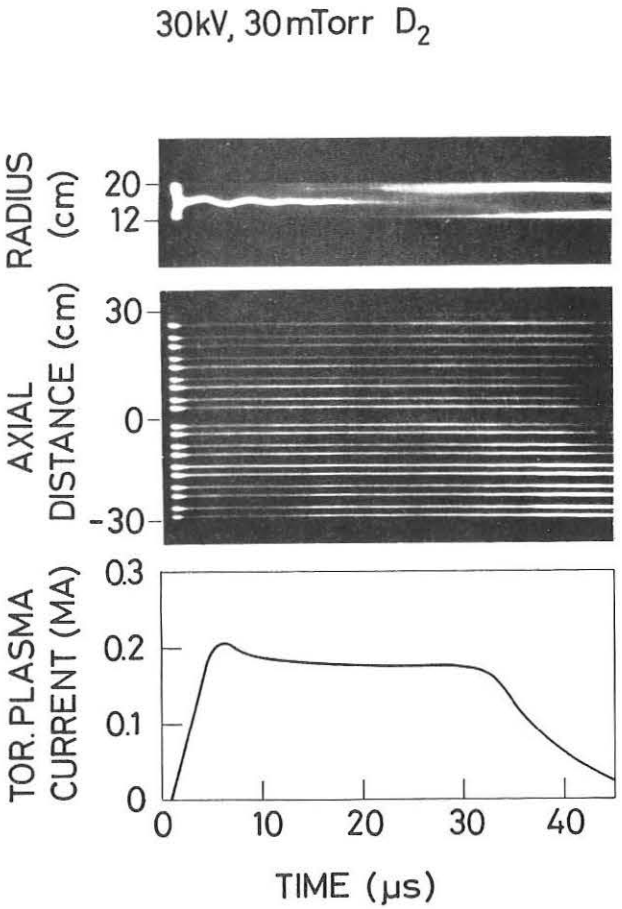

Fig. 3: Streak photographs and plasma current at 30 mTorr D_2.

Fig. 4 shows the effect of lowering the filling pressure: At 20 mTorr, the confinement time is somewhat reduced and the toroidal current starts dropping about 10 μs earlier than it did at 30 mTorr. Note that, here again, we see no axial contraction.

From streak pictures such as the ones shown in Figs. 3 and 4, we can measure the major radius of the plasma in its equilibrium position. The plasma radius depends on the radius of the conducting shell, as is shown in Fig. 5. The three circles are measurements, and the solid curve is a theoretical result, where the parameter β_θ has been adjusted to produce the best fit with the measurements. β_θ, in our terminology, is the toroidal beta. a is the radial width of the plasma as measured on streak photographs. There is good agreement between theory and experiment (Fig. 5), and, in addition, the β_θ-value that was used in the theoretical model agrees, to within experimental error, with the one that is obtained from direct measurements of density and temperature. From this we conclude that the theoretical model is probably valid. The model assumes constant-pitch, force-free fields between the plasma and the glass walls. Such fields are commonly observed in screw pinches.

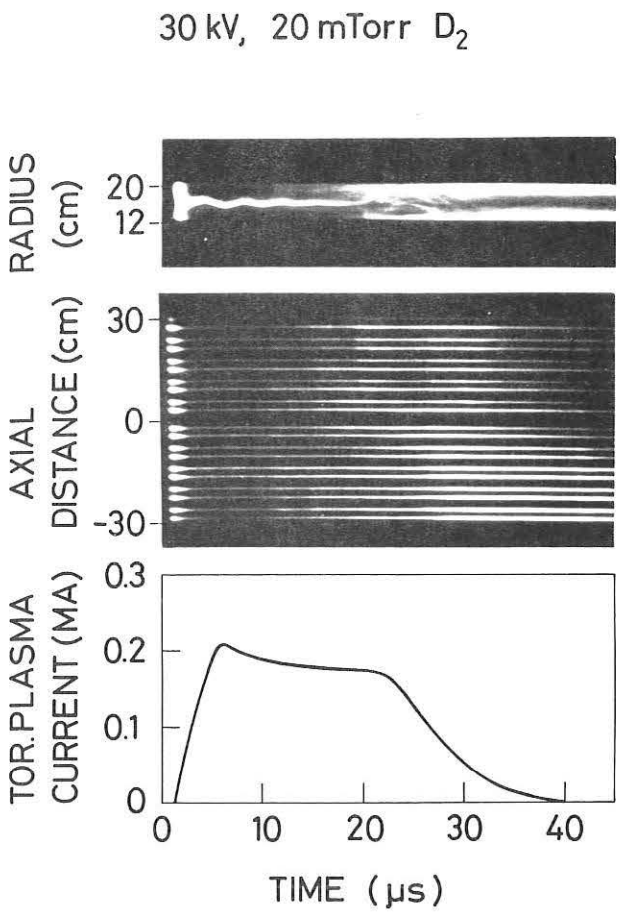

Fig. 4: Streak photographs and plasma current at 20 mTorr D_2.

3.3. Magnetic Fields and Currents

The magnetic field configuration, at the time of maximum compression (5 μs) is shown in Fig. 6. B_θ and B_z are the toroidal and poloidal field components, respectively. The curves (Fig. 6) were constructed in the following way: The fields outside the coil were measured with probes. Between the coil and the glass walls, vacuum field distributions were assumed. In the pressureless plasma, the fields were calculated according to the constant pitch force-free field model. This model is known to be accurate from radial equili-

brium measurements (Fig. 5). Finally, in the dense plasma the fields were drawn such that the total beta corresponds to the experimental value which is obtained from density and temperature measurements. Thus, we believe that the curves shown in Fig. 6 are fairly accurate representations of the actual fields in the pinch. These will, of course, have to be verified with magnetic probe measurements in the plasma.

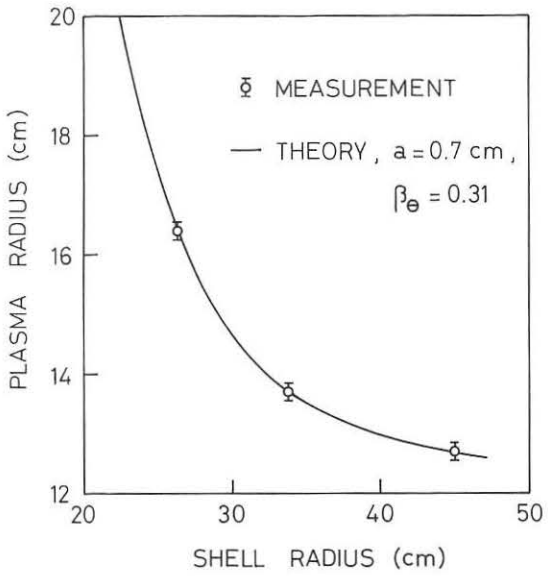

Fig. 5: Plasma radius vs. shell radius

A close inspection of Fig. 6 reveals that the force-free currents are parallel to the magnetic field lines on the outside, but anti-parallel on the inside of the belt shaped plasma. This behaviour has already been seen in computer simulations [16]. It implies that, near the ends of the belt, there must be a transition region, where the angle between $\vec{j}$ and $\vec{B}$ changes from zero to π. In that region we expect $\vec{j} \times \vec{B}$ forces having azimuthal components. These forces tend to rotate the "pressureless" plasma.

Another consequence of the phenomenon mentioned above is that the force-free currents have a large influence on the radial equilibrium. It is interesting to note, for example, that the poloidal field at the outer wall is actually smaller than it is at the inner wall. This is just the opposite of the usual situation in Tokamaks, where the plasma is surrounded by vacuum fields.

Clearly, the radial equilibrium configuration shown here (Fig. 6) is only valid during the early stages of the pinch, because, in a true two-dimensional equilibrium, there is a separatrix somewhere between the plasma and the outer wall, and outside the separatrix, there must be vacuum fields. However, the transition from the one-dimensional radial equilibrium to the two-dimensional toroidal equilibrium is still somewhat of a mystery.

Fig. 7 shows the coil current and the toroidal plasma current as functions of time. The coil current decays exponentially with a time constant of about 400 μs. The plasma current reaches 200 kA in 5 μs, as was already seen in Figs. 3 and 4, then it stays flat for some time, and finally, it switches itself off rather abruptly. The duration of the plasma current depends mainly on two parameters: First, it increases with the filling pressure, and second, it depends quite critically on the crowbar firing time: The earlier the crowbar fires, the longer the current stays up. The first of these two effects seems rather obvious: At higher pressure, the mass of the plasma is greater and consequently, any unstable motion is slowed down.

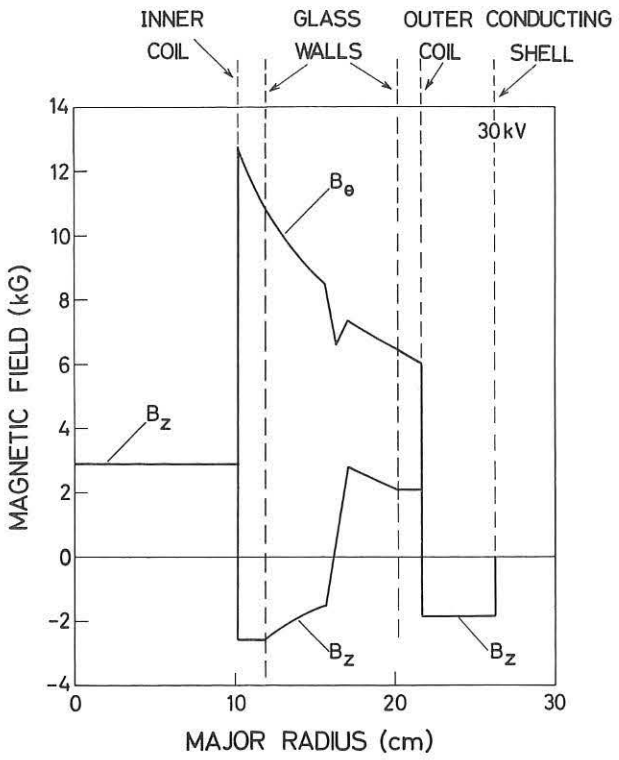

Fig. 6: Radial magnetic field profiles

The second effect might be explained as follows: When the crowbar fires early, the adiabatic compression phase is cut short, and the plasma remains relatively thick. Consequently, the pinch may be closer to its final equilibrium where, according to theory, the plasma must be thick.

Inspite of a number of efforts to clear up this loss-of-current phenomenon, the actual cause has not been found as yet. In order to find out whether the plasma might be unstable in the axial direction, we have measured the toroidal current in the conducting shell. The result is shown in Fig. 8. Here, we have plotted the current density, in kA per cm of axial length, as a function of the axial distance, z, and as a function of time. We note that the current remains symmetric with respect to the midplane, z = 0, and that its axial distribution does not change appreciably until about t = 20 μs. This seems to indicate that there is very little axial plasma

motion, because if the plasma were moving axially, it would induce image currents in the shell, and the axial current distribution would change drastically. After 20 μs, however, the current in the shell starts to increase, first at the right and then at the left. The resulting current asymmetry correlates with the asymmetric appearance of light, at the wall as seen on the side-on streak photographs (Figs. 3 and 4). The asymmetry is probably caused by radial and/or axial displacements of the ends of the plasma.

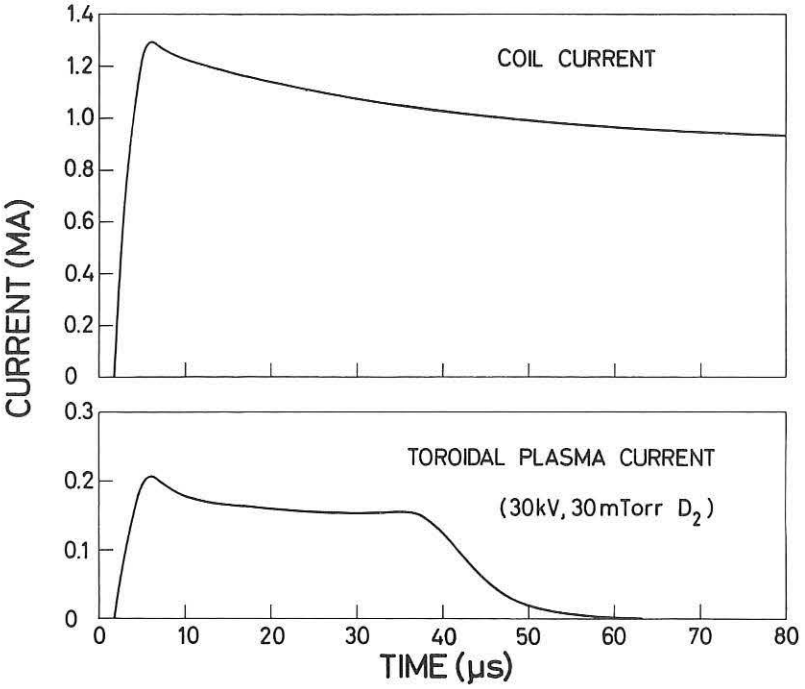

Fig. 7: Coil and plasma currents

3.4. Thomson Scattering Measurements

A Thomson scattering system has been built for this experiment in order to measure electron densities and temperatures. The system uses a 7 Joule ruby laser and a 9 channel polychromator, both mounted on a movable plat-form. The laser beam traverses the plasma parallel to the major axis of the torus and the scattered light is observed at 90^{o}, on the midplane of the torus. Radial scanning is achieved by displacing the entire system horizontally.

Fig. 9 is a typical radial profile of temperature and density, taken in the midplane of the torus, at 5 μs. The maximum temperature is 55 eV and the temperature distribution is quite flat. Note that the plasma is very narrow, about 7 mm FWHM. This seems to contradict a theoretical result [17] which says that there can be no equilibrium when the radial width of the plasma is less than half the width of the chamber. It has been pointed out recently [18], however, that this condition does not apply to plasmas surrounded by force-free currents. Temperatures and densities were also measured at later times and the corresponding beta values were calculated, assuming $T_i = T_e$.

The result is shown in Fig. 10. Note that the beta decays rather slowly, which indicates that radiation losses are small.

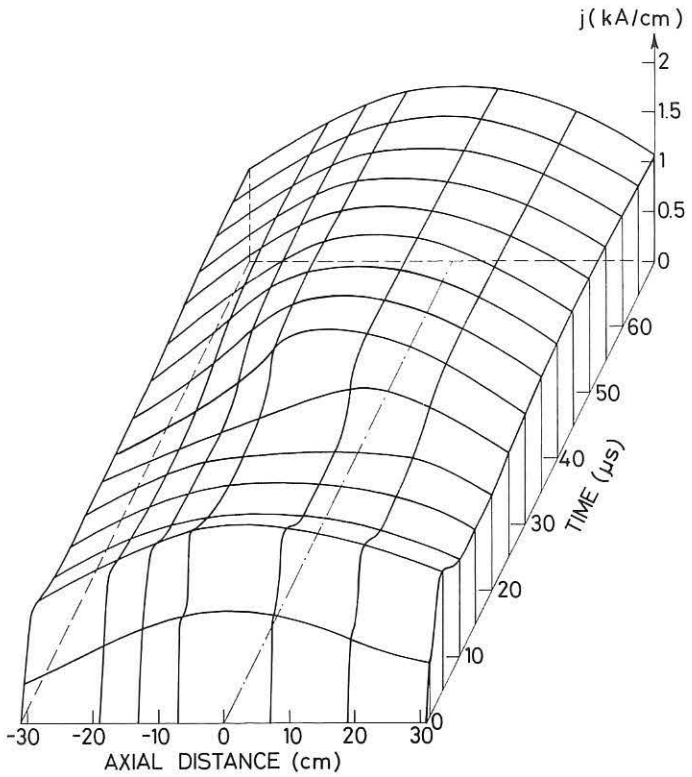

Fig. 8: Toroidal current per unit length of conducting shell.

From these results we can compute a number of interesting parameters. β-poloidal turns out to be 8, i.e., roughly equal to the initial aspect ratio of the pinch. The safety factors q is about 4, and the energy confinement time, defined as the total energy in the plasma divided by the ohmic power input, is equal to 180 μs. This is considerably longer than the plasma confinement time.

3.5. Conclusions

Measurements in the Lausanne belt pinch have shown that: (1) High beta equilibria with highly elongated plasma cross-section can be established. (2) These equilibria appear to be grossly stable for a certain time and then decay abruptly. The duration of stable confinement is proportional to the filling pressure and varies between 20 and 40 μs. (3) The plasma major radius can be conveniently controlled by varying the radius of a conducting shell placed around the outside of the torus. (4) Force-free currents circulate in the pressureless plasma surrounding the pinch. These currents are parallel to the magnetic field lines on the outside, and antiparallel on the inside of the belt-shaped plasma. (5) No axial contraction of the plasma has been observed. This is probably a consequence of image currents in the conducting shell as well as force-free currents in the pressureless plasma. (6) As a result of a high value of $\dot{B}$ at t=0 and extreme care to reduce the amount of impurities in the

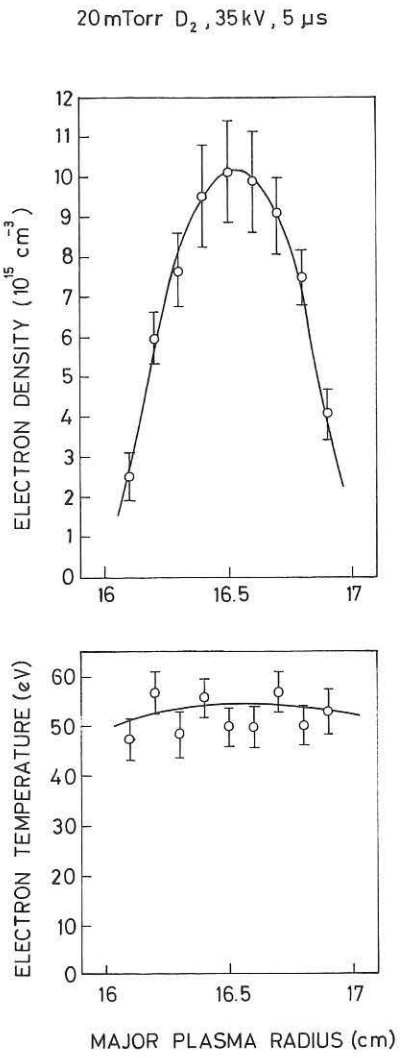

Fig. 9: Radial electron density and temperature profiles in Lausanne Belt Pinch

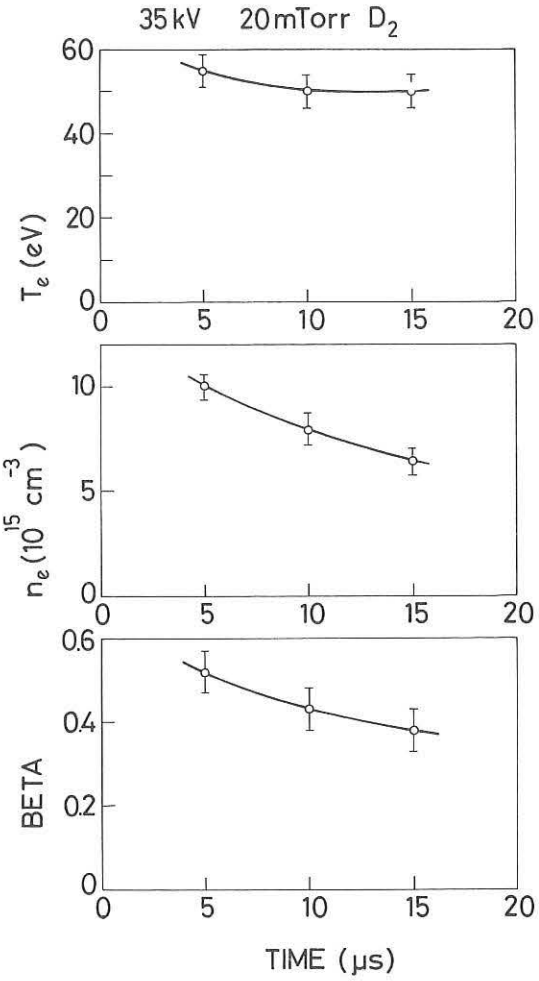

Fig. 10: Electron temperature, electron density and total beta as functions of time.

pinch, a relatively high temperature has been reached. The temperature is seen to remain almost constant as long as the plasma is stably confined. Consequently, it will be possible to study the stability properties of the high-beta phase in the Lausanne Belt Pinch.

4. Acknowledgement

This work was supported by the "Fonds National Suisse de la Recherche Scientifique".

References

[1] R. Wilhelm et al, in Plasma Physics and Controlled Nuclear Fusion Research (Proc.4th Int.Conf.Madison, 1971) 1, IAEA, Vienna (1971), 259

[2] A.C. Kolb et al, in Plasma Physics and Controlled Nuclear Fusion Research (Proc.3rd Int.Conf.Novosibirsk, 1968) 2, IAEA, Vienna (1969) 567

[3] D. Düchs et al, 2nd Topical Conf.Pulsed High Beta Plasmas, Garching IPP 1/127 (1972)

[4] U. Plantikow et al, Proceedings of the Third International Symposium on Toroidal Plasma Confinement, Garching 26-30 March 1973, paper A6

[5] H.J. Belitz et al, in Plasma Physics and Controlled Nuclear Fusion Research (Proc.4th Int.Conf.Madison, 1971) 3, IAEA, Vienna (1972) 179

[6] K.H. Dippel et al, Proceedings of the Third International Symposium on Toroidal Plasma Confinement, Garching 26-30 March 1973, Paper G7

[7] K.H. Dippel et al, in Plasma Physics and Controlled Nuclear Fusion Research (Proc.5th Int.Conf.Tokyo, 1974) 3, IAEA, Vienna (1975) paper E4-2

[8] H. Krause et al, 2nd Topical Conf.Pulsed High Beta Plasmas, Garching IPP 1/127 (1972)

[9] H. Krause, Garching Report IPP 1/150 (1974)

[10] R. Wilhelm et al, Proceedings of the Third International Symposium on Toroidal Plasma Confinement, Garching 26-30 March, 1973, paper G6

[11] G. Becker et al, in Plasma Physics and Controlled Nuclear Fusion Research (Proc. 5th Int.Conf.Tokyo 1974) 3, IAEA, Vienna (1975) paper E4-1

[12] O. Gruber, paper 43, these proceedings

[13] F. Hofmann, Nuclear Fusion 15 (1975) 336

[14] A.W. Allen et al, Proceedings of the Third Topical Conference on Pulsed High Beta Plasmas, Culham 9-12 Sept. 1975, paper D1.8 (to be published in Plasma Physics)

[15] F. Söldner et al, Proceedings of the Third Topical Conference on Pulsed High Beta Plasmas, Culham 9-12 Sept. 1975, paper D2.1 (to be published in Plasma Physics)

[16] F. Hofmann, Nuclear Fusion 13 (1973) 297

[17] A. Kadish, Nuclear Fusion 13 (1973) 756

[18] J.A. Hoekzema, private communication (1975)

RECENT HIGH-ß STELLARATOR EXPERIMENTS AT GARCHING

E. Fünfer, M. Kaufmann, J. Neuhauser, G. Schramm

Max-Planck-Institut für Plasmaphysik, Garching, Germany, EURATOM Association.

Abstract: After a short description of the basic ideas of the High-ß Stellarator (HBS), we summarize the results of the toroidal HBS experiment ISAR T1-A /1/ and present new results from the modified version ISAR-T1-B with large $\ell = 1$ plasma distortion ($\delta_1 \gtrsim 3$; helically shaped quartz tube and magnetic field coil). In spite of the large helical distortion, the equilibrium was obtained without strong helical oscillations. Furthermore, no $ß * \delta_1$ restriction was found in contrast to sharp boundary theory, but in agreement with a recent unscaled calculation. The equilibrium was unstable to the $m = 1$, $k \approx 0$ mode (high compression ratio, i.e. no wall stabilization). Only in the absence of gyrostabilization ($\omega_g \cdot \tau_{ii} \lesssim 1$, $r_p/r_g \gtrsim 7$) $m = 2$ instability was observed.

Introduction: Confinement at high-ß is very attractive for a fusion reactor. At Garching, two different high-ß concepts are in work: The Belt Pinch and the High-ß Stellarator (HBS). While the Belt Pinch can be regarded as high-ß Tokamak with highly elongated cross section, the HBS is completely different from low-ß machines: it is a slender configuration with large aspect ratio, the toroidal equilibrium is achieved without a toroidal net current and without Pfirsch-Schlüter currents parallel to the field lines. As a consequence of these properties, transport mechanisms should be more classical than in low aspect ratio machines.

The question of whether a possible HBS-reactor should be a short-pulsed machine (as in the Los Alamos concept) or a quasi-stationary one without strong shock-heating, seems to be of minor importance at present.

The main problem concerning the HBS is the question of stability against the long wavelength, low m-number MHD-modes. Since complete MHD-stability may be impossible for a total ß near 1, it is important to consider also real plasma effects, such as the finite gyroradius.

At high-ß, the $\ell = 1$ stellarator configuration is obviously superior to other ℓ-stellarators with respect to m = 1 stability (wall stabilization) /2-6/ and because of the possible selfstabilization of high m-number modes by magnetic well-deepening which occurs only at high-ß /7/. Toroidal equilibrium can be achieved by adding $\ell = 0$ and/or $\ell = 2$ fields with the same magnetic field period /3/. These additional components must be kept small in order to retain the favourable $\ell = 1$ stability. Linear experiments with $\ell = 1$ symmetry started at Garching in 1969 using the 5.4 m coil of the ISAR-1 θ-Pinch (ion temperature 50 eV ... 2 keV; bank energy o.5 ... 2.6 MJ). After a toroidal sector experiment, the first complete toroidal experiment ISAR-T1-A was put in operation at the end of 1972, using the same ISAR-1 condenser bank. The modified version ISAR-T1-B has now been in operation since April, 1975. In the following, we summarize the results of ISAR-T1-A /1/ and present results of ISAR-T1-B concerning toroidal equilibrium and stability for large $\ell = 1$ plasma distortion ($\delta_1 \gtrsim 3$). Special attention is paid to the $m \geq 2$ stability in the collision-free as well as in the collision-dominated regime. Finally, the results and their impact on the future HBS-development are discussed.

1. Summary of ISAR-T1-A Results. Isar T1-A was designed as a flexible, toroidal HBS with a fairly large $\ell = 1$ distortion ($\delta_1 \lesssim 1.5$) and a moderate elliptical deformation ($\delta_2 \lesssim 0.25$). The $\ell = 1$ and $\ell = 2$ fields were generated by helical wires inside the toroidal θ-Pinch coil and could be varied independently. Part of the experiments were also carried out with a small, but fixed $\ell = 0$ component ($\delta_0 \lesssim 0.06$). The main results were:

a) Toroidal HBS-equilibrium close to that predicted by theory /3/ could be achieved. Initial dynamic effects were explained by a simple dynamic model.

b) m = 1 instabilities with $n \leq 6$ were observed with growth-rates close to theorectical predictions /4/ (instability of form $\exp[m\theta - n\varphi]$; θ in azimuthal, φ in toroidal direction).

c) Indications for $m \geq 2$ instability were found in collision-dominated plasmas only ($\omega_g \tau_{ii} \lesssim 1$; ω_g = ion gyroradius, τ_{ii} = ion-ion collision time). The open questions regarding the m = 2 mode required further investigations on the ISAR-T1-B experiment.

A detailed description and the results of ISAR-T1-A as well as references to the preceding experiments can be found in /1/.

2. The New Version ISAR-T1-B

2.1 Description of ISAR-T1-B

Based on the experience with the flexible ISAR-T1-A experiment, a new version, ISAR-T1-B, has been constructed, using a helically shaped coil and vacuum vessel. By this technique, the following main characteristics could be achieved:

a) The helical $\ell = 1$ distortion could be doubled.

b) The initial $\ell = 1$ oscillations were nearly suppressed.

c) The $\ell = 2$ and $\ell = 0$ sidebands could be made sufficiently small, thus preserving the $\ell = 1$ stellarator properties also in toroidal geometry.

In the experiment, the toroidal field coil was shaped like a toroidal flux surface with a strong $\ell = 1$ stellarator field (screw-type deformation) and with small $\ell = 2$ (elliptical) and $\ell = 0$ (bumpy) sidebands. Reasonable flexibility was ensured by additional $\ell = 2$ windings. The number of identical periods was reduced from N = 24 to 16, i.e. $\varepsilon = h \cdot r_p$ ($h = 2\pi/\lambda$, λ length of a period) became smaller. Because of lower average coil inductance, the magnetic field rise-time was slightly decreased. The quartz tube was shaped like a toroidal cork-screw with a round local cross section, fitting the main $\ell = 1$ deformation of the coil only. The main data of both experiments are compared in the following table 1 (bank energy 0.5 MJ; values in brackets for 1.5 MJ):

	ISAR-T1-A	ISAR-T1-B
Large diameter	2.71 m	2.71 m
Minor average coil diameter	21 cm	17 cm
Inner tube diameter	9.2 cm	9.2 cm
Number of periods	24	16
Maximum magnetic field	1.4 T	1.5 ...(3.3 T)
Rise time	5.5 μs	4.7 ...(6.4 μs)
δ_1	0... 1.5	$\gtrsim 3$
δ_2	0... 0.3	0.05...0.15
δ_0	0 or 0.06	0.1

Figure 1 shows a segment of the coil (cast aluminum) and the toroidal arrangement of segments together with the screw-type quartz vessel. The asymmetric corrugation of the inner coil surface is readily seen. In Fig. 2, a photograph of about two periods is shown. The front part of the coil is removed revealing the helical tube and the $\ell = 2$ correction windings.

The same preionization by a toroidal z-Pinch and a preceeding HF-discharge was applied as in ISAR-T1-A /1/.

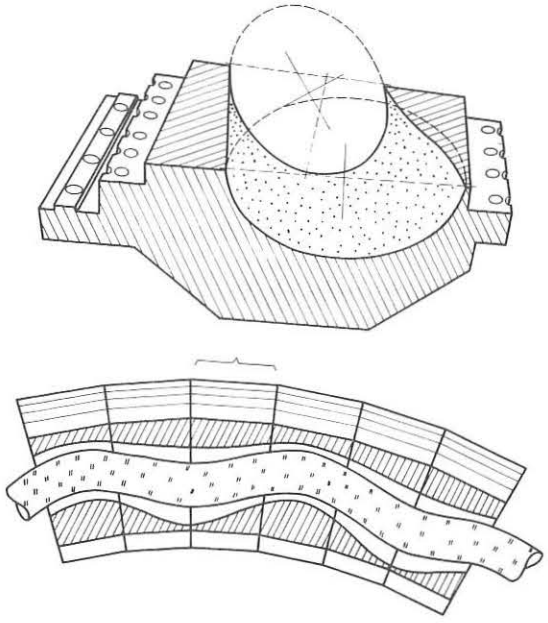

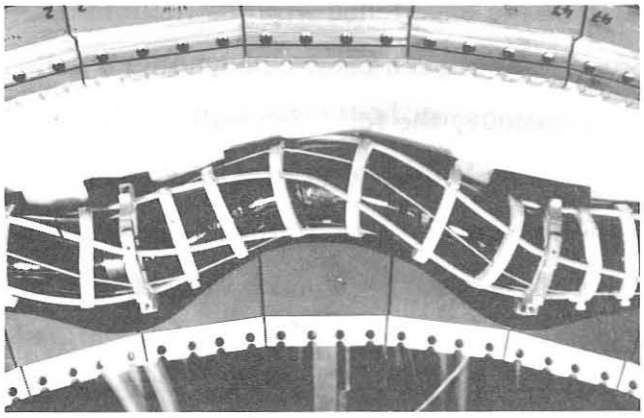

Fig. 2: Part of the ISAR-T1-B torus. The front segments of the shaped coil are removed.

Fig. 1 Top: Toroidal field coil segment with inner surface shaped like a magnetic surface; the rotating ellipse is indicated. - Bottom: Toroidal arrangement of coil segments. The screw-type quartz vessel is also shown.

2.2 Diagnostics and Plasma Parameters

The gross plasma behaviour (equilibrium, low m-number instabilities) was observed by stereoscopic image converter streak cameras and a rotating mirror camera which could be moved around the torus individually. Observation was concentrated on two opposite parts of the torus, each one two and a half periods long and covered by 10 observational slits.

Discharges were made with a filling pressure between 10 and 60 mTorr deuterium. The electron temperature for $p_o \gtrsim 20$ mTorr was measured by laser scattering (ruby laser, $\lambda = 6943$ Å). No special windows were used. A triple monochromator /8/ was used to suppress the high stray light level. In Fig. 3, the electron temperature is given for different filling pressures. The electron temperature during the magnetic field rise-time was also determined from the time dependence of the intensity of oxygen lines by solving the rate equation. Curves for 10, 20 and 40 mTorr are also drawn in Fig. 3, showing reasonable agreement. For filling pressures $p_o \gtrsim 20$ mTorr deuterium, the ion temperature is approximately equal to the electron temperature because of rapid collisional relaxation. At $p_o \lesssim 10$ mTorr T_i should be higher than T_e.

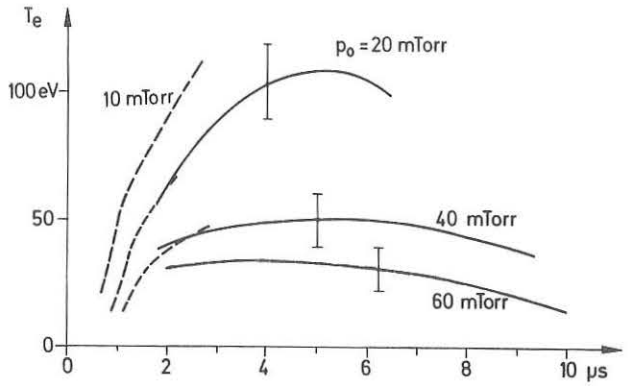

Fig. 3: Electron temperature for different filling pressure p_o and 0.5 MJ bank energy taken from laser scattering (full lines) and from oxygen impurity lines (dashed lines).

The area density was measured side-on by an infrared laser interferometer ($\lambda = 3.4\,\mu$). Because of the distorted plasma cross-section, especially in case of $m \gtrsim 2$ instability, reliable Abel inversion was possible only in some cases. The density obtained in this way was used to calibrate the local density measured by laser scattering (integrated spectrum).

Average density values are included in Table 2 (see below). At 4 μs the ß on axis was about 0.65 ± 0.15 and the oxygen impurity content was $\lesssim 0.2$ % for all filling pressures.

2.3 Toroidal Equilibrum and Initial Dynamics

Shock compression in the toroidal helical quartz tube (radius of local curvature ≈ 27 cm) yielded a well-compressed plasma column ($r_p \lesssim 1$ cm) with the same helical displacement ($r_H \approx 3$ cm) as the quartz tube. The average plasma helix radius did not change afterwards, as shown in Fig. 4, i.e. no helical oscillation were excited in contrast to the preceeding experiment with a non-distorted vessel. Obviously, $r_H \approx 3$ cm corresponded to the equilibrium plasma position as predicted by the sharp boundary relation $r_H = r_M / (1-\beta/2)$, though the latter was used far beyond the expected range of validity (radius of vacuum magnetic axis $r_M \approx 2.25$ cm, $\langle\beta\rangle \lesssim 0.5$: $r_H \lesssim 3.2$ cm). The

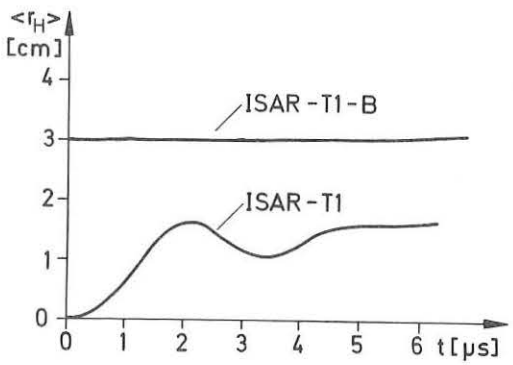

Fig. 4: Variation of the average radius of the plasma helix ($\ell = 1$ distortion) in ISAR-T1-B and the preceding ISAR-T1-A experiment. The average plasma radius is $r_p \lesssim 1$ cm, i.e. $\delta_1 \gtrsim 3$ in ISAR-T1-B (20 mTorr, 0.5 MJ).

$\beta \cdot \delta_1$-limit for a circular sharp bondary plasma /5/ was exceeded by a factor of three without visible effect ($\beta \cdot \delta_1 \gtrsim 2$). On the other hand, the experimental results were in excellent agreement with a recent straight $\ell = 1$, high-β equilibrium calculation /6/ with realistic pressure profile without small parameter expansion. The $\ell = 0$ and $\ell = 2$ plasma deformations should be about $\delta_2 \approx \delta_o \approx 0.1$ ($\beta \approx 0.5$). A detailed investigation is underway.

When the self-induced toroidal plasma current (see /1/) of about 10 kA had been compensated, the plasma still moved slowly in the drift direction. Driving a small current in the $\ell = 2$ correction windings proportional in time to the main field (2.7 kA at maximum, i.e. increasing δ_2 by about 30 %), excellent toroidal equilibrium was achieved. Above this value, the plasma moved towards the torus centre, i.e. the toroidal drift force was overcompensated. In Fig. 5, the motion of the plasma helix is drawn for different current $I_{\ell=2}$. In the case of an optimum balance of the toroidal drift force, a displacement was found in the toroidal drift direction similar to that in ISAR-T1-A, but with lower amplitude (Fig. 5). Though δ_1 is nearly constant in time, the oscillations connected with the formation of the $\ell = 0$ and $\ell = 2$ distortions can cause such a shift /1/.

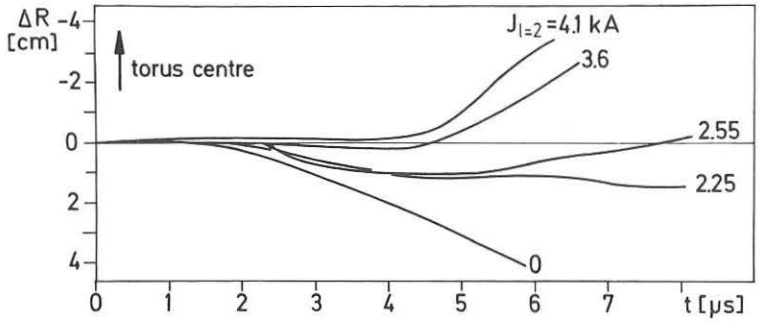

Fig. 5: Toroidal displacement of the plasma helix for different current $I_{\ell=2}$ in the $\ell = 2$ correction windings (20 mTorr, 0.5 MJ).

2.4 m = 1 Instability

An extensive m = 1 mode analysis has been made at ISAR-T1-A, where unstable modes with $n \lesssim 6$ and growthrates close to those of sharp boundary calculations were found /2, 3/ ($\gamma_{m=1,\ \ell=1} \approx h\, v_A \varepsilon \delta_1 \sqrt{\beta(2-\beta)\,(4-3\beta)/\,8\,(8-\beta)}$). In ISAR-T1-B, only a rough m = 1 growth rate was deduced from the average helix motion parallel to the main axis which should not be influenced by eventually non-perfect toroidal equilibrium. The sum of the displacements observed in two opposite parts of the torus (7 observational slits each) corresponds to the amplitude of m = 1 modes with even toroidal wave number

(n = 0,2,4), the difference represents the amplitude of odd modes (n = 1,3,5). For both cases the same e-folding time of 1.5 ± 0.4 μs was found for 20 mTorr, compared to an extrapolated theoretical value of 1.7 μs. Again, the simple sharp boundary theory obviously predicts the correct growth rate for m = 1 modes also in toroidal geometry and for large δ_1. The stabilizing wall effect, predicted by the same theory for small wall distance, was completely negligible in both experiments because of the high compression ratio (wall radius/plasma radius $\gtrsim 10$).

2.5 $m \gtrsim 2$ Instability

Fast growing $m \gtrsim 2$ instabilities are predicted by sharp boundary theory /2/ with a growth rate much larger than for the m = 1 mode. A diffuse pressure profile leads to slightly decreased growth rates /6, 12/ only.

These instabilities have not been observed in hot pinch plasmas, and it was claimed that the finite gyroradius has a damping or even stabilizing effect /9, 10/. In ISAR-T1-B, collisionless ($\omega_g \cdot \tau_{ii} \gg 1$) as well as collision-dominated ($\omega_g \cdot \tau_{ii} < 1$) plasmas could be produced by varying the filling pressure between 10 and 60 mTorr. The high δ_1, the small ε ($\gamma_{m=2}/\gamma_{m=1} \approx \beta/\varepsilon \gtrsim 7$ in sharp boundary theory) and the absence of δ_1 oscillations facilitated the $m \gtrsim 2$ investigations. In Table 2 average plasma data are given for $t \gtrsim 4$ μs (n_A = density on axis, r_g = ion gyroradius). For a filling pressure $p_o \gtrsim 30$ mTorr the gyration is strongly affected by collsions and, in parallel, the ratio r_p/r_g becomes smaller than required for gyrostabilization /10/.

Table 2

p_o [mTorr]	n_A [cm^{-3}]	r_p [mm]	r_p/r_g	$\omega_g \cdot \tau_{ii}$
10	10^{16}	6	4	16
20	2.10^{16}	7	5	6
30	$2.5.10^{16}$	8	7	2.3
40	$2.5.10^{16}$	9	8	2
60	4.10^{16}	10	10	0.8

In Fig. 6, selected stereoscopic smear pictures for 10, 20, 40, and 60 mTorr are shown taken at the same position (bulge region): At 10 and 20 mTorr only a m = 1 instability is found, while a m = 2 mode develops for higher pressure and correspondingly lower temperature. Usually the mode structure is much more complex and one cannot deduce a single m-mode with a definite wavelength. In selected cases, a wavelength of

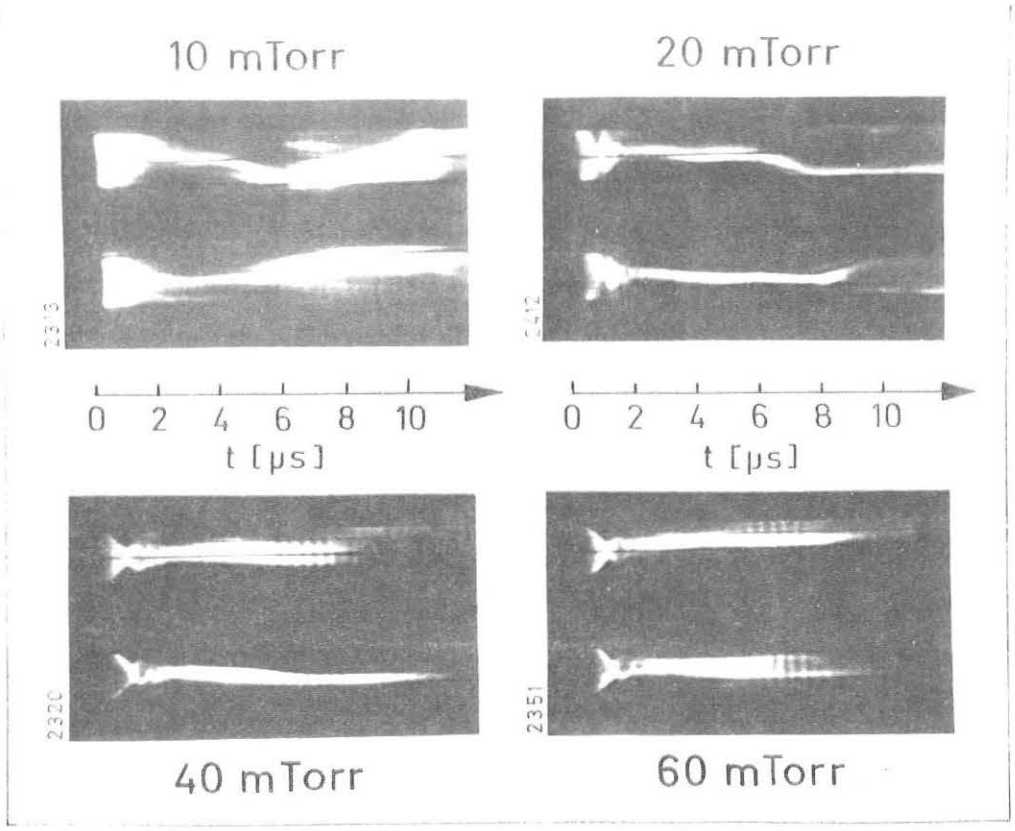

Fig.6: Selected stereoscopic smear pictures at the same positon for 10,20,40 and 60 mTorr (0.5 MJ) showing m = 1 and m = 2 instabilities, respectively. The ripple for $t > 5$ μs is caused by an electronic signal pick-up in the image converter.

at least 4 helical periods has been deduced from simultaneous smear pictures at three different positions.

For a typical case (30 mTorr), the m = 2 distortion $\xi_2 \equiv (a-b)/2 \cdot b$(a, b: major and minor axis of the ellipse) obtained from smear pictures, is drawn as a function of time (Fig. 7a). The curve can be interpreted as a superposition of a damped m = 2 oscillation and a growing m = 2 instability. The frequency and the damping coefficient of the oscillation are close to those of the short-wavelength, helical m = 2 oscillation of a diffuse plasma column /1,11/. The remaining unstable motion (Fig. 7b) yields a growth rate of $\gamma \approx 1.2 \cdot 10^6 \pm 0.3\ s^{-1}$ for $\xi_2 < 0.3$ which decreases continuously to about $0.5 \cdot 10^6\ s^{-1}$. The initial growth rate is by a factor of two smaller than the sharp boundary value $\gamma_2 \approx k v_A \delta_1 \sqrt{\beta^3 / (2-\beta)} \approx 2.5 \cdot 10^6\ s^{-1}$) /2/, but would roughly agree with recent calculation with diffuse pressure profile and arbitrary δ_1 /6/ and also with an unscaled numerical calculation /12/.

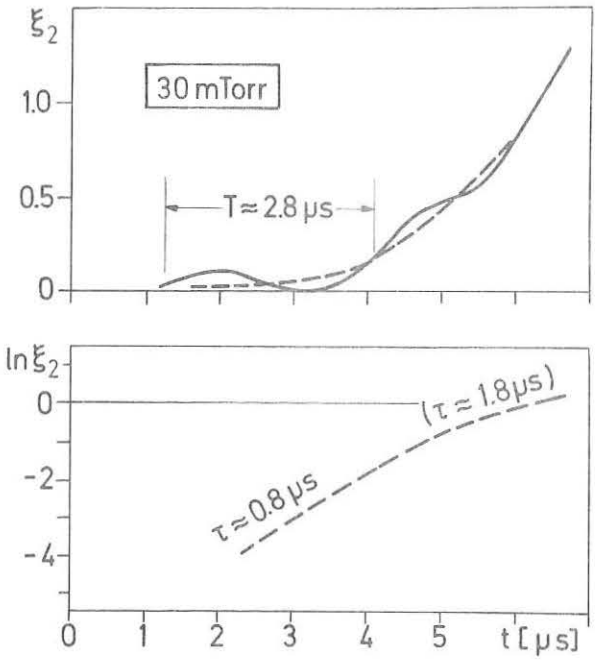

Fig. 7: The time dependence of the elliptical distortion $\xi_2 = (a-b)/2\,b$ is shown (full line). For the averaged growing motion (dashed lines) the logarithm is drawn also.

Conclusions: The experiments, carried out on ISAR-T1-A and ISAR-T1-B, give clear results regarding the toroidal equilibrium and the behaviour of the m = 1 mode. The toroidal drift was compensated with helical distortions ($\ell = 1, 2, 0$) of the plasma column close to theoretically predicted values. Even for extremely large $\ell = 1$ deformations ($\delta_1 \gtrsim 3$), the known formulas keep their validity. The m = 1 long-wavelength modes were unstable in these highly compressed plasmas ($K \approx 10$) and the growth rates were in agreement with the sharp boundary model. These results have been confirmed by the results from the closed SCYLLAC torus, reported recently /13/. Following the same theory as above, it can be expected that the m = 1 mode becomes wall-stabilized in a possible new experiment with a low compression ratio of the plasma column.

In contrast to the situation with the global m = 1 mode, modes with $m \geq 2$ were not observed under standard conditions, although large growth rates are predicted by the MHD-theory. In the experiment, m = 2 instabilities were detected only when the plasma was collision-dominated ($\omega_{gi}\,\tau_{ii} \lesssim 2$). In that case, rough agreement with growth rates, calculated for diffuse profiles is found. In the collision-free regime, the finite gyroradius is believed to stabilize $m \gtrsim 2$ modes. There remains, of course, the important question of how a reactor-like plasma, with long ion mean free path but with a rather small gyroradius (e.g.: $r_p/r_g \approx 20$), will behave. Apart from further experiments approaching that regime, advanced theoretical models are required to answer that question.

Acknowledgements:

The authors want to thank Dr. H. Röhr for laser scattering measurements, Dr. W. Lotz for vacuum magnetic field calculations and R. Wunderlich for data processing. Helpful discussions with Dr. F. Herrnegger, Dr. B.M. Marder (Los Alamos Scientific Laboratory), Dr. J. Nührenberg and Dr. W. Schneider are also gratefully acknowledged.

References:

/1/ E. Fünfer, M. Kaufmann, W. Lotz, J. Neuhauser, G. Schramm, U. Seidel; Nucl. Fusion 15, 133 (1975) (references to preceding l = 1 experiments can be found there)

/2/ M.N. Rosenbluth, J.L. Johnson, J.M. Green, K.E. Weimer; Phys. Fluids 12, 726 (1969)

/3/ H. Weitzner, in Plasma Physics and Controlled Nuclear Fusion Research, IAEA, Vienna (1971), Vol. III, p. 223

/4/ J.P. Freidberg; Phys. Fluids 14, 2454 (1971)

/5/ J.P. Freidberg, B.M. Marder, H. Weitzner, Nucl. Fusion 14, 809 (1974)

/6/ B.M. Marder, to be publ.

/7/ F. Herrnegger, J. Nührenberg; Bull. Am. Phys. Soc. 18, 1291 (1973) and Nucl. Fusion (to be published)

/8/ R.E. Siemon; Los Alamos Scientific Lab., (priv. com.)

/9/ M.N. Rosenbluth, N.A. Krall, N. Rostocker; Nucl. Fusion Suppl. 1, 143 (1962)

/10/ J.P. Freidberg; Phys. Fluids 15, 1102 (1972)

/11/ W. Grossmann, J. Tataronis; Z. Physik 261, 217 (1973)

/12/ F. Herrnegger, W. Schneider; this conference

/13/ E.L. Cantrell et al.; Fifth IAEA Conference on Plasma Physics and Controlled Nucl. Fusion Research, Tokyo, Japan, Nov. 11-15, 1974 paper E1-2.

RECENT MIRROR MACHINE RESULTS AND THEIR IMPLICATIONS FOR MIRROR SYSTEMS*

R. F. POST

Lawrence Livermore Laboratory, Livermore, California USA

Abstract: Improved confinement recently achieved in the Livermore 2XIIB experiment is interpreted in terms of warm plasma stabilization of the drift-cone mode. The same theoretical model explains present and earlier mirror observations and also predicts improved prospects for achieving classical plasma loss rates in mirror fusion reactors.

I. The Mirror Fusion Reactor - The goal of the Livermore magnetic confinement program is to prepare the way for the development of mirror fusion reactors. Over the years during which mirror physics and technology has been studied we have developed concepts for mirror fusion reactors, as driven systems, i.e. ones in which the plasma temperature and density is maintained by external sources, power for which is provided by recirculating a portion of the energy generated in the reactor.

An example case of the "classic" DT mirror reactor is illustrated in block diagram form in Fig. (1). The system operates steady-state, at high ion temperatures (>100 keV). Plasma temperature and density are maintained by neutral beam injection. Fusion energy is generated at a rate Q times the injection power rate, Q being dependent on mirror ratio and ion temperature. The neutron energy is further multiplied, by a factor m, by n,2n and capture reactions in the blanket surrounding the plasma chamber. Kinetic energy carried by charged particles, both charged reaction products and plasma ions and electrons, is recovered by a direct converter. High temperature heat derived both from the blanket and from thermal losses in the direct converter is converted to electricity in a steam plant. A portion of the power is recirculated to drive the injectors. We believe that the implied technological goals can be met and that

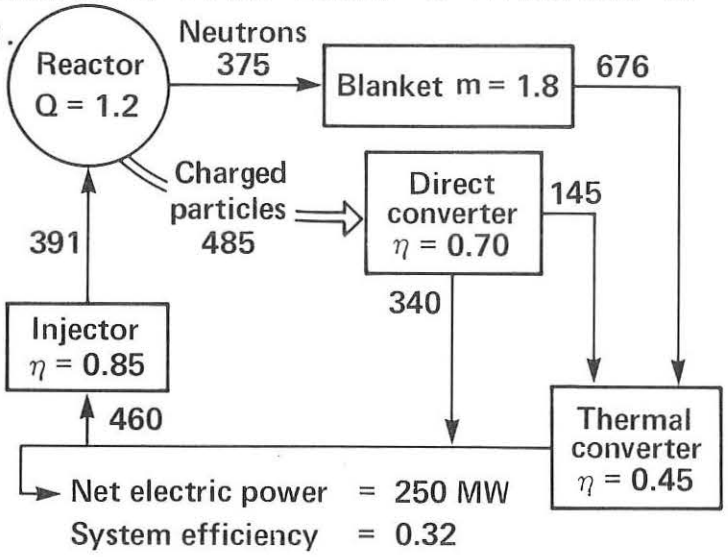

FIG. 1 - MIRROR REACTOR POWER FLOW DIAGRAM

our recent progress toward the scientific goal of stable confinement gives us renewed optimism concerning mirror reactors.

II. Implications of the New Results - Results obtained with the 2XIIB mirror machine at Livermore are described in the accompanying paper.[1] Here we mention only key points:

- Demonstration of means for the suppression of high frequency instabilities in hot mirror confined plasmas with an accompanying marked reduction in anomalous losses.
- Experimental evidence, spanning the range from about 2 to 10 keV ion temperature, that upon stabilization $n\tau$ increases with energy; τ itself increased by an order of magnitude ($\gtrsim$5 ms).
- Demonstration of a freely decaying stabilized hot plasma, exhibiting a binary decay law, i.e. 1/n proportional to t.

Being preliminary, the results are not conclusive. In particular we cannot claim that loss rates agree with the Fokker-Planck classical result. However, taken together with our proposed theoretical explanation one predicts that the reactor regime, involving higher temperatures, higher magnetic fields, and larger plasma sizes should be a more favorable one for achieving classical confinement than the present experimental situation.

III. Theoretical Interpretation - The new data are too limited to permit an unambiguous interpretation. We here advance a tentative explanation, representing an extension of earlier results, [2] results previously cited to explain stabilization effects observed in PR-6.[3]

The starting point is the long-predicted existence of the so-called drift cyclotron loss cone mode [4] (abbreviated; the drift-cone mode). In theory this mode is stable when the mean density gradient, a_i/R_p, is sufficiently small. However a_i/R_p in present machines, such as 2XIIB and PR-7, is considerably too large for stability, even according to criteria which include the stabilizing influence of finite beta.[5] Fig. (2) illustrates the circumstance, theory vs 2XIIB parameters. Because its growth rate is of order ω_{ci} the drift-cone mode would be expected to cause rapid plasma loss, of order the ion bounce time. The question has been how to explain the apparent absence of this supposedly virulent mode, especially in those cases where near-classical confinement seems to have been observed.[6]

We believe a coherent explanation for both the quiescent and non-quiescent cases can be found through an extension of an old concept, warm plasma stabilization.[7] The idea is simple: introducing a small percent-

age of lower energy ions exerts a large effect on loss cone instabilities, whose properties depend sensitively on this region of velocity space.

The most pronounced effect that warm plasma has on the drift-cone mode is to force it toward shorter azimuthal wavelengths (large $k_\perp a_i$), inhibiting growth rates and reducing particle losses. Depending on mirror ratio and beta (high values of both of which are stabilizing) a few percent of warm plasma can suppress the drift-cone mode. These effects are illustrated in Fig. (3), which shows theoretically predicted [8] increases in $k_\perp a_i$ and reductions in growth rates caused by introducing warm plasma into 2XIIB. In these calculations additional stabilizing effects, such as wave dispersion, were omitted, thus underestimating the stabilization. Another result: the addition of enough warm plasma to stabilize the drift-cone mode should at the same time suppress other loss cone modes, such as the Rosenbluth-Post high frequency convective mode [9] and negative-energy waves, [10] thereby apparently explaining the high degree of plasma quiescence observed in 2XIIB when stabilized by streaming

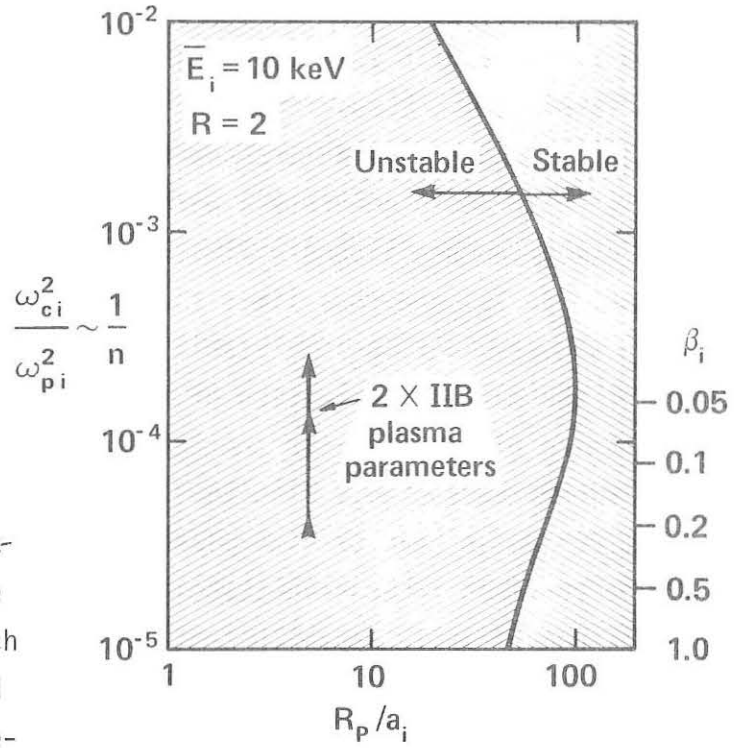

FIG. 2 - DRIFT-CONE STABILITY DIAGRAM

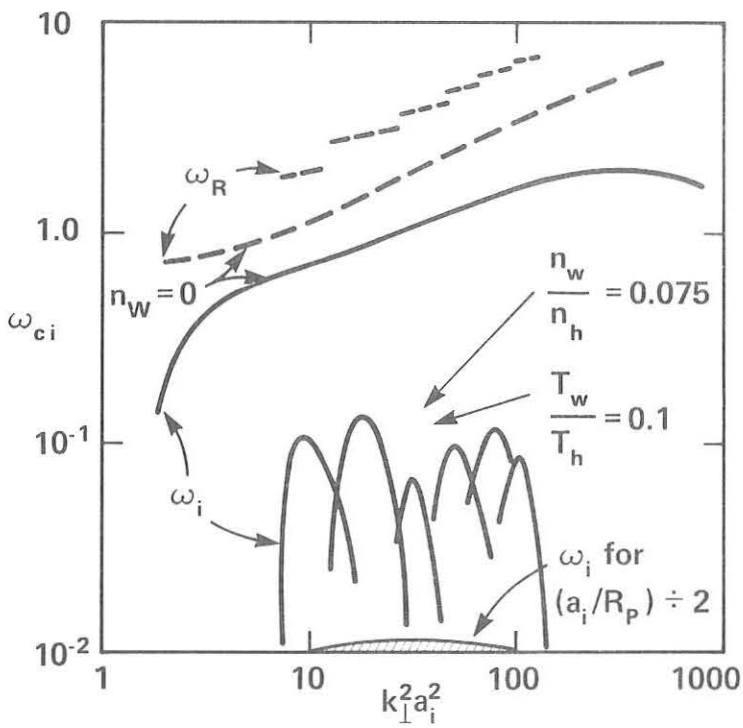

FIG. 3 - DRIFT-CONE ω_R AND ω_i 2XIIB PARAMETERS

plasma.

In corroboration of the above picture, warm plasma stabilization has been proposed [11] also to explain the relatively low rates of enhanced transport observed in 2XII and 2XIIB, even when no external source of warm plasma is present. Quasi-linear arguments, resembling those advanced by Galeev, [12] show that the transport in velocity-space caused by the instability itself should generate a warm plasma component directly from the main plasma, in turn strongly limiting fluctuation amplitudes to a level comparable to T_e, and thus limit the anomalous losses.

In summary, warm plasma stabilization appears to offer an explanation both for the marked suppression of losses observed in 2XIIB using a source of streaming plasma, and for the "anomalously stable" behavior of previous mirror experiments. Note also that warm plasma stabilization would be even more effective in reactor-size plasmas, the implication being that less would be required to achieve stability, with the expectation therefore that the confinement would approach that calculated for classical confinement.

IV. Summary of Results and Future Directions - Results from past experiments and from 2XIIB imply the following about mirror confinement at high plasma temperatures and densities:

- Magnetic well mirror fields suppress hydromagnetic instability up to high values of beta. Experimental values of order 0.5 agree with theoretical predictions.[13] The same theory, extended to include neutral beam injection, predicts hydromagnetically stable plasmas at beta values of order 0.9.[14]
- In most past mirror experiments there have been anomalous losses associated with high frequency instabilities. We believe that the dominant mode at high densities is the drift-cone.[15]
- In the presence of a low density externally generated source of streaming plasma high frequency activity is strongly suppressed, and the confinement time rises with increasing ion energy, although absolute loss rates may exceed classical in the present circumstances.

Future Directions - Assuming that some form of warm plasma stabilization permits near-classical confinement at reactor densities and temperatures, what are the possibilities for mirror fusion reactors?

Note that plasma stabilization by low density warm plasma represents one end of a continuum of systems the other end of which is the "two-com-

ponent mirror reactor" approach.[16] On the basis of our present theoretical understanding we would expect this entire continuum to be free from high frequency instability modes, such as the drift-cone mode, given adequate control over the plasma parameters.

We can correspondingly define a spectrum of possible mirror reactor systems and thereby define the physics and technology issues. We have already discussed the classic mirror reactor, but this case does not exhaust the possibilities, although beyond this example matters become increasingly speculative:

- A fusion-fission mirror system. With increased blanket energy multiplication comes lowered demands on confinement and system efficiencies, but also disadvantages.
- Two-component mirror reactors. These offer the possibility of increased Q, are expected to be free from high frequency instabilities, and require shorter confinement times for the ions (milliseconds). There are however unresolved questions associated with sheath energy transport and practical problems of high power density and large length.
- Variations on the mirror theme, including multiple mirror systems and mirror-torus hybrids. These might possess considerable advantages, but are as yet in an earlier stage of thinking.

As a class, the advantages of mirror systems as reactors are:

- Steady-state capability, high power density, and smaller size
- Relative insensitivity to impurities
- Adaptability to high efficiency direct conversion
- Well defined technological problems, possibly simpler than those for other systems

We intend to vigorously pursue the potentialities for mirror systems as looking toward modifications of our present experiments (2XIIB and Baseball II) as well as toward a scaled-up mirror experiment capable of achieving reactor temperatures (100 keV) and densities.

References:

[1] F. H. Coensgen, et. al., "Recent Experiments on the 2XIIB Mirror Machine", (Companion paper to author's paper; this proceedings).

[2] H. L. Berk, et. al., Plasma Physics and Controlled Nuclear Fusion Research, Vol. II. p.151, IAEA Vienna 1969.

[3] B. I. Kanaev, E. E. Yushmanov, Fifth European Conference on Controlled Fusion and Plasma Physics, Grenoble (1972).

[4] R. F. Post and M. N. Rosenbluth, Phys. Fluids 9, 730 (1966).
[5] W. Tang, L. D. Pearlstein, and H. Berk, Phys. Fluids 15, 1153 (1972).
[6] F. H. Coensgen et. al. Paper D2-1, Fifth Conference on Plasma Physics and Controlled Nuclear Fusion Research, Tokyo, Japan, Nov. 1974.
[7] R. F. Post, Proceedings of International Conference on Plasma Confined in Open-Ended Geometry, Gatlinburg, Tenn. 1967. Oak Ridge Report, CONF-671127, p.309.
[8] L. D. Pearlstein (to be published).
[9] M. N. Rosenbluth and R. F. Post, Phys. Fluids 8, 547 (1965).
[10] H. L. Berk, L. D. Pearlstein and J. G. Cordey, Phys. Fluids 15, 891 (1972).
[11] D. E. Baldwin, H. L. Berk, and L. D. Pearlstein (to be published).
[12] A. A. Galeev, Plasma Physics and Controlled Nuclear Fusion, Vol. I, p.393. IAEA, Vienna (1966).
[13] A. W. Molvik, et. al., Phys. Rev. Ltrs. 32, 1107 (1974).
[14] M. E. Rensink, et. al., Paper D1-2, Fifth Conference on Plasma Physics and Controlled Nuclear Fusion Research, Tokyo, Japan, Nov. 1974.
[15] T. C. Simonen (to be published in Phys. Fluids).
[16] R. F. Post, T. K. Fowler, J. Killeen and A. Mirin, Phys. Rev. Ltrs. 31, 280 (1973).

*Work performed under the auspices of the U.S. ERDA

RECENT EXPERIMENTS ON THE 2XIIB MIRROR MACHINE*

F.H. Coensgen, W.F. Cummins, B.G. Logan, A.W. Molvik, W.E. Nexsen, T.C. Simonen, B.W. Stallard, W.C. Turner

Lawrence Livermore Laboratory, Livermore, California, U.S.A.

Abstract: Plasma confinement experiments with neutral beam injection in the 2XIIB Magnetic mirror facility are described. Ion heating to 13 keV and build-up of hot ion densities to $4 \times 10^{13} cm^{-3}$ are measured when streaming plasma is introduced to suppress microinstabilities. Increasing ion energy is found to increase $n\tau$.

I. Introduction. We report initial results of plasma confinement experiments with neutral beam injection in the 2XIIB magnetic mirror facility. The magnet is similar to that of 2XII which has been described previously [1,2] (2XIIB central field 6.7 kg, mirror ratio 2.0, distance between mirrors 150 cm). 2XIIB target plasma densities, energies and lifetimes indicated on Table 1 are similar to those of 2XII.

Table 1

Operating mode	E_i(keV)	T_e(eV)	τ(ms)	$n\tau(cm^{-3}sec)$
Target	2-5	80	.2-.4	$\sim 10^{10}$
Target + Beams	13	200-300	.2-.4	$\sim 10^{10}$
Target + Stream	2.5-4	--	1.4	$\sim 2.8 \times 10^{10}$
Target + Beams + Stream	13	--	>5	$>7.5 \times 10^{10}$

The principle new feature of 2XIIB is the neutral beam injection system which consists of twelve injectors [3]. Currents of up to 370 Amperes of deuterium atoms were injected in the present experiments. Injectors operated in the range 15 to 19 keV with extraction currents divided approximately .5, .4 and .1 between full, half, and one-third energy components.

The second new feature of 2XIIB is a streaming plasma injector which provides a flow of warm plasma along the magnetic field lines. This plasma is produced by a deuterium loaded titanium washer gun with a pulse line limited to 1.1 msec duration in the present experiments. This duration has now been extended to permit future experiments to be conducted over longer time durations.

II. Measurements. Table 1 summarizes characteristics of plasmas formed

in different operating conditions, all with titanium gettering throughout the entire vacuum chamber preceding each shot. Beam injection increases the mean ion energy from several keV to 13 keV in a few hundred μs. Thompson scattering electron temperature measurements indicate that this ion heating results in electron heating. Without streaming plasma, neutral beam injection does not result in increased particle lifetimes or density build-up. This behavior is attributed to an enhanced level of ion cyclotron noise produced by beam injection.

The level of ion cyclotron fluctuations is reduced with the introduction of streaming plasma. With the lower fluctuation levels, the beam input is sufficient to cause density build-up as shown in Fig. 1. This figure shows microwave density, diamagnetic loop and neutron measurements as a function of time. The agreement between these measurements, together with beam attenuation and charge exchange measurements which are not described here, provides a consistent picture, namely that the measured density build-up is of 13 keV average ion energy plasma rather than cold ion accumulation from the streaming plasma. Fig. 1 shows a rapid density loss after the streaming plasma is terminated and the fluctuation intensity increases.

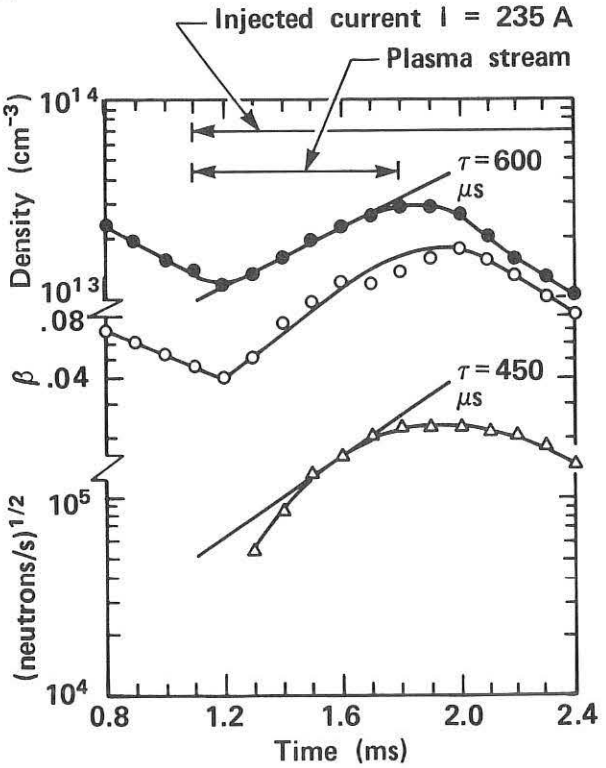

Without beam injection, if the plasma stream is brought on early during the magnetic compression, the plasma decay after compression is consistent with losses arising from binary collisions as shown by the fact that a plot of 1/n vs. time (shown in Fig. 2) is a straight line (i.e. $n\tau$ is a

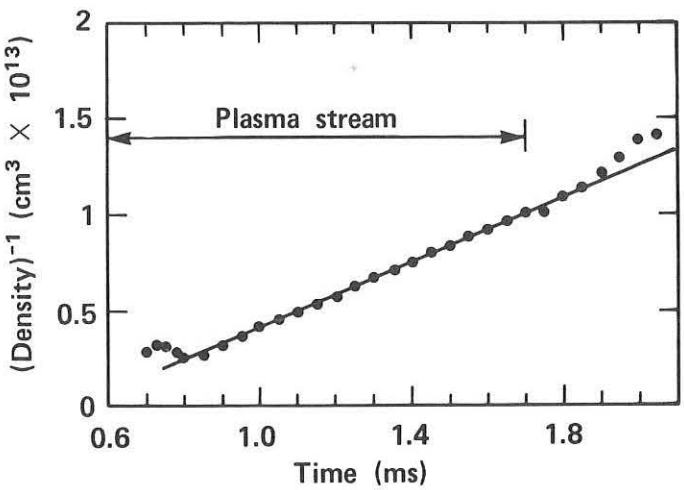

constant) for the duration of the plasma stream. During this shot the mean ion energy remains nearly constant, in contrast to shots without plasma stream which show rapid hardening of the ion energy spectrum due to fluctuations.

III. Interpretation of Data. The build-up of hot ion density n_h is described by a rate equation:

$$\frac{1}{\tau} = \frac{1}{n}\frac{dn}{dt} = \frac{1}{n_h + n_w}\left[\frac{dn_h}{dt} + \frac{dn_w}{dt}\right] = \frac{1}{n_h + n_w}\frac{dn_h}{dt}$$

where we assume a constant warm plasma component density n_w. The build-up time constant is a linear function of beam current.

$$\frac{1}{\tau} = \frac{I\ell}{eV}\left[(\sigma_i + f\sigma_x)(1 - \alpha) + (\sigma_i + \sigma_x)\alpha\right] - \frac{1 - \alpha}{\tau_L} \qquad (1)$$

where ℓ and V are the plasma diameter and volume, σ_i and σ_x are ionization and charge exchange cross sections. Here $\alpha = n_w/(n_h+n_w)$ is estimated from line density measurements with only the plasma stream to be $\sim$0.2. Equation (1) includes inputs due to ionization on both hot and warm components as well as charge exchange on the warm component. The factor f describes density changes due to changes in angular distribution and is taken to be zero after a beam dominated equilibrium is established. The loss time τ_L includes all losses including coulomb scattering, electron drag, charge exchange on cold gas, scattering due to electric field fluctuations, etc.

$$\tau_L^{-1} = \tau_{coul}^{-1} + \tau_{drag}^{-1} + \tau_{cx}^{-1} + \tau_{wave}^{-1} + \ldots\ldots$$

This lifetime also implicitly includes any residual particle input due to trapping of the streaming plasma by processes other than charge exchange with the neutral beam. One such possible process is trapping of streaming ions which gain energy perpendicular to the magnetic field from r.f. electric fields. However, the data shown in Fig. 1 indicates that the magnitude of such effects is small with respect to the (neutral beam) trapping rate.

In Fig. 3 we have plotted experimental τ^{-1} values, obtained from microwave interferometer measurements, as a function of injected neutral beam current. From equation (1) such plots provide two basic pieces of information: (a) the slope provides an estimate of the hot plasma volume (in this case 6 liters) and (b) the zero current intercept provides the lifetime τ_L (in this case 13 ms). The range of uncertainty of the inter-

cept of the least squares straight line fit to the data points is shown by the standard deviation error bar which indicates a lower limit of 5 ms for τ. As statistically the τ^{-1} intercept could even be positive the upper limit of τ_L in this evaluation is indeterminate.

In Fig. 4, this indeterminacy is indicated by an arrow on the upper end of the error bar. Values of $n\tau$ obtained in this manner at mean plasma energies of 13, 7 and 4 keV are shown as solid circular points in Fig. 4 where $n\tau$ is shown as a function of E_i. A second measurement of τ_L is obtained by switching off the neutral beam input and measuring the plasma density decay rate. Such measurements are shown as open circles in Fig. 4. For comparison a curve is shown, $n\tau = 2 \times 10^9 E_i^{3/2}$. The coefficient of this curve is about a third of that found in Fokker-Planck calculations without the streaming plasma [4]. For a more accurate comparison the Fokker-Planck model is being modified to include the plasma stream.

Fig. 3

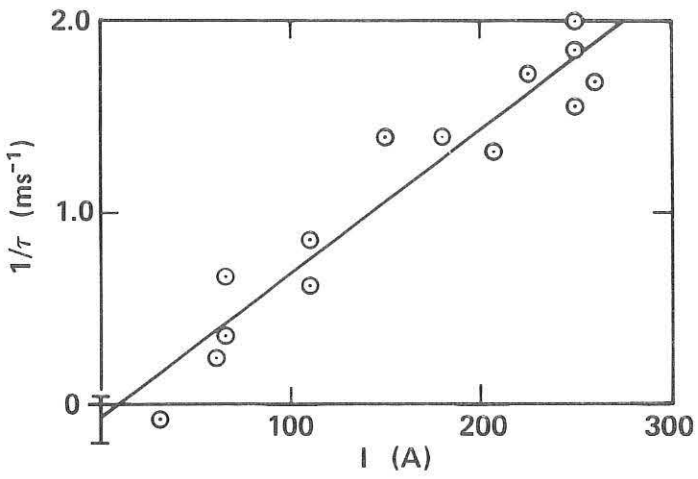

Fig. 4

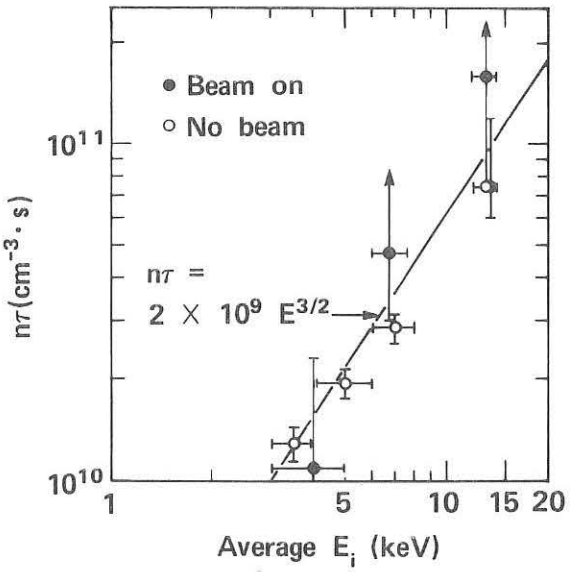

IV. Conclusions. These initial experiments, though somewhat preliminary, do demonstrate several significant points:

- Ion heating up to 13 keV by neutral beam injection
- Plasma betas up to 0.4
- Electron heating with neutral beam injection
- Density build-up to 4×10^{13} cm^{-3} by neutral beam injection
- Reduction in ion cyclotron noise with streaming plasma injection
- Energy scaling, $n\tau$ increasing with energy.

References:

[1] F.H. Coensgen, W.F. Cummins, A.W. Molvik, W.E. Nexsen, T.C. Simonen "Confinement Studies in 2XII", Fifth European Conference on Controlled Fusion and Plasma Physics. (Proc. Conf. Euratom-CEA Grenoble, 1972) 2, 71.

[2] F.H. Coensgen, W.F. Cummins, A.W. Molvik, W.E. Nexsen, Jr., T.C. Simonen, B.W. Stallard, "Plasma Containment in 2XII", IAEA Fifth Conference on Plasma Physics and Controlled Nuclear Fusion (Proc. Conf., Tokyo, 1974)1.

[3] W.R. Baker, K.H. Berkner, W.S. Cooper, K.W. Ehlers, W.B. Kunkel, R.V. Pyle, J.W. Stearns, "Intense-Neutral-Beam Research and Development", IAEA Fifth Conference on Plasma Physics and Controlled Nuclear Fusion, (Proc. Conf., Tokyo, 1974), 1.

[4] A.H. Futch, Jr., J.P. Holdren, J. Killeen, A.A. Mirin, "Multi-Species Fokker-Planck Calculations for D-T and D-He^3 Mirror Reactors, Plasma Physics 14 (1972) 211.

*Work performed under the auspices of the U.S. ERDA.

THE INVESTIGATIONS ON THE POWERFULL ELECTRON BEAM APPLICATION FOR THERMONUCLEAR FUSION INITIATION

L.I.Rudakov, M.V.Babykin

I.V.Kurchatov Institute of Atomic Energy
Moscow, USSR

A B S T R A C T

The problem of the designing of the pulse thermonuclear reactor with triggering by the relativistic electron beam is discussed. It is necessary to produce an energy output $\sim 10^{10}$ joules per one explosion in a reactor with neutron absorbing shell [I] which after evaporation plays also the role of the working gas. If the energy gain will be $\sim 100 \div 1000$ one must have $\gtrsim 10^{7}$ joules in electron beam with pulse duration $50 \div 100$ nsec that may be achived with modern technology. Such beam generator may be built consisting of 60 to 100 modules with 3×10^{12} watt in one module. The elaboration of physical and technical problems may be carried out with one full-size module in the coming 5 years in order to answer the quastion about the possibility of the construction of the test thermonuclear reactor.

I. INTRODUCTION

In the last years more and more attention is devoted to the realization of the pulsed thermonuclear reaction with triggering by the relativistic electron beam which has been suggested by E.K. Zavoisky (USSR) and by F. Winterberg (USA) in 1968. The application of the shell for beam stopping, for the hydrodynamic plasma compression and for slowing of expansion (L.I. Rudakov, 1972 [7]) allow to decrease the critical energy of the initiation and to prolonge the target irradiation time. In view of the relatively large electron penetration ability one has to use the thick shells, such as 0,1-0,3 mm of lead or copper for electron energy from 1 to 3 MeV. The shell which compresses and heats the DT mixture must be accelerated to the velocity more than 150 km/sec for the reaction initiation. Therefore the shell radius must be about 1 cm to use the full energy of the beam with pulse duration near to 50 nsec for the acceleration of the shell. From these conditions one can estimate the shell mass and the acceleration energy which must be from 1 to 3 gramms and from 20 to 30 Megajoules. The fusion energy from such target may be from 10^9 to 10^{10} joules. For the pointed target dimensions the irradiation time corresponds to the pulse time range of the modern accelerators. The producing of the energy up to $2\ 10^7$ joules in the beam is also quite possible at the to-day level of technology.

II. THE REQUIREMENTS TO THE PARAMETERS OF THE FUSION REACTOR WITH TRIGGERING BY AN ELECTRON BEAM

In thermonuclear reactors with external neutron absorbers the fast damage of the vacuum chamber walls will take place if this walls is made from the materials known now. It demands often replacements of the chamber. For example, in the Tokamak reactor the

chamber work period is estimated be equal to three years. It complicates the reactor structure and makes it more expensive.

In the conception of the pulsed fusion reactor which is developed by E.P.Velikhov, V.S.Golubev and V.V.Chernúkha [1] the massive screen shell for the neutron slowing down and absorbing is placed in the capsule structure. This screen after evaporation serves as the working gas in the energy conversion cycle. It let to decrease significantly the radiation damage and the activation of the explosion chamber walls and to prolonge the chamber work period up to 20-30 years that corresponds to usual work period for the electric stations. This blanket must indude the lithium in the sufficient quantity for the tritium breeding. The thickness of the screen must be 20-30 cm or more for the absorption of the main part of the neutron energy.

At the sufficiently big energy of the explosion ($\gtrsim 10^{10}$ joules) the matter of such blanket may be heated up to 10^4 °K that let to use the effective thermodynamical cycles. It let to refuse from the turbine cycle with efficiency not more than 40% and to pass to magnetohydrodynamical methods which gives the power station efficiency up to 70-80%.

The frequency of explosions in one chamber can not be very large. It is limited by processes of preparing the chamber to the next explosion such as the removal the products of the previous explosion, the injection of the target, and the charging of the beam energy storage. It is expected that this time may be drive to 10 sec.

The energy of explosion $\sim 10^{10}$ joules can be confine in the chamber with diameter near to 20÷30 m and weight near to $(0{,}5 \div 1) \times 10^3$ ton which may be create now.

If we assume that the energy gain will be equal to 10^2 or 10^3 then for initiation such explosion it is necessary to have $\gtrsim 10^7$ joules in the electron beam.

III. THE PROBLEM OF THE CONSTRUCTION OF THE ELECTRON BEAM ACCELERATOR WITH ENERGY IN THE BEAM UP TO 10^7-10^8 JOULES

The electron beam accelerator with the total energy in the beam of about $(2\div3)\times10^7$ joules and power up to $(2 \div 3)\times10^{14}$ watts can be imagined for instance as the assembly of several modules located around vacuum chamber, as it is shown on the fig.1, or as the double disk water line with diameter near to 20-30 m or more which generates beam converging to the center of the chamber. In the first case the application of the vacuum line with magnetic insulation for achieving the necessary current and power density is needed. The parameters of the single module are approximately the same as parameters of the existent accelerators and it is necessary to design the sinchronization system only. In time of elaboration of the module variant it is necessary to optimize the parameters of separate modules to recieve the maximum power at the fixed dimensions. The sinchronization problem of the big number of commutation channels takes place in the case of the disk variant also as the commutation of the disk line must be multychannel on principle. At the present time there are not sufficiently big disk lines and therefore it is difficult to estimate the possibility and the difficulties of their construction.

Let us consider the requirements to the diode of the such big accelerator assuming for example the use of the disk type line. At output voltage equal to 3 MV the current must be from 70 to 100 Ma.

It is known that the diode current may not exceed some critical value

$$I \approx 10^4 \frac{R}{d} \gamma.$$

Here R is the radius of the cathode, d is the distance between anode and cathode, γ is the relativity factor. One can define the ratio R/d or R from this relation if the d value is chosen. At $d=1$ cm the current equal to 70 Ma can be obtained with radius R near to 10m that corresponds to explosion chamber radius needed for the necessary explosion power.

It is evident that in the module variant in which the input beam splits will be located alonge the equator of the chamber the necessary chamber diameter must be approximately the same as for the disk line. If accelerator with power equal to 3×10^{12} watts is chosen as a module it is necessary from 60 to 100 such modules for the total power equal to $(2\div3)\times10^{14}$ watts. The power equal to 3×10^{12} watts may be obtained in the water line with the 3 ohm impedance at diameter near to 1,5÷2 m and with electric field between 100 and 150 kv/cm. In order to use the volume more effectively these modules may be located in two or three storey parallel to the equtorial plane of the chamber. In this case the energy supply to the diodes which is located just in the equtorial plane may be realized by the vacuum lines with magnetic insulation. These lines play double role, firstly, they allow to increase the energy flow density, secondly, due to their small dimensions they allow to bring the energy of all modules to one plane where all sections of the high voltage diode is located.

On the way to the creation of the powerful accelerators with $10^7\div10^8$ joules in the beam and on the way of their application for the triggering of the pulsed thermonuclear reaction many physical and technical problems must be solved. From technical problems here must be mentioned the problems of the sinchronization of multy-

channel commutation and the injection of the beam into explosion chamber in particular the elaboration of the protection of the inlet window and the foil replacement or the elaboration so called, "without an anode" beam inlet trough the open hole with the appropriate differential pumping out of the diode.

The main physical problems are the beam transportation to the center of the vacuum chamber through the distance near to 5 or 10 m and the problem of the effective homogeneous irradiation of the thermonuclear target. The problem of the beam transportation one can try to solve with the application of the magnetic guiding field and with the gas filling of the chamber for the electric and magnetic neutralization of the beam [2] . As a guiding field one can use the cusped magnetic field, the field of two coils with opposite directions of currents. During the explosion ard expansion of the target this field may be used for MHD cycle of the conversion of the explosion energy to the electric energy.

In the case of the module scheme of the accelerator one can elaborate all technical and some physical problems with one separate module in real scale, in particular it is possible to model the all-round irradiation of the target in the vacuum chamber inside of the ring high voltage diode (the scheme of such experiments is shown on fig.2).

IV. EXPERIMENTAL INVESTIGATIONS.

For the study of the problems of the creation of powerful beams the problems of beam transportation and irradiation of targets the Angara-1 accelerator (fig.3) was built at the Kurchatov Institute of Atomic Energy. The energy of electrons must be 2,5 MeV, the beam current will be near to 400 ka and pulse duration is equal to 60 nsec.

This accelerator has the single water line devided on three stages. The first stage of the line is charged from the separate Marx generator which works in the air and can generate the voltage up to 2MV with total energy in pulse up to 150 kilojoules. The first stage of the line has external diameter of 1,8m, length of 1,2 m and impedance of 1,5 ohm. It plays a role of the intermediate energy storage which is charged up to 2,8-2,9 MV. After the selfbreakdown of the first gas switch the first stage forms the pulse with amplitude up to 1,3-1,4 MV and the front time near to 50-60 nsec. The second stage has the same impedance 1,5 ohm, the length equal to 1 m and the diameter equal to 1,1 m. Between the second stage and the third one the sharpening gas switch with the ring electrode is placed. The diameter of these electrodes is 0,3m, the gap between them is 6 cm and the gas pressure may approach to 10-15 atmosphers. In this switch several sparks have to develope [3].

The third stage is the transformer line. It is 3 m long and 0,7 m in diameter. The impedance of this line changes from 1,5 ohm to 6 ohm (the transformation factor is equal to 2). The whole length of the accelerator is about 7 m.

The installation Angara-1 began work from february 1975. In the experiments at electrone energy equal to 1 MeV and the current equal to 150 ka with the graphite cathode of 80 mm in diameter the selffocusing of the beam in the diode down to 5 mm in diameter was observed. The photograph of the beam made in X-rays by the pin hole camera is shown on fig.4. The pin hole camera was placed behind the thick (5mm) stainless steel anode. The spall with diameter of 7-8 mm is observed on the back side of the anode.

The form of the voltage pulse after the multychannel sharpening switch is shown on fig.5. The pulse has the form near to the rectangular form. The front of the pulse is 30 nsec, the plateau is 40 nsec, and the fall down time is 30 nsec.

The producing of necessary power density demands increasing electrical strength of lines. Some hopes in this direction are connected with the magnetic insulation [4,5] . Experimental investigations of the magnetic insulation have been fulfilled at MS accelerator. The voltage pulse with amplitude up to 400kV was transmitted to the cathode of the diode through the piece of the vacuum coaxial line. It was shown that electric field in vacuum line overcomes breakdown value if the magnetic field of diode current is higher than limiting level. In this conditions the line input current is equal to the anode current and it is the evidence of the absence of breakdown. The electric field up to 2.5 MV/cm and power flow density about 10^{10} watt/cm^2 have been registered in the coaxial gap equal to 2 mm with pulse duration of 50 nsec.

Regimes of the selffocusing of high current beams in diodes were investigated on a number of small scale devices with low impedance forming lines ($\sim$2,5 ohm). The cathodes that were used were either polyethylen cones (Triton device) or thin metallic needles (Ural device). In the first case the beam current density approached to 5 Ma/cm^2 due to preliminary injection of a plasma in the diode (total current of 200 ka). The current density up to 30 Ma/cm^2 with total current equal to 90 ka and power flow density of 5×10^{12} watt/cm^2 [6] have been obtained on the Ural accelerator without preliminary injection of a plasma in the diode. The time measurements of X-rays which were fulfilled with a collimator and without it gave the possibility to define the moment of the focusing and its duration which is equal to 35 nsec. Besides, time variation of X-ray energy have been investigated by means of absorbers located before X-ray scintillation detectors with a time resolution $\lesssim 5$ nsec. The results show that the effective electron energy corresponding to focusing time interval

differs not much from the accelerating voltage at that moment.

V. CONCLUSION

In this paper the problem of the creation of the pulsed fusion reactor was considered from the point of view of the thermonuclear reaction initiation feasibility. The realization of this task seems to be real now. However for this purpose it is necessary to solve a number of complex physical and technical problems. Intensive theoretical and numerical calculations have to be performed to optimize the structure and parameters of the target, to elaborate the methodes of transformation of the thermal energy into electricity, to study problems of a fabrication DT target and the lithium absorbing shell for the tritium breeding and other problems.

The module scheme of the accelerator for the irradiation of the thermonuclear target allow to fulfill the elaboration of all technical solutions and some physical tasks by one separate full-size module. The elaboration of the structure of one module and the modelling of the physical processes of a beam transportation and a target irradiation will allow to come up to answer the question concerning the feasibility of the fusion reactor with triggering by relativistic electron beam and to put up the question about building the demonstrative fusion reactor.

In conclusion we express with plesure our gratitude to E.P.Velikhov, A.M.Pasechnikov, V.P.Smirnov, E.Z.Tarumov, and V.V.Chernukha with which we work at I.V.Kurchatov Institute on investigation of the described problems.

REFERENCES

I. E.P.Velikhov, B.S.Golubev, B.B.Chernukha. Atomnaja energia, v. 36, No 4, 258 (I974). Nuclear Fusion Special Suppl., I974, p. 235.

2. M.V.Babykin, E.K.Zavoisky, A.A.Ivanov, L.I.Rudakov "Plasma Physics and Controlled Nuclear Fusion Research", IAEA, Vienna, I97I, p. 635.

3. I.P.Afonin, M.V.Babykin, A.V.Bartov. Pribory e technica experimenta. I97I, N 2, p. I38.

4. A.V.Gordeev et al. Report on the Conf. on Electrostatic and Electromagnetic Confinement of Plasmas and Phenomenology in the Relativistic Electron Beams. New York, March I974.

5. B.Bernstein, I.Smith. IEEE Trans.on Nucl.Sci. NS-20, 294 (I973).

6. Yu.V.Koba et al. 5th Int.Conf. on Plasma Phisics. Report IAEA-CN-33/F2-I, Tokio, Japan, Nov. IO-I5, I974.

7. L.I.Rudakov, A.A.Samarsky. Proc. 6th European Conference on Plasma Physics. Moscow. July I973, p. 487.

FIGURE CAPTIONS

Fig.1. The scheme of the pulsed fusion reactor with triggering by the electron beam.

The modules of the electron beam generator are charged from pulsed voltage generators or from inductive storages. The beam are injected into the steel explosion chamber through the narrow splits along the equator of the chamber. For the prevention of the possible leakage of electrons and for the lightening of beam transportation to the target the magnetic field from 5 to 10 kilogauss is used generated by two coils with the currents flowing in opposite directions. This magnetic field may be used also as the element of the inductive MHD generators. The target in common with the blanket included lithium are injected into the explosion chamber by means of special device. The neutrons are slowing down and are absorbed in lithium, they reproduce the tritium and heat the working gas (lithium) up to temperatures equal to 10^4 °K.

Fig.2. The scheme of the diode modelling the all-round irradiation of a target.

Fig.3. The scheme of the Angara-1 accelerator.

Fig.4. The photograph of the beam in X-rays, obtained by pin hole camera with the hole diameter equal to 1 mm. The diameter of the beam is 4÷5 mm.

Fig.5. The voltage pulse, registered after the sharpening switch with ring electrods (pulse inputed into transformer line). The pulse front is 30 nsec, the amplitude is 0,5 MV.

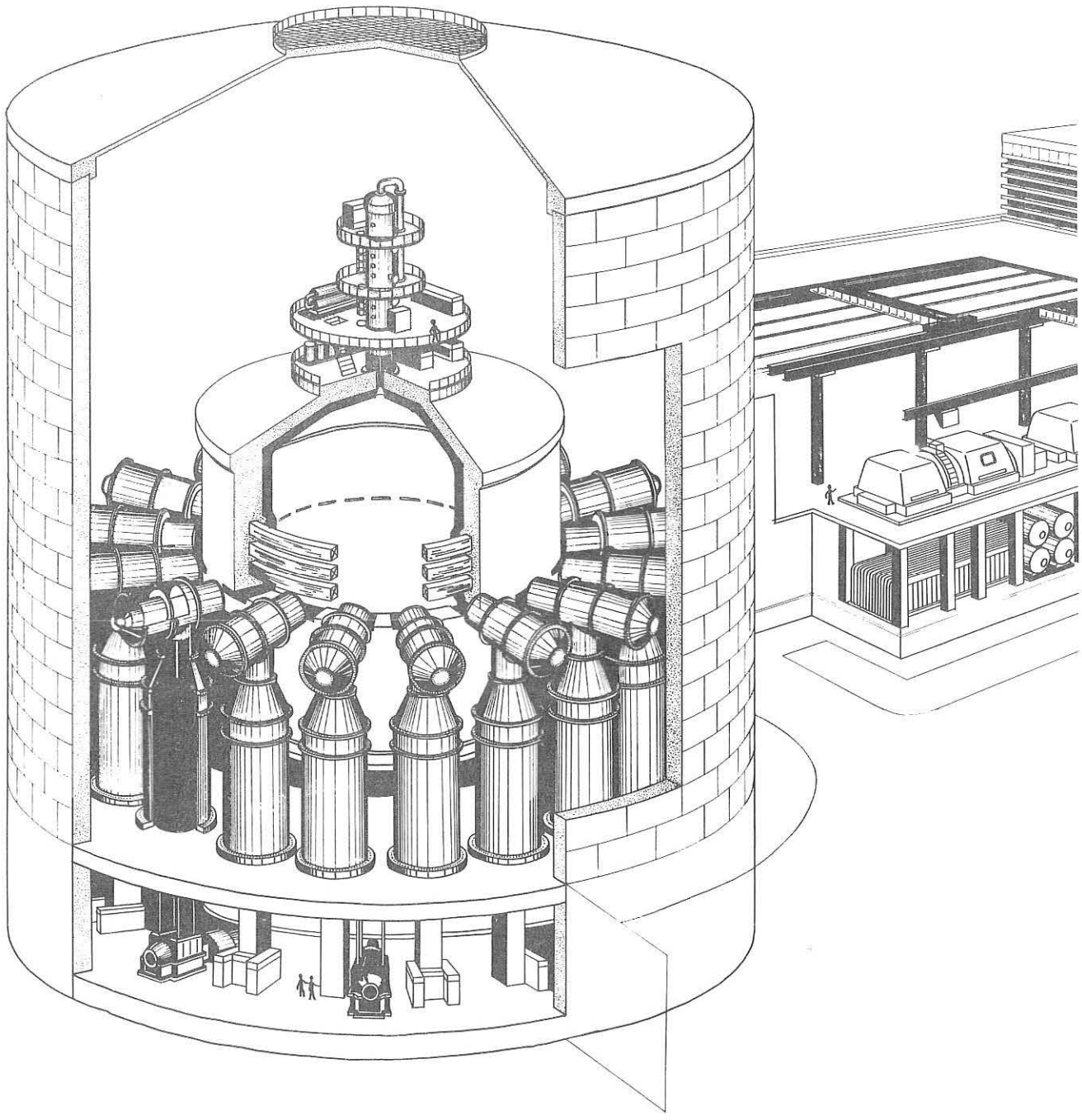

Figure 1

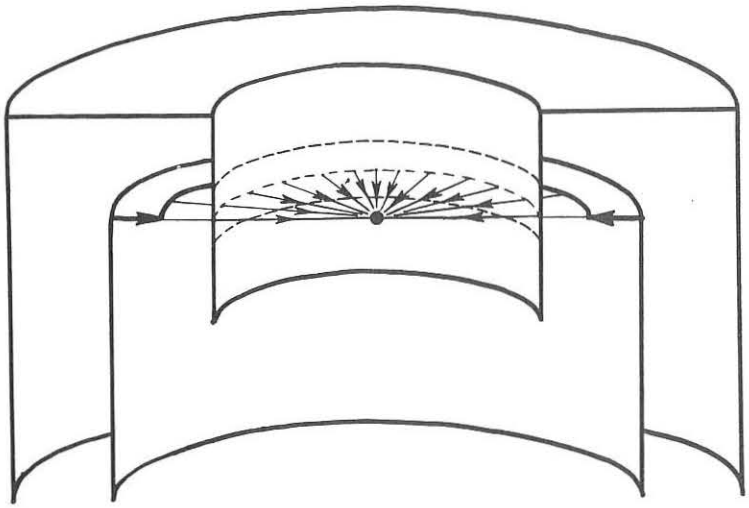

Figure 2

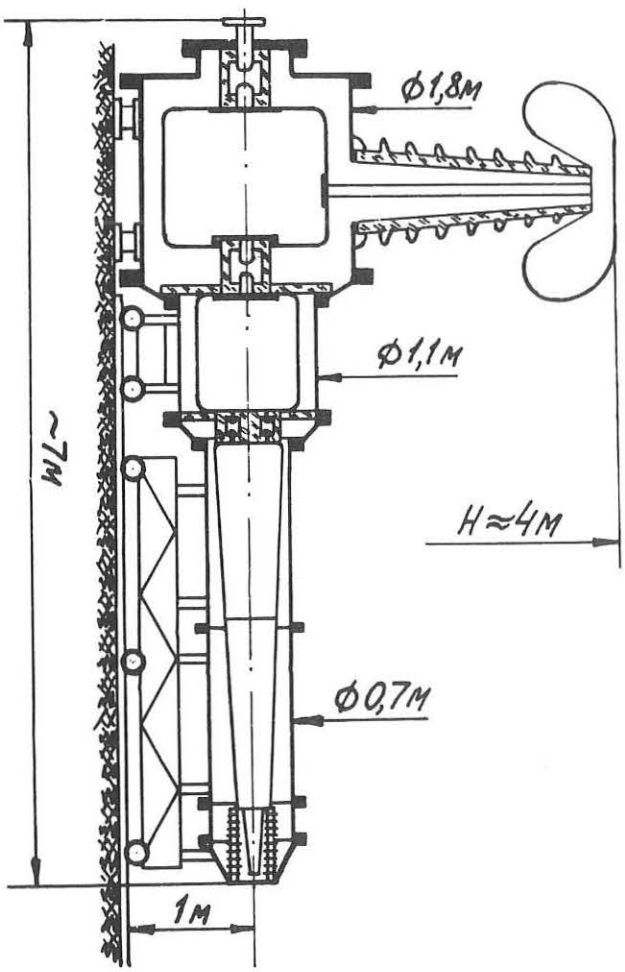

Figure 3

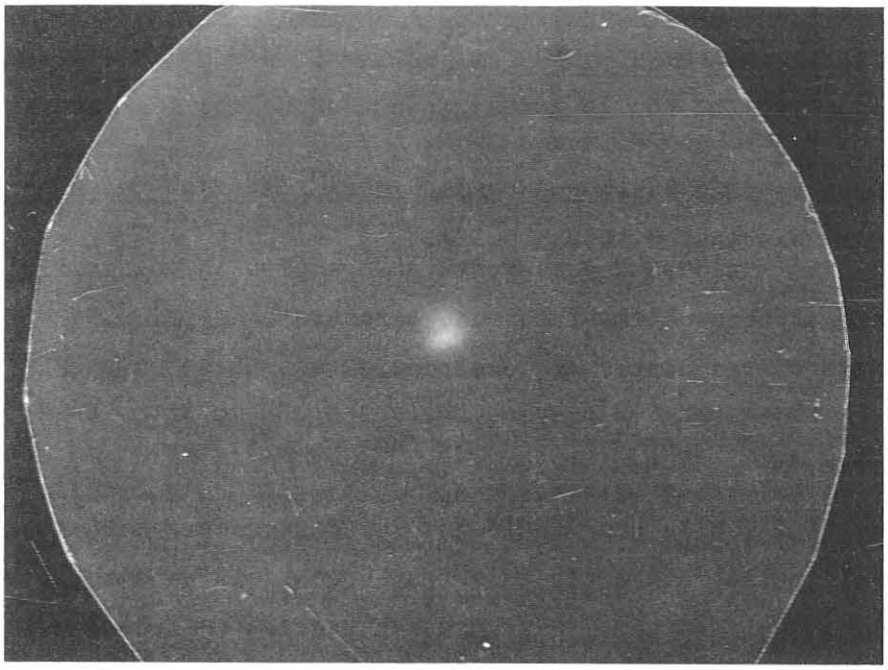

Figure 4

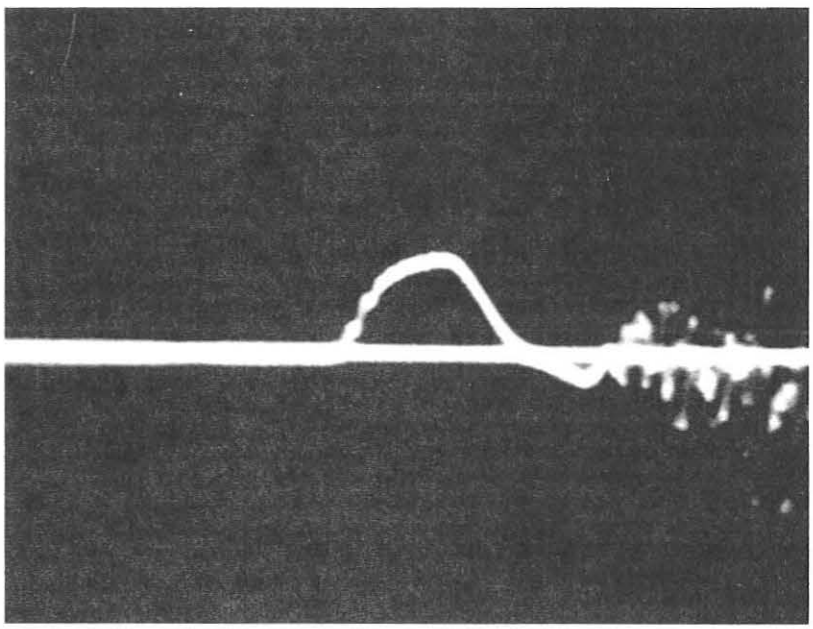

Figure 5

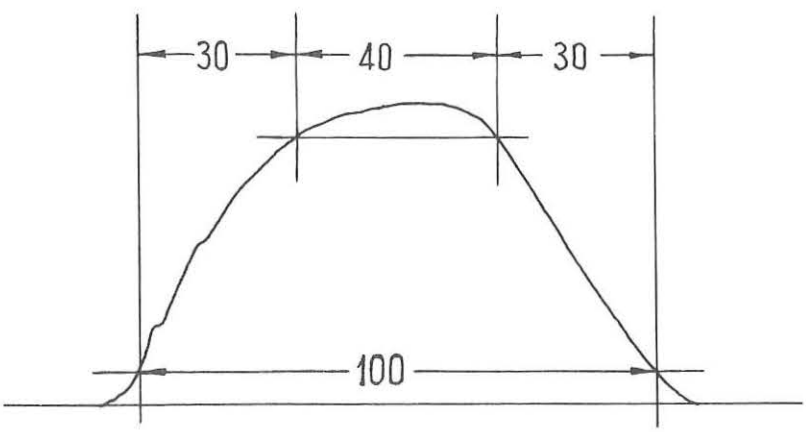

OVERVIEW OF ENERGY RESEARCH AND DEVELOPMENT ADMINISTRATION INERTIAL CONFINEMENT FUSION PROGRAM

Glenn W. Kuswa
Energy Research and Development Administration
Washington, D.C. U.S.A.

Abstract: The basic aspects of the laser and particle beam induced fusion program in the United States are outlined.

Introduction

The goal of the inertial fusion program is to produce a thermonuclear burn in a small yield pellet and apply this result to civilian energy needs and to research applications. Our research program includes two main-line approaches to accomplishing inertially confined fusion, and several unorthodox approaches are also being considered. All approaches seek to symmetrically drive a spherical shell of material toward its center, thereby compressing, heating, and containing the fusile material within so that more energy is yielded than was expended.

One means employed is to apply a laser pulse to the surface of a sphere in as uniform a manner as possible and with as short a wavelength as practicable. Neodymium glass systems are most commonly used for this class of experiments, and other possible superior lasers are under development. The second approach is to employ powerful electron beams to deposit their energy in the outer regions of targets to be imploded, and is attractive because of the great efficiency available from a beam device (~50%). The unorthodox approaches are various variations for using ion pulses to implode pellets, and if adequate ion beam generators can be developed it is an extremely promising approach because of the favorable energy deposition properties of ions.

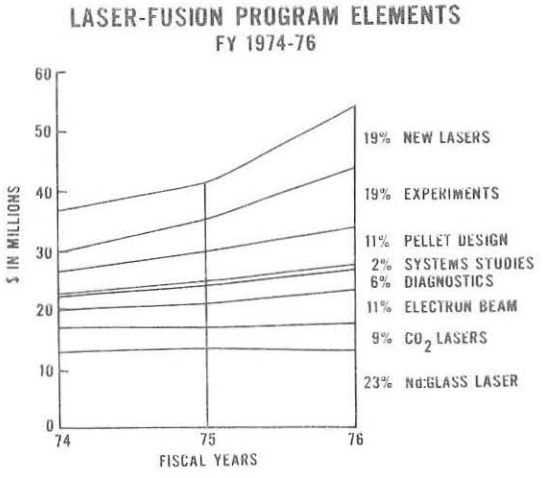

Before we describe the basic technical features of our program it is instructive to examine the program funding broken down by the budget catagories which describe the program.

The program office in Washington is very small and gives the maximum possible freedom to the ERDA laboratories to manage their own programs. The over-all philosophy is expressed by the following table.

A Balanced National Laser-Fusion Program Involves:

Utilization of Unique ERDA Laboratory Expertise

- Over 20 years Experience with TN Burn
- Experimental Diagnostic Base
- Large Computers
- Sophisticated Codes
- Management of Large Applied Science R&D Endeavors

Utilization of Industrial and University Expertise

- Laser and Optical Development
- Industrial Research Capability
- More Ideas Stimulated and Incoporated
- Fabrication Technology for Hardware and Diagnostics

Development of Capability that Extends Program

- Development Pool of Trained Experts
- Preparation by Partnership for Eventual Industrial Takeover

The major projects supported by the ERDA program and their respective managers are listed in references 1-6. In addition, some seventy smaller research contracts are planned or awarded in support of program goals. It is instructive to examine the fusion power decision tree below, which shows the schedule for making major decisions (diamonds) for starting activities or construction, and the estimated useful life of the facilities. The more distant decisons are subject to change, and the entire program is under continuing review.

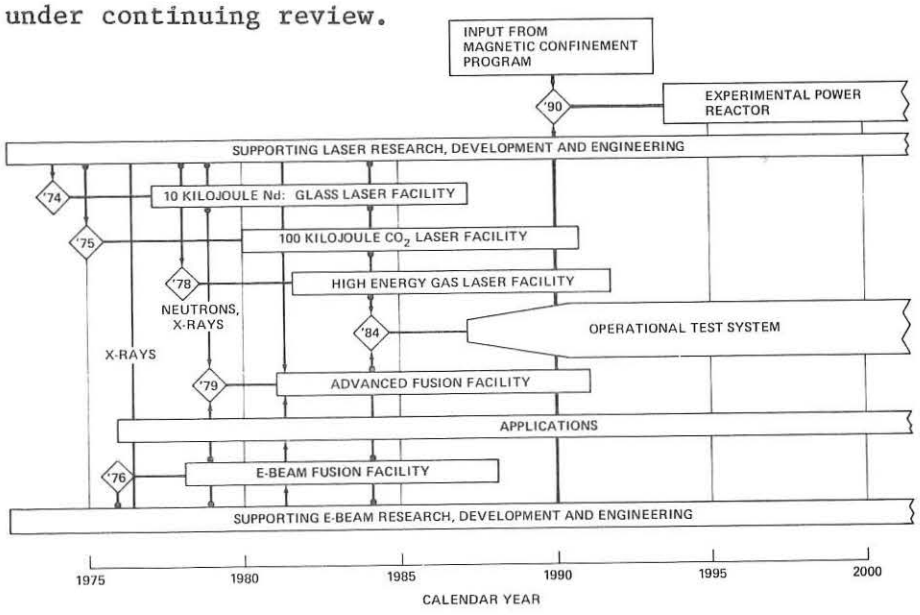

I. Nd: Glass Laser Research [7]

There are problems which limit the uniform power density which can be placed on a target, which is the ultimate measure of a fusion laser's usefulness. Nevertheless, glass systems are the present work horses of the laser fusion effort.

Oscillators are designed to produce a series of mode locked pulses, one of which is switched out by means of an electro-optical shutter which is triggered by the first sufficiently large pulse of the mode locked train. Mode locked pulses may be varied by changing dye concentration, cavity size, or etalons within the oscillator cavity. In addition, one pulse may be split into many beams and passed through a series of delay legs with various absorbing filters, and then recombined to form a tailored pulse. Since the resulting series of pulses carries coherent phase information, adjacent pulses may interfere, resulting in a rather "rough" effective wavefront on target. The effect of this is not fully known. Alternatively a pulse may be smoothly tailored by passing it through a series of bleachable absorbers of varying thickness and concentration, or by using active optical elements. In general, oscillators are one of the more erratic components of a system and extreme care must be used to preserve any measure of reproducibility.

The pulse from the oscillator is amplified in a series of increasingly large aperture amplifiers. Between stages either the natural beam divergence or expanding telescopes are used to increase the beam diameter. This is necessary so the damage thresholds and limits imposed by non-linear optical effects are not exceeded. Soft apertures designed to optimally shape the beam spatial intensity profile and reduce the effect of high spatial frequency "hot spots" are used in some systems, while others rely on large interstage separation to accomplish similar results. Spatial filters are also used to maintain high beam quality.

Saturable absorbers and/or additional electro-optic shutters are required to prevent prepulses from the oscillator and rod fluorescence from altering the target before the main pulse arrives. In addition Faraday rotators are used to prevent back-reflected light from re-entering the optical train and destroying the early stages after amplification in the final stages.

Frequently discs are used in the final stages. The critical parameter is the B integral in the optical medium, where ℓ = length, and I = intensity.

$$B = C\int I d\ell \quad , \; C = .024 \text{ cm/GW for ED-2 glass}$$

When B>3-10, the beam will abruptly go unstable and be transformed into a few filaments of excessive energy density due to the beam induced non-linear refractive index; this may destroy the optical components or cause the beam intensity on the target to drop at peak laser intensity.

Improved optical materials are expected to permit a two fold increase in power density. The advantage of disc systems is that the glass can be more highly doped with neodymium than a rod and still be uniformly pumped. With higher gains, less glass can be used in the optical train and the beam will be more focusable. Lenses and windows must be also treated as non linear elements, and typically contribute about 30% to the B integral.

To reduce the lossy effects of refraction of light incident non-radially on spherical targets, large aperture specialized mirror systems have been designed. As more beams become available it will be possible to uniformly flood spheres with nearly normal light rays without using the special mirror systems, but fairly elaborate pointing and tracking apparatus will be required to keep all beams on target. The Shiva system under construction at LLL will yeild subnanosecond 10 kilojoule pulses with 20 beams.

II. CO_2 Laser Program [8]

Gas lasers offer advantages of faster repitition rates, adjustable laser medium parameters, and non-damagable laser media. In addition the CO_2 system and certain other gas systems are more efficient than Nd:glass systems. The penalty paid for these advantages is increased complexity, and in the case of CO_2, a wavelength which is harder to handle with optical components and possibly less desirable for producing implosions at a given light energy.

The CO_2 program at Los Alamos uses a broad area electron beam from a cold cathode to continually ionize the lasing medium during the pumping pulse. A thin foil separates the electron gun at high vacuum from the lasing medium at $\sim$1 atm. A discharge is also passed through the medium, and potentials and pressures are adjusted to avoid avalanching into the arc mode. In this manner the medium is uniformly pumped over a large percentage of the active volume.

Since CO_2 lases on a number of discrete lines spanning a 2000Å region of the spectrum, and the cross relaxation times are of the order of one nanosecond under typical conditons, a multiline oscillator must be used to obtain efficient nanosecond energy extraction. Using a single-line oscillator only the energy partitioned in the oscillator line and its nearest neighbors is extracted. Multiline oscillators have been demonstrated and work continues to improve their reliability. Another important task is to further develop saturable absorbers and inexpensive Faraday rotators for CO_2 wavelengths (10.6 microns). Both mixtures of bleachable gases with the laser medium and the incorporation of separate gas cells in the laser system are being studied. The CO_2 system planned for construction will yield 100 kilojoules in a one nanosecond pulse.

III. Electron Beam Induced Fusion [9]

The electron beam fusion program is the most recent, arising from the growing realization after 1970 that highly concentrated electron beams can be produced and directed onto a target. Since large electron beam accelerators already existed for weapons effects simulation, progress has been quite rapid.

Electron beam accelerators are based upon straightforeword principles. Energy is stored by charging capacitors in a Marx generator. This energy can be transferred in $\sim$.5μsec (by triggering switches which effectively connect these capicators in series) into an intermediate pulse forming line. This line is designed to discharge its energy into the diode in 20-100 nanoseconds upon closure of a low inductance switch. Diodes consist of a field emission cathode (frequently graphite surfaces) and a nearby anode plane containing the target. During the past two years it has been demonstrated experimentally and modeled numerically to show that the pinching beam acts much as a hot electron gas would, and can

deposit kilojoules of energy with a uniformity of $\pm$10% over a spherical target mounted to the anode plane on a stalk. Two-sided irradiation will considerably improve this uniformity. More detail is presented in a paper at this conference by M. Widner. Low jitter, low inductance switching technology required for simultaneously charging transmission lines and connecting them to the diode now exist as prototypes. The development of improved low inductance interfaces between the energy storage network and the diode electrodes is one of the most important and difficult problems. Limitations on power density flowing across insulators makes it necessary to design diodes of larger diameter to accomodate larger insulators. To maintain low inductance the cathode must be of large diameter. The pinch formation times for beams from large diameter cathodes is not presently known and experiments are currently underway to study this problem. It may be necessary to preintroduce plasma into the diode to speed formation of the pinch.

The currently planned electron beam fusion accelerator at Sandia Labs will operate at powers of 4×10^{13} watts with beams incident on the target from both sides. Investigation of ion beam generation and focusing is part of the electron beam program. The space charge created by intense electron flows can give rise to very large electric fields which can accelerate ion currents comparable to the primary electron current.

IV. Diagnostics for Electron Beam and Laser Fusion [7, 8, 9, 10]

Electron beam devices operate at $\sim$1 MeV into high -z targets and consequently produce large x ray yields. Pin hole cameras and various x-ray detectors viewing the anode plane and target through collimators are used to estimate the uniformity of illumination on target and determine the beam pinching dynamics. To examine the collaspse phase of electron beam targets after the electron beam pulse is over a method has been devised to permit taking shadow x-ray pictures of the target. A relatively weak flash x-ray machine is pulsed at the desired time and a specially designed camera with a high on/off sensitivity ratio is simultaneously gated on to record the shadow image of the collapsing pellet at times when plasma and

vapor completely obscure the field of view from optical diagnositcs. Optical diagnostics have also been useful in the beam fusion program. A velocity interferometer used to monitor the rear suface of targets yields information on the arrival of shock waves and the breakup of target material into small segments. The latter effect is important because wall breakup may contaminate the thermonuclear fuel and prevent burn in later experiments. Optical holography of plasma evolution in diodes has been instrumental in improving computer simulation. A new system takes a series of 3 ns "snaphots" spaced by $\sim$10 ns and allows complete separation of each image thus obtained.

The diagnostics used for laser fusion include the familiar Faraday cups, particle spectrometers, calorimeters and impulse measuring probes, which are all used to measure the pellet energy inventory. The fraction of laser energy which couples into fast ions is particularly important because ions in the supra-kilovolt and above region carry away large amounts of energy without imparting a sigificant share of momentum to the imploding shell. In addition fast ions may contribute to neutron counts and cause erroneous interpretation of experiments. Recently with the advent of neutron production from pellets it has become possible to measure alpha particle energies from the T(d,n) He_4 reaction. The measured energy spread reflects the fuel temperature and the thickness of the pellet wall during the time of the reaction. The temperature of the pellet changes the stopping power so that interpretation is complicated. Both KMS Fusion in cooperation with the group at Los Alamos, and the group at LLL are using alpha measurements to interpret their respective neutron results.

Both light and x-ray streak cameras are essential diagnostic tools for implosion studies. Picosecond light cameras exist, but there are difficulties in reliably producing stable photocathodes sensitive in the 1.06 micron region. The time resolution of x-ray streak tubes has been limited to a great extent by the angular dispersion of photoelectrons from the cathode. It is expected that a specially designed image tube incorporating a means for reducing angular dispersion will yield <5 ns resolution for x ray pulses.

An important additional diagnostic will be the improved grazing incidence x ray microscope. Using technqiues developed for solar x ray studies, these instruments will collect and focus 3 orders of magnitude more photon intensity than equivalently resolving pin holes. These units will be coupled to streak cameras, and projected resolutions extend below 5 picoseconds and 2 microns.

V. Systems Studies [7, 8, 9]

Systems studies have been undertaken to examine the critical factors in utilizing laser fusion for power production. Parameters such as pellet gain, laser efficiency, laser energy, repitition rate, required wall life, pellet costs, radiation damage, and many others are included in such studies. The result of one such study is the figure shown below which shows how laser efficiency governs the economics of a power plant incorporating various fission energy multiplicaton options and different percentages of recirculating power. The trajectory on the graph shows the expected evolution of the laser fusion concept using inefficient lasers and high fission multiplication to an eventual pure fusion device employing so far unidentified lasers.

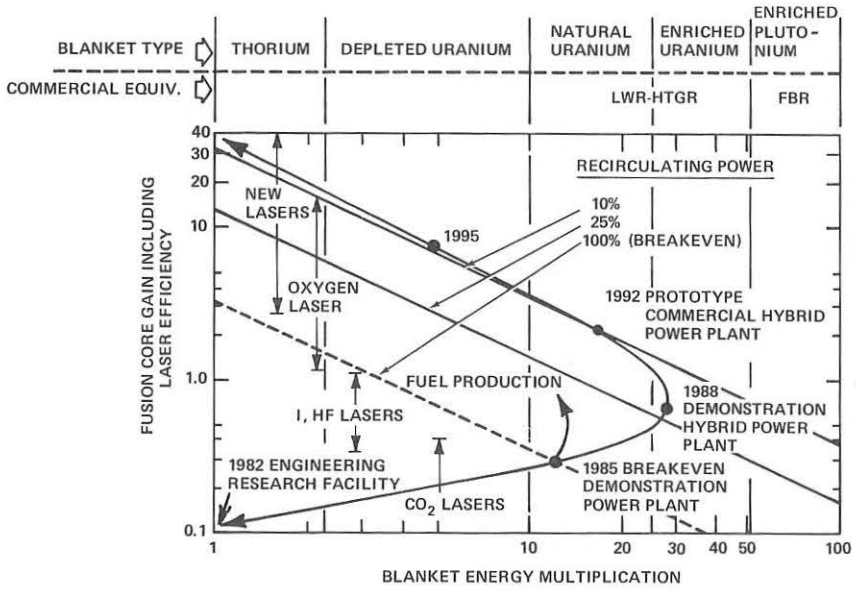

Pellet Fabrication [7, 8]

The present generation of fusion pellets is designed to study implosion physics and may not bear much similarity to the pellets which we hope someday to use in power plants. Presently most pellets are selected from miniature glass spheres manufactured in carload lots as plastic filler material. The selection is accomplished by screening, flotation and application of "crushing" pressure to select the proper outside diameter, wall thickness, and uniformity, respectively. Wall uniformity is measured by light interface methods or by x-radiography. Filling is accomplished by diffusion of D and T through the walls at temperatures just below the glass softening point. Upon cooling the pellets remain filled for weeks. Measuring the fill can be done by destructive testing or by measuring the x-rays produced by tritium beta particles interacting with the pellet walls.

Ultimately liquid or frozen drops are expected to be used for fuel. They can be generated by forcing the liquid fuel through a nozzle which is vibrated, and can be accurately accelerated and aimed by electrostatic means. Present generation electron beam targets are simple gold shells slightly thicker than an electron range.

New Lasers [9, 8, 7]

The search for fusion laser systems is directed toward identifying a medium which is approximately 10% efficient, emits in the visible region, and can be scaled to yield hundreds of kilojoules in the nanosecond regime at a repitition rate of 100 hertz. Certainly there will be less ambitious developments on the learning path, and interaction experiments for the next few years will be performed with glass and CO_2 systems. Some systems under investigation are outlined in terms of main features.

Iodine (1.3 microns) is excited by flash photolysis and has been demonstrated at the 1 ns 300 joule level by the Garching group with efficiency of .3-.5%. The present U.S. effort seeks to improve flash lamp efficiency in a prototype expected to operate at the~100 joule~1% efficient level, and a 1 kilojoule facility is being considered.

HF lasers are being investigated in a collaborative Sandia-Los Alamos effort. Five kilojoule 26 nanosecond pulses of apparently high beam quality 3 micron light have been produced by initiating a mixture of F_2, O_2, H_2, and SF_6 in a solenoidal magnetic field. The field was used to guide an intitiating 2 MeV 50 kamp electron beam into the gas. In terms of chemical energy this system was 3% efficient.

Other lasers such as the rare gas excimer systems are under investigation. These system have the potential for fusion applications, but are not presently well enough understood to consider scaling.

Interaction Studies [7, 8, 9, 10]

Interaction experiments are being pursued at a fundamental level to study plasma physics, diagnostics, heat conduction, effect of prepulse, and other parameters. Of greater note in the news, there have been a number of reports of neutron production in compressed pellets, which we hope but are not presently certain will prove to be of truly thermonuclear origin. Since these experiments are certain to be covered in other papers at this meeting we conclude with a comment that enough basic physics remains to be learned that small efforts are as important to progress as are the large interaction programs. ERDA policy reflects this view in its support of many university and industrial research and development efforts.

REFERENCES

1. Glass systems - Lawrence Livermore Laboratories, Livermore, California (Dr. John Emmett)
2. CO_2 lasers - Los Alamos Scientific Laboratories, Los Alamos, New Mexico (Dr. Keith Boyer)
3. Electron beam fusion - Sandia Laboratories, Albuquerque, New Mexico (Dr. Everet Beckner)
4. KMS Fusion, Incorporated, Ann Arbor, Michigan (Dr. Henry Gomberg)
5. U.S. Government partnership with University of Rochester and industrial participants, Rochester, New York (Dr. M. Lubin) (At the time of writing this proposed effort was being negotiated.
6. Glass Laser - Matter Interaction Studies, Naval Research Laboratory, Washington, D.C. (Dr. S. Bodner)
7. Annual Report 1974, Lawrence Livermore Laboratories, Livermore, California report UCRL-50021-74
8. Semiannual Report LASER Program July 1 - December 31, 1974 Los Alamos Scientific Laboratories, Los Alamos, New Mexico report LA5019-PR
9. Laser-Fusion and Electron-Beam-Fusion Research Progress Report, Sandia Laboratories, Albuquerque, New Mexico, SAND 74-0439.
10. Laser Fusion Studies at NRL, Naval Research Laboratory Washington D.C. Report 7838, October 1974.

HYDRODYNAMICS AND COMPRESSION OF A LASER IRRADIATED TARGET

J.L. BOBIN - J.M. REISSE

C.E.L. - B.P. N° 27 - 94190 Villeneuve-St-Georges
(France)

ABSTRACT

In order to match fusion energy balance requirements, the target should be compressed isentropically. The efficiency of the process is investigated. In order to deal with limited energy lasers, similarity laws are emphasized and the energetics for small targets are evaluated.

1/-SCOPE

The principle of pellet compression by a high power laser in order to achieve a significant thermonuclear burn is now theoretically firmly established. No doubt that provided sufficiently energetic lasers with suitably tailored pulse shapes are built, breakeven conditions will be eventually achieved. It looks very likely a long and costly endeavour. Accordingly, it is of interest to investigate how smaller scale experiments might yield intermediate milestones. A first attempt has been made mainly by KMS Fusion irradiating DT filled glass microballon with a Nd laser in the 100 joules range. However, the final density of the thermonuclear fuel is of the order of solid state although the compression ratio is high /1/ .

It is the purpose of the present paper to show how, starting from analytical theories, similarity laws may help the design of experiments in which the laser energy and power are limited and the target is initialy in the solid state.

2/- ISENTROPIC COMPRESSION

Following KIDDER /2/ we use a lagrangian formulation to investigate the dynamics of a homogeneous isentropic compression process : every fluid element has the same time history. Let then h(t) be a dimension-less function of time only. In a one dimensional situation the coordinate is :

$$r(r_0,t) = h(t) r_0 \tag{2-1}$$

and the particle velocity is :

$$u(r_0,t) = \frac{\partial r}{\partial t} = r_0 \frac{dh}{dt} . \tag{2-2}$$

Let $\nu = 1, 2$ or 3 be the exponent characteristic of the plane, cylindrical or spherical geometry respectively. The gas dynamical equations then read with obvious notations.

$$\begin{cases} dm = \rho r^{\nu-1} dr = ct = \rho_0 r_0^{\nu-1} dr_0 = dm_0 \\ \dfrac{du}{dt} = -r^{\nu-1}\left(\dfrac{dp}{dm}\right) \\ p(r_0,t)\,\rho^{-\gamma}(r_0,t) = p_0(r_0,0)\,\rho_0^{-\gamma}(r_0,0). \end{cases} \tag{2-3}$$

By combining these equations one gets :

$$h^{\nu\gamma-(\nu-1)} \frac{d^2h}{dt^2} = -\frac{1}{\rho_0 r_0} \frac{dp_0}{dr_0} . \tag{2-4}$$

Since r_o and t are independant lagrangian variables, both sides should be equal to one and the same constant whose dimension is the reciprocal of a time squared : $-1/t_o^2$ say. The temporal part is then integrated once with the boundary condition $h(o) = 1$, hence the first order differential equation :

$$\frac{t_0\sqrt{2\mu}\; h^{\mu}\, dh}{\sqrt{2 + (a-2)\, h^{2\mu+1}}} = -\, dt \tag{2-5}$$

where $\mu = \frac{\nu}{2}(\gamma - 1)$ and $q = \frac{\nu}{2}(\gamma - 1)\, t_0^2 \left(\frac{dh}{dt}\right)_0^2$.

In the case $q = 2$, the solution does not depend on γ and reads

$$h = \left(1 - \frac{\mu+1}{\sqrt{\mu}}\,\frac{t}{t_0}\right)^{\frac{1}{\mu+1}}. \tag{2-6}$$

Hence the applied pressure at the external boundary ($r = R$)

$$p(R,t) = p(R,0)\left(1 - \frac{\mu+1}{\sqrt{\mu}}\,\frac{t}{t_0}\right)^{-\frac{\nu\gamma}{\mu+1}} \tag{2-7}$$

with for
- $\nu = 3$ (sphere) $\quad \frac{\nu\gamma}{\mu+1} = \frac{6\gamma}{3\gamma-1}$,
- $\nu = 2$ (cylinder) $\quad \frac{\nu\gamma}{\mu+1} = 2$,
- $\nu = 1$ (plane) $\quad \frac{\nu\gamma}{\mu+1} = \frac{2\gamma}{\gamma+1}$.

The last value can also be obtained using Stanyukovich's analysis of converging characteristics /3/.

If one has $q \neq 2$, an analytical solution can be obtained only for special values of γ

$$\gamma = \frac{2}{(2n+1)\nu} + 1, \tag{2-8}$$

n being any integer or zero, a general result according to the theory of isentropic flows /4/. The simplest case corresponds to $\mu = 1$, $n = 0$ which for spherical geometry implies $\gamma = 5/3$. The solution if furthermore $q = 0$ (fluid initially at rest) reads /2/ :

(2-9) $$h = \sqrt{1 - \frac{t^2}{t_0^2}}$$

and the applied pressure is

(2-10) $$p(R,t) = p(R,0)\left(1 - \frac{t^2}{t_0^2}\right)^{-5/2}.$$

Numerical simulations confirm that both (2-7) and (2-10) lead to isentropic compression of nuclear fuel pellets.

However, since the entropy is not significantly decreased by having P_o smaller than half a megabar /3/ the high value of p_o thus induces a shock ahead of the isentropic compression. The medium is then set into motion which means q may equal 2 and (2-7) is the more suitable solution. By looking at the way the impinging laser light creates an ablative flow /6/ the incident power should be /7/ .

(2-11) $$P_L = P_0 \left(1 - \frac{t}{t_f}\right)^S$$

where $t_f = \sqrt{\mu}\, t_0/(\mu+1)$ and $S \sim 2$ according to numerical simulations. These results apply to homogeneous media whether they are in the form of bulk spheres or shells. It can be also shown that the spatial part of eq (2-4) is fulfilled in either case.

A surrounding heavier material might help the isentropic process thanks to its greater inertia /8/. Such effects will not be considered here.

3/- EFFICIENCY OF THE ISENTROPIC PROCESS

Actually, the aim of laser compression of spherical pellets is the achievement of a high value of the parameter

(3-1) $$I = \int_0^R \rho \, dr$$

which is simply related to the fractional burn up of the thermonuclear fuel /5/ . Given a self similar density profile which satisfies the temporal part of equation (2-4) and the pressure law (2-7) it turns out that since

(3-2) $$R = R_0 \left(1 - t/t_f\right)^{\frac{2}{3\gamma-1}},$$

(3-3) $$I = I_0 \left(1 - t/t_f\right)^{-\frac{4}{3\gamma-1}}.$$

Now , the mechanical power applied at any time on the sphere with external radius R is

(3-4) $$\mathcal{P}_M = 4\pi R^2 p \frac{dR}{dt} = \frac{8\pi p_0 R_0^3}{(3\gamma-1)\, t_f} \left(1 - \frac{t}{t_f}\right)^{\frac{7-9\gamma}{3\gamma-1}}.$$

Hence

(3-5) $$\mathcal{P}_M = \frac{8\pi p_0 R_0^3}{(3\gamma-1)\, t_f} \left(\frac{I}{I_0}\right)^{\frac{9\gamma-7}{4}}.$$

In the special case $\gamma = 5/3$ (Fermi degenerate gas) one finds

(3-6) $$\mathcal{P}_M \propto I^2 ;$$

such a dependance was also found by KIDDER /9/ using (2-10) instead of (2-7). It basically depends on the value of γ and not on the details of the isentropic compression process.

On the other hand, in order to drive such a process the time behaviour of the laser pulse should be of the form (2-11) and numerical simulations show that the critical density where most of the incoming radiation is absorbed stands at an almost constant radius R_c from the center. Since for $\gamma = 5/3$ one has $S \sim 2$ and $\frac{7-9\gamma}{3\gamma-1} = -2$, one finds

(3-7) $$\mathcal{P}_M / P_L \sim \text{constant} .$$

The same conclusion holds for the energies :

(3-8) $$\eta_I = \frac{W_M}{W_L} = \frac{\int \mathcal{P}_M \, dt}{\int P_L \, dt} = \text{constant}.$$

Thus, if, during one and the same implosion process according to (2-7), the whole mechanical energy is converted into internal energy of the compressed material (which is a very good approximation close to the time of focalisation), the compression efficiency does not depend on the final state. Furthermore one has between the maximum laser power and the sought value of $\int \rho \, dr$ the same relationship as (3-6) i.e.

(3-9) $$P_L \propto I^2.$$

The large value of I ($\sim$ 3 g/cm^2 /5/) necessary for a thermonuclear burn, requires a high value of P_L. However due the square root dependance a significant I might be obtained with a reasonable laser power i.e. compatible with present day state of the art.

Now using (3-4) and (2-11),

(3-10) $$\eta_I = \frac{4\pi R_0^3}{3} \frac{p_0}{(\gamma-1) t_f P_0},$$

and the absorbed flux at time zero is

(3-11) $$\phi_0 = \frac{P_0}{4\pi R_c^2}$$

where R_c is the radius of the critical layer. Since one has

(3-12) $$t_f \propto R_0 \phi_0^{1/3}$$

(3-13) $$p_0 \propto \phi_0^{2/3},$$

it comes out that

(3-14) $$\frac{p_0}{t_f} \propto \frac{\phi_0}{R_0} = \frac{P_0}{4\pi R_c^2 R_0},$$

and finally :

(3-15) $$\eta_I \propto \frac{R_{oH}^2}{R_c^2}$$

R_{oH} initial radius of the part of the pellet eventually compressed depends on the available laser energy through the well known similarity law : $W\rho^2$ = cte. On the contrary R_c depends on the initial size of the pellet on the laser frequency and on the way energy is transfered from the critical density to the ablation front by electron thermal conductivity . Roughly the higher the frequency, the smaller is R_c and the higher the ratio R_{oH}/R_c. Also, shells in which R_{oH} initial radius of the eventually compressed part is large , look more attractive than bulk spheres from this view point. Any way the efficiency η_I remains comparatively low : about 5%.

4/- SIMILARITY LAWS

The original 1 or 2 dimensional calculations of implosion and thermonuclear burn of DT spheres /5/ , /7/ , deal with comparatively large systems and involve a laser energy (ν 60 KJ) far beyond the capabilities of present and predictable laser technology. Here we are more interested in what can be done with smaller inputs. Hence the problem of adjusting the parameters of either the pressure law (2-7) or the laser power law (2-11). Before optimizing one has to start from some guess educated by similarity laws.

In order to get a high compression, the characteristic time t_f should be nearly equal to the focusing time t_s of the initial shock induced by application of the laser power P_o onto the surface. Notice that, given properties of the laser induced flow, some preparation (prepulse) is necessary in order that the initially solid spheres sorrounded by a plasma corona which absorbs the radiation. Afterwards only, P_o is applied. The corresponding shock velocity is proportional to $P_o^{1/3}$. Hence :

(4-1) $$t_f \propto R_o P_o^{-1/3} .$$

Taking as a reference parameter instead of the laser power, the pressure actually applied to the eventually compressed sphere, the result is :

$$t_f \propto R_{on}\, p_o^{-1/2} \cdot \tag{4-2}$$

Now if the initial radius is changed by a factor Λ , t_f is modified the same way, pressure and density being conserved. Therfore setting $R'_o = \Lambda R_o$, $p'_o = p_o$, the mean thermodynamical path (a line in the diagram $\ln T, \ln \rho$) remains the same. On the contrary, if $p'_o = \Lambda p_o$ with $R'_o = R_o$, $p' = \Lambda p$, $t'_f = t_f \Lambda^{-1/2}$ and the density does not change. Thus one gets parallel lines in the same diagram as before. These similarity laws are rigourous.

This is not the case of those obtained starting from the laser power. Indeed the critical radius changes with time . So the influence of the target size can be evaluated in two ways. First let the applied flux density be constant : $R'_o = \Lambda R_o$, $\phi'_o = \phi_o$. Hence, since one has $R_c \propto R_o$, $P'_o = \Lambda^2 P_o$. This is again a case of constant pressure, density and temperature are conserved, $t'_f = \Lambda t_f$, but the required energy :

$$E' = \int_0^{t'<t_f} \frac{P_o}{\left(1 - \frac{t}{t_f}\right)^s} dt = \frac{P_o t_f}{s-1}\left[\frac{1}{\left(1 - \frac{t'}{t_f}\right)^{s-1}} - 1\right] \propto \Lambda^3 E \,. \tag{4-3}$$

The alternative possibility consists in keeping a constant P_o . Then $\phi' = \Lambda^{-2}\phi$, $p' = \Lambda^{-4/3} p$, $t'_f = \Lambda^{5/3} t_f$, $E' = \Lambda^{5/3} E$ which yields for an unchanged density $T' = T\, \Lambda^{-4/3}$.

By the same token, given the initial target radius, the influence of the initial power $P'_o = \Lambda P_o$ leads to $\phi' = \Lambda \phi$, $p' = \Lambda^{2/3} p$, $t'_f = \Lambda^{-1/3} t_f$, $E' = \Lambda^{-2/3} E$ and consequently for an unchanged density , $T' = \Lambda^{2/3} T$. In this case an alternative approximate similitary law can be also useful. Assume that in order to achieve a given $\int \rho \, dr$,

the required energy does not vary that much. Hence starting from (4-3) in a slightly different form :

$$E = \frac{P_0 t_f^s}{s-1}\left[\frac{1}{(t_f' - t')^{s-1}} - \frac{1}{t_f^{s-1}}\right] \tag{4-4}$$

and assuming a fair constancy of the bracket [ ]

$$P_0 t_f^s \sim ct. \tag{4-5}$$

The previous derivation would have given :

$$P_0 t_f^3 \sim ct. \tag{4-6}$$

But the motion of the critical radius is over looked. According to every special case either one of the relationships (4-5) or (4-6) can prove more accurate according to computer runs.

An example of the results obtained by a one dimensional lagrangian code for the case of a 1 µg DT pellet irradiated by a laser pulse of the form (2-11) and using the similitary law (9-6) to chose the parameters in order to compare with Nuckoll's results /5/ , is given on fig.1. The maximum value of $I = \int \rho \, dr$ in our case is 0.79 g/cm^2, provided a large (> 50%) amount of energy is delivered in the last few picoseconds.

5/- ENERGETICS

The energy cycle of a fusion process involving a laser is shown on fig.2 . Obviously one-wishes that the gain G overcomes the losses represented by the efficiencies η_σ , so that the multiplication factor

$$Z = \eta_s \, \eta_A \, \eta_I \, G \geq 1. \tag{5-1}$$

In the present state of the art one may expect the laser efficiency η_s to be about 1% (Nd glass) or 10% (CO_2). η_A is about 80%. η_I as seen in section 3 is around 5%. Hence the necessary values for G given by table 1 for two cases : Z = 1 (breakeven), Z = 10 (reactor). Now, starting from a fuel in

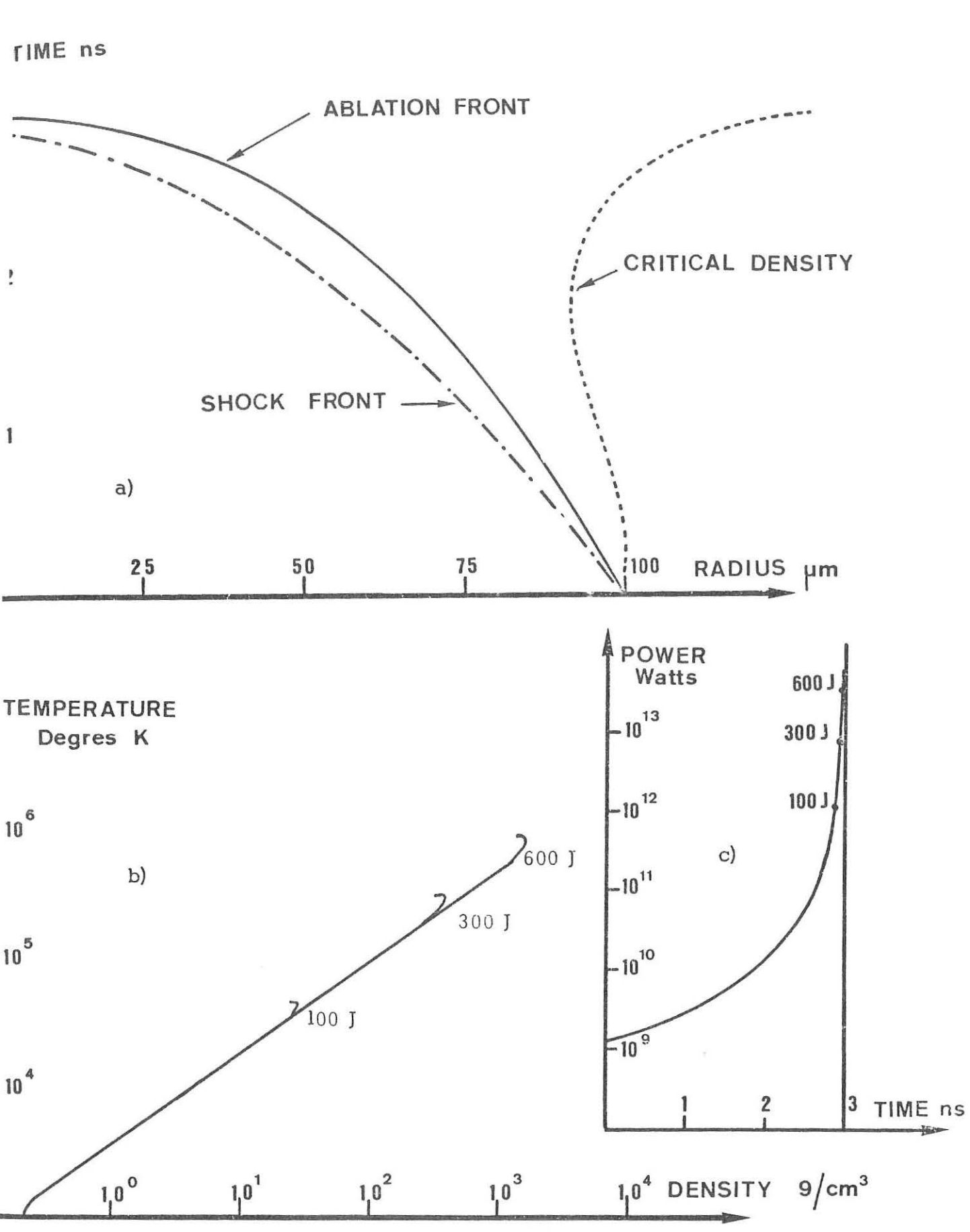

Fig. 1 - Laser driven implosion of a 0.89 μg DT target

a)- trajectories for a 600 J pulse. b)- Thermodynamical pathes for the same pulse c)- up to different energies.

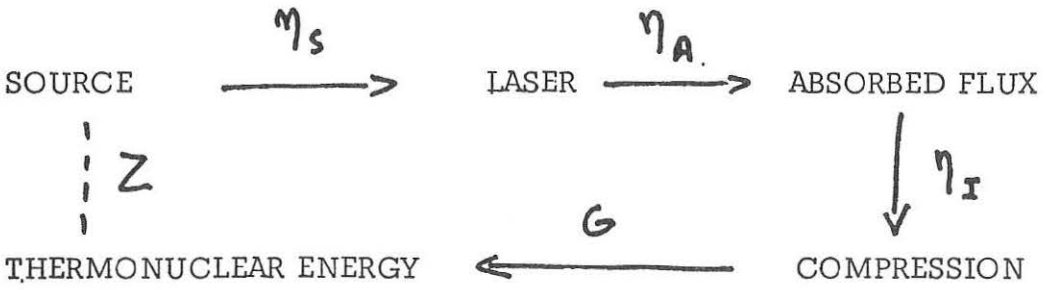

Fig. 2 - ENERGY CYCLE

TABLE 1

Z	η_S	η_A	η_I	G
Breakeven 1	10^{-2} 10^{-1}	8.10^{-1} 8.10^{-1}	5.10^{-2} 5.10^{-2}	$2.5\ 10^{3}$ $2.5\ 10^{2}$
Reactor 10	10^{-2} 10^{-1}	8.10^{-1} 8.10^{-1}	5.10^{-2} 5.10^{-2}	$2.5\ 10^{4}$ $2.5\ 10^{3}$

which the mean energy per particle is 3,5 keV the yield per reaction is 17 MeV so that the maximum expected gain is :

(5-2) $$G_{max} = \frac{17.10^6}{4 \times 3.5\ 10^3} = 1.2\ 10^3.$$

Comparing this value with those of table 1 would lead to definitely pessimistic conclusions. However central hot spot ignition provides a clue to overcome this. Provided enough energy is fed into the innermost part of the imploved shell at thermonuclear temperatures, the ignition propagates around. The phenomenon obeys a scaling law of the type

(5-3) $$M \left(\frac{n}{n_s}\right)^2 = k_0$$

/10/ which is the same as the scaling law for a given fractional burn up /11/ :

(5-4) $$M\left(\frac{n}{n_s}\right)^2 = k,$$

where M is the interested mass, n_s the solid state density. Fortunately one has $K \gg K_0$.

Now, different systems, whether they are centrally ignited or not compare through (5-4). The energy necessary to isentropically compress the pellet is readily calculated :

(5-5) $$W_c = M \int_{V_s}^{V} p\,dV = M \int_{\rho_s}^{\rho} p\,\frac{d\rho}{\rho^2},$$

V being the specific volume ($V = 1/\rho$) . Taking into account

(5-6) $$p\,\rho^{-\gamma} = p_s\,\rho_s^{-\gamma}$$

and (5-4) one finds :

(5-7) $$W_c = \frac{p_s M}{(\gamma-1)\rho_s^{\gamma}} \left[\left(\frac{K}{M}\right)^{\frac{\gamma-1}{2}} - \rho_s^{\gamma-1}\right].$$

This function of M has a maximum for $M \sim 0.3\ K/\rho_o^2$ and for small M varies as $M^{2/3}$ both laws being valid for $\gamma = 5/3$ (Fermi degenerate gas). When the isentropic process follows a shock wave , the results are similar. However, the maximum value corresponds to the shock conditions.

Now, one is interested in getting the highest fractional burn up with the smallest energy investment. Since a central ignition is thus required, the energy invested is composed of two parts : the one necessary to compress most of the fuel, the other to also heat the innermost part up to ignition propagation conditions. The latter is proportional to the mass of the central hot spot. By the same token, one would also find an energy proportional to the mass of the whole sphere was to be at the ignition temperature. The corresponding calculations yield the results shown in fig. 3 . The required energy for ignition is then either proportional to the mass according to line I for the case of total ignition, or is the sum of energies resulting from curves II (central hot spot) or III (isentropic compression). The most favourable conditions are obtained with fairly large masses isentropically compressed while the energy necessary for heating the central hot spot remains comparatively low /12/ . Taking into account the results of section 3 it can be infered that the results obtained on fig. 3 also apply to the laser energy, changing the ordinate scale by a factor $1/\eta_I$.

6/- CONCLUSIONS

According to the above results, small scale experiments can be of significance for the laser fusion problems : equation (3-9) shows that interesting values of $I = \int \rho\, dr$ can be reached with comparatively low laser powers and energies. Furthermore the preceding section evidences favorable energetics. However the pulse durations should be in the picosecond range for target masses in the microgram range unless one uses tricks in target design. The problem of implosion stability have been completely overlooked here. Thus our results are valid as far as instabilities do not actually limit the maximum expected density.

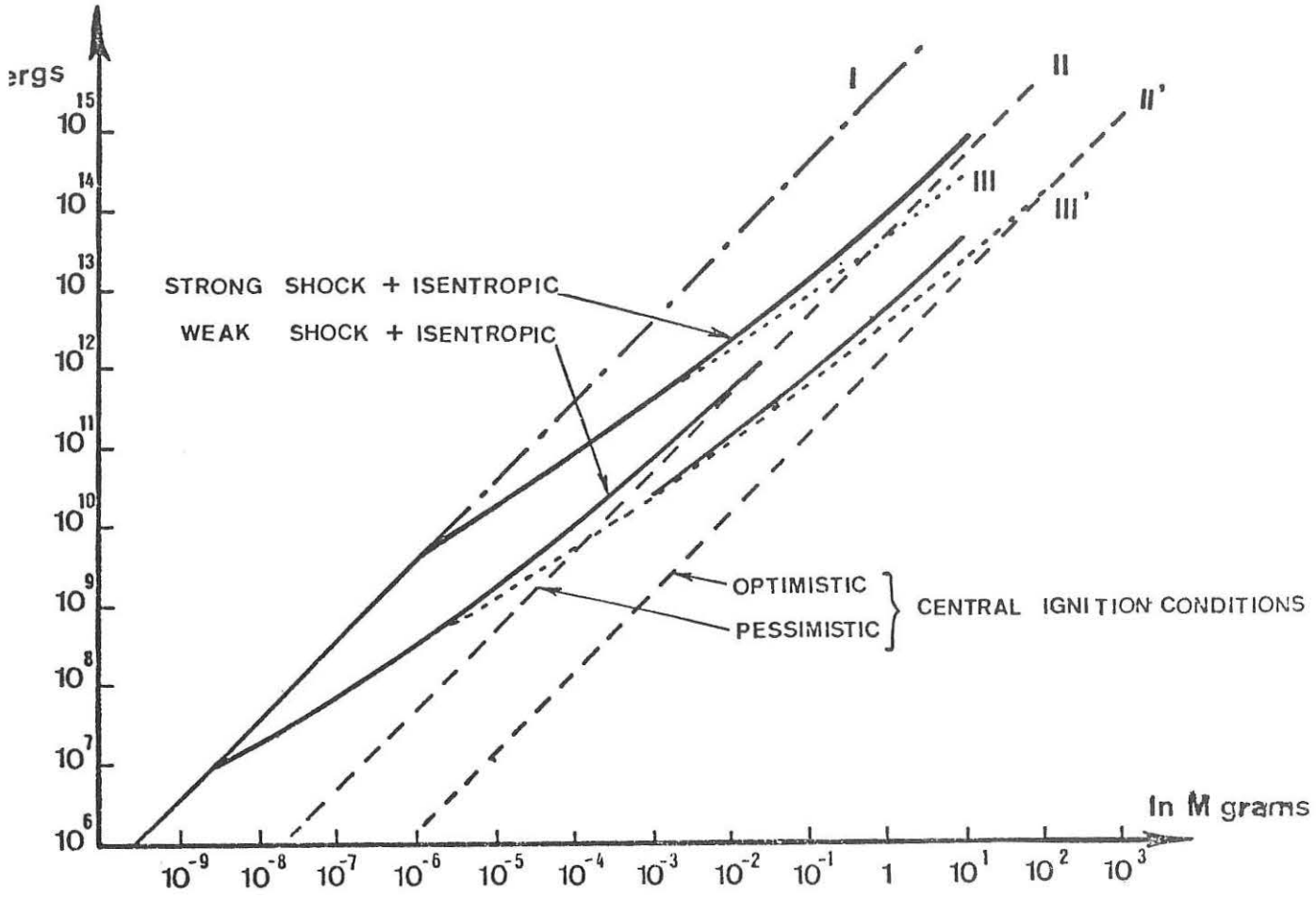

Fig. 3 - Energy required to compress and ignite a given mass of DT satisfying the scaling law Mn^2 = constant.

I - Total mass at ignition temperature 3.5 keV.

II - and II' pessimistic and optimistic energies for hot spot ignition ($T \sim 1,5$ keV).

III - and III' strong and weak shocks followed by an isentropic compression disregarding ignition conditions.

Solid lines correspond to actual trajectories of compressed and ignited final states.

Not that due to equation of state effects /5/, the intersection of lines I and III' gives lower limits for W and M.

REFERENCES

/1/ - G. CHARATIS et al..... Vth EAIA Conference on fusion - Tokyo (1974)

/2/ - R.E. KIDDER - in. Laser interaction with matter Yamanaka ed (1972)

/3/ - K.P. STANYUKOVICH - in. Unsteady motion of continuous media (1959)

/4/ - L.D. LANDAU, E.M. LIFSHITZ - in. Fluid Mechanics - § 98

/5/ - J.H. NUCKOLLS - in. Laser Interaction and related Plasma Phenomen Schwarz- Hora ed. Plenum vol. 3 (1974) 399

/6/ - J.L. BOBIN - Phys. Fluids 14 (1971) 2341

/7/ - J.H. NUCKOLLS, L. WOOD, A. THIESSEN, G. ZIMMERMAN - Nature 239 (1972) 135

/8/ - Yu. AFANASIEV et al..... Vth EAIA Conference on fusion - Tokyo (1974)

/9/ - R.E. KIDDER - Nucl. Fusion 14 (1974) 797

/10/ - J.P. PLANTEVIN - CEA Int^{1} Rept Unpublished (1965) - J.G. LINHART, Nucl. Fusion 10 (1970) 211 - M.S. CHU, Phys. Fluids 15 (1972) - J.P. SOMON Nucl. Fusion 12 (1972) 461

/11/ - See. e.g. J.L. BOBIN, J.M. REISSE - paper submitted to Journal de Physique and references therein

/12/ - J.L. BOBIN - Paper submitted to Nuclear Fusion.

DENSITY DIAGNOSTICS OF SUPERCOMPRESSED LASER-THERMONUCLEAR TARGETS

F.A. Nikolaev, V.D. Rozanov

Lebedev Physical Institute, Moscow, U.S.S.R.

The problem of the laser thermonuclear fusion is strongly connected with both the progress in construction as well as the investigation of gas dynamic and heating processes in the laser pellet. These experiments require the development of new methods of plasma diagnostics specifically suited to the extreme conditions of temperature, density, size and time resolution typical of laser fusion problems. The main object of this report is to review the techniques developped in our laboratory for measuring the density of imploding pellets.

The pinhole X-ray camera has been used by Dr. B.R. Guscott et al to demonstrate compression in experiments reported elsewhere [Vol 1, p. 66]. It is this technique which has been used to demonstrate a compression of 20 in diameter of the pellet. This diagnostic does not provide a time resolved measurement of the density. We discuss here spectroscopic and various other methods.

1. SPECTROSCOPIC METHODS

These well-known methods are very attractive because of their long history, both the experimental techniques and the methods of analyzing the results are well developped. The examination of possible spectroscopic methods has been done by Dr. I.I. Gobelman and collaborators [1].

From the condition for small bremsstrahlung absorption,

$$\varkappa l \approx 0.26 \times 10^{-40} z_0 \left(\frac{Ry}{\hbar\nu}\right)^3 \left(\frac{Ry}{kT_e}\right)^{1/2} \left(1-\exp\left(-\frac{\hbar\nu}{kT_e}\right)\right) N^2 l < 1 \quad (1)$$

it is easily seen that, for pellet densities $10^{21} \div 10^{25}$ cm^{-3} (pellet diameter 10^{-2} cm and less), the useful diagnostic wave length interval is $\lambda = 1 \div 10$ Å. This is the range of hydrogenlike and heliumlike transitions for ions with $Z \sim 10 \div 30$.

For plasma having the expected parameters there exists some physical effects that are directly related to the plasma density. They are:

a) Line broadening
b) Relative line intensities
c) Plasma satellites
d) Raman scattering of external X-ray radiation

We shall discuss each effect in more detail.

a) Line Broadening

In the paper [1] it has been shown that for hydrogenlike ions with $Z \approx 20$ and for a temperature $T \simeq 2$ KeV, line broadening due to the density is larger than the Doppler broadening. This effect is well described by Holtsmark theory [2,4]

$$\hbar\Delta\omega = 21.6\, Ry\, \frac{n^2}{Z} \left(a_0^3 N_i\right)^{2/3} \quad (2)$$

(Ry = 13.6 eV, a_0 = Bohr radius). The density range in which this method can be used is shown in Fig. 1. The region of N between curves 1 and 2 corresponds to the quasistatic ion broadening. In the region above the curve 3, ion density broadening is greater than Doppler broadening. Below the curves 4 and 5, the effects of Coulomb repulsion of perturbing ions

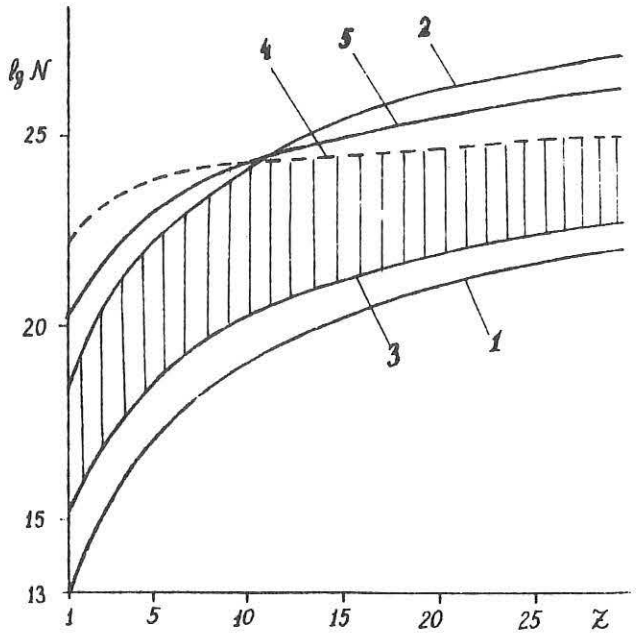

Figure 1

and Debye shielding are not important. The broadening of nonhydrogenlike ion lines can also be used for plasmas with $N \approx 10^{22} \div 10^{26}$ cm^{-3}, but the widths of these lines are small. This implies that instruments with extremely good resolution have to be used. As an example the Fe XXIV (λ = 11 Å) and Fe XXV (λ = 1.87 Å) lines have a width of about $\Delta\lambda \approx 10^{-2}$ Å.

b) Relative Line Intensities

This method has been used in many cases [5,6] for plasmas with $N < 10^{23}$ cm^{-3}. In the density region $N > 10^{23}$ cm^{-3}, some complications arise because threebody recombination becomes important. Calculation accuracy of these processes is low and prevent using this method for plasmas with $N > 10^{23}$ cm^{-3}.

c) Plasma Satellites

For densities $N \approx 10^{24} \div 10^{26}$ cm^{-3} observation of plasma satellites is possible. These satellites are due to the interaction of radiation with the neighboring ions. The shift in wave length of the satellite is related to the Langmuir frequency ω_L: $\omega \approx \omega_o + 2\omega_L$ ($\omega_L = \sqrt{2\pi e^2 N/m}$), and for $N > 10^{24}$ cm^{-3} the satellite becomes visible. Ratio of the intensity of the satellite line to that of the resonance line for $N > 10^{24}$ cm^{-3} is about 10 %. That means that the position of the satellite and the corresponding density can be determined with a good accuracy.

d) Raman Scattering

This method can be applicable for densities as high as $N > 10^{23} \div 10^{26}$ cm^{-3}. In the forward scattering spectrum of an external X-ray beam it is possible to observe the peak corresponding to the excitation of plasma oscillations ($\omega' \approx \omega \pm \omega_L$). The highest density region of the plasma is responsible for this peak. Therefore its position provides information only on the maximum plasma density. The intensity of the external X-ray source needed is very high. Sufficient intensities may be obtained with laser produced plasmas, the parameters of which are specially adjusted for this purpose [7-9].

As a conclusion to this short review of spectroscopic methods, we make two remarks. Methods a, b and c are useful for plasmas with $Te \gtrsim 200 \div 300$ eV; method d is effective in the low temperature region and for $N > 10^{23}$ cm^{-3}. All these methods, except d, have one deficiency, that is you must keep a percentage (about 2 %) of heavy elements in the pellet ($A \approx 20$-60).

2. NEUTRON YIELD AND SPECTRUM

a) Relative yield and D-T-neutrons spectrum.

It is well known that in the neutron spectrum from a laser heated pellet, there exists neutrons with energy 2.5 MeV coming from $D(D, He^4)n$ reactions

[10]. In paper [11] it was proposed to use this effect to determine the pellet density. Fast D-T-neutrons (velocity $v_o \approx 8 \cdot 10^8$ cm/sec) are produced not only in the low density "corona", but also in compressed core of the pellet. Calculations [11] have shown, that starting from a temperature Te $\approx$ 0.1 - 0.3 KeV and densities $N \approx 10^{25}$ cm^{-3}, the relative yield of D-T-neutrons Q_{DT}/Q_{DD} increases with the temperature and in the Te $\approx 1 \div 3$ KeV region it reaches 10 % (Fig. 2). From Fig. 2 we can see that relative neutrons yield can give information about the density and temperature of the compressed pellet core. If the core is "cold" D-D processes occur only in the corona and the relative yield from the core remains of the order of 10^{-5}.

Information about the temperature of compressed core can be obtained from the spectrum of D-T-neutrons. In Fig. 3, the calculated spectrum of D-T neutrons for "cold" and "hot" core pellet is shown. The horizontal part of

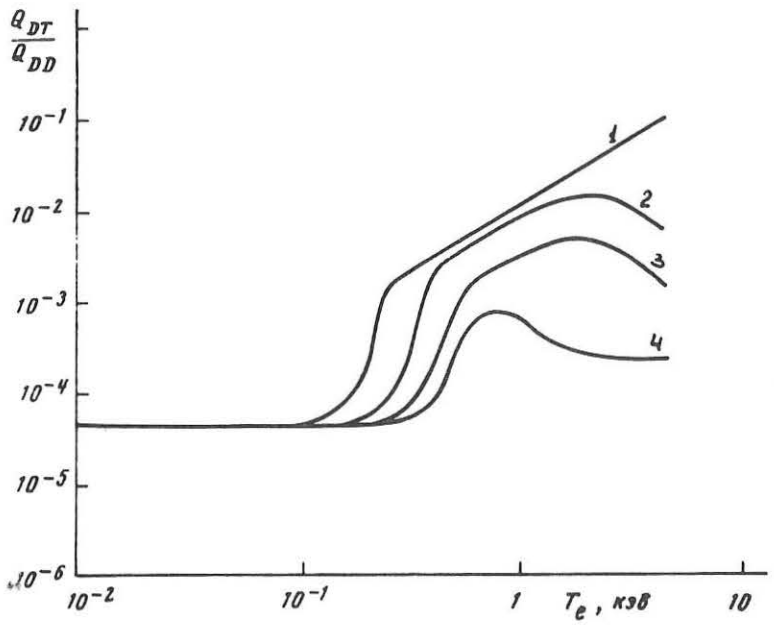

Figure 2

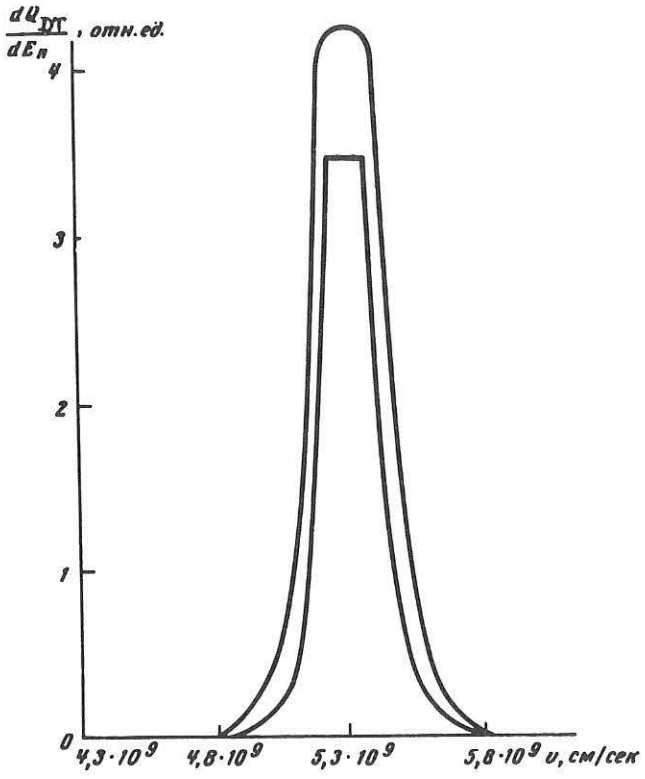

Figure 3

the "hot" spectrum is connected with the effect that occurs when a tritium nucleus leaves the core. The width of horizontal part is given by

$$\Delta V = \frac{2 m_T}{m_T + m_D} \left(V_0 - \frac{4.76 \times 10^{-13} N 4 r_0}{T_e^{3/2}} \right) \qquad (3)$$

The main part of the D-T-neutron yield takes place at the moment of maximum compression. For this reason yield and spectrum measurements of neutrons from laser imploding pellets can give information about temperature and density only on the last moment of the compression process.

b) D-D-neutron scattering on pellet substance.

Fusion neutrons can be scattered before leaving target. Monte-Carlo numeral

calculations [12] for $(C\ D_2)_n$ pellet show that some percentage of D-D-neutrons lose energy by scattering. Fig. 4 shows the results of these calculations for uniformly distributed sources (dense line), point source (dotted line) and for various densities 1 g/cm^3 (1), 10 g/cm^3 (2), 100 g/cm^3 (3), 1000 g/cm^3 (4). The scale on the right side is for unscattered neutrons.

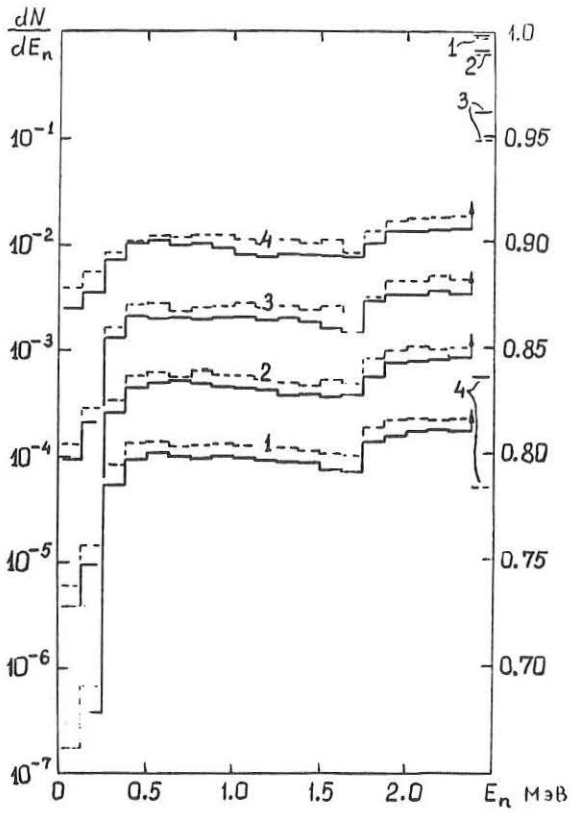

Figure 4

From the calculated spectrum the effect of the first scattering on deuterium ($E \approx 0.25$ MeV) and carbon ($E \approx 1.75$ MeV) are clearly seen. These calculations are not sensitive to the form of the neutron source. Results of the numeral calculation for a density distribution close to that of the real pellet is shown in Fig. 5.

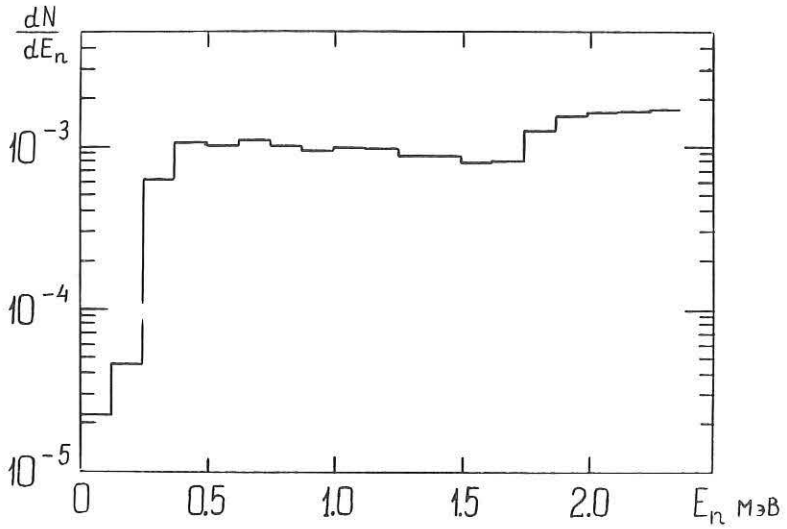

Figure 5

As for the D-T-spectrum, the D-D-spectrum only gives information about average pellet density at the moment of maximum compression. Accuracy and effectiveness of neutron spectroscopy methods increase with the number of neutrons produced in one shot. For 10^{10} neutrons per shot the accuracy could reach about 10 %.

3. POSITRON ANNIHILATION [13]

The decay time of stopped positrons before annihilation is given by the expression

$$\tau_o = (\sigma v N)^{-1} = 2.3 \times 10^{-10} (A/\rho Z) \qquad (4)$$

where $\sigma = \pi r_o^2$ c/v. v is the relative electron-position speed, r_o is the classical electron radius and ρ, A and Z the density, atomic weigth and charge number respectively of the nuclear pellet substance. From (4) it follows that decay time measurements can give in a very simple way the

density of the pellet. If the pellet is located in the positrons flux, the main part of the positrons that enter the pellet volume would be thermalized and the positron's concentration would soon reach equilibrium. If the compression time $t < \tau_o$, the number of annihilations would increase with increasing density. These annihilations are very easily recorded by Cerenkov or scintillation counters.

Estimations show that, for compression $\gtrsim 10^2$, pellet diameter $\sim 200\mu$ and statistical accuracy ~ 10 % the positron flux must be $N_+ \simeq 10^{18}$ cm^{-2} sec^{-1}.

Construction problems of a positron source with such intensity are complicated. Fluxes of this order may be generated by impulse betatron type accelerator [4] with convertor from heavy elements. We now have done some analysis on the possibility of construction of a high current accelerator particulary suited for use as a density diagnostic [15]. The advantage of this method, apart from the simplicity of interpretation of the experimental results lies in the possibility of investigating the history of the compression.

CONCLUSION

In conclusion this short review of diagnostics methods suitable for the study of compressed pellets, we can say that, at the present time, there exists enough different ways of measuring densities up to 10^{26} cm^{-3}.

REFERENCES

[1] A.V. Vinogradov, I.I. Gobelman, E.A. Yukov
Quant.elect. 1, 268 (1974)

[2] B. Mozer, M. Baranger, Phys.Rev. 118, 626 (1960)

[3] C.F. Hooper, Jr. Phys.Rev. 165, 215 (1968) and
169, 193 (1968)

[4] L.A. Minaeva, Astron.Journal 45, 578 (1968)

[5] H.J. Kunze, H.R. Griem, A.H. Gabriel, Phys.Rev. 165, 261 (1968)

[6] A.H. Gabriel, C. Jordan, Case Studies in Atomic Collision Phys.
2, 208 (1972)

[7] A.V. Vinogradov, I.I. Gobelman, JETP 63, 2113 (1972)

[8] P.J. Mallozzi, H.M. Epstein et al. Final Report on X-Ray
Emission from Laser Produced Plasma, Battelle, 1972

[9] P. Jaegle, A. Carilon, P. Dhez et al. Phys.Lett. 36A, 167 (1971)

[10] N.G. Basov et al. Quantum El. 8 (1974)

[11] E.G. Gamaly et al. JETP Letters 21, 156 (1975)

[12] E.G. Gamaly et al. Quantum El. 2, No 10 (1975)

[13] O.N. Krakhin, F.A. Nikolaev, G.V. Sklizkov
JETP Letters 19, 389 (1974)

[14] A.I. Pavlovskiy et al. DAN USSR 160, 68 (1965)

[15] V.K. Lugavskiy, F.A. Nikolaev, G.V. Sklizkov
Preprint Lebedev Inst. No 56 (1975)

LOWER HYBRID HEATING OF LARGE TORI USING WAVEGUIDES

M.BRAMBILLA

ASSOCIATION EURATOM-C.E.A.
Département de Physique du Plasma et de Fusion Contrôlée
Service IGn - Centre d'Etudes Nucléaires
BP 85 - Centre de TRI 38041
GRENOBLE CEDEX (FRANCE)

Abstract: H.F. waves launching using a phased array of waveguides (the Grill) in the Lower Hybrid Resonance frequency domain appears to be a promising method to heat large toroidal plasmas. The theory of such a launching structure is reviewed, and an application is presented in view of heating a large tokamak.

---

1 - INTRODUCTION. - Among the possible h.f. methods for large confined plasmas, the Lower Hybrid Resonance heating occupies an interesting position. Indeed, at the required frequency (between 0,5 and 1GHz) waveguide launching is easily compatible with the access available on large toroidal devices, so that coils or antennas permanently built within the plasma chamber can be avoided.

It is well known however that the L.H.R. region is accessible from outside the plasma only for waves whose wave number along the confining magnetic field satisfies the condition (1) $k_{//}^2 c^2/\omega^2 \geq 1 + (\omega_{pe}^2/\Omega_{ce}^2)_{Res}$. To comply with this condition, as well as to fully exploit the large access area available on the large devices, a multiwaveguide launching structure, nicknamed "the Grill" has been proposed (2). It consists of an array of waveguides, mounted with their small side parallel to the equatorial plane of the plasma chamber, each excited in the TE_{01} mode with adjustable phase, so as to stimulate a retarded wave structure.

Because of the mutual coupling between the guides, and of the excitation of higher evanescent modes at the guide openings on the plasma chamber, the behaviour of the Grill as a launching structure is not completely obvious (3). To improve the understanding of this behaviour, and to have a basis for the practical design of the Grill, a theory of this structure in a simplified plane geometry was developed (4). This theory is summarized

in the next section. In section 3 we present the application of this theory to the design of the Grill appropriate to a large Tokamak. Finally, in section 4 the results are reformulated in terms of elementary microwave theory, and applied to the solution of the matching problem.

It will be shown that the reflection coefficient (or equivalently the standing wave ratio) can be made acceptably low, and is not critically dependent on the plasma parameters. Thus for example the power required to bring a "feasibility test" tokamak to ignition, estimated to be a few tens of MW, could be launched with electric field not exceeding a few kV/cm.

It is worth mentioning that the present theory has received a satisfactory confirmation from the results of a low power coupling experiment made at Princeton on the linear device H-1.(5)

Since in the L.H.R. frequency range h.f. sources capable of delivery up to 1 MW for several secs. with 50-60% efficiency are well within present day's technology, the satisfactory solution of the launching problem makes L.H.R. heating a serious candidate to satisfy the power requirements of large plasmas of thermonuclear interest.

2 - THE THEORY OF THE GRILL. - We simplify the geometry as sketched in fig. 1. Each guide extends indefinetly in the vertical direction ; the chamber occupies the $x \geqslant 0$ halfspace, with the plasma edge at $x = x_p \geqslant 0$.

The method of solution is as follows. We first express the field in the waveguide in terms of the incident amplitudes α_p, $p = 1, 2, \ldots N$, the unknown reflected amplitudes β_{0p} and the unknown coefficients β_{np} characterizing the excitation of higher evanescent modes at the $x = 0$ discontinuity.

$$E_z = \sum_{p=1}^{N} \textcircled{H}_p(z) \left\{ \alpha_p e^{i k_{0x} x} + \beta_{0p} e^{-i k_{0x} x} + \sum_{n=1}^{\infty} \beta_{np} e^{\gamma_n x} \cos \frac{n\pi (z - z_p)}{b} \right\} \quad (1)$$

and similar expressions for E_x and By (the other components vanish by symmetry). Here $k_0 = \omega/c$, $\gamma_n = \left(n^2\pi^2/b^2 - k_0^2\right)^{1/2}$, b being the width of the waveguides ; $\textcircled{H}_p(z)$ is unity in front of the p-th guide, $z_p \leqslant z \leqslant z_p + b$ and zero anywhere else.

The electromagnetic field for $x \geqslant 0$ is then written as a Fourier integral over $k_{//}$: for example :

$$E_z = \int dk_{//}\, \sigma(k_{//}) \left[e^{ik_\perp x} + Y(k_{//})\, e^{-ik_\perp x} \right] e^{ik_{//} z}$$

where $k_\perp^2 = k_0^2 - k_{//}^2$, and the integration path runs above the $k_{//}^2 = k_0^2$ branch point and is symmetric with respect to $k_{//} = 0$. $Y(k_{//})$ describes the wave reflected back from the plasma ; it is mainly determined by the cut-off at the surface where the local electron plasma frequency equals the applied frequency. To a very good approximation, waves with $k^2 c^2/\omega^2 < 1$ are totally reflected there. On the other hand waves with $k_{//}^2 c^2/\omega^2 > 1$, once tunneled to the cut-off layer, propagate forming the "resonance cone" and suffer no further reflection. Note that we do not need to specify the absorption mechanism to evaluate $Y(k_{//})$. Its expression assuming a linear density profile near the plasma edge can be found in ref.4 .

Imposing the continuity of $\vec{E}$ and $\vec{H}$ at the waveguide throats, and the vanishing of E on the metallic wall, one eliminates $\sigma(k_{//})$ and obtains a linear system for the unknown coefficients β_{mp}. This system, truncated to include up to 10 waveguide eigenmodes, has been solved numerically.

According to the theory sketched above, the coupling efficiency of the Grill depends mainly on two parameters, namely the distance x_p between the wall and the plasma, and the density gradient length, $L_n = n_{Res} \left(dn/dx \right)^{-1}_{x = x_p}$ near the plasma edge. When x_p is not small compared to the vacuum wavelength the coupling becomes rapidly poor, because of the evanescense in vacuum of the waves which satisfy the accessibility condition. However, it is expected that a tenuous plasma will exist between the wall and the limiter. It is therefore appropriate to assume $x_p = 0$, and L_n much larger than the actual distance from the wall to the resonance. (The existence of steeper density gradients beyond the limiter does not affect the results, as long as was WKB solution will be valid there). The energy reflection coefficient R always shows a broad minimum for large but not unreasonable values of L_n. It corresponds to the best compromise between the mismatching due to the fast variation of the refractive index and polarization for steep gradients, and the increasing importance of the evanescence layer $\omega_{pe} < \omega$ for too gentle gradients. It is important to note that the exact value of L_n is by no means critical. This fact, together

with the insensitivity of the results to other parameters, (magnetic field, temperature, etc.) makes expensive dynamical tracking of the load impedence unnecessary.

3 - APPLICATION TO A LARGE TOKAMAK. - We proceed now to present some quantitative results obtained using the theory outlined in the previous section. The frequency chosen is 1 GHz, and $\omega_{pe}^2/\Omega_{ce}^2 = 0{,}4$ was assumed.
The simplest Grill is constituted by two waveguides only. As shown in fig. 2 and 4, the minimum value of the energy reflection coefficient is obtained for b=12 cm, and a phase difference 180° between the guides. Under these conditions the $k_{//}$ spectrum peaks at $k_{//} = 1{,}25$. The results of fig. 4 are for $L = 10^4$. On fig.3, R is plotted as a function of L_n for b=11.4 cm and $\Delta\Phi = 180^\circ$. It is seen that L_n can vary by more than three orders of magnitude without R exceeding 15 %.
In large devices, the width of a port in the toroidal direction will be appreciably larger than the width of the 2-waveguides Grill of the previous example. Fig. 5 shows R as a function of $\Delta\Phi$ for Grills with 4,6 and 8 guides, fitting in a port of 46 cm (b=11.4,7.5 and 5.cm respectively). In all cases, best coupling is obtained for the same value of the average $k_{//}$ as above. However, the minimum value of R for 6 and 8 guides is about twice as high than for 4 (and 2) guides. Fig.3 also gives R versus L_n for 4 guides, $\Delta\Phi = 180^\circ$ (curve b) and 8 guides, $\Delta\Phi = 90^\circ$ (curve c) showing similar features. In the next section we will give additional and stronger arguments to rule out Grill's realizations with more than 4 guides.

4 - IMPEDENCE MATCHING. - For our present purpose, it is useful to introduce the scattering matrix $\underline{\underline{W}}$, whose element W_{pq} is the complex amplitude of the wave reflected in the p-th guide, when the q-th guide is excited alone with unit amplitude. This definition allows W to be computed using the theory described above, or to be measured in an experiment. Then if $\vec{\alpha} = (\alpha_1 \ldots \alpha_p)$ is the set of incident amplitudes, the reflected amplitudes will be $\vec{\beta} = \underline{\underline{W}}\,\vec{\alpha}$
As a first application, we can minimize the reflection coefficient by choosing the excited amplitudes so that $\underline{\underline{W}}\,\vec{\alpha} = \lambda\vec{\alpha}$ (3)

where λ is the eigenvalue of W with smallest modulus, and R $R = |\lambda|^2$. By symmetry, it is clear that for the 2-guides version of the Grill this will be achieved with $\alpha_2 = \pm \alpha_1$, which is not new. For the 4-guides Grill, on the other hand, while the symmetry requires $\alpha_3 = -\alpha_2$, $\alpha_4 = -\alpha_1$, the ratio α_2/α_1 remains free for optimization. With the above parameters R is found to be 2.74 %, appreciably less than for the equal moduli, $\Delta\phi = 180^\circ$ excitation. Unfortunately, to divide the h.f. power in an adjustable manner between the guides is so difficult that this optimization is of little pratical value.

Now suppose that a matching section is introduced, characterized by a set of reflection and transmission coefficients R and T. If losses can be neglected, it can be easily proved that R and T are related by

$$\underline{\underline{T}} = i \left(\underline{\underline{R}}^{-1} . \underline{\underline{R}}^{*-1} - \underline{\underline{I}} \right)^{1/2} . \underline{\underline{R}} \qquad (4)$$

where I is the identity matrix.

The set of amplitudes reflected back towards the generator is then given by

$$\vec{\beta}' = \underline{\underline{R}} \vec{\alpha} + \underline{\underline{T}} . \underline{\underline{W}} . \left(\underline{\underline{I}} - \underline{\underline{R}} . \underline{\underline{W}} \right)^{-1} \underline{\underline{T}} . \vec{\alpha} \qquad (5)$$

Matching is achieved if $\vec{\beta}' = 0$ independently on the set of incident amplitudes, $\vec{\alpha}$. Using Eq. (4), it is easily shown that this happens if and only if

$$\underline{\underline{R}} = \underline{\underline{W}}^* \qquad (6)$$

An important consequence of this result is that matching is impossible using independent quadrupoles in each waveguide, for in this case R would be diagonal, which is incompatible with Eq. (6). The number of quadrupoles required to achieve the matching is equal to the number of independent components of $\underline{\underline{W}}$. Fortunately, this number is considerable reduced by the symmetries of this matrix. In addition to reciprocity, $W_{i,k} = W_{k,i}$, the right-left symmetry of the array ensures that: $W_{ik} = W_{N+1-i, N+1-k}$. For even N, this leaves (N/2).(N/2+1) independent components. Thus two quadrupoles (or one hexapole) are sufficient for N=2, six quadrupoles are required for N=4, 20 quadrupoles for N=8, and so on. It is clear that beyond N=4 the complexity and cost increase prohibitively.

Finally, the previous results can be used to evaluate the electric field required to transmit a given power to the plasma, taking into account the standing wave ratio in the matched section. Assuming a total area of 5.10^3 cm^3, covered either by two independent (on different ports) 2-waveguide Grills, or by a single 4-waveguide Grill, it is found that in the example above the electric field required to transmit 10 MW to the plasma is 2,5 kV/cm in the first case, and 3.05 kV/cm in the second case.

References

(1) T.H. Stix, Phys. Rev. Letters 15, (1965),878

(2) P.Lallia Proc. 2nd Topical Conf. on R.F. Plasma Heating Lubbock 1974, paper C3.

(3) S.Puri, M.Tutter, report IPP-IV/66, February 1974.

(4) M.Brambilla, to be published

(5) S.Bernabei, M.Heald, W.M. Hooke F.L. Paoloni Phys. Rev. Letters 34, (1975),866.

Figure Captions

Fig. 1 - The idealized model of the Grill

Fig. 2 - R versus b; 2 waveguides, $\Delta\phi = \pi$, $L_n = 10^4$, $\varkappa_p = 0$, $\nu = 1.$ Ghz, $\omega_{pe}^2/\Omega_{ce}^2)_{Res} = 1.$

Fig. 3 - R versus L_n, b = 11.4 cm, other parameters as in fig. 2.

Fig. 4 - R versus $\Delta\phi$, a) $L_n = 10^4$, other parameters as in fig. 3
b) without plasma

Fig. 5 - R versus $\Delta\phi$ for 4, 6 and 8 guides, total width 46 cm.
other parameters as in fig. 2

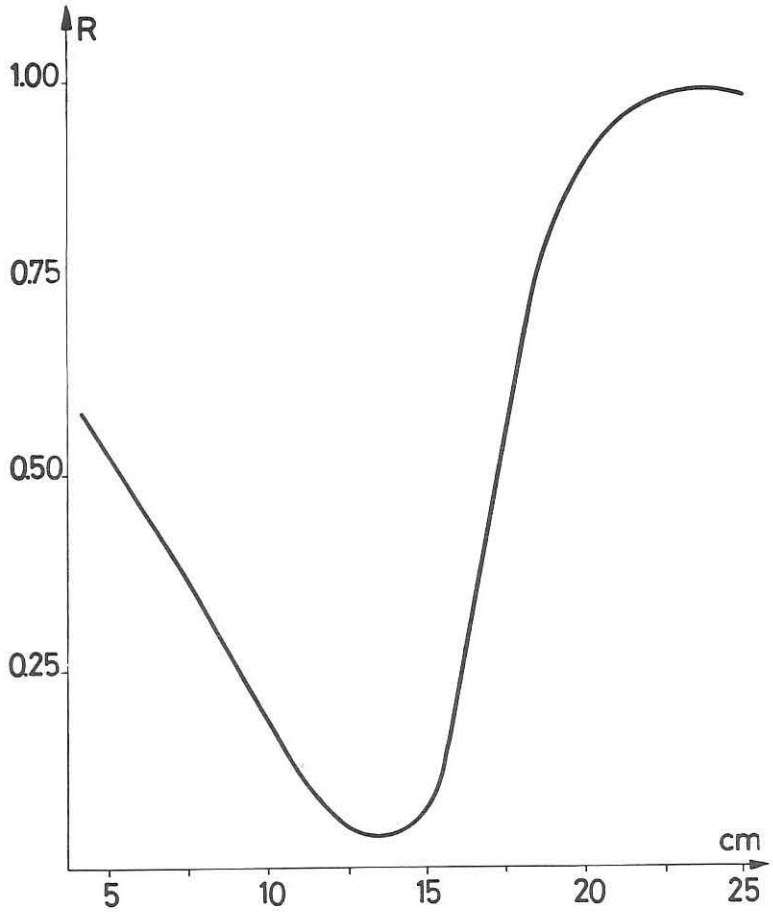

FIG : 2

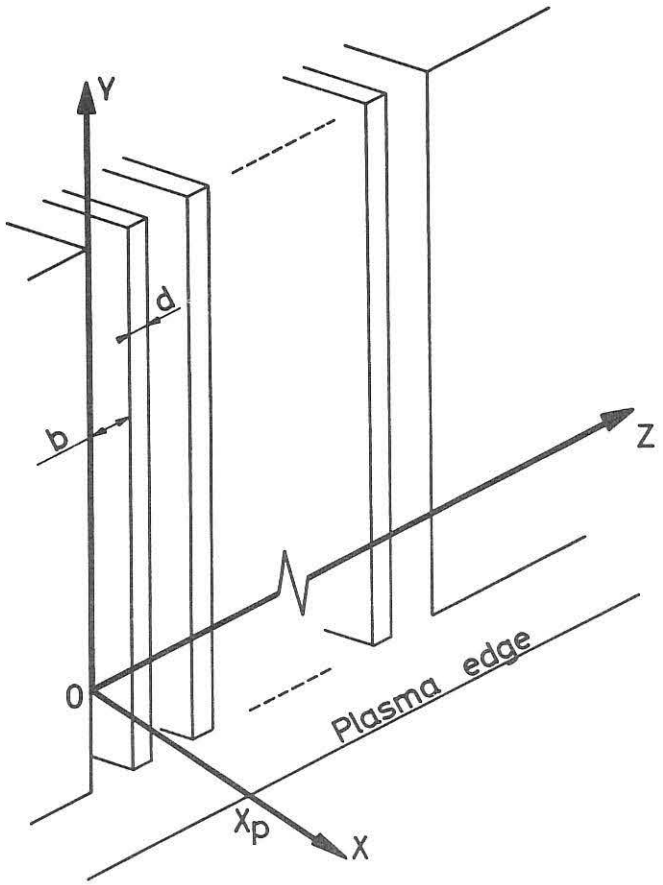

FIG : 1

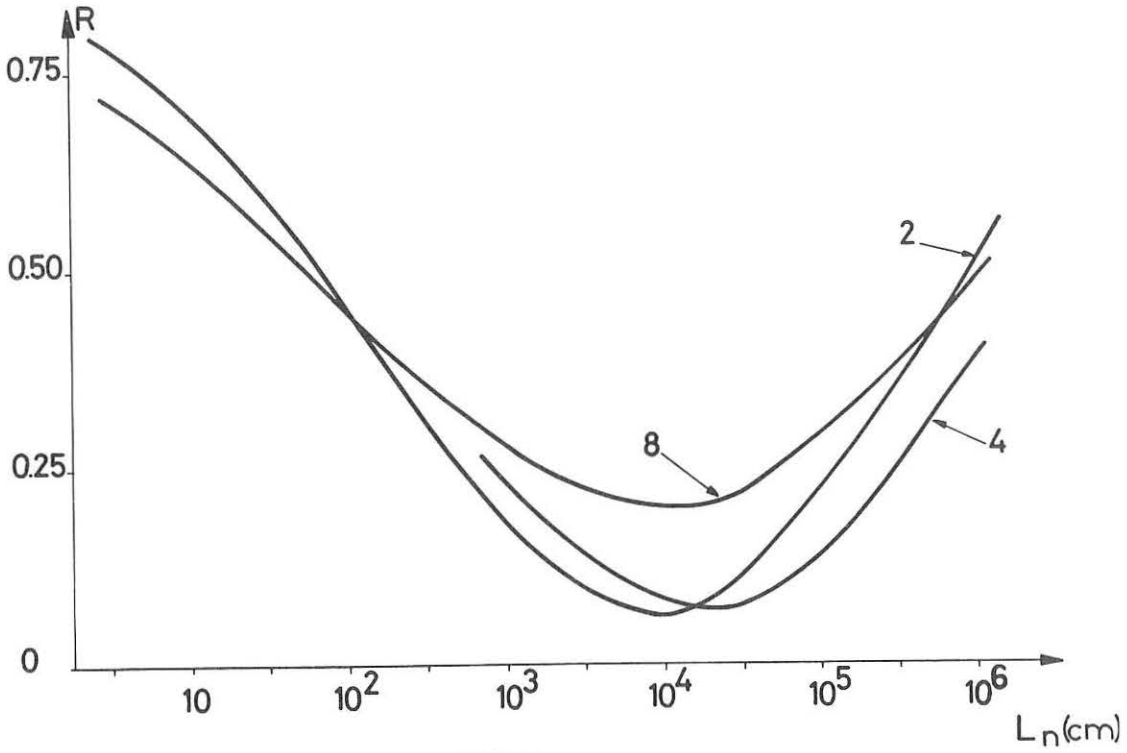
R
0.75
0.50
0.25
0
10
10^2
10^3
10^4
10^5
10^6
L_n(cm)
2
4
8

FIG : 3

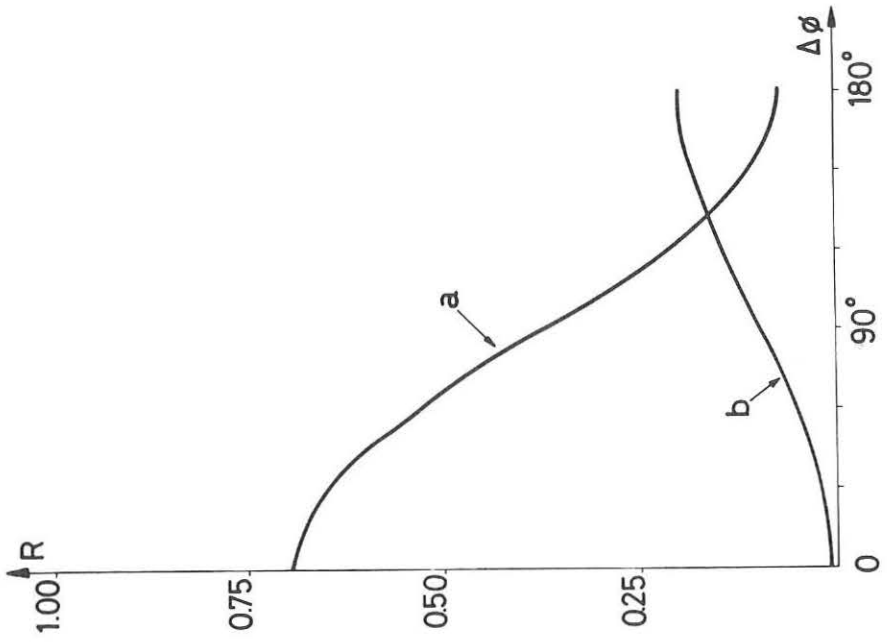
R
1.00
0.75
0.50
0.25
Δφ
180°
90°
0
a
b

FIG : 4

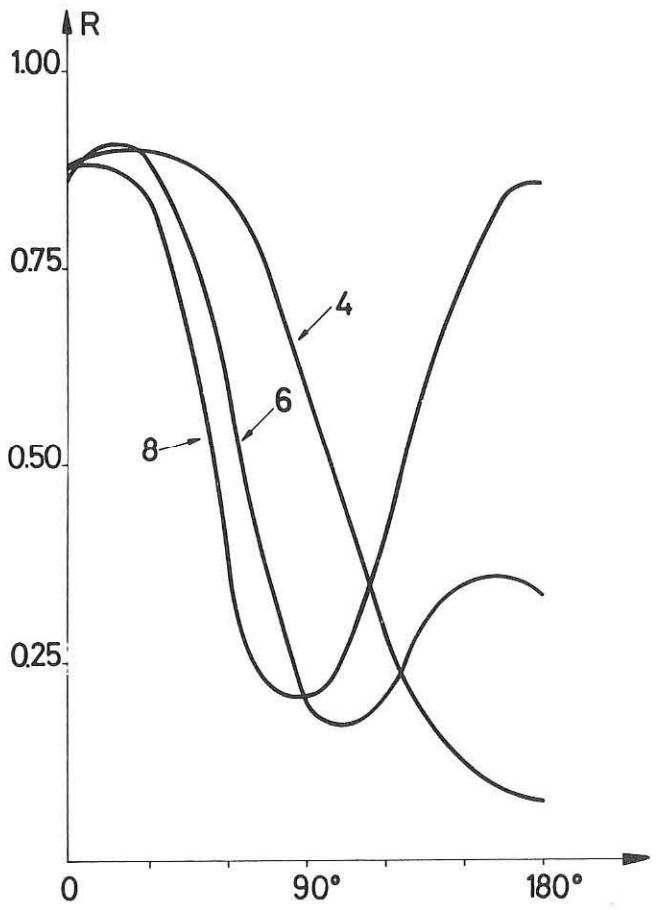
R
1.00
0.75
0.50
0.25
0
90°
180°
4
6
8

ON THE PARAMETRIC HEATING OF PLASMAS OF THERMONUCLEAR INTEREST

Andre Rogister
Institut für Plasmaphysik der Kernforschungsanlage Jülich GmbH
Association EURATOM-KFA
517 Jülich, Federal Republic of Germany

1. INTRODUCTION

It is presently generally accepted that ohmic heating will not be sufficient to bring plasma to ignition temperatures in large toroidal devices and reactors. It is therefore imperative to investigate the potentialities of auxilliary heating methods. The present review aims at describing experimental and theoretical results concerning radio frequency heating, one of the major alternative to supplement ohmic heating in toroidal devices.

Engineering and economics considerations readily limit the discussion to frequencies around and below the lower hybrid frequency of large devices, since relatively cheap sufficient radio frequency power is presently not available and will likely not be available for a long time to come at higher frequencies. We shall therefore not discuss heating by electron cyclotron waves and oscillations near the electron plasma frequency and the upper hybrid frequency; rather we shall merely concentrate on the lower hybrid and ion-cyclotron frequency ranges. We need further to distinguish between linear and non-linear absorption processes. Direct absorption of ion cyclotron waves /1/ and linear mode conversion at the lower hybrid frequency /2/,/3/ belong to the first category; the various parametric instabilities that we shall here discuss belong to the second.

The heart of the problem of parametric instabilities is to transfer the energy of a long wavelength, usually electromagnetic, oscillation (the pump wave) into short wavelength electrostatic waves which are more readily Landau damped in the plasma thereby

producing anomalous absorption and heating. The questions to be answered are twofold: (i) What is the instability mechanism and what are the various electrostatic modes excited? (ii) What is the saturation level of the electrostatic turbulence, the anomalous absorption rate of radio frequency energy and the corresponding plasma heating rate? In the following, we shall analyse these questions successively.

II. IDENTIFICATION OF PARAMETRIC INSTABILITIES

The parametric instabilities, known today, can be classified in three categories:

1) the three-wave resonant decay instability /4/ whereby two slightly damped electrostatic plasma modes of frequencies $\omega_{\underline{k}}^{r}$ and $\omega_{\underline{k}}^{s}$ satisfying the resonance relation

$$\omega_o = \omega_{\underline{k}}^{r} - \omega_{\underline{k}}^{s}$$

[ω_o is the pump frequency, and we assume $|\underline{k}_o| \ll |\underline{k}|$ (dipole approximation)] are driven unstable by the pump wave. The process is really one of nonlinear energy transfer from long wavelength to short wavelength oscillations until an equilibrium is reached between the three waves (obviously such an equilibrium can be attained only for a sufficient pumping level, which besides increases with increasing linear damping of the electrostatic modes).

2) the nonresonant decay instability /5/,/6/ whereby a single electrostatic mode is excited, the energy difference

$$\omega_o - \omega_{\underline{k}} = \underline{k} \cdot \underline{v}$$

being taken up by a particle. This parametric process is akin to the phenomenon of (inverse) nonlinear Landau damping well-known in wave kinetic theory. It can be noted that "quasi-modes", which have no counterpart in equilibrium plasmas (i.e. in the absence of the rf field) appear at the beat frequencies $\omega_o - \omega_{\underline{k}}$;

3) the oscillating two-stream instability /4/ in which case one of the two excited modes has zero frequency (purely growing mode). It seems that this instability will not play an important role in heating experiments; it will not be further discussed here.

Each of the categories listed above can be subdivided according to the nature of the pump wave and the type of excited electrostatic waves. Table I summarizes some of the instabilities which have been considered either theoretically or experimentally (the list is clearly not exhaustive). The first column gives the frequency range and the nature of the pump wave ($\omega_{\ell h}$ is the lower hybrid frequency, ω_{ci} is the ion cyclotron frequency); the second indicates the nature of the excited electrostatic waves, and reference is given in the third and fourth columns to the theoretical and experimental works, respectively.

Frequency range $\omega_o \gtrsim \omega_{1h}$:

We should first like to note that a damped ion acoustic wave can be viewed as a special case of the ion "quasi mode" in the limit where the beat frequency $\omega_o - (\omega_{\underline{k}})_{1h}$ approaches the real part of the frequency of the ion sound wave [$(\omega_{\underline{k}})_{1h}$ is the frequency of the excited lower hybrid wave.] In this limit $\mathrm{Re}\,\epsilon\,[\underline{k}, \omega_o - (\omega_{\underline{k}})_{1h}] = 0$ and the growth rate of the instability usually reaches a maximum as will be evident from the considerations of Sec. III. Clearly the nonresonant instability can excite a much broader spectrum of waves than the resonant instability.

Some of the important experimental results in this frequency range are:

a) Strong heating of the ions has been observed in the direction orthogonal to the magnetic field, whereas the electrons were heated in the parallel direction /17/.
b) The energy in the decay spectrum was observed to be up to twice the energy in the pump wave /9/.
c) Optimum heating is obtained when the pump frequency is in the range $\omega_{1h} \lesssim \omega_o \lesssim 2\,\omega_{1h}$ /14/.

These observations will be compared with the results of an analytical nonlinear theory /12/,/13/ and of two and one-half simulation /8/-in Sec. III.

Frequency range $\omega_{ci} \lesssim \omega_o < \omega_{lh}$.

Important experimental results in this frequency range are

a) Heating takes place mainly in the ionic component;
b) The plasma lifetime was approximately doubled in the experiment of Ref. /20/; this is interpreted as due to the stabilization of long wavelength drift oscillations, which are deleterious to plasma confinement, by the magneto-acoustic wave.

One should emphasize that the theoretical works generally do not take the effect of gradients and shear properly into account, nor do they address themselves to the important question of turbulence saturation levels and anomalous absorption rates. These problems were, however, respectively treated in Ref. /25/ and /12/,/13/. The nonlinear theory of parametric instability in the lower hybrid frequency range will be reviewed in the next Section.

III. THEORY OF PARAMETRIC HEATING IN THE LOWER HYBRID FREQUENCY RANGE

Our purpose now is to briefly review a recent theory /12,13/, which discusses-the nonlinear fate of lower hybrid microturbulence driven parametrically by a whistler pump wave.

Theoretical approach

Assuming that the increments are small compared to the wave frequencies, the starting point of the calculation is to split the distribution functions in three parts

$$f_j = \langle f_j \rangle_{r,t} + (\langle f_j \rangle_r - \langle f_j \rangle_{r,t}) + (f_j - \langle f_j \rangle_r) \equiv F_j + \delta f_j + \delta f_j$$

where the space and time averages are taken over distances and intervals of time long compared to the Debye wavelength (which is the typical length scale of the turbulence; we work in the dipole approximation so that $\lambda_o = 2\pi/k_o \gg \lambda_D \sim 2\pi/k$) and the periods of the waves ($2\pi/\omega_o \sim 2\pi/\omega_k$), respectively. Vlasov's equations for the background distribution functions F_J, the rf pump field distributions f_J and the electrostatic turbulent fluctuations δf_J are coupled through nonlinear terms. The pump wave is essentially described by the cold plasma relations and one easily derives the propagation equation

$$\left(\frac{c^2}{\omega_{pe}^2}\frac{\partial^2}{\partial x_\perp^2} - 1\right)\left[\frac{\omega_{pe}^2}{\omega_{ce}^2}\left(\frac{\partial^2}{\partial x_\perp^2} - \frac{\omega_{pe}^2}{c^2}\right)\frac{\partial^2}{\partial t^2}\Psi + \left(\frac{\partial^2}{\partial t^2} - \omega_{pi}^2\right)\frac{\partial^2}{\partial x_\perp^2}\Psi\right]$$

$$= -c^2\frac{\partial^2}{\partial x_\perp^2}\frac{\partial^2}{\partial x_\parallel^2}\Psi + c^2\left(\frac{\partial^2}{\partial x_\perp^2} - \frac{\omega_{pe}^2}{c^2}\right)\frac{1}{\omega_{ce}}\frac{\partial}{\partial t}\hat{B}\times\frac{\partial}{\partial \underline{x}_\perp}\cdot\left\langle\frac{\partial\delta\Psi}{\partial \underline{x}_\perp}\,\delta n_e\right\rangle_{\underline{r}} \qquad (1)$$

where Ψ is the electrostatic potential of the pump wave ($\underline{e} = -\nabla\Psi - \nabla\times\underline{\chi}$ with $\nabla\cdot\underline{\chi} = 0$), $\delta\Psi$ is the potential of the electrostatic fluctuations, and the subscripts $\perp$ and $\parallel$ refer to the direction $\hat{B}$ of the background (homogeneous) magnetic field. Except for the last term, which describes the interaction with the turbulence, this equation is the well known whistler dispersion relation.

Taking advantage of the fact that $(\omega_{\underline{k}})_{lh} \ll \omega_{ce}$, the Fourier transform of the electron fluctuation distribution function $\delta f_{e,\underline{k}}$ can be written in the form

$$\delta f_{e,\underline{k}} = \delta\bar{g}_{e,\underline{k}}\exp\left[-iz_{\underline{k}}\sin(\varphi-\theta_{\underline{k}})\right]J_o(z_{\underline{k}})$$

$$+\frac{q_e}{m_e}\delta\Psi_{\underline{k}}\frac{1}{v_\perp}\frac{\partial F_e}{\partial v_\perp}\left\{1 - \exp\left[-iz_{\underline{k}}\sin(\varphi-\theta_{\underline{k}})\right]J_o(z_{\underline{k}})\right\} \qquad (2)$$

in the frame moving with the time dependant velocity $\underline{v}_e = c\,\underline{e}\times\hat{B}/B$ induced by the pump field. Here $\varphi = -\tan^{-1}(v_x/v_y)$ is the velocity space angle around the direction of the magnetic field and $\theta_{\underline{k}} = -\tan^{-1}(k_x/k_y)$; $z_{\underline{k}} = k_\perp v_\perp/\omega_{ce}$ and a bar denotes φ-independant quantities or φ averages. $\delta\bar{g}_{e,\underline{k}}$ satisfies a nonlinear Vlasov equation from which the magnetic field has disappeared:

$$\left(\frac{\partial}{\partial t} + i\underline{k}_\perp \cdot \underline{u}_{e\perp} + ik_\parallel v_\parallel\right) \delta\bar{q}_{e,\underline{k}} J_o^2(z_{\underline{k}}) = \frac{q_e}{m_e} \delta\Psi_{\underline{k}}\, ik_\parallel \frac{\partial F_e}{\partial v_\parallel} J_o^2(z_{\underline{k}})$$

$$- \frac{c}{B}\int \frac{d\underline{k}'}{(2\pi)^3}\, \hat{B}\cdot \underline{k}'' \times \underline{k}'\, \delta\Psi_{\underline{k}'}\, \delta\bar{q}_{e,\underline{k}''} \prod_{\underline{\ell}=\underline{k},\underline{k}',\underline{k}''} J_o(z_{\underline{\ell}}) \qquad (3)$$

where $\underline{k}''=\underline{k}-\underline{k}'$. The ion fluctuation $\delta f_{i,\underline{k}}$ essentially satisfies the linear equation

$$\left(\frac{\partial}{\partial t} + i\underline{k}_\perp \underline{v}_\perp\right) \delta f_{i,\underline{k}} = \frac{q_i}{m_i}\, \delta\Psi_{\underline{k}}\, i\underline{k}_\perp \frac{\partial F_i}{\partial \underline{v}_\perp} \qquad (4)$$

($k_\parallel \ll k_\perp$); $\delta f_{e,\underline{k}}$ and $\delta f_{i,\underline{k}}$ are of course coupled through Poisson's equation.

Equations (1-4) where derived without the usual assumption $v_e < c_i \equiv (KT_i/m_i)^{1/2}$. Assuming now

$$\frac{v_{ei}}{c_i} \sim \mu < 1 \quad \text{and correspondingly} \quad \frac{q_e \delta\Psi}{KT_e} \sim \mu < 1 \qquad (5)$$

and expanding in powers of μ, Eqs. (2,4) lead to a wave kinetic equation, whereas (1) yields the expression for the anomalous absorption rate of rf energy. The wave kinetic equation is

$$\frac{1}{2}\frac{\partial N_{\underline{k}}}{\partial t} = (\gamma_{\underline{k}} + \Gamma_{\underline{k}p} + \Gamma_{\underline{k}t})\, N_{\underline{k}} \qquad (6)$$

($N_{\underline{k}}$: plasmon density per mode). $\gamma_{\underline{k}}$ is the linear Landau damping of the lower hybrid waves. $\Gamma_{\underline{k},p}$ is the parametric growth rate and describes the interaction of lower hybrid modes with the pump; in the limit $k_\perp c_e/\omega_{ce} < 1$, which marginally applies for Tokamaks, one finds:

$$\Gamma_{\underline{k},p} \sim -\left[\frac{\partial \epsilon(\underline{k},\omega)}{\partial\omega}\right]^{-1}_{|\omega_{\underline{k}}|} \left(\frac{\underline{k}\cdot\underline{u}_{ei}}{2\omega_o}\right)^2 \frac{|\chi_e(\omega_{\underline{k}}-\omega_o,\underline{k})|^2}{|\epsilon(\omega_{\underline{k}}-\omega_o,\underline{k})|^2} \operatorname{Im}\chi_i(|\omega_{\underline{k}}|-\omega_o,\underline{k}) + P_{ei} \qquad (7)$$

[$\chi_{i(e)}$: ion (electron) susceptibility; ϵ : dielectric function]. It is worth noting here that the parametric growth rate would usually reach its maximum value should $\operatorname{Re}\epsilon(\omega_{\underline{k}}-\omega_o,\underline{k})$ vanish (the frequency difference $\omega_o-\omega_{\underline{k}}$ approaching, e.g. the (real part) of the ion sound frequency in a plasma with $T_e \gg T_i$. $\Gamma_{\underline{k},t}$ describes the nonlinear interaction of lower hybrid modes

among themselves:

$$\Gamma_{\underline{k},t} \cong -\left[\frac{\partial \epsilon(\underline{k},\omega)}{\partial \omega}\right]^{-1}_{\omega_{\underline{k}}} \omega_{\underline{k}}^{-1} \frac{c^2}{B^2} \int d\underline{k}' \,(\hat{B}\cdot \underline{k}\times\underline{k}')^2 \, I_{\underline{k}'} \frac{k''^2}{k^2} \frac{1}{k''_{\parallel}} \left(\frac{k_{\parallel}}{\omega_{\underline{k}}} - \frac{k'_{\parallel}}{\omega_{\underline{k}'}}\right)$$

$$\times\left[1 + \frac{1}{2} \frac{\omega_{\underline{k}} - \omega_{\underline{k}'}}{k''_{\parallel}} \left(\frac{k_{\parallel}}{\omega_{\underline{k}}} - \frac{k'_{\parallel}}{\omega_{\underline{k}'}}\right)\right] \frac{|\chi_e(\omega_{\underline{k}} - \omega_{\underline{k}'}, \underline{k}'')|^2}{|\epsilon(\omega_{\underline{k}} - \omega_{\underline{k}'}, \underline{k}'')|^2} \, \mathrm{Im}\,\chi_i(\omega_{\underline{k}} - \omega_{\underline{k}'}, \underline{k}'') + P(e \rightleftharpoons i) \tag{8}$$

($\underline{k}''=\underline{k}-\underline{k}'$. $I_{\underline{k}}=k^{-2}\,[\partial\epsilon(\underline{k},\omega)/\partial\omega]^{-1}\,N_{\underline{k}}$). The similarity of structure between $\Gamma_{\underline{k},t}$ and $\Gamma_{\underline{k},p}$ as one lets $\underline{k}'\rightarrow 0$ and $\omega_{\underline{k}}\rightarrow\omega_0$ is particularly striking since $c^2(i_z\cdot\underline{k}\times\underline{k}')^2 I_{\underline{k}'}/B^2$ can be identified with $(\underline{k}\cdot\underline{u}_{\underline{k}'})^2$.
The saturation level of the turbulence is estimated from

$$\int d\underline{k}\; \omega_{\underline{k}} N_{\underline{k}} \,(\gamma_{\underline{k}} + \Gamma_{\underline{k},p} + \Gamma_{\underline{k},t}) = 0 \,. \tag{9}$$

Note that from the right-hand-side of (8) only the second term contributes to the above integral and corresponds to damping; the first term integrates out and thus corresponds to pure energy transfer through $\underline{k}$-space.
Finally the anomalous absorption rate of rf power is given by

$$\nu_a = \left[\left(1 + \frac{\omega_{pe}^2}{\omega_{ce}^2}\right) + \frac{\omega_{pi}^2}{k_o^2 c_A^2}\right]^{-1} \frac{c^2}{B^2} \int d\underline{k}\,(\hat{B}\cdot\underline{k}\times\underline{k}_o)^2 \, I_{\underline{k}} \frac{k^2}{k_o^2} \frac{1}{|\omega_o|}$$

$$\frac{|\chi_e(\omega_{\underline{k}} - \omega_o, \underline{k})|^2}{|\epsilon(\omega_{\underline{k}} - \omega_o, \underline{k})|^2} \, \mathrm{Im}\,\chi_i(\omega_{\underline{k}} - \omega_o, \underline{k}) + P(e \rightleftharpoons i) \tag{10}$$

Results: (1) We note that $\Gamma_{\underline{k},p}$ will be largest when $|\omega_o| - |\omega_{\underline{k}}| \simeq |k_{\parallel}|\, c_e \simeq k_{\perp} c_i$. Since $(|k_{\parallel}|\, c_{e\parallel},\, k_{\perp} c_i) \ll |\omega_{\underline{k}}|$, this implies the existence of an optimum pumping frequency: $\omega_o \cong \omega_{1h}(1+T_i/T_e)^{1/2}$. This result agrees well with experimental conclusions /14/
(2) At saturation and for a pump frequency chosen according to (1) the ratio of the electrostatic energy density of turbulence estimated from Eq.(9) to the energy density of the pump is of the order $\omega_o/\Delta\omega$ where $\Delta\omega$ is a measure of the frequency width of the excited modes. This ratio is estimated to be of order 3-4. This result should be compared with the experimental finding of Hooke and Bernabei /9/ that "By careful adjustment of the plasma parameters, however, the integrated energy in the

decay in some cases was observed to exceed that in the pump wave by a factor 2". Simulation in 2 1/2 D also leads to the same conclusion. Note that the right-hand-side of Eq. (8) vanishes in one dimension; this explains why 1 D simulation /7/ yields unrealistic results.
(3) The particle kinetic equation shows that heating is essentially parallel to $\hat{B}$ for the electrons and perpendicular for the ions. This result is also borne out by numerical simulation /8/ and by experiments /17/.

In order to illustrate the results obtained in this work, we have computed in table II, for reactor parameters, the absorption rate of electromagnetic energy ν_a, the plasma heating rate ν_h, the parameter u_e/c_i in the plasma core, where the energy must be deposited and the corresponding electric field at the plasma vacuum interface $|\underline{e}|_v$, as a function of the central density N assuming that the absorption length l_a, i.e. the thickness of the heated layer, is of the order of the plasma radius. It should here be noted that

$$l_a = \frac{\partial \omega_o / \partial k_{o\perp}}{\nu_a} \lesssim \frac{c_A}{\nu_a}$$

(c_A = Alfvén speed in plasma core), is inversely proportional to the turbulence level and thus to the pump energy density. For the calculation we assumed $T_e = T_i$ and the optimum frequency $\omega_o = 2^{1/2}\omega_{lh}$ has been chosen.

REFERENCES

/1/ See the Review Paper by W. Hooke, "Selected Topics in Radio Frequency Heating of Toroidal Plasmas", International School of Plasma Physics, Varenna, Italy (1971); published by the Commission of the European Communities, Luxembourgh, EUR 267 (1974)

/2/ T.H. Stix, Phys. Rev. Lett. 15, 878 (1965)

/3/ V.E. Golant, M.V. Krivoskeev and V.I. Federov, Zh. Tek. Fiz 40, 382 (1970) [Sov. Phys. Tech. Phys. 15, 282 (1970)]

/4/ K. Nishikawa, J. Phys. Soc. Japan 24, 916, 1152 (1968)

/5/ N. Martinov and A. Samain, Plasma Phys. 15, 783 (1973)

/6/ K.D. Harms, G. Hasselberg and A. Rogister, Nucl. Fusion 14, 251 (1974)

/7/ J.M. Kindel, H. Okuda and J.M. Dawson, Phys. Rev. Lett. 29, 995 (1972)

/8/ C.Chu, J.M. Dawson and H. Okuda, PPG-219, UCLA (1975)

/9/ W.M. Hooke and S. Bernabei, Phys. Rev. Lett. 29, 1218 (1972)

/10/ V.I. Farenik, V.V. Vlasov and A.M. Kozhkov, Zh. ETF Pis. Red. 18, 409 (1973) [JETP Lett. 18, 240 (1973)]

/11/ M. Porkolab, Phys. Fluids 17, 1432 (1974)

/12/ A. Rogister, Phys. Rev. Lett. 34, 80 (1975)

/13/ A. Rogister and G. Hasselberg, to appear in Phys. Fluids

/14/ R.P.H. Chang and M. Porkolab, Phys. Rev. Lett. 32, 1227 (1974)

/15/ M. Brusati, G. Cima, M. Fontanesi and E. Sindoni, Lettere al Nuovo Cimento, 10, 67 (1974)

/16/ A.K. Sundaram and P.K. Kaw, Nucl. Fusion 13, 901 (1973)

/17/ A.B. Kitsenko, V.I. Panchenko, K.N. Stepanov and V.F. Tarasenko, Nucl. Fusion 13, 557 (1973)

/18/ V.V. Alikaev, Yu.I. Arsen'ev, G.A. Bobrovskii, V.I. Poznyak, K.A. Razumova, and Yu.A. Sokolov, in Controlled Fusion and Plasma Physics (Proc. 6th Europ. Conf. Moscow) 1, 63 (1973)

/19/ A.A. Ivanov and V.V. Parail, Zh. Eksp. Teor. Fiz. 62, 932 (1972) [Sov. Phys. JETP 35, 494 (1973)]

/20/ V.L. Vdovin, O.A. Zinov'ev, A.A. Ivanov, L.L. Kozorovitskii, M.F. Krotov, V.V. Parail, Ya.R. Rakhimbabaev, V.D. Rusanov and N.Y. Shapotkovskii, Zh. ETF Pis.Red. 17, 4 (1973) [JETP Lett. 17, 2 (1973)]

/21/ V.L. Vdovin, O.A. Zinov'ev, A.A. Ivanov, L.L. Kozorovitskii, V.V. Parail, Ya.R. Rakhimbabaev and V.D. Rusanov, Zh. ETF Pis. Red. 14, 228 (1971) [JETP Lett. 14, 149 (1971)]

/22/ K.D. Harms, G. Hasselberg and A. Rogister, Nucl. Fusion 14, 657 (1974)

/23/ A.B. Kitsenko and K.N. Stepanov, Zh. Eksp. Teor. Fiz. 64, 1606 (1973) [Sov. Phys. JETP 37, 813 (1973)]

/24/ J.L. Sperling and F.W. Perkins, Phys. Fluids 17, 1857 (1974)

/25/ J.L. Sperling and F.W. Perkins, MATT-1126, Princeton (1975)

TABLE 1

Pump wave	Decay waves	Theoretical works	Experimental works	Remarks
$\omega_{LH} \lesssim \omega_0$ (low frequency whistler or lower hybrid mode)	1) lower hybrid wave + ion acoustic wave	Kindel et al. /7/ Chu et al. /8/	Hooke a. Bernabei /9/ Farenik et al. /10/	
	2) lower hybrid wave + ion "quasi-mode"	Porkolab /11/ Rogister and Rogister a. Hasselberg /12,13/	Chang a. Porkolab /14/	Nonresonant interaction
	3) lower hybrid wave + ion cyclotron wave		Brusati et al. /15/	
	4) lower hybrid wave + low frequency drift wave ($\omega \ll \omega_{ci}$) or drift cyclotron wave ($\omega \simeq \omega_{ci}$)	Sundaram a. Kaw /16/		Low frequency waves which may be the byproduct of parametric heating schemes, can be deleterious to plasma confinement.
	5) non identified		Kitsenko et al. /17/ Alikaev /18/	

Pump wave	Decay waves	Theoretical works	Experimental works	Remarks
	Ion cyclotron wave + short wave length drift wave	Ivanov and Parail /19/	Vdovin et al. /20,21/	
	Ion Bernstein waves + quasi modes	Martinov a. Samain /5/ Harms et al. /6/		nonresonant interaction
$\omega_{ci} \leq \omega_0 < \omega_{lh}$ (magneto-acoustic waves)	A pair of Ion Bernstein waves	Harms et al. /6,22/ Kitsenko and Stepanov /23/		The instabilities considered in /22/ and /23/ are driven by the relative drift between two ion species.
	A pair of Ion cyclotron waves	Sperling a. Perkins /24,25/		The instability is driven by the relative drift between two ion species.

TABLE II

B = 100 kG, T = 5 keV, a = 200 cm, $l_a = a/s$

$N(cm^{-3})$	1.10^{14}	2.10^{14}	3.10^{14}
$\omega_o(sec^{-1})$	$1.2\ 10^{10}$	$1.7\ 10^{10}$	$2.0\ 10^{10}$
$\nu_a(sec^{-1})$	$1.5\ 10^{7}$	$1.1\ 10^{7}$	$0.9\ 10^{7}$
$\nu_H(sec^{-1})$	22	4.4	1.8
$\frac{u_e^2}{c_i^2}$	$1.5\ 10^{-3}$	$0.85\ 10^{-3}$	$0.6\ 10^{-3}$
$X_{tp}(cm)$	1.3	4.7	6.6
$e_v(V/cm)$	500	1150	4000

INTERACTION OF INTENSE ELECTROMAGNETIC RADIATION WITH PLASMA

N.L. Tsintsadze
Institute of Physics, Academy of Sciences of the Georgian SSR, Tbilissi, USSR

I.R. Gekker
Lebedev Physical Institute, Academy of Sciences of the USSR Moscow, USSR

The progress in laser and high frequency engineering led to such conditions when nonlinear processes of various types appear in the interaction of the incident electromagnetic radiation with plasma. They manifest themselves in anomalously strong absorption of wave energy in the collisionless plasma, electron and ion heating, self-effect of the wave on plasma, creation of plasma turbulence, etc. A considerable number of theoretical and experimental works is devoted to the above problems including a series of review papers and monographs /1-7/. The obtained information is of essential interest for understanding many physical phenomena occurring in plasma when intense electromagnetic wave falls on it. It is noteworthy that the success in the development of the theory and numerical experiment in this little studied field of science and in experiments in the UHF wave range and recently in HF and laser ranges is essential. The physical unity of the studied phenomena allows to study the interaction processes of electromagnetic waves with plasma in the wide range of wavelengths, thus obtaining data which supplement each other.

Representations of the linear electrodynamics, in the framework of which many investigations have been accomplished (for instance /5/), become non-acceptable at large values of the strength of the electric field E_o when

the plasma pressure is comparable to that of the wave $n\kappa T \simeq E_o^2/8\pi$, or, for the case $\omega \simeq \omega_{pe}$, when the thermal velocity of the electron $V_{T_e} = \sqrt{\frac{\kappa T_e}{m}}$ becomes comparable with that of the electron oscillating in the wave electric field $V_E = \frac{eE_o}{m\omega}$ i.e. when $V_{T_e} \cong V_E$. Note that under certain conditions, say near the plasma resonance, the nonlinear effects are observed due to the considerable field amplification at $V_E \ll V_{T_e}$. Condition $V_E \simeq V_{T_e}$ is easily fulfilled in UHF range (for hydrogen plasma at $\lambda = 10$ cm, $\omega = 2 \times 10^{10} sec^{-1}$, $n_c = 10^{11}$ cm^{-3} and $T_e = 1$ eV we have $V_E \simeq V_{T_e}$ at $E_o = 300$ V/cm) and noteably hard in the optical range (for hydrogen plasma and neodim laser at $\lambda = 1.06$ microns, $\omega = \omega_{pe} = 2 \times 10^{15}$ sec^{-1}, $n_c = 10^{21}$ cm^{-3} and $T_e = 1$ KeV we have $E_o = 10^9$ V/cm or $P = 2 \times 10^{15}$ W/cm^2).

Recent years are characterized by an increase in the number of papers on the interaction of electromagnetic waves with plasma. We shall note the most important results (in our opinion).

Theory:

1) Study of the effect of inhomogeneity of the spatial distribution of plasma particles on the thresholds of the parametric instability development.

2) Investigation on nonlinear theory of plasma oscillations (saturation, stabilization, etc.).

3) Study of mechanisms of particle acceleration in plasma.

4) Development of research in linear and nonlinear wave transformation in plasma.

5) Increase of the computer experiments.

6) Tendency towards comparison of the theoretical and experimental results.

Experiment:

1) Observation and connection with the parametric instability of nonlinear phenomena in the interaction of intense laser radiation with the plasma created by it (absorption, generation, harmonics, oscillations, intense light reflection).

2) Creation of stationary plasma in large volumes and measurements in the range of plasma resonance (cavitons, particle acceleration, wave acceleration, etc.).

3) Obtention of experimental plots of the effective particle collision frequency versus UHF field strength as predicted by the theory.

There are parametric instabilities of the following types [8]:
1) Aperiodic when quasi decay of the transverse wave t into a Langmuir wave ℓ takes place.

2) Periodic (potential, parametric, decay) when the decay of $t \to \ell + s$ type takes place, where s is the ion-sound wave (range of existence $\omega \simeq \omega_{pe}$).

3) Decay into two plasmons (electron Langmuir oscillations) $t \to \ell + \ell$ (range $\omega_{pe} \simeq \frac{1}{2}\omega$).

4) Stimulated Mandelstam-Brillouin (SSMB) scattering into ion-sound oscillations with the decay of $t \to t' + s$ type (range $\omega \geq \omega_{pe} > \frac{M}{2m} \frac{V_{Te}^2}{c^2} \omega$).

5) Stimulated combined scattering (SCS) into electron Langmuir oscillations with the decay of $t \to t' + \ell$ type (range $\omega > \omega_{pe} > \frac{V_{Te}^2}{c^2} \omega$).

6) Decay of the plasma wave $\ell \to \ell + s$ (range $\omega_{pe} \leqslant \omega$).

Apart from the above mentioned instabilities a great attention is given to the relativistic effects in plasma. The point is that by developing the laser technique it is possible to obtain strong radiation fields for which the ordered velocities of the electrons may become comparable with the light velocity. Taking into account the relativistic character of the electron motion in the external alternating field leads to the fact that the parameter of the medium-electron mass undergoes an oscillation with the frequency of the external field. In its turn the oscillation of the electron mass leads to a sufficient change in the dispersive properties of plasma and to the excitation of the potential and nonpotential plasma oscillations [9-15].

The given review presents some new papers on the nonlinear interaction of the electromagnetic fields with plasma, and the importance of the obtained results is discussed.

S.V. Bulanov and L.M. Kovrizihnikh /16/ have considered the stimulated Langmuir oscillations of the inhomogeneous plasma in the two-fluid approximation. In addition to the linear mechanisms connected with collisions and transformation of waves, the nonlinear phenomena of the type of self-crossing of the electron trajectories are studied which arise due to plasma inhomogeneity or to relativistic effects and may lead to the limitation of the electromagnetic field amplitude in the range of plasma resonance. For cold plasma, maximum values of the field increase towards the resonance. In the general case the ratio of the external fields E_o amplitude to its maximum value at the resonance E_m is finite and equal to:

$$\frac{E_o}{E_m} = S = \max\left\{ S_\nu = \frac{\nu}{\omega} , S_T = \left(\frac{r_{pe}}{L}\right)^{2/3} , S_H = \left(\frac{r_E}{L}\right)^{1/2} , S_p = \left(\frac{r_E}{\lambda}\right)^{2/3} \right\}$$

where ν is the collision frequency, ω is the external field frequency, $L = \left[\frac{\partial \ell n\, n}{\partial x} \right]^{-1}$ characteristic size of the plasma inhomogeneity, $r_{pe} = \sqrt{\frac{3\kappa T}{m\omega_p^2}}$ Debye length of electrons, $r_E = \frac{eE_o}{m\omega^2}$ amplitude of electron oscillations in the field of the pump wave.

The size of the field localisation in the resonance region is of the order of $\Delta x \simeq sL$, the establishing time of the maximum value of the field is $\tau \sim \frac{1}{s\omega}$. For the case $\omega = 2 \times 10^{10}\,sec^{-1}$, $T_e = 3$ eV, $\lambda = 10$ cm, $n = 2 \times 10^{10}$ cm^{-3}, $E_o = 1$ kV/cm, we have $S_\nu = 10^{-8}$, $S_T = 4 \times 10^{-3}$, $S_H = 2 \times 10^{-2}$ and $S_p = 2 \times 10^{-2}$. Hence in this case the most important are nonlinear effects in comparison with the collisions and spatial dispersion. For the laser plasma $\omega = 2 \times 10^{15}\,sec^{-1}$, $T_e = 1$ KeV, $L = 10\ cm^{-2}$, $E_o = 3 \times 10^7$ V/cm we have $S_\nu = 10^{-6}$, $S_T = 6 \times 10^{-3}$, $S_H = 10^{-3}$, $S_p = 9 \times 10^{-3}$, i.e. S_T and S_p turn to be comparable. Further, they [17] have studied the effect of the localised high frequency field on the distribution function of electrons in a weakly collisional plasma. Nonadiabaticity of the particle interaction with the

field in the resonance (due to rare collisions) at $V_E \gg V_{T_e}$ leads to the appearance of the group of accelerated electrons with velocities up to $\sim 2\,V_E$. In the first case of the high frequency interaction when $S = 2 \times 10^{-2}$ we obtain the particle energy of the order of 100 - 400 eV at the density of $2 \times 10^{8}\,cm^{-3}$, in the second case (laser) at $S = 6 \times 10^{-3}$ we have $\sim$ 60 keV and $5 \times 10^{12}\,cm^{-3}$ respectively.

In the case when maximum field amplitude is determined by the value S_H, the electron oscillation amplitude in the resonance region is of the order of the width of the resonance region and hence the electron motion becomes nonadiabatic also in the absence of the collisions. This nonadiabaticity is also the cause of the appearance of fast electrons with the energy of the order of eE_oL.

The density of the accelerated particles is $\sim n$.

V.I. Barinov, I.R. Gekker, V.A. Ivanov, D.M. Karfidov /18-20/ have studied the interaction of a pulsed UHF radiation in the 10 cm range with the flow of a collisionless plasma in a waveguide, for initial conditions both favourable and unfavourable for the manifestation of the linear transformation of the waves. It is shown that in the wide range of UHF output change interval corresponding to $V_E/V_T = 10^{-5}$-10 the absorption coefficient $|D|^2$ under the conditions of linear transformation $\left(\frac{n}{n_c} \gtrsim 1,\ \vec{\Delta}\, n \parallel \vec{E}\right)$ is approximately constant. The absorption comes instantaneously ($t < 0.01$ μsec), is accompanied by the fast decay of plasma and generation of the accelerated electrons. For initial conditions unfavourable for the linear transformation ($\vec{\Delta}\, n \perp E$), the anomalous strong absorption arises with a time delay (1 - 3 μsec) when the wave pressure exceeds the plasma pressure $\left(\frac{E_o^2}{8\pi} \gtrsim nkT_e\right)$. The notable absorption is preceded by the deformation of the front plasma increase at the dominating increase of the concentration in the central part of the flow. The mentioned peculiarities of the "anomalous" absorption and a series of other specificites allow to connect it with the so-called "slow" nonlinear phenomena, caused by the variation of plasma parameters under the effects of the incident wave pressure. They lead in the end to the rise of the favourable conditions for the linear transformation.

The possibility of UHF energy absorption in plasma beyond the range of linear transformation ($\omega < \omega_{He}$) was experimentally studied in the paper of S.I. Nanobashvili, G.I. Rostomashvili, N.L. Tsintsadze /21/. The experiments were done with a stationary plasma obtained in a UHF discharge (f = 2400 MHz, P = 150 W), located in a longitudinal homogeneous magnetic field of 0 ÷ 1400 Gauss. Argon was used as the operating gas at the pressure of 10^{-5}-10^{-2} Torr. Effective absorption of waves up to 1.6 times exceeding the cyclotron magnetic field was found. The connection of this phenomena with nonlinear processes was established. The authors /24/ have studied the nonlinear effects in the interaction of UHF waves with plasma in the range of linear transformation ($\omega > \omega_{He}$). It turned out that for a field strength of the pumping wave $E_o \simeq 30$ V/cm the satellite near the Langmuir frequency arises and the ion sound appears, i.e. the decay of the external electromagnetic wave into the plasma wave and ion sound ($t \rightarrow \ell + s$) takes place.

In /23/ the interaction of modulated UHF oscillations with the magnetoactive plasma was studied experimentally. It was shown, that when the modulation frequency is near the ion-cyclotron frequency, the effective absorption of the modulation frequency by plasma takes place. This fact, obviously, gives the possibility to heat simultaneously the electron and ion components of plasma.

In the work of L.L. Pasechnik, V.V. Pustovalov, V.F. Semenyuk, V.P. Silin, V.T. Tikhonchuk /24/ a detail comparison of the theoretical and experimental results on the parametric turbulence caused by the decay excitation of fast magnetosonic wave and the oscillations at the frequency of the lower hybrid resonance in the magnetoactive plasma was performed. The investigations were carried out on a plasma created with a capacitive HF discharge (f = 20 - 40 MHz) located in a longitudinal homogeneous magnetic field of 300 - 2000 Gauss. Helium was the operating gas at the pressure of $(1\text{-}7) \times 10^{-3}$ Torr, the electron concentration was $(0.2\text{-}2) \times 10^{9}$ cm^{-3} and T_e = 3-7 eV. It was shown that all the phenomena found in the experiment- instability threshold, characteristic wave numbers of the excited oscillations, instability increment

and its time variation, the number and energetic distribution of the generated fast electrons and the stationary amplitude of low frequency oscillations- may be explained on the basis of the parametric resonance theory in plasma taking into account the finite pumping wave length and the quasilinear theory of parametric turbulence. It was also shown that the parametric instability is stabilized due to the quasilinear effect of particle redistribution of plasma over the velocities, leading to the generation of fast electrons. The theoretical and experimental results are in good qualitative and quantitative agreement.

A.A. Galeev, R.Z. Sagdeev, Yu.S. Sigov, V.D. Shapiro, V.I. Shevchenko /25/ considered the nonlinear theory of plasma oscillations. In the absence of the pumping wave the self-consistent solutions of the nonlinear equation describing the evolution of plasma waves have been found. On the basis of the obtained solutions the possibility of wave "Collapse" in the two- and three-dimensional cases discussed depending upon the symmetrc rate of the initial conditions. In the presence of the pumping wave the effect of phase mixing on the interaction of plasma turbulence with the pumping wave was considered. Assuming that the main process of conversion to shorter wavelength is the Langmuir wave collapse, the turbulence spectrum was obtained on the basis of Kolmogorov's hypothesis.

O.N. Krokhin, Yu.A. Mikhailov, V.V. Pustovalov, A.A. Rupasov, V.P. Silin, G.V. Sklizkov, A.S. Shikanov /26/ studied the direction of the reflected light and X-ray radiation in laser plasmas. The experiments were done at the focusing of the linearly polarized laser beam (λ = 1.06 μ) onto the surface of solid target for a flux density of 10^{14} W/cm^2 and a pulse duration $\sim$ 3 ns. It was found that a portion of light of some percent remained unsaturated by laser plasma is reflected by it in mirror at normal and oblique incidence of laser beam on the surface of alluminium and polyethylene targets; at normal incidence a considerable part of the reflected light fell into the body angle of the focusing system. The study of the time variation of the second harmonics radiation (λ = 0.53 μ) showed that, differing from the reflected radiation on the main frequency, the intensity of the second harmonics does not oscillate in time. In the energy range of 2 - 4 KeV an

anisotropy in the X-rays emission was found (of the order of 200 - 300 %) in the direction perpendicular and parallel to the laser beam polarization vector. The obtained experimental result is interpreted on the basis of the representations of the theoretic parametric effect of radiation of great power on plasma.

N.L. Tsintsadze, D.D. Tskhakaya /27/ considered the effect of the relativistic character of electron motion on the propagation of nonlinear waves in plasma. A conclusion of the bounded system of hydrodynamical equations of plasma is given not limiting the amplitude value of the external HF wave (electron velocity in the external field $v < c$). If the external field is polarized circularly, the system of equations discribing the interrelating slow and fast transverse plasma motions has a form of

$$\frac{\partial n_i}{\partial t} + \operatorname{div}\left(n_i \vec{v}_i\right) = 0$$

$$\frac{\partial \vec{p}_i}{\partial t} + \vec{v}_i \frac{\partial}{\partial \vec{r}} \vec{p}_i = - m_e c^2 \frac{\partial}{\partial \vec{r}} \sqrt{1 + |\vec{p}|^2 / m_e^2 c^2} - T_e \frac{\partial}{\partial \vec{r}} \ell n\, n_i$$

$$\operatorname{rot}\operatorname{rot} \tilde{\vec{p}} + \frac{1}{c^2} \frac{\partial^2 \tilde{\vec{p}}}{\partial t^2} + \frac{4\pi e^2 n_i}{m_e c^2} \frac{\tilde{\vec{p}}}{\sqrt{1 + |\vec{p}|^2 / m_e^2 c^2}} = 0 \qquad (1)$$

These equations are correct under the conditions that the sizes of plasma inhomogeneities are much greater than the distances traveled by an electron in a period of the external HF wave. The amplitude of the fast transverse pulse of electrons is related to that of the HF wave by the ratio $\tilde{\vec{p}} = \frac{e \vec{E}_0}{\omega}$.

In conclusion, one may say that the nonlinear phenomena found in the interaction of intense electromagnetic waves with collisionless plasma have a general character. The theoretical investigations and the experimental results obtained in HF, UHF and laser ranges of wavelengths compel to think that anomalous absorption of radiation and plasma heating are connected with nonlinear wave transformation, plasma parametric instability. The nonlinear character of the observed phenomena is expressed in the availability of threshold values for the field strength, appearance of accelerated particles, increase of the effectice collision frequency, perturbation of the oscillations of different types, etc. Further investigations should be directed towards broadening the experimental conditions, increasing the measurement precision and removing the possible influence of the by-pass processes, making the theoretical models closer to the experimental schemes. Direct measurements of plasma oscillations, radiations spectra, perturbation increments, charged particle spectra and their development in the time and space are of essential importance.

It is obvious that the study of the phenomenon of anomalous wave dissipation in plasma is useful to perform in different frequency ranges, using the conditions facilitating the measurements of any parameter and the comparison of the obtained results. The computer experiments are also of great importance despite some limitation.

The obtained information got at present on the specifities of the nonlinear effect of waves on plasma may promote not only a better understanding of the physical processes occurring at the interaction of the intense electromagnetic radiation with plasma, but also open definite hopeful perspectives in the realization of laser nuclear fusion with moderate radiation sources and broadening the possibilities of UHF and HF plasma heating in the magnetic traps of thermonuclear reactors.

REFERENCES

/1/ V.P. Silin, Uspekhi Fiz.nauk.108, 625 (1972).

/2/ V.P. Silin, A Survey of Phenomena in Ionized Gases, Vienna, 205 (1968).

/3/ V.P. Silin, Parametric Radiation Effect of a High Power on Plasma, M., "Nauka", 1973.

/4/ P.Co, J. Dawson, W. Kruer, C. Oberman, E. Valeo, Quantum Electronics, No 3, 3 (1971).

/5/ V.E. Golant, A.D. Pilia, Uspekhi Fiz,nauk, 104, No 3, 413 (1971).

/6/ V.E. Golant, A.D. Pilia, Problems of Modern Physics,M,"Nauka", 92 (1974).

/7/ I.R. Gekker, Proc.2nd Meeting on Plasma Physics and Technique (1968) Review Papers, Rostok, 56 (1970).

/8/ N.G. Basov. O.M. Krokhin, V.V. Pustovalov, A.A. Rupasov, V.P. Silin, G.V. Sklizkov, V.T. Tichonchuk, A.S. Shikanov, Lebedev Inst.Preprint No 17 (1974).

/9/ N.L. Tsintsadze, JETP 59, 1251 (1970).

/10/ D.D. Tskhakaya, M.Y. El-Ashri, Proc.Vth Europ.Conf.on Nucl.Fis.and Plasma Phys. Grenoble, August 1972.

/11/ N.L. Tsintsadze, D.D. Tskhakaya, M.Y. El-Ashri, Problems of Plasma Physics Theory, Proc.Conf.Plasma Theory, Kiev, October 1971.

/12/ N.L. Tsintsadze, D.D. Tskhakaya, Tenth Int.Conf.Phen.Ionized Gases, 1971, Oxford, England, 13-18, 1971, p.352.

/13/ E.M. Khirseli, N.L. Tsintsadze, Tenth Int.Conf.Phen.Ionized Gases,1971 Oxford, England, 13-18, 1971, p. 318.

/14/ E.M. Khirseli, N.L. Tsintsadze, Problems of Plasma Theory, Proc.Conf. Plasma Theory, Kiev, 19-23 October 1971.

/15/ E.M. Khirseli, JTP, 49,26 (1973).

/16/ S.V. Bulanov, L.M. Kovrizhnikh, Plasma Physics (in press), 1, No 6 (1975).

/17/ S.V. Bulanov, L.M. Kovrizhnikh, Pis'ma v JETP (in press), 1975.

/18/ V.I. Barinov, I.R. Gekker, V.A. Ivanov, D.M. Karfidov, Proc. 7th Europ. Conf.Control.Fusion and Plasma Phys. 1975, Lebedev Inst. Preprint No 80, 1975.

/19/ V.I. Barinov, D.M. Karfidov, Plasma Physics, 1, No 4, 638 (1975).

/20/ V.I. Barinov, I.R. Gekker, V.A. Ivanov, D.M. Karfidov, Plasma Physics 1, No 4, 647 (1975).

/21/ S.I. Nanobashvili, G.I. Rostomashvili, N.L. Tsintsadze, JTP, 45, 445 (1975).

/22/ S.I. Nanobashvili, G.I. Rostomashvili, N.L. Tsintsadze, Proc. 12th Int. Conf.Phen.Ionized Gases, Eindhoven, 1975.

/23/ S.I. Nanobashvili, G.I. Rostomashvili, N.L. Tsintsadze, Paper Submitted to the Europ.Conf.Plasma Physics and Nucl.Fusion, Losanna, Switzerland 1975.

/24/ L.L. Pasechnik, V.V. Pustovalov, V.F. Semenyuk, V.P. Silin, V.T.Tikhonchuk, Plasma Physics, 1, No 1, 21 (1975).

/25/ A.A. Galeev, R.Z. Sagdeev, Yu.S. Sigov, V.D. Shapiro, V.I. Shevchenko, Plasma Physics, 1, No 1, 10 (1975).

/26/ O.N. Krokhin, Yu.A. Mikhailov, V.V. Pustovalov, A.A. Rupasov, V.P. Silin, G.V. Sklizkov, A.C. Shikanov, JETP 69, No 1 (1975).

/27/ N.L. Tsintsadze, D.D. Tskhakaya, Europ.Conf.Plasma Physics and Contr. Nucl.Phys. Losanna, Switzerland 1975.

COLLECTIVE ION ACCELERATION WITH RELATIVISTIC ELECTRON RINGS

C. Andelfinger

Max-Planck-Institut für Plasmaphysik

D-8046 Garching/Fed.Rep. of Germany

The principle of collective ion acceleration involves the use of an electron cluster as a carrier for transporting and accelerating ions. This ensemble is an incompletely neutralized plasma with a relativistic electron component. This is the motivation for research on it in an institute of plasma physics. The experimental and theoretical know-how largely has its origin in fusion research.

What are the main differences and possible advantages compared with a traditional accelerator ?

In a traditional system the particles are accelerated in an external electric field. The acceleration is proportional to this field and the ratio of ion charge to ion mass:

$$b_t = \frac{eZ}{M_i} \cdot E$$

In this case of a collective ion accelerator the acceleration is given by

$$b_{coll.} = \frac{eN_e}{N_i M_i + N_e m\gamma} E \quad \text{for } ZN_i \ll N_e$$

where ZN_i/N_e is of the order of 10^{-3} to 10^{-2}.

Here N_e, N_i are the particle numbers, M_i is the ion mass and $m\gamma$ is the mass of relativistic electrons, and Z is the ion charge.

The acceleration of ions in equal external fields is then more efficient than in an traditional system by the ratio

$$b_{coll}/b_t = Z \left\{ \frac{N_i}{N_e} + \frac{m\gamma}{M_i} \right\}^{-1}$$

For practical cases this ratio will be of the order of 30 to 60.

This is true on the assumption that the electric self-field of the electron cluster is high enough to trap the ions. First experiments in this direction were conducted by Alfvèn and Wernholm [1] more than twenty years ago, but without positive results. At the CERN meeting on high energy accelerators in 1956 two papers opened the way to stable self-focused electron clusters. G.I. Budker [2], as well as W.H. Benett in 1934, showed that the repulsive space charge force in

an electron cluster is reduced by a factor $1/\gamma^2$, using relativistic electrons, and, furthermore, that the residual force can be compensated by a small fraction of positive ions when $ZN_i \geq N_e/\gamma^2$. It was V.I. Veksler [3], who suggested using this self-focusing property of relativistic electron beams for collective ion acceleration. His concept was a relativistic electron ring which can be accelerated perpendicularly to the ring plane.

The force which binds the ions on the electrons, the so-called "holding power", is given by the electrostatic field of the electron ring

$$E_h = \eta \cdot \frac{aN_e}{2\pi 2\varepsilon_o R(a+b)}$$

Here R is the ring radius and a and b are the semi-axis of the minor cross-section. The factor η depends on the special distribution of the electrons and ions [4]. It is 0.2 to 0.8.

Hitherto holding powers of the order of 10 MV/m have been achieved in unaccelerated electron rings. According to the present theoretical understanding a holding power of 50 ./. 100 MV/m seems possible. We have to compare these numbers with maximum values of 5 MV/m in traditional systems, mostly working with 1 ./. 2 MV/m.

Fig.1 shows in a very simple manner the principle of the electron ring accelerator (ERA). In a weak magnetic mirror field a relativistic electron beam with an energy of a few MeV and a current of a few 100 A is inflected and bound to an electron ring. The external magnetic field is weakly focusing as in a betatron. The field index $n = RdB_z/BdR$ is $0<n<0.5$. At this early time no ions are in the ring, so that the above-mentioned self-focusing effect does not work. The ring is now adiabatically compressed by the fast increasing magnetic field. The field rises from a few 100 Gauss to about 20 kilogauss. This increases the electron density and the holding power by a factor of about 30. At the end of compression, when the electron flux density becomes large (10^{22} $cm^{-2}s^{-1}$), ions will be trapped by impact ionization of the residual gas. This is a second advantage of the electron ring accelerator: no additional ion source is necessary. The ionization time for light ions is of the order of microseconds, while for heavy ions with the required charge to mass ratio of about 1/5 it is of the order of 10 ms.

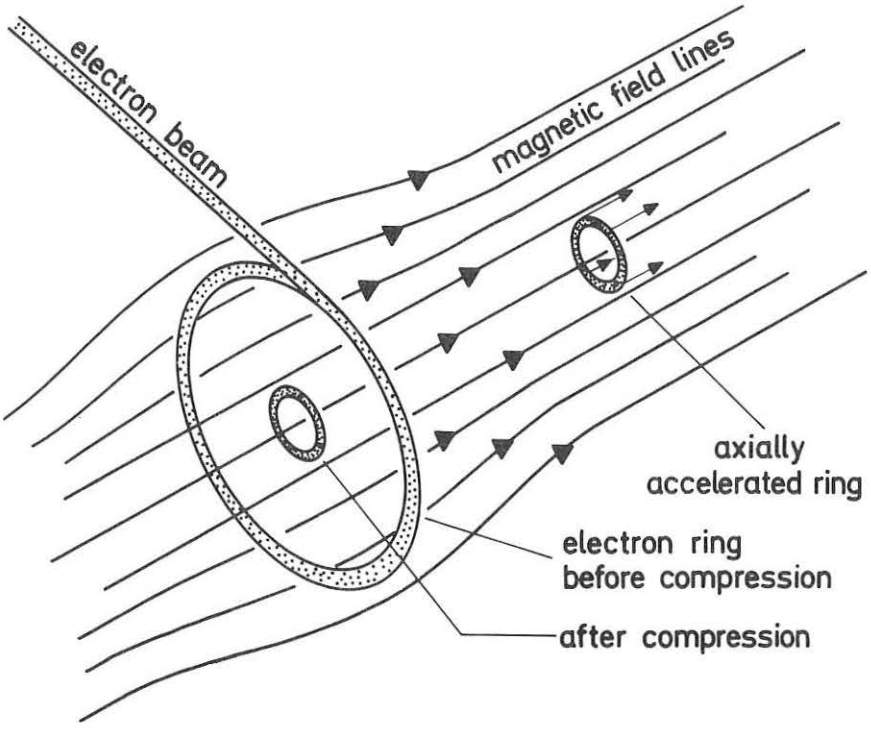

Fig.1: Principle of electron ring accelerator

Now the collective ensemble can be accelerated perpendicularly to the ring current either by an electric field or, in a simpler manner, by Lorentz forces $v_\phi \cdot B_r$ in a slightly divergent magnetic field which is needed in any case as a guiding field for the electron ring. Part of the azimuthal electron energy will be transmitted in the axial direction and energy gains of many hundred MeV for protons or a few times ten MeV/nucleon for heavy ions should be possible.

The admissible acceleration force is limited by the holding power. The relation is obtained from the equation of motion of the total ring and from that of the ions in the electron ring. It is

$$v_\phi \cdot B_r \leq E_h \cdot Z \left\{ \frac{N_i}{N_e} + \frac{\gamma m}{M_i} \right\}$$

In practical cases B_r will be of the order of 5 to 10 Gauss, this being comparable with guiding fields of 20 kilogauss.

There are, of course, effects which limit the efficiency of such an accelerator.

1. In the early phase, before ion loading, the residual repulsive force of the space charge must be smaller than the focusing force of the external magnetic field. Therefore, the maximum electron number can be about $3 \cdot 10^{13}$.

2. During ring compression several betatron resonances are crossed. They can increase the minor cross-section of the elctron ring. Especially in the extremely fast compression of the Garching ERA experiment each resonance is crossed during few electron revolutions and no ring "blow up" can be observed.

3. There are collective instabilities resulting from interactions between the particles themselves or between the particles and their surroundings. These are problems which are restrictive also for intense circular accelerators and storage rings.

One of these collective instabilities results from the "ion-electron resonance" when

$$k\omega_e + l\omega_i = m\omega_o$$

where ω_e is the electron betatron frequency, ω_i the ion frequency and ω_o the gyration frequency; k, l and m are integers.

This resonance depends on the ion loading and can be suppressed by a favourable ion to electron ratio and, furthermore, by sufficient Landau damping.

The most severe effect is the "negative mass instability" [5]. The reason lies in the fact that in a focusing magnetic field, with a field index $0<n<1$, the revolution frequency of the electrons decreases with increasing energy. Fig.2 illustrates this phenomenon.

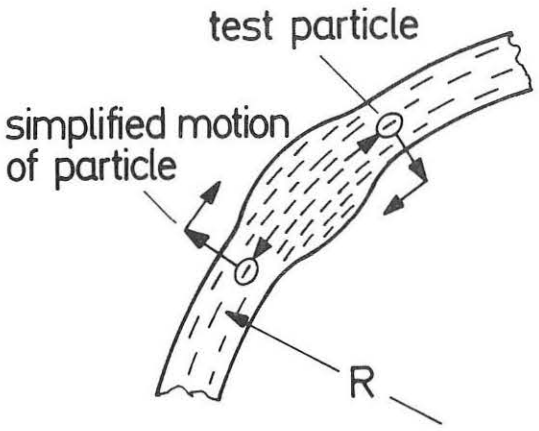

Fig.2: Illustration of "negative mass instability"

A relativistic electron in front of a small increase in line density gains energy from the repulsive force and shifts to larger radius, the revolution frequency is reduced and the line density in the bunch will be increased. An electron behind the bunch goes the opposite way. There exists a limit in the electron number for this instability.

$$N_e < \frac{\gamma R(\Delta E/E)^2}{2r_o|Z_m/mZ_o|}$$

A large energy spread $\Delta E/E$ is favourable but impairs the radial ring extent and therefore reduces the holding power. Z_m is the coupling impedance of mode number m and Z_o is the coupling impedance of the electron ring in the free space. The ratio Z_m/mZ_o is practically limited to larger values than 0.2. r_o is the classical electron radius.

It is mainly the "negative mass instability" which limits the theoretical possible holding power to 50 ./. 100 MV/m [6].

What is the present state of art and what are the prospects of an electron ring accelerator ?

The running Garching ERA experiment [7] was built to study fast ring compression and the initial acceleration of rings loaded with light ions. This device combines in a single-turn coil, very similar to a thetapinch coil, the ring compressor with the acceleration part, existing in a slightly divergent magnetic field. Fig.3 gives a schematic view of the experimental set-up. Owing to the fast field rise there is constant flux along the axis. Therefore, the field distribution is controlled by the cross-section of the coil. Within a section about 10 cm long in the axial direction, the B_r-value is small enough for smooth acceleration.

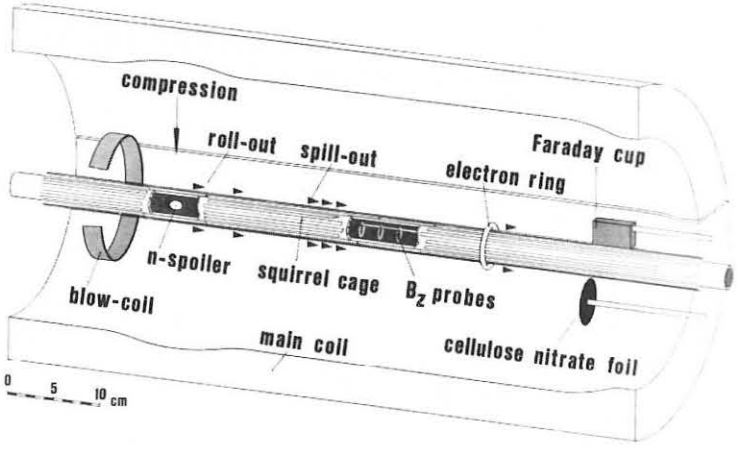

Fig.3: Schematic of the magnetic field coil with squirrel cage and diagnostic probes

The electron injector, consisting of a commercial high-voltage Marx generator and a specially developed field emission tube, produces electron beams of 1000 A with an energy of 2 MeV and pulse length of 100 ns. About 300 A was inflected in the ring compressor in an acceptance of 0.13 cmrad.

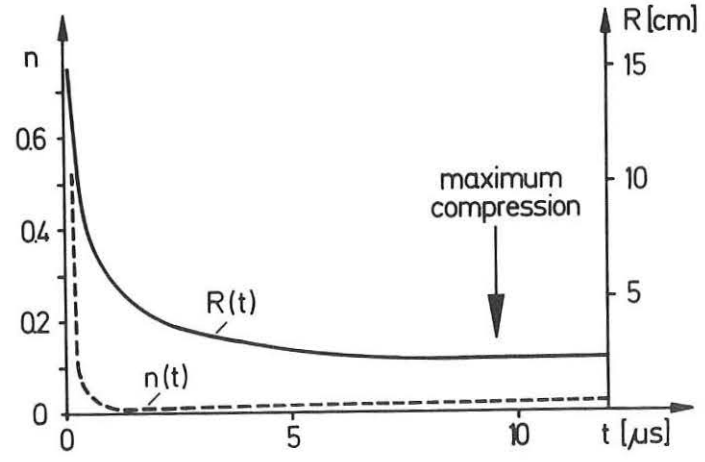

Fig.4: Time dependence of ring radius R and magnetic field index n

Fig.4 shows the time dependence of the ring radius during compression and the very fast change in the magnetic field index. All betatron resonances are crossed within less than 100 ns.

At the end of ring compression the ring data are: $R = 2.3$ cm
$a = b = 0.3$ cm
$N_e = (5 \pm 2) \cdot 10^{12}$
$E_{hold.} = 15$ MV/m

This holding power would be large enough for a very attractive accelerator.

Towards the end of compression and during the so-called roll-out phase, when the loaded ring is shifted in the acceleration part, the magnetic field index becomes very small. This entails two problems:

1. Strong collective radial oscillations are observed with a frequency of $S = \omega_o (1- \nu_r)$, where ν_r is the ratio of the radial betatron frequency to the gyro-frequency. This oscillation corresponds to a precession motion and its occurrence and growth depends strongly on the amount of ion loading and on the magnitude of field distortion. The loading dependence can be explained as electron-ion dipole instability, first studied by Koshkarev and Zenkevich and, for the relevant parameters in this application, by Dommaschk [9]. Fig.5 shows for four different times and three different gas pressures the coupling coefficients Q_i and Q_1 of the ions and electrons.

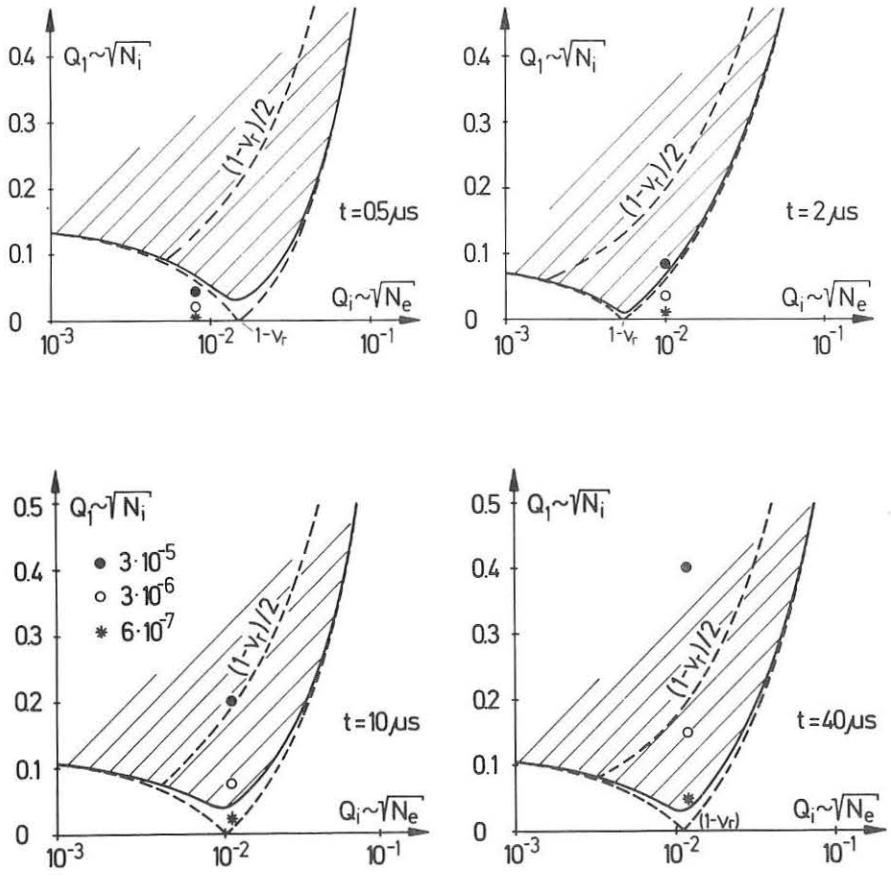

Fig.5: Coupling coefficients Q_i, Q_1 in the stability diagram of the electron ion dipole instability, plotted for different times and gas pressures

The hatched areas are the unstable regions, with Landau damping taken approximately into account. In accordance with the theory the instability starts when the instability area crosses the Q_i, Q_l-values of the loaded electron ring, and, furthermore, the collective radial frequency decreases with higher ion loading. This instability can be reduced by small ion loading and by large Landau damping coefficients [10] EdS/SdE. The latter depends among other quantities on the radial variation of the field index dn/dR. This parameter can be varied by passive, well conducting structures, so-called "n-spoilers", on the axis of the configuration. Fig.6 represents a collection of the ring behaviour with different field shaping structures and gas pressure.

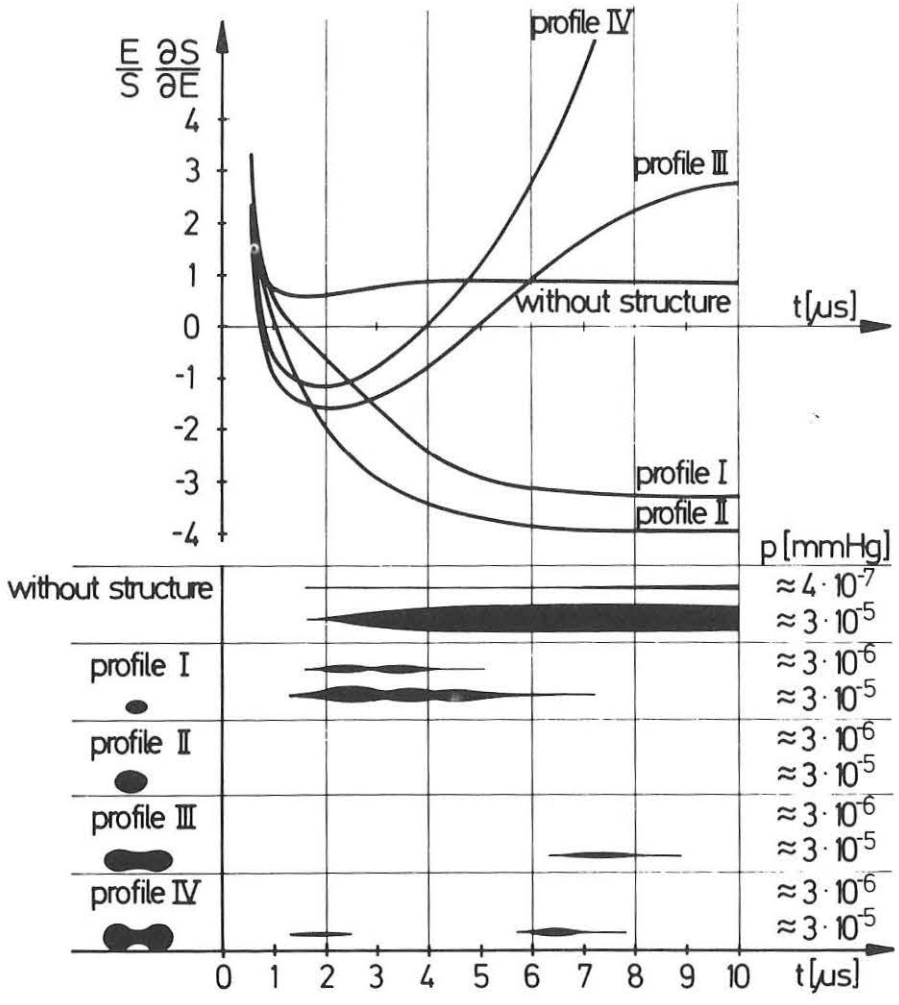

Fig.6: Occurrence of radial collective oscillations for different field shaping profiles together with the Landau damping coefficients

The upper figure shows the Landau damping coefficients for the different n-spoilers. The width of the streaks drawn in the lower figure represents the time behaviour of the amplitudes of these collective oscillations. The main result is that these oscillations can be suppressed and the growth rates will be reduced when the Landau damping coefficient becomes larger than about unity or when the gas pressure of the residual gas, which determines the ion loading, is smaller than a few 10^{-7} torr, corresponding to an ion fraction of about 10^{-3}.

2. Such small ion fractions are unsufficient for the above mentioned self-focusing of the electron ring. On the other hand, during the acceleration in the divergent magnetic field there is no axial focusing by external magnetic fields. The missing space charge compensation inside the electron ring can be replaced by image charges on walls close to the electron ring when image currents, producing a defocusing effect, are avoided.

The so-called "squirrel cage" inside the ring (see Fig.3) accomplishes this condition owing to the anisotropic conductivity, and with it we were able to accelerate even pure electron rings as an intactly coherent entity

The acceleration was determined by magnetic probes, which measure the $\dot{B}_z$ of the ring field when the ring passes by. There are several probes along the acceleration direction, and at the end a Faraday cup determines the number of the accelerated electrons. Fig.7 presents an example for the signals. From the evaluated velocity and the width of the Faraday cup signal one gets the axial extent of the ring; it is smaller than 1 cm.

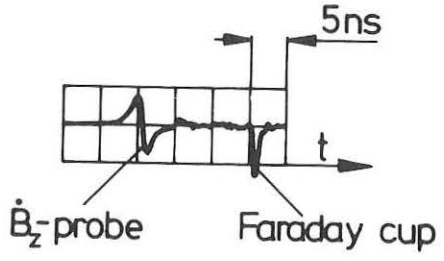

Fig.7: Addition of a $\dot{B}_z$-signal and a Faraday cup signal

Increasing the gas pressure in the range of 10^{-7} to 10^{-5} torr, the ion-electron ratio becomes 10^{-3} to several 10^{-2} The influence of the ion loading can immediately be seen in Fig.8. The signals become smoother and the time difference between the two signals becomes larger with hydrogen loading.

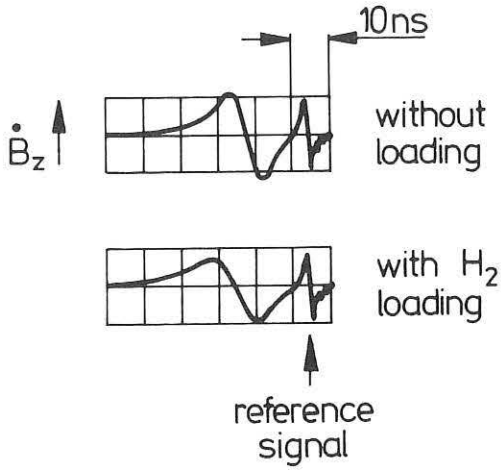

Fig.8: Magnetic probe signal without and with ion loading

The measured pressure dependence, in Fig.9 corresponds to the expected curve (solid line) and is proportional to $(1+M_i N_i/m\gamma N_e)^{-1}$.

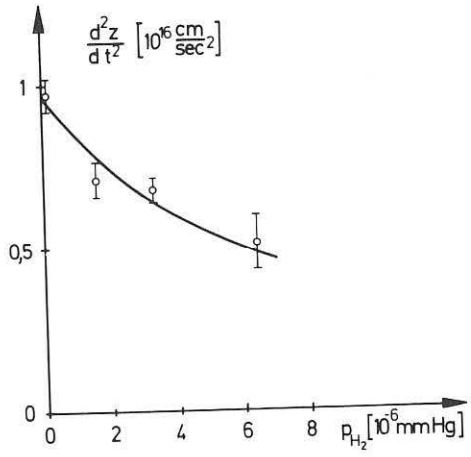

Fig. 9: Ring acceleration as a function of the hydrogen pressure

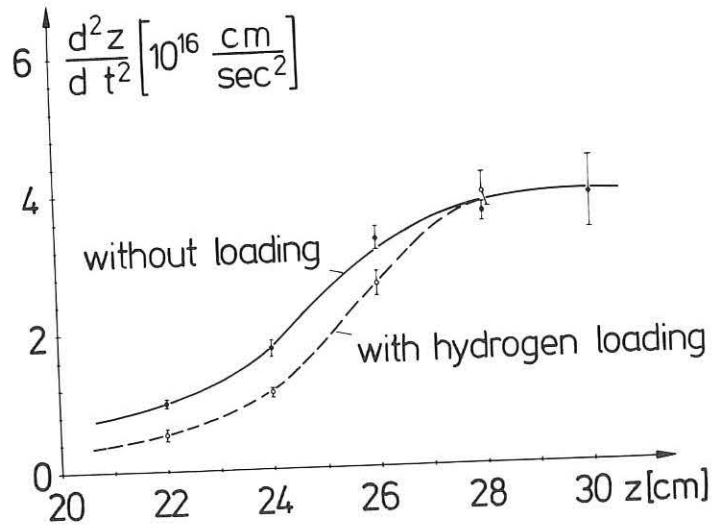

Fig.10: The axial dependence of the ring acceleration without and with hydrogen loading

In Fig.10 the acceleration of the ring with and without hydrogen loading is plotted over the axial distance from the compression plane.

As the accelerating force increases monotonically along the axis, the ions will be lost at a critical value of d^2z/dt^2. Together with the known B_r distribution one gets the holding power of the accelerated electron ring. In these experiments it was 3 - 4 MV/m[11].

The collective acceleration of He-ions is further confirmed by nuclear track recording with thin foils of cellulose nitrate. These tracks become visible after an etching process when the He-ion energy is larger than 200 keV, and, furthermore, the foils are insensitive to electrons and X-rays.

Fig.11 shows an electron scanning microscope photograph of an irradiated and a covered area.

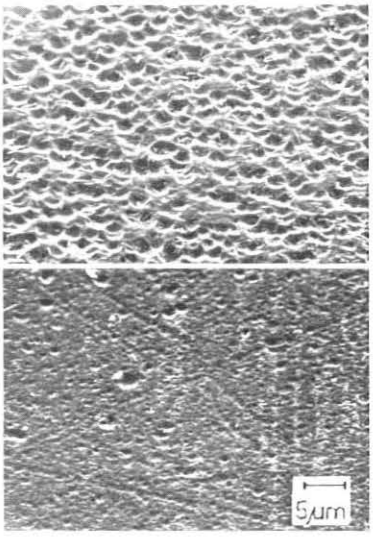

Fig.11: Electron scanning microscope photograph of a foil

In the running experiment the ion energy is limited to a few hundred keV gained over an acceleration length of 5 - 10 cm.

In a new experiment we will extend the acceleration structure to about 1.5 m. We then expect energies of about 5 MeV/nucleon for light ions and about 2 MeV/nucleon for Xenon. If this experiment is also successfull the way will be open for even larger energies. The diagram in Fig.12 shows the potential of an electron ring accelerator on the assumption of realistic ring data, i.e. a holding power of 10 MV/m and an electron number of $5 \cdot 10^{12}$, with $\gamma_o = 30$.

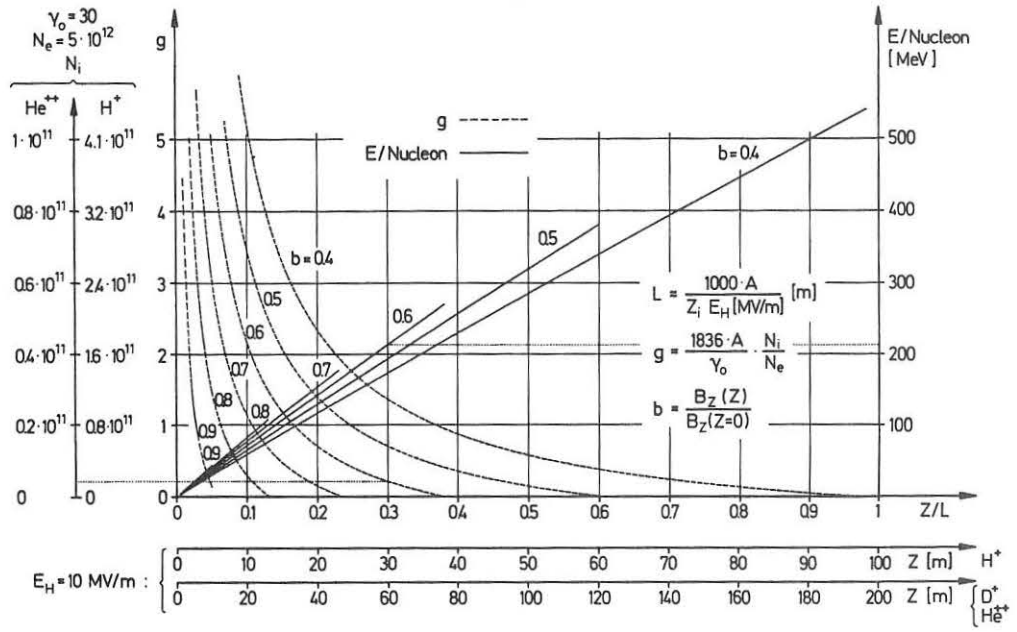

Fig.12: Ion energy and ion number as functions of the acceleration length z and magnetic field decay b

One obtains $b = B_z(z)/B_z(z = 0)$ and $g = N_i M_i / N_e m\gamma$. With a handy length of about 30 m, it may be possible to have proton acceleration to about 200 MeV and heavy ions to about 50 MeV/nucleon. With an accelerator length comparable to the "Unilac" of the GSI, Darmstadt, energies of more than 100 MeV/nucleon seem possible instead of 10 MeV/nucleon in that machine. The particle number results from the quantity g. Ion numbers of 10^{10} protons and, for example, 10^{11} Xe-ions per pulse are to be expected. The pulse duration is of the order of 10^{-10} s, so that the instantaneous ion flux is of the order of 10^{20} to 10^{21} ions per second.

For cancer therapy only a few pulses would be necessary. A wide field of application can be expected in the field of ion implantation for affecting material properties. In nuclear physics new research with heavy ions, e.q. the excitation of shock waves, needs energies of about 100 MeV/nucleon. We believe that an electron ring accelerator could fill a gap in demand for particle accelerators.

References

1 Alfvèn H. and O. Wernholm, Arkiv Fysik, 5 175 (1952)

2 Budker, G.I., Proc. of the CERN Symposium on High Energy Accelerators, Geneva 1956, Vol.1, p.68

3 Veksler, V.I., dto. p.80

4 Hofmann, I., Proc. of the 9th Int. Conf. on High Energy Accelerators, Stanford 1974, p.245

5 Nielsen, C.E., A.M. Sessler and K.R. Symon, Proc. of the Conference on High Energy Accelerators, CERN 1959, p.239

6 Möhl, D., L.J. Laslett, A.M. Sessler, Part. Acc. Vol.4, 159 (1973)

7 Andelfinger, C., et al., Proc. of the 9th Int. Conf. on High Energy Accelerators, Stanford 1974, p.218

8 Koshkarev, D.G., P.R. Zenkevich, Part. Acc. Vol.3, 1 (1972)

9 Dommaschk, W., IPP-Report 0/19 (1973) Garching

10 Laslett L.J., Lawrence Berkeley Lab. ERAN 126

11 Schumacher, U., C. Andelfinger, M. Ulrich, Phys. Letters 51A, 367 (1975)

SUPPLEMENTARY PAPERS

THE IONS IN T.F.R. THROUGH ANALYSIS OF FAST NEUTRALS AND NEUTRON EMISSION.

T.F.R. Group presented by M. Chatelier

ASSOCIATION EURATOM-CEA SUR LA FUSION
Département de Physique du Plasma et de la Fusion Contrôlée
Centre d'Etudes Nucléaires
Boite Postale n° 6 . 92260 FONTENAY-AUX-ROSES (FRANCE)

. Ion temperature profile :

In part I of our paper we described the measurements of the ion erature profile by detection of fast neutrals emitted mostly in the me- plane between 2 main magnetic field coils. We have now repeated this urement, the electrostatic analyser making an angle of 8° with the magne- axis, in order to decrease the influence of localized particles in the neutrals signal. In the same discharge conditions as in figure 2 (Part 1) ion temperature profile nearly becomes symmetric (fig 1) with the same mum temperature. This profile is very similar to the decreasing tempe- re part of the profile reported previously. So the asymmetry can correct- e attributed to localized particles. Our result is in agreement with the lts first obtained by Petrov (1).

. General Scaling of the central ion temperature :

All the experimental results obtained in Deuterium plasma con- the dominance of an ion conduction loss following a "plateau" depen- e. The temperature closely follows the relation (1) :

$$T_i \sim \left\{ \bar{n}_e \cdot B_\varphi \cdot I_\varphi \cdot R^2 \right\}^{1/3} \cdot A_i^{-1/2} \qquad \text{(fig 2)}$$

experiments have been done, keeping I_φ constant but varying B_φ at cons- filling pressure in which case the product $\bar{n}_e B_\varphi$ stays nearly constant. ion temperature also stays constant.

r experiments have been made keeping I_φ and $\bar{n}_e$ constant but varying B_φ the ion temperature closely follows a $B^{1/3}$ relation.

le analytical calculations show that the profile can also be explained by lateau conduction loss. In any case the simulation calculations (2) repro- e the experimental measurements with this law.

ever experimental results show some dispersion around the relation (1) and ve do not introduce an increase of the ion-ion collision frequency due to arity the plasma should be in some cases in the "banana" regime. That is we calculated the relation (1) in the presence of impurity more carefully. a deuterium plasma we found (3) :

$$T_i \sim \left\{ \bar{n}_e \cdot B_\varphi \cdot I_\varphi \cdot R^2 \right\}^{1/3} \cdot A_i^{-1/2} \cdot \left(\bar{n}_e / \bar{n}_p \right)^{-1/3}$$

is the deuteron density which can be different from the electron densi- $\bar{n}_e$. The same calculations done for a hydrogen plasma show a less impor- influence of the impurity on the heating of hydrogen ions. So the crepency from the relation (1) for hydrogen (fig 2) could be due to this c. But some other explanations cannot be excluded as the influence of rge-exchange losses or the formation of a more unstable plasma in hydro- than in deuterium. In any case (D_2 or H_2 plasma) the calculation of ion energy confinement time requires the introduction of impurity. simistically if we suppose that the observed Zeff is only due to O^{8+} find that the ion energy confinement is of the same order as the elec- n energy confinement time (10 - 20 ms).

M.P. Petrov. Plasma physics and controlled nuclear Fusion research 4. Vol 1. Tokyo 1974

C. Mercier. Soubaramеyer this conference

Group T.F.R. Rapport EUR-CEA n779. to be published.

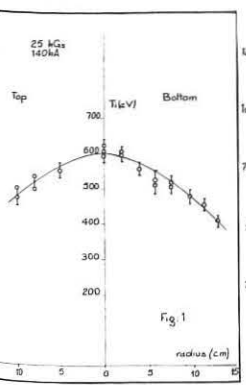

Fig. 1

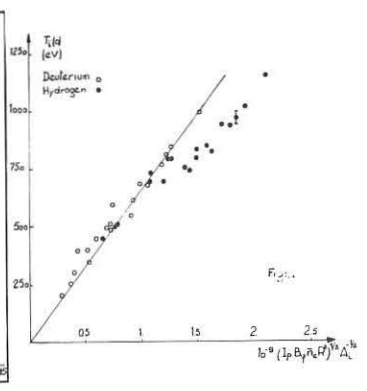

Fig.

3

DYNAMICS OF HIGH ENERGY RUNAWAY ELECTRONS IN ORMAK*

H. Knoepfel†, D. A. Spong‡, and S. J. Zweben#
Oak Ridge National Laboratory, Oak Ridge, Tennessee, U.S.A.

Abstract: The production and control of strong runaway discharges in ORMAK is discussed.

Tokamak discharges, in which the majority of the current was carried by runaway electrons, were inadvertently produced during the initial operation of ORMAK [1]. Since then there has been some interest in using such beams (or those produced by external injection) for supplementary heating and/or confinement of normal tokamak plasmas [2]. We report here a preliminary experimental investigation of the production and confinement of runaway-dominated ORMAK discharges.

Production

The runaway discharges were produced by introducing a significant amount of argon impurity (>10 % of the number of hydrogen atoms present) via a fast gas valve 100 ms before the shot. Attempts to produce such discharges by lowering the hydrogen filling pressure and/or eliminating the preionization were unsuccessful.

Characteristics

The voltage characteristic was generally similar to normal ORMAK shots, but the length was limited to ≈ 25 ms to avoid possible damage to the machine liner. The maximum current varied from 50-80 kA among the set of about 20 shots attempted; in all cases there were negative current steps (≈ 1 kA), positive voltage spikes, and hard x-ray bursts observed simultaneously during the current decay [3]. A large, fast current dump (up to 30 kA/2 ms) usually terminated the discharge. The MHD pickup loops showed an absence of poloidal mode rotation; the line averaged electron density was ≈ .5 - 1 x 10^{13} initially. No temperature measurement was available due to the large x-ray background, however, a radiometer probe showed a sharp decrease in power flow out of the discharge after the voltage ended.

*Research sponsored by the Energy Research and Development Administration under contract with the Union Carbide Corporation.

†On leave from Laboratorio Gas Ionizzati (Euratom-CNEN), Frascati, Italy.
‡ORAU Participant from the University of Michigan, Ann Arbor, Michigan.
#ORAU Participant from Cornell University, Ithaca, New York.

Confinement

An attempt to control the equilibrium of these beam-like plasmas was made by programming the applied vertical field. It was observed that an increasing vertical field lengthened the lifetime of the current (up to 50 ms past the voltage end) and tended to reduce the final dump magnitude. A larger field than usual was expected to better confine the high longitudinal momentum beam component; calculated β_{pol} values increased slowly over the discharge up to a maximum of ≈ 4 near the end. Without increasing the vertical field the plasma shift signal showed a strong outward movement; with a programmed increase in field the shift was stabilized or driven inward. The slowest current decay occurred for shots which showed a gradual inward plasma shift, such as would be expected to confine an outward-shifting runaway component.

The hard x-ray diagnostic was used to show that the maximum electron energy in these discharges was ≈ 5-7 MeV (≈ 30-50% less than that expected from free fall from t = 0). The observed energy components above 3 MeV contributed on the order of 10 kA to the toroidal current. No information could be obtained on lower energy components.

A distinctive feature of these shots was the appearance of the fairly regular, fast dumps of hard x-rays (rise time < 100 μs); most of these could be identified with current-step, voltage spike signals. These dumps were not accompanied by any observable plasma shift, and in most cases constituted ≈ 20-40% of the total x-ray intensity produced by the runaways. It is not yet clear whether all of the current step can be attributed to runaway loss, nor is the physical mechanism of this process understood. These dumps persist even in the best-confined shots, and therefore contribute significantly to the runaway loss rate.

Erratum

In Fig. 3 of our paper, the runaway density vs. r_c was plotted using the "ORMAK Type-B" intersection condition, instead of the "orbit-expansion" condition. The latter result is very nearly given by simply subtracting 1 cm from the given values of r_c and keeping the curve as drawn.

References

[1] D. A. Spong, J. F. Clarke, J. A. Rome, and T. Kammash, Nucl. Fusion 14, 397 (1974).
[2] A. Mohri et al., Phys. Rev. Letters, v. 34, No. 10, 574 (1975).
[3] V. S. Vlasenkov et al., The Runaway Electron Discharge Regime in the Tokamak-6 Device, Nucl. Fus. 13, 509 (1973).

8

DEVELOPMENT AND APPLICATIONS OF THE FONTENAY TRANSPORT CODE.

C. Mercier, Soubbaramayer

ASSOCIATION EURATOM-CEA SUR LA FUSION
Département de Physique du Plasma et de la Fusion Contrôlée
Centre d'Etudes Nucléaires
Boîte Postale n° 6. 92260 FONTENAY-AUX-ROSES (France)

I- Simplified study of the stationary state with the transport laws used in the simulation

Transport equations are reduced to the electronic temperature equation $\frac{1}{r}\frac{d}{dr}\left(r\,K_e\frac{dT}{dr}\right)+\frac{E_0^2}{\eta_0}\frac{T^{3/2}}{Z_{eff}}+\gamma S=0$

If we put :

$$g = r B_\theta = \int_0^r J_\varphi\, r\, dr = \frac{E_0}{\eta_0}\int_0^r \frac{T^{3/2}}{Z_{eff}}\, r\, dr$$

The boundary conditions are :

$$g(a) = \frac{I}{2\pi} = \frac{\text{total current}}{2\pi} \qquad g'(a) = 0 \qquad g(o) = 0$$

the electron heat conductivity K_e is assumed to have the following functional form

$$K_e = K_o\, W(\rho)\, T_e^{\alpha}\,(1+\omega\, q^k)$$

The density $n_e(\rho)$, heat sources or sinks and the profile $Z_{eff}(\rho)$ are supposed to be given. The non linear differential equation so obtained is investigated analytically and numerically. $W(\rho)$ includes the effects of both the density and Z_{eff}. The coefficient K_e used in the simulation of a normal regime (no skin effect and $q > 1$) corresponds to :

$$W = n_e^2 \qquad \alpha = -\frac{1}{2} \qquad \omega = 1.6 \qquad k = 2$$

We take $n_e = \exp\left(-\frac{\gamma}{2}\rho^2\right)$

The influence of the density profile is very characteristic in this case. Let us characterize the peaking of the temperature and current profiles by the quantity $Q = q_{edge}/q_{axis}$. The figure 2 represents Q versus γ for different values of $\beta = \frac{1}{1.6\, q_{edge}^2}$. Only the dashed region can give $q_{axis} > 1$, and this implies $\gamma \gtrsim 4$. It is remarquable that stationary discharges with $q_{axis} > 1$ observed in TFR correspond to

$$\gamma \simeq 4 \qquad Q = 10 \qquad \beta \simeq 0.01$$

and this point coincides with the diagram 2.

The other discharges have density profiles corresponding to $\gamma \simeq 2$. So the steady state with this type of transport coefficient leads to $q_{axis} < 1$. In such cases an instability is developping and an average turbulent state is established, characterized by the transport coefficient (4)

$$W = \sqrt{n_e} \qquad \alpha = -\frac{3}{4} \qquad k = -\frac{1}{2} \qquad \omega \gg \infty \quad \text{with } K_o\omega \text{ finite.}$$

II- The results of the simulation of the discharge TFR (Deuterium, 400 Kamps, 60 kG) without and with neutral heating (injected power $\simeq$ 170 KW, 37 keV) are represented on the figure 3. The agreement between computations and experiments is quite satisfactory.

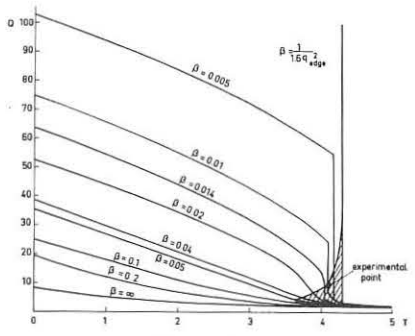

Fig 2 - Q versus T

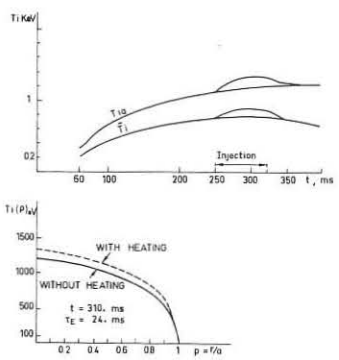

Fig 3 - Simulation results (TFR, 400 kamps, 60 KG)

12

FIRST RESULTS ON PETULA TOKAMAK

PETULA GROUP

ASSOCIATION EURATOM-CEA
Département de Physique du Plasma et de la Fusion Contrôlée
Service IGn - Centre d'Etudes Nucléaires
B.P.85 - Centre de Tri - 38041
GRENOBLE CEDEX (France)

The plasma current in PETULA has been increased to 80 kAmps. ($q_{limiter} = 3.1$) with the plasma centered by vertical and radial DC magnetic fields. Fig. 1 to 3 show typical results for 73 kAmps. discharges, as well as a numerical simulation of the discharge using the Mercier Soubbaramayer code. The best fit is obtained when neglecting charge exchange (radial density profils has of course to be entered into the data) and when increasing electron losses on axis as soon as q = 1 at 20 ms. The largest discrepancy is on loop voltage which is found experimentally to vary from 3 to 5 volts as the time of maximum current depending on wall conditions. Plasma resistivity tends to increase with shot number. Energy confinent time is in the range 1.4 to 2.ms and poloïdal β is.25 while the ratio of plasma resistivity to Spitzer's formula is 4.5.

Ion temperature on axis (Fig. 4) as measured by neutral charge exchange (solid line) or by Doppler broadening of O^{VII} line (broken line) are in good agreement with Artsimovitch law (points).

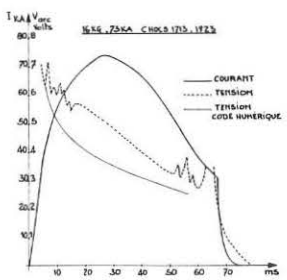

Fig. 1

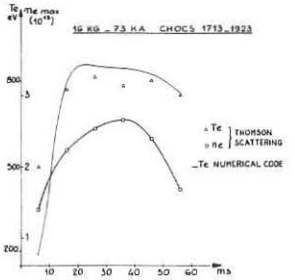

Fig. 2

Fig. 5 shows intensity of 1623 Å O^{VII} line in arbitrary units as a function of time for three plasma currents. Due to the faster increase in electron temperature, the line appears sooner the higher the plasma current. The maximum intensity remains constant which indicates a constant amount of oxygen impurity.

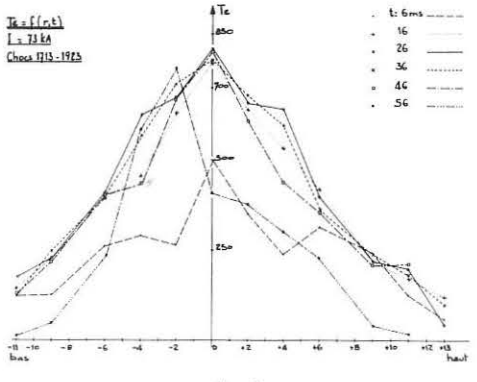

Fig. 3

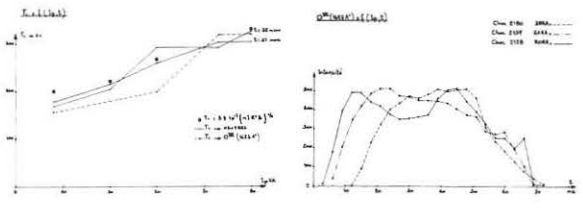

Fig. 4

Fig. 5

FINEMENT OF HIGH β PLASMA IN TPE-1 (REVERSED FIELD PINCH)

K. Ogawa, T. Shimada, S. Kiyama, Y. Hirano,
Y. Maejima and I. Hirota
Electrotechnical Laboratory, Tanashi, Tokyo, Japan

The new results have been obtained in the experiments of on TPE-1. The RFP configuration is set up by the fast pro-ming of the currents (Z and θ) in the rather higher plasma rent, ~ 120kA. The two cases of plasma currents, 114kA (case and 128kA (case B) are intensively analyzed. Fig.1 shows time histories of the magnetic field configurations observed the six magnetic probes being in a line with the same charac-istics. The motion of the centre of the plasma current was erved by a set of four small pick up coils on the circumfer-e of the same cross section of the torus. The ion tempera-e was estimated by the Doppler broadening of HeII4686Å. radial distributions of the electron temperature and density variable times are measured by Laser scattering technique.

From Fig.1 four characteristic phases of the formation of on TPE-1; (1) the fast Z-pinch implosions obtained by the rt current rise time, 0 ~ 4 μs in case A, 0 ~ 3 μs in case B ime is from the start of main Z) and ions is heated, ~ 50eV; in the centre region of plasma column the fast diffusion of due to some turbulent motion of plasma, at 3 ~ 5 μs (A), 3.5 μs (B); (3) RFP configurations are established at 5 ~ 6 μs , 3.5 ~ 4 μs (B) and the field reversal ratio, F, and θ, [1], estimated at -0.53, 1.15 (A) and -0.51, 1.25 (B) and θ ~ 0.6 0.65. In both cases the bias magnetic field (2.7kG) might large for generating the ideal stable RFP configuration. these phases, (1) ~ (3), a small oscillatory motion of the tre of plasma current (~ 500kHz) is observed by the pick up ls, but it does not develop to destroy the whole current in se phases. Whether the wall stabilization is effective in se configurations from the both points of views of ideal MHD k and tearing instabilities or not, was examined. The malized r_w is 3.3 ~ 3.4 (FFBFM) and 2.1 (PPM) in our con-urations. The growth times of m=1 kink and tearing modes

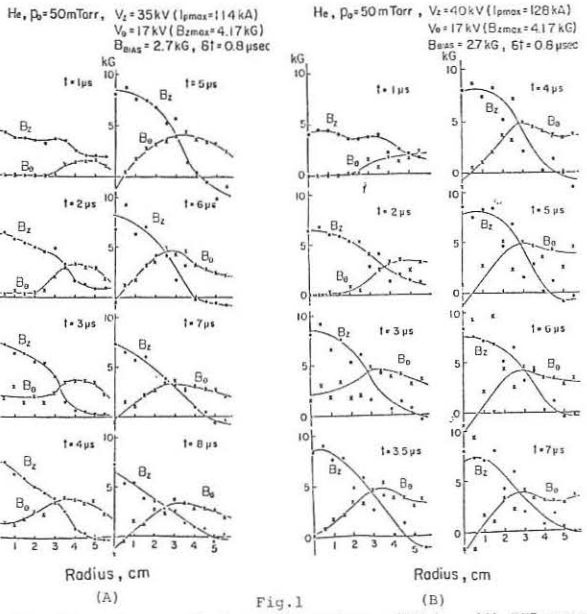

Fig.1

20 ~ 30 μs (magnetic Reynolds number ~ 100). (4) RFP con-urations start to decay at ~ 8 μs (A), ~ 7 μs (B) and the sma current column starts to move rapidly like m=1 helical ion and then touches to the wall. The plasma current decay e is estimated at 20 ~ 25 μs from the observed T_e and n_e and netic field.

erences;

Butt E.P. et al. 5th IAEA Conf. Tokyo (1974) CN-33/E9-2

THERMONUCLEAR LASER IMPLOSION EXPERIMENTS *

J. H. Nuckolls, J. L. Emmett, H. G. Ahlstrom, C. D. Hendricks, L. W. Coleman, J. A. Glaze, J. H. Holzrichter, G. H. Dahlbacka

University of California/Lawrence Livermore Laboratory
Livermore, California, U.S.A.

Abstract: Strong evidence for thermonuclear fusion has been obtained from implosions of glass microballoons filled with DT gas by 1/2 - 1 terrawatt Nd glass lasers. Up to 10^7 14 MeV neutrons have been produced. Diagnostics with 3 μm, 30 ps resolution have been obtained.

The energies of the reacting deuterons and tritons were determined to be 10-20 keV by measuring the temporal spreading with distance of the DT alpha particles. From the measured energy loss of the alpha particles in traversing the imploded fusion capsule it was determined that the alphas originated in the imploded DT fuel. Volume compression ratios of about 100 fold were measured with a 3 micron resolution x-ray microscope. The Lawson number is $10^{12} cm^{-3} s$. These results are generally in good agreement with the LASNEX MHD energy transport computer calculations. An implosion time of approximately 150 ps was measured with a 30 ps resolution x-ray streaking camera.

These implosion experiments were carried out with the Janus and CYCLOPS lasers developed at the Livermore Laboratory. Eight and one half cm aperature disc amplifiers are used in the 2-beam half terrawatt JANUS laser system and 20 cm aperature disc amplifiers in the single beam, one terrawatt CYCLOPS laser system. Focusing is by F1 lenses in Janus and F2.5 lenses in CYCLOPS. The pulse is a 100 ps FWHM gaussian with less than 100 microjoules prepulse to avoid target damage. In the focal region the beam has a partially hollow spatial profile. This improves the fusion capsule implosion symmetry. The spatial profile has been carefully measured in full power laser shots. In order to produce a clean, precise, reproducible beam despite non-linear effects, the "B integral" has been limited in the JANUS system (by limiting the total thickness of glass traversed) and in addition, spatial filters have been used in the CYCLOPS system.

The physics design of the fusion targets, and the postshot analysis of the diagnostic data was carried out with the LASNEX computer program. This code is two-dimensional (axially symmetric), magneto-hydrodynamic; with multi-energy group transport of x-rays, electrons, and fusion reactor products; laser light transport and absorption; and contains approximations to collisionless plasma processes. Several target designs using a glass microballoon filled with low density DT gas have been tested. The microballoon diameter varied from 40-100 m, and the thickness from 1/2 - 1 micron. The DT fuel density varieds from 5×10^4 to 8×10^3 g/cm^3. In order to enhance absorption of laser light as well as implosion symmetry, in some target designs the fusion capsule was mounted on a glass disc, or enclosed in plastic foam. These targets were precisely fabricated and characterized. When the glass capsule wall is suddenly heated by intense laser light, its outer surface ablates and accelerates the glass inward compressing DT gas. Meanwhile the glass is heated internally by x-rays and electrons from the hot laser heated plasma, and decompresses or explodes. Both the glass and the DT undergo large entropy changes and neither reaches high densities. The DT ions are heated by rapid compression to thermonuclear temperatures. This exploding pusher target design was chosen for initial laser implosion experiments because the neutron yield is relatively insensitive to irradiation symmetry, pulse shape (providing the pulse width and capsule design are matched), fluid and plasma instabilities and imperfections in the target fabrication.

*Research performed under the auspices of the U.S.E.R.D.A.

A diversity of optical, x-ray, ion, and neutron detecting instruments were used to diagnose these laser implosion experiments. Our x-ray microscope uses grazing incidence crossed cylindrical lenses to image the target's x-ray emission. Four energy channels are obtained by K-edge filters. This microscope has a resolution of 3 microns. Pinhole cameras are also used to image the target x-rays. Our x-ray streaking camera consists of an optical streaking camera with an x-ray photo-cathode. Five energy channels are obtained via K-edge filters. The resolution of this instrument is about 30 ps. Our alpha particle time of flight spectrometer consists of a time of flight tube and a magnet to bend the alphas out of the line of sight into a scintillator-photo-multiplier combination. This instrument measures the energy distribution of the alpha particles with a resolution of 100 keV at a target yield of a few million (DT fusion events). The spatial distribution of light from the target is determined with a diode array, and is integrated with a box calorimeter. A combination of K-edge and crystal spectrometers are used to measure the x-ray spectra from the target over a range of 500 ev to 100 keV. Plasma ions are measured with caliorimeters and spectrometers.

A dozen different target designs were imploded with one and with two laser beams giving neutron yields varying from 250 to 11 million. Over this five orders of magnitude, LASNEX calculations are within a factor of 3 of the data. In one beam experiments mounting the capsule on a disc degrades the neutron yield 3-fold, and foam mounting degrades the yield 100-fold. Both the disc and foam absorb energy and reduce the DT temperature, and LASNEX predicts the strong self-generated magnetic fields inhibit transport of energy through the foam. A 30-fold enhancement was obtained with the complex target design. In 2-beam experiments, the disc degrades the neutron yield 8-fold and the complex design provides a 2-fold enhancement. Data from the x-ray streaking camera for a typical implosion show peaks in the 7.7 and 9.7 keV channels about 150 ps after the onset of detectable signals on the low energy channels. LASNEX calculations predict such peaks at the culmination of the implosion at approximately this time. The experimental and calculated x-ray spectra beyond 3 keV are in good agreement. The high energy portion of the x-ray spectra indicates the presence of superthermal electrons generated by collisionless plasma processes and by inhibited electron transport in the plasma due to plasma instabilities and self-generated magnetic fields. The x-ray micrographs of these implosions typically show compression ratios of about 100 fold. The measured alpha particle pulses at a distance of 9 feet from typical implosions yielding about 5×10^6 neutrons have a time width of about 11 nanoseconds.[1] This time width corresponding to an energy width of 330 keV. The measured alpha energy is about 3.3 MeV corresponding to an energy loss of 220 keV in traversing the compressed target. These results correspond to reacting DT energies of about 10-20 keV, and to uncorrected ion temperatures of 3.5 keV. Analysis with LASNEX shows a Doppler broadening of about 150 keV due to hydrodynamic motion of the assymetrically imploded DT fuel and various smaller effects. The corrected ion temperature is about 2 keV. The LASNEX predicted alpha energy loss is 200 keV, in excellent agreement with the experimental results.

The next major step in laser fusion will be demonstration of implosions in which entropy changes are minimized and very high densities are achieved. High density isentropic implosions are sensitive to fluid and plasma instabilities and require pulse shaping. Such implosions will be carried out with the multi-terrawatt ARGUS laser during 1976. Experiments which may approach breakeven will be carried out with the 10^4 Joule 30 TW SHIVA laser in 1977 - 1978.

REFERENCE

[1] V. W. Slivinsky, H. G. Ahlstrom, K. G. Tirsell, J. Larsen, S. Glaros, G. Zimmerman, and H. Shay, UCRL 76938, to be published in Phys. Rev. Lett.

78

EXPERIMENTAL INVESTIGATION OF LASER-HEATED PLASMAS IN A SOLENOIDAL MAGNETIC FIELD PART II

Z.A. Pietrzyk, H.L. Rutkowski and G.C. Vlases

University of Washington, Seattle, Washington, U.S.A.

The density, temperature, and streak photography measurements described above have been analyzed in detail in an attempt to determine the mode of plasma column propagation and to construct an energy balance. A comparison of experimentally determined front trajectories with finite β bleaching wave theory[1] and detonation wave theory[2] is shown in Figure 1. The best fit slope of the experimental data matches bleaching wave theory fairly well over several orders of the appropriate dimensionless parameter, but the theoretical detonation trajectories are also close to experiments. Bleaching waves are further suggested by the transverse density measurements, which indicate no compression over ambient, but the weak dependence of breakdown velocity on filling density is more consistent with detonation waves. It should be noted that the published theories do not account for the effects the expansion wave propagating inward from the end of the column, and thus may be too idealized to describe these experiments. We therefore conclude that although the bulk of the evidence suggests the waves are "bleaching-like," the question has not yet been resolved either theoretically or experimentally, and further work is needed.

From our measurements, the mean value of the plasma parameters for fixed (150 joules) laser energy and B = 100 kG are estimated to be $\bar{T}_e \approx \bar{T}_i \approx 130$ eV, $\bar{n}_e \approx 5 \times 10^{17}$, $\bar{Z} = 1.5$, plasma radius 2.5 mm, and plasma volume 1.6 cm^3. An energy balance was made which shows that 31% of the laser energy went into thermal energy, 25% into kinetic energy, 7.5% into ionization, 6% was transmitted, 4% backscattered, and 26% was lost by axial heat conduction. Bremsstrahlung and transverse heat conduction losses were estimated to be negligible, as was the change in B field energy for the achieved β of 30% in the 2.5 cm bore. This accounts for essentially all of the laser energy. However, estimates of the heat conduction losses are difficult to make precisely, and it is possible that some of the laser energy is refracted near the orifice by the axially-expanding plasma.

References

1. L.C. Steinhauer, H.G. Ahlstrom, Phys. Fluid 18, 5 (1975).
2. S.A. Ramsden, P. Savic, Nature 203, p. 1217 (1964).

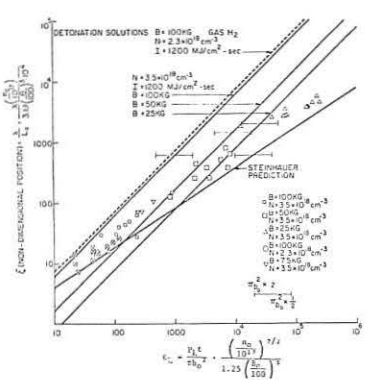

Fig. 1

82

CO_2 LASER-HEATING EXPERIMENTS

T.P. Donaldson,* J.W. van Dijk,+ A.E. Elkerbout,+ and I.J. Spalding*
Queen's University, Belfast,* R.K. Hogere Technische School, Rijswijk, The Netherlands,+ and UKAEA Culham Laboratory, United Kingdom.*

Abstract A strong modulation in axial density profile is measured in a CO_2 laser-generated plasma. The density cavity occurs near the critical density and is probably driven by non-linear ponderomotive forces.

Further analysis of the holographic interferograms discussed in Vol I has been made at distances of 0, 50, 100, 200, 400 and 500 μm from a semi-infinite carbon target. The axial variation in electron density (ie along the laser beam) is shown in Fig. 1. The interferograms can readily be measured within half a fringe, giving an estimated error of ± 10% at peak density, and proportionately higher errors at lower density. The axial expansion is thought to be isothermal, because of the close similarity in the shape of $[n_e(z)]^2$, plotted in Fig. 2, and the Abel-inverted soft X-ray intensity - (corresponding radial variations in this X-ray intensity for a SiO_2 target are shown in Fig. 3.)

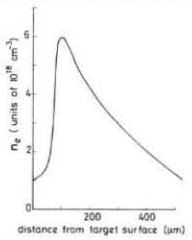

Fig. 1. Variation of n_e along the laser (z) axis for a carbon plasma at t = 25 ns.

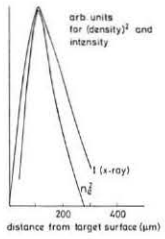

Fig. 2. Variation of n_e^2 and X-ray intensity (I) with z. (n_e^2 plotted from Fig. 1, I taken from pinhole picture of a SiO_2 target).

Note that a very strong modulation in density is observed, having a scale length ≤ 50 μm, ie of order 100 electron Debye lengths. The density scale length of the outer corona is ~ 200 μm; the critical surface is not detected by the interferometer, and is thus within the target surface at the time of measurement (t = 25 ns). The radiation pressure of the focussed laser beam approaches plasma kinetic pressure, since the (unpolarized) free-space intensity produced by the f/4 mirror is ~ 9 x 10^{12} w/cm^2; its angle of incidence ranges from 0° to ~ 7°, so that resonant absorption near the critical surface may be expected[1]. Under these experimental conditions, ponderomotive force effects may drive density perturbations[2,3], and accompanying self-focussing and filamentation may occur[4]. This observation provides a laser analogue of the microwave "caviton" experiment reported by Wong et al[5].

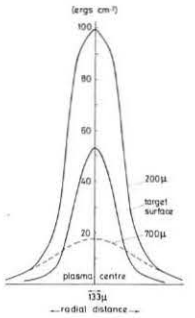

Fig. 3. Variation of radial X-ray intensity at various distances from the surface of a SiO_2 target.

References

1. J.P. Freidberg, R.W. Mitchell, R.L. Morse and L.I. Rudsinski, Phys. Rev. Letts. 28, (1972) 795.
2. J.F. Drake, P.K. Kaw, Y.C. Lee, G. Schmidt, C.S. Liu and M.N. Rosenbluth, Phys. Fluids 17, (1974) 778.
3. R. Bingham and C.N. Lashmore-Davies, Culham Lab. Preprint CLM P421 (1975).
4. See, for example, V.V. Korobkin and A.J. Alcock Phys. Rev. Letts. 21, (1968) 1433, and M.H. Key, D.A. Preston and T.P. Donaldson, J. Phys. B 3, (1970) L88.
5. A.Y. Wong, R.L. Stenzel, H.C. Kim, and F.F. Chen, IAEA Tokyo Conference Paper IAEA-CN-33/H4-1 (1974).

83

INTERACTION OF AN INTENSE LASER FIELD WITH A PLASMA : A KINETIC APPROACH.

by R. Balescu
Université Libre de Bruxelles, Association Euratom-Etat Belge
and I. Paiva-Veretennicoff
Vrije Universiteit Brussel, Fakulteit van de Wetenschappen,
Brussels, Belgium.

Abstract : Consideration is given to the parametric resonances involving the coupling of an external harmonic electric field to the plasma waves and to the purely damped plasma dynamical modes of zero frequency. A new type of thresholdless instability appears in this class of processes.

Eq. (4) in the main text describes the evolution of the amplitudes $a_{n,k}$ of the plasmadynamical (PD) modes under the influence of an external electric field. The present work is restricted to the study of the first term of the r.h.s. of eq.(4), neglecting all collisional and Vlassov non-linearities.
We consider an electric field of the form

$$\vec{E}(t) = 2\vec{E} \cos \omega_o t \qquad (5)$$

where $\vec{E}$ is a real, constant vector.
The most effective couplings of PD modes is obtained when a resonance condition can be satisfied :

$$\mathrm{Re}\,(\omega_{n,k} - \omega_{m,k}) \pm \omega_o = 0 \qquad (6)$$
$$[n,m=1,\ldots,14]$$

Eq. (4) then reduces to

$$\dot{\tilde{a}}_{n,k}(t) + \lambda_{n,k}\,\tilde{a}_{n,k}(t) = \sum_m^{(R)} E_{n,k;m,k}\,\tilde{a}_{m,k}(t) \qquad (7)$$

(where $\tilde{a}_{n,k}(t)$ includes the time dependence due to the imaginary part of the PD frequency $\omega_{n,k}$).
This equation contains in particular the classical parametric instabilities. Besides, it contains effects which have not been considered before. Indeed, resonant triplets can be constructed, involving one mode of zero frequency and one high frequency plasma wave. The former are purely dissipative decay modes, whose damping rates are determined, in a first approximation, by the friction and heat exchange transport coefficients. Under these resonance conditions, ten modes can be simultaneously coupled. Looking for solutions of eq. (7) in the form

$$\tilde{a}_{n,k}(t) = e^{\Lambda t}\,\tilde{a}_{n,k}(0) \qquad (8)$$

we obtain a dispersion equation of tenth degree.
In the PD approximation, (i.e. $kc_e/\omega_e \ll 1$) it has the following form :

$$\Lambda(\Lambda+\tilde{\lambda})^4\left[\Lambda(\Lambda+\tilde{\lambda}) - \frac{2}{3}\varepsilon^2 \sin^2\theta \frac{\mu}{1+\mu} k^2 c_e^2\right]\Phi(\Lambda) = 0 \qquad (9)$$

where $\Phi(\Lambda)$ is a third degree polynomial, whose roots have negative real parts and will not be discussed here. $\tilde{\lambda}$ is the damping rate of the plasma waves (see eq.(1)). In the PD approximation it reduces to

$$\tilde{\lambda} = \frac{1}{2}(1+\mu)\,\zeta\,\omega_e \qquad (10)$$

θ is the angle between the wave vector $\vec{k}$ and the external field $\vec{E}$. The latter is expressed by the dimensionless parameter ε^2:

$$\varepsilon^2 = e^2E^2/\omega_e^2 m_e k_B T \qquad (11)$$

One of the roots of the bracketted factor in eq. (9) is definite negative. The other provides the zero mode instability. For all values of the external field it is definite positive. Its growth rate for small k is given by

$$\Lambda_1 = (4/3)\,\mu(1+\mu)^{-2}\zeta^{-1}\,(kc_e/\omega_e)^2\varepsilon^2\sin^2\theta\,\omega_e \qquad (12)$$

It can be shown that under conditions of interest in laser fusion, this rate is by no means negligible compared to other decay instabilities. Furthermore, the main feature of this instability is the absence of any threshold.

Erratum : The two last lines of eq.(1) in the main text should be replaced by :

$$\omega_e^{-1}\,\omega_9 = \omega_e^{-1}\omega_{13} = i\zeta(ck/\omega_e)^2$$

$$\omega_e^{-1}\,\omega_{10} = \omega_e^{-1}\omega_{14} = -i\frac{\mu}{1+\mu}\,(\eta_e+\eta_i)(c_e k/\omega_e)^2$$

References

R. Balescu and I. Paiva-Veretennicoff, three papers to appear in J. Plasma Phys.

101

Stability of Tokamaks with Respect to 'Slip' Motions (Supplement)

E. Rebhan, A. Salat
Max-Planck-Institut für Plasmaphysik, 8046 Garching bei München,
Federal Republic of Germany

Abstract: The relation between 'slip' motions and general axisymmetric perturbations is considered.

According to the main paper the 'slip' motions which minimize δ^2W are special axisymmetric perturbations. Obviously, they are minimizing among all axisymmetric perturbations in the limiting case $\Lambda_o \to \infty$. This case is obtained if, for example, $A \to \infty$ for fixed β_p and fixed safety factor q. For finite Λ_o, lower values of δ^2W may be reached by more general axisymmetric perturbations. For these, δW_{pl} contains the additional term $\Lambda_o^2 \int \mathrm{curl}^2\,(\underline{\xi} \times \nabla\theta)d\tau$, whereas δW_s and δW_{vac} are the same as for 'slip' motions. The Euler equations now obtained by minimizing δW_{pl} for ξ_n given on the plasma boundary may again be integrated analytically and used to reduce δW_{pl} to a surface integral

$$\delta W_{pl} = \pi\,\gamma\,p \oint \frac{R^2+\alpha^2}{R}\,f(R)\,\xi_n dl \ ,$$

$$\alpha^2 = \Lambda_o^2/\,p\gamma .$$

f(R), which is obtained from this integration, is determined by the boundary condition $\underline{n} \cdot \underline{\xi} = \xi_n$ or

$$\ddot{f} + \left[\frac{R\dot{R}}{z}\left(\frac{z}{R\dot{R}}\right)^{\cdot} + \frac{6R^2}{\alpha^2+R^2}\frac{\dot{R}}{R}\right]\dot{f} - \frac{4\alpha^2R^2}{(\alpha^2+R^2)^2}f = -\frac{4\alpha^2}{(\alpha^2+R^2)^2}\frac{\dot{R}}{z}\,\xi_n^s$$

(the dot denotes differentiation with respect to the arc length on the plasma boundary). For given antisymmetric ξ_n, the minimum of δW_{pl} vanishes both for 'slip' motions and general axisymmetric perturbations. From this and the foregoing it follows that the corresponding stability boundaries coincide exactly. For symmetric ξ_n, the difference in δW_{pl} leads to different stability boundaries. However, this difference is practically negligible for $A \geq 4$. Only for lower A and $q \leq 1$ does the stable region of general axisymmetric perturbations become visibly narrowed as compared to 'slip' modes. Two examples of such cases are shown in the figure below (the boundary for symmetric 'slip' motions is dotted).

"This work was performed under the terms of the agreement on association between the Max-Planck-Institut für Plasmaphysik and EURATOM".

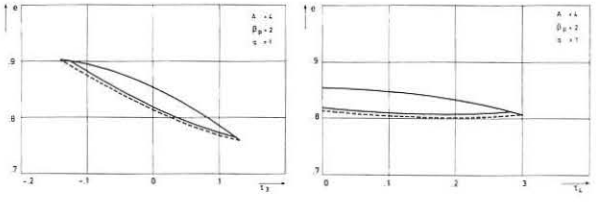

120

MULTISPECIES DIFFUSION COEFFICIENTS IN THE PFIRSCH-SCHLUTER AND BANANA REGIMES FOR ALL TEMPERATURE AND MASS RATIOS

P.ROLLAND - F.WERKOFF*

ASSOCIATION EURATOM-CEA
Département de Physique du Plasma et de la Fusion Contrôlée
Service IGn - Centre d'Etudes Nucléaires
BP 85 - Centre de TRI 38041
GRENOBLE CEDEX (FRANCE)

We have improved the results presented in the first version of this paper, in which we have used a simplified Fokker-Planck operator (5) based on the usual assumption that

$$\partial f_i/\partial v_{\parallel} \gg \partial f_i/\partial v \qquad (18)$$

This assumption which has been used in most papers concerning this problem, allows to simplify considerably the F.P. operator /8/ and leads to a friction force depending on the Rosenbluth Potential for diffusion g and not on the R.P. for friction h. However, the integration of the full F.P. operator /2/ shows that the friction force R_j depends upon the R.P. for friction h and not on the R.P. for diffusion g /8/. We have :

$$R_{jk} = \mathcal{R}_{jk} + \mathcal{R}'_{jk} = m_j \int d\underline{v}\, v_{\parallel}\, C(f_{oj}, f_{ok}) + m_j \int d\underline{v}\, v_{\parallel}\, C(f_{oj}, f_{ik}) \quad \text{where} \qquad (19)$$

$$\mathcal{R}_{jk} = 2\pi m_j F'_j \int dv\,dp\, p v^2 f_{oj}\, \partial_v h_{jk} \quad ; \quad \mathcal{R}'_{jk} = -\mathcal{R}_{kj} \qquad (20)$$

whereas the assumption (18) would give :

$$\mathcal{R}_{jk} = -2\pi m_j F'_j \int dv\,dp\, p f_{oj}\, \partial_v g_k \quad (F'_j = 4\pi e^4 Z_j^2 Z_k^2 \ln\Lambda / m_j^2) \qquad (21)$$

Eq.(20) and (21) are fortuitously equivalent when $m_k \gg m_j$. Similarly, the variational principle using the assumption (18) leads to expressions of the fluxes depending on a quantity F (eq A8 /2/) function of g only. Theses considerations have led us to recalculate the coefficients :

$$A_{jk} = -m_j \int d\underline{v}\, v_{\parallel}\, C(v_{\parallel} f_{oj}, f_{ok}) \quad ; \quad B_{jk} = -m_j \int d\underline{v}\, v_{\parallel}\, C(v_{\parallel} v^2 f_{oj}, f_{ok}) \qquad (22)$$

using the exact F.P. operator. We obtain :

$$A_{jk} = \frac{4}{3}\sqrt{2\pi}\, e^4 \ln\Lambda N_j N_k Z_j^2 Z_k^2 \left\{ \frac{(m_j m_k)^{\frac{1}{2}} (m_j + m_k) T_j}{(m_j T_k + m_k T_j)^{3/2} m_j} \right\}$$

$$B_{jk} = A_{jk} \frac{T_k T_j^2}{m_j (m_k T_j + m_j T_k)} \left\{ 2\frac{m_k}{T_k} + 5\frac{m_j}{T_j} \right\} \qquad (23)$$

with these new coefficients, the expression (16) of T'_j in the Pfirsch-Schluter regime remains formally valid. It gives :

$$T'_j = -\sum_k \frac{16}{3} \frac{\sqrt{\pi} e^2 \ln\Lambda}{B_\theta^2} N_j N_k \frac{Z_k}{T_j} \left(\frac{r}{R}\right)^2 \left(\frac{m_j + m_k}{m_k}\right) \frac{b_j^{4/2} b_k^{3/2}}{b_{jk}^{3/2}} \left\{ T_j Z_k \left[\frac{N'_j}{N_j} - \frac{T'_j}{2T_j} + \frac{3}{2}\frac{b_j}{b_{jk}} \frac{T'_j}{T_j} \right]_j - T_k Z_j \left[\frac{N'_k}{N_k} - \frac{T'_k}{2T_k} + \frac{3}{2}\frac{b_k}{b_{jk}} \frac{T'_k}{T_k} \right]_k \right\} \qquad (24)$$

$b_j = \frac{m_j}{2T_j}$; $b_{jk} = b_j + b_k$.

we note that the bracket $[\ ]_j$ reduces itself to $\frac{N'}{N} - \frac{T'}{2T}$ if $\frac{m_j}{T_j} \ll \frac{m_k}{T_k}$ and to $\frac{N'}{N} + \frac{T'}{T}$ if $\frac{m_j}{T_j} \gg \frac{m_k}{T_k}$.

In the banana regime, we obtain :

$$T'_j = \frac{1.46\sqrt{\varepsilon}}{Z_j e^2 B_\theta^2} \sum_k \left\{ m_j A_{jk} \left(-\frac{1}{Z_j} \left(\mathcal{A}_{1j} + \frac{m_j}{2} \frac{B_{jk}}{A_{jk}} \mathcal{A}_{2j} \right) \right) + \frac{m_j A_{jk}}{T_j} \frac{\sum_{ab} m_a A_{ab} \mathcal{A}_{1a} / Z_a + m_a^2 B_{ab} \mathcal{A}_{2a} / 2 Z_a}{\sum_{ab} m_a A_{ab} / \tau_a} \right\} \qquad (25)$$

For 2 species with $m_k \gg m_j$ we find :

$$T'_j = \frac{4}{3}\sqrt{2\pi} \frac{\sqrt{\varepsilon}}{Z_j e B_\theta^2} e^4 \ln\Lambda N_j N_k Z_j^2 Z_k^2 \left\{ 2.49 \left(-\frac{N'_j}{Z_j N_j} + \frac{T_k}{T_j} \frac{N'_k}{Z_k N_k} \right) + 0.47 \frac{T'_j}{Z_j T_j} + 0.62 \frac{T'_k}{Z_k T_j} \right\} \qquad (26)$$

The expression given by Rosenbluth was, for e-i = /2/

$$T'_e = \frac{4}{3}\sqrt{2\pi} \frac{\sqrt{\varepsilon}}{e B_\theta^2} e^4 \ln\Lambda N^2 \left\{ -2.24 \left(1 + \frac{T_i}{T_e}\right) \frac{N'}{N} + 0.36 \frac{T'_e}{T_e} + 0.38 \frac{T'_i}{T_e} \right\}$$

The heat fluxes Q_j will be given in a future publication.

Reference :

/8/ - F.WERKOFF - DPh-PFC-Note interne n° 1140.

*Present address : Association Euratom-CEA - Département de Physique du Plasma et de la Fusion Contrôlée - Service STGI - Centre d'Etudes Nucléaires - B.P. 6 - 92 FONTENAY-aux-Roses (France).

131

IMPURITY PROFILES IN A STEADY-STATE D-T REACTOR

J.A. Markvoort and J. Rem
Association Euratom-FOM, FOM-Instituut voor Plasmafysica
Rijnhuizen, Jutphaas, The Netherlands

In the model of the reactor in which the thermal force arising from ion-ion collisions is introduced, i.e.

$$\left\langle \frac{d\bar{p}}{dt} \right\rangle_{ij} = \frac{3}{2} \alpha_{ij} \frac{n_i k}{\omega_i \tau_{ij}} \frac{\bar{B} \times \nabla T}{|B|}$$

where

$$\alpha_{ij} = \frac{m_j^2}{(m_i + m_j)^2} \left(1 - \frac{m_i^2 \omega_i}{m_j^2 \omega_j} \right), \quad \omega_i = \frac{z_i e B}{m_i}$$

and $$\tau_{ij} = \sqrt{\frac{m_i m_j}{m_i + m_j}} \frac{(kT)^{3/2} 12\pi^2 \varepsilon_o^2}{\sqrt{2\pi}\, n_j e^4 z_i^2 z_j^2 \ln\Lambda}$$

we find radial distributions of the carbon (n_c) and the "deuterium" (n_d) densities (Figs. 3 and 4 in the addendum) completely different from the case in which only Nernst terms due to ion-electron collisions are taken into account (Figs. 1 and 2 of the paper).

From these representative numerical solutions of the complete set of MHD equations it is seen that the impurity density decreases towards the axis. This behaviour agrees with the analytical solutions given in the proceedings of this conference.

$$n_c T^{(1+z_c/4)} = \text{const.} \ (n_4 \gg n_d) \text{ and } n_c T^{(1+\frac{1}{4}z_c)} = \text{const.}$$

$(n_4 \ll n_d)$.

It must be noted that although the analysis refers to our specific reactor model, the results are also applicable to any low-β plasma column that is ohmically heated.

Conclusion: It is found numerically as well as analytically that the thermoforce due to ion-ion collisions dominates and will lead to an impurity profile which has a minimum at the axis.

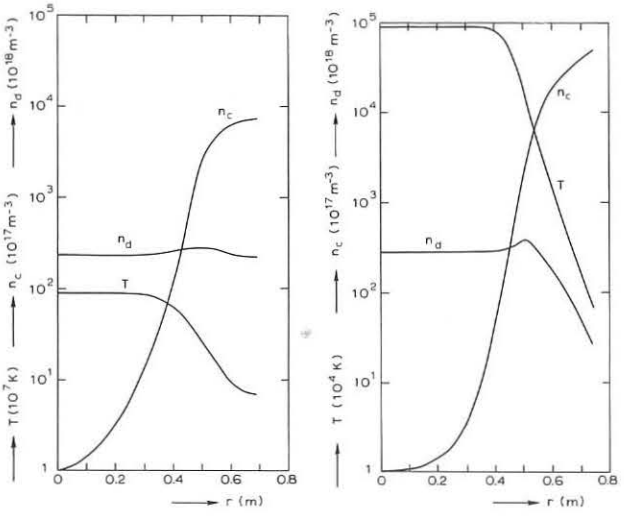

Fig. 3.
Radial profiles of n_c, n_d, and T.
z = 2
T_{axis} = 0.9×10^9 K
B_{axis} = 0.5 T
$\frac{n_4}{n_d}_{axis}$ = 1
p_{axis} = 150 atm.
$n_{c_{axis}}$ = 10^{17} m^{-3}

Fig. 4.
Radial profile of n_c, n_d, and T.
z = 1
T_{axis} = 0.9×10^9 K
B_{axis} = 0.1 T
$\frac{n_4}{n_d}_{axis}$ = 0.8
p_{axis} = 150 atm.
$n_{c_{axis}}$ = 10^{17} m^{-3}

134

INTERACTION OF NEUTRAL HYDROGEN AND PLASMA INCLUDING WALL REFLECTION*

J. F. Clarke and D. J. Sigmar
Oak Ridge National Laboratory and Massachusetts Institute of Technology

We present results from numerical calculations using the model we have described. We first consider the scaling of the size of the neutral gas boundary layer, as one proceeds to larger and hotter plasmas. We arbitrarily define the inner edge of the neutral gas layer (denoted as radius a^*) as that point at which the neutrals' source strength, S_{FC}, has dropped to 1% of its external value. The Table gives results for sizes from 15 to 170 cm, and for temperatures from 700 ev to 5.6 keV. For these results we assume equal electron and proton densities.

As a second case, we consider the effects of wall reflection, as described by the Robinson model, for a contemporary experiment: ORMAK. In Figure 1a we show the ratio of total neutral density to edge neutral density, and the ratio of mean neutral energy to the central ion temperature. We note a substantial difference in the expected central neutral density. In Figure 1b we show the neutrals' parallel velocity, both with and without effects of reflection. The friction due to charge exchange, and the resulting non-ambipolar flux, are both considerable.

Acknowledgment

We are grateful to D. E. Arnurius, of the Computer Sciences Division, ORNL, for these numerical calculations.

Table I: Neutral density effects at the edge of the neutral layer

$T_i(0)$ (ev)	$N_i(0)$ (cm^{-3})	Plasma Minor Radius (cm)	Neutral Layer Thickness (a^*/a)	$\tau_{cx}(a^*)$ (Msec)
700	$5 \cdot 10^{13}$	15	.70/.70	34/28
1400	$5 \cdot 10^{13}$	40	.84/.85	34/22
2800	10^{14}	60	.93/.96	18/7.1
5600	10^{14}	170	.97/.98	7.1/2.8

Note: The two cases are: first, $T_i(a) = 10$ ev, constant as $T_i(0)$ varies; second, $T_i(a) = 0.1\ T_i(0)$. The latter simulates operation with a divertor, with relatively flat temperature profiles.

*Research sponsored by the U. S. Energy Research Administration under contract W7405-eng-26 with Union Carbide Corporation and contract AT(11-1)3070 at Massachusetts Institute of Technology.

FIGURE 1a

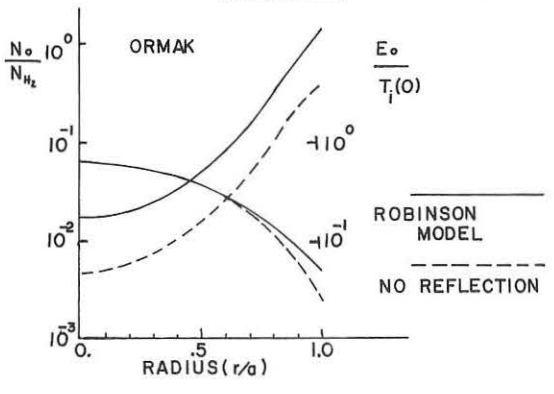

FIGURE 1b

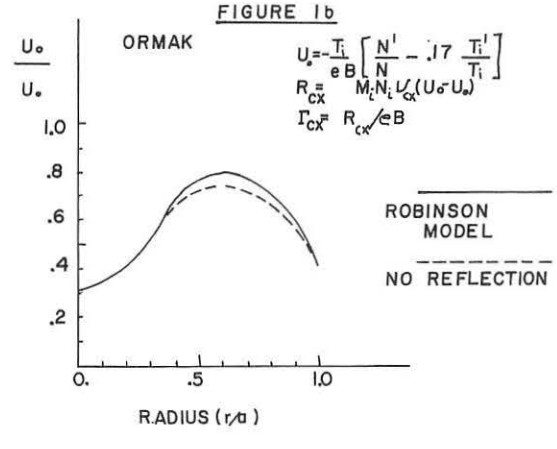

136

LOWERING THE IMPURITY LEVEL IN PULSATOR BY PULSED GAS INFLOW

B. Cannici, W. Engelhardt, J. Gernhardt, E. Glock, F. Karger, O. Klüber, G. Lisitano, D. Meisel, P. Morandi, S. Sesnic
Max-Planck-Institut für Plasmaphysik, 8046 Garching, Germany

In part I of our contribution we gave a comparison of discharges with and without pulsed gas inflow. It was found that for a given neutral influx, the increase in density was dependent on the appearance of MHD-modes. Further experiments showed that it is easier to attain high densities in discharges with higher current (and consequently lower q-values). An example is given in Fig. 1. In this case the maximum electron density reaches more than 10^{14} cm^{-3} whereas the electron temperature drops only slightly. Fig. 2 shows line intensities of oxygen and molybdenum for the same discharge. It is evident that oxygen stays constant and molybdenum is reduced when the density is raised by the neutral influx. Since the contribution of molybdenum to Z_{eff} is small compared that of oxygen, we conclude that the reduction of Z_{eff} is mainly due to adding hydrogen at a constant influx of oxygen, whereas the suppression of molybdenum plays a minor role. At late times ($>$ 70 msec), for some unknown reason the impurity influx of both oxygen and molybdenum increases again, which probably prevents a further reduction of Z_{eff}. It seems, however, that the relative content of impurities does not rise again.

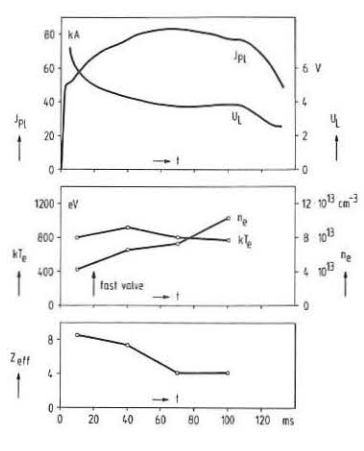

Fig. 1: Plasma parameters in high current discharges ($q \approx 2.5$) with gas inflow. Electron temperatures and densities are peak values on axis taken from Thomson scattering.

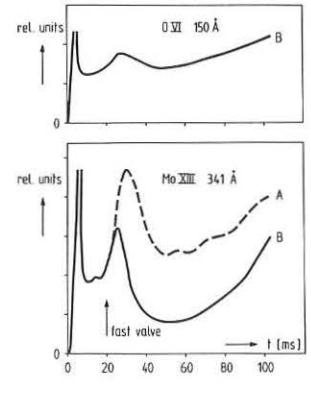

Fig. 2: Impurity line intensities in high current discharges with (B) and without (A) gas inflow.

156

FILAMENTATION INSTABILITY OF AN ION-SOUND WAVE

E. CANOBBIO

ASSOCIATION EURATOM-CEA
Département de Physique du Plasma et de la Fusion Contrôlée
Service IGn - Centre d'Etudes Nucléaires
B.P.85 - Centre de Tri - 38041
GRENOBLE CEDEX (France)

In this supplementary paper we write the dispersion relation for filamentation instability without imposing the restriction $|\omega| \ll \omega_o$. At the same time, we correct an algebric error which occurred in the derivation of Eqs. (4) of the main paper (Vol. 1, p. 156). The main effect of this correction is the disappearing of the explosive character of the filamentation instability.

If $|\omega/kv_{ti}|$ and $|\omega/\omega_o|$ are arbitrary, while

$$|\omega_\pm|^2/k_\pm^2 \equiv |\omega \pm \omega_o|^2/(\vec{k} \pm \vec{k}_o)^2 \gg v_{ti}^2,$$

the following Fourier coefficients of the ion density are obtained (instead of Eqs. (4)) :

$$4\pi e\, n_i^{(o)} = -\, k^2 \chi_i^{(o)} \left\{ \phi^{(o)} + \frac{e\phi_o}{T_e} \sum_{\pm} \left(\frac{\pm\omega_o^2}{\omega_\pm^2}\right) \phi^{(\pm 1)} \right\} ,$$

$$4\pi e\, n_i^{(\pm 1)} = -\, k_\pm^2 \chi_i^{(\pm 1)} \left\{ \phi^{(\pm 1)} \mp \frac{e\phi_o}{T_e} \left(\frac{\omega_o}{\omega_\pm}\right)^2 \left\{ 4\pi e\, (1 + \frac{2\omega}{\omega_\pm}) n_i^{(o)} + \right.\right.$$

$$\left.\left. + \frac{\omega_{pi}^2}{\omega_\pm^2} (1 \pm \frac{2\omega_o}{\omega_\pm}) \phi^{(o)} \right\} ,$$

where $\chi_i^{(o)}$ and $\chi_i^{(\pm 1)}$ are defined as in the main paper.

The dispersion relation which can be derived, with the help of Poisson Equation, from these equations and from the corresponding ones for the electrons is :

$$\frac{T_i}{T_e} + (1 + x\, Z\,(x)) \left\{ 1 + \left|\frac{e\phi_o \omega_{pi}}{T_e \omega_o}\right|^2 \sum_{\pm} \frac{(1 + (\frac{\omega_o}{\omega_\pm})^2)((\frac{k_o}{k})^2 - 1 \mp 2\frac{\omega_o}{\omega_\pm})}{(\frac{\omega}{\omega_o})^2 - (\frac{k}{k_o})^2 \pm \frac{2\omega}{\omega_o}} \right\} = 0$$

This equation admits unstable solutions only if $|\omega| \ll \omega_o$. Then, defining y, F(y), and Q as in the main paper, we find :

$$\frac{T_i}{T_e} + F\,(y) \left\{ 1 - \frac{Q((k_o/k)^2 - 3)\ (1 + 3(y/x_o)^2)}{(y/x_o)^2 + \frac{1}{4}\,(k/k_o)^2 (1 + (y/x_o)^2)^2} \right\} = 0$$

Marginal stability (y = 0) corresponds to curve A in Fig. 1 of the main paper; instability occurs everywhere below this curve in the $(+\sqrt{Q},\ (k/k_o)^2)$-plane. On the other hand, the growth-rate never goes to infinity, and both curve B and Fig. 2 should be disregarded.

If $3\,Q(k_o/k)^2 \gg 1$, the growth rate is essentially a linear function of the pump amplitude, as :

$$y^2 = x_o^2\, 3\, Q\, (k_o/k)^2 .$$

The conclusions drawn in the main paper are still valid. More details about low-frequency parametric instabilities in the absence of a static magnetic field may be found in the reference.

REFERENCE.

E. CANOBBIO, Parametrically unstable ion-sound waves, Nuclear Fusion, in press.

166

Mass Dependence of Ion Heating in Turbulently Heated Plasmas (THE MACH II)

K. Adati, H. Iguchi, Y. Ito,* T. Kawabe,** K. Kawasaki,* T. Oda,* R. Sugihara and T. Yokota***

Institute of Plasma Physics, Nagoya University, Nagoya, Japan
* Faculty of Science, Hiroshima University, Hiroshima, Japan
** Also Plasma Physics Group, Physics Dept., University of Tsukuba, Ibaragi, Japan
*** Physics Dept., Kyoyobu, Ehime University, Matsuyama, Japan

An additional experiment has been performed with THE MACH II device in which the initial plasma have been produced by a theta pinch gun, also furnished with the same mixture gas. It can produce highly ionized plasmas from the start.

Two energy distributions have been also found. Fig. 1 shows the mass dependence of the ion temperatures, T_i, in this case: that of the hot component is of the form, $T_i \propto M^\alpha$. α is estimated to be between 1/3 and 7/9. The cold components have not shown clear mass dependence in the heating. Fig. 2 shows the velocity at the transition point from the cold component to the hot one in the energy distribution of the ions, indicating almost constant value with the ion mass. Ratio of the particle number of the hot component to that of the cold one decreases with increase of the ion mass (Fig. 3).

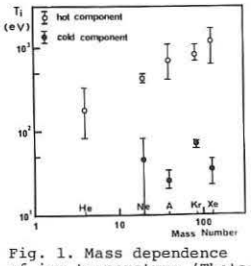

Fig. 1. Mass dependence of ion temperature (Theta-pinch gun)

On the basis of these experimental results, a possible explanation about the mass dependence of the ion heating is as follows: In the case $\alpha \geq 1$ (the result of the experiment with the T_i-washer gun), the ion being trapped in a certain wave in the plasmas are accelerated to its phase velocity. In the case $\alpha < 1$, the quasi-linear diffusion in the velocity space of the ions due to excited waves dominantly produces the high energy tail.

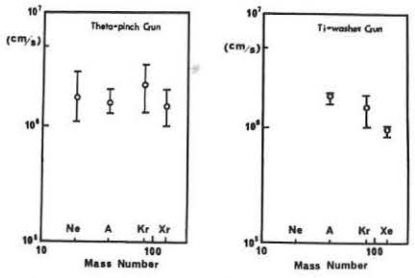

Fig. 2. Velocity at the transition point.

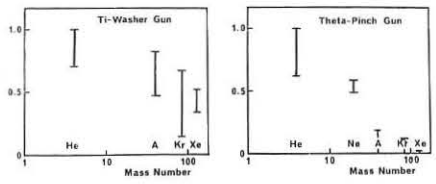

Fig. 3. Ratio of the particle number of the hot component to that of the cold one.

POST-DEADLINE PAPERS

NEUTRON YIELD ENHANCEMENT IN A FOCUS - LASER EXPERIMENT

S.Kaliski, J.Baranowski[x], M.Borowiecki, S.Denus, M.Gryziński[x], K.Jach, A.Jerzykiewicz[x], M.Kielesiński, S.Kowalski, J.Kubicki, Z.Kurzyński, J.Nowikowski[x], P.Parys, T.Rusinowicz, M.Sadowski[x], J.Wawer, J.Wolski, J.Wołowski.

Institute of Plasma Physics and Laser Microfusion, Warsaw, Poland

INTRODUCTION

As part of the studies on laser heating and plasma compression / 1 / the construction was started at the Institute of Plasma Physics and Laser Microfusion / IPPLM / in Warsaw of a combined Focus-Laser system according to the concept of one of the authors of this paper. The aim of this system was to obtain better parameters of heating and a higher total neutron yield than is the case with the Focus alone. This system, described later in this paper, is based on a F-150 plasma-focus machine of an energy of 150 kJ and a CO_2 laser of an energy of about 200 J in a pulse of some tens of nanoseconds. Similar work has been taken up at the Lebiediev Institute in Moscow / 2 /.

The theory / 3,4 / developed on the basis of an approximate one-dimensional average description enabled a statement to be made that for assumed combined system an increase by 200-300 per cent in the neutron yield, in relation to the Focus, is possible / 5 /. In accordance with the results of the theoretical computations we have obtained experimentally an about threefold increase in neutron emission from the F-L system, i.e., up to 10^{10} neutrons per shot, and about 10^8 neutrons per 1 J of the absorbed laser energy. This means a 10^5 - 10^6 times higher neutron output than that from the solid targets heated by lasers. An extension of this experiment on a MJ-Focus and kJ-lasers may enable a critical condition to be reached, i.e., assure 10^{15} - 10^{16} neutrons per discharge.

[x] Institute of Nuclear Research, Świerk near Warsaw , Poland

THEORY

The general equations of the F-L system have been given in the paper / 3 /. Assuming the approximation of a one-temperature plasma and one-dimensional system r/t/ we have obtained, according to the paper / 5 / the following approximate, averaged equations of the Focus heating by the laser beam:

$$\frac{3}{4}\frac{d}{d\tau}\left[(X\dot{X})^{\cdot} + S + \frac{4}{3}S\ln X\right] = \bar{Q}_0\left(1 - \frac{v_0 \tau t_0}{2l}\right)$$

$$\bar{Q}_0 = \frac{Q_0 t_0^3}{G_0 r_0^2}, \qquad S = \frac{I_0^2 l t_0^2}{G_0 c^2 r_0^2}$$

where: Q_0 - laser radiation intensity, G_0 - Focus mass, $I_0 = I_0/r/$ - current /constant value/, $\tau = t/t_0$, $x = r/r_0$. The following parameters of the F-L system are assumed / 5 /: $Q = 10^{16}$ erg/sec, $r_0 = 0{,}1$ cm, $l = 1{,}0$ cm, $n_0 = 10^{19}$ cm^{-3}, $T_0 = 2$ keV, $t_0 = 10^{-7}$ sec, $v_0 = 2 \cdot 10^7$ cm/sec / mean velocity of the axial plasma flow through the Focus/. If instead of Q_0 we assume νQ_0 the critical condition $x = 2$ for $\tau = 1$ gives $\nu \simeq 1{,}4 \div 2{,}8$.

For a more detailed analysis, the delay time, before the uniform expansion occurs, must be taken into account. This is approximately:

$$\tau_D = \frac{2 r_0}{D} \quad \text{where} \quad D = \sqrt{\frac{P}{\rho}\frac{\gamma+1}{2}} \sim \sqrt{\frac{kT_0}{m}} \simeq 1 \div 2 \cdot 10^7 \text{ cm/sec}$$

which gives: $\tau_D \approx 20$ ns

On this assumption it can be shown that taking into account this delay time only without the uniform expansion we obtain the experimental results. That is, if we assume the laser energy E_L to be 200 J in $\tau_0 = 80$ nsec, then in time of 20 ns the energy absorbed, without the expansion, is ~ 50 J, and the increase in temperature is: $\Delta T = E/\frac{3}{2} k N_0 = 10^9/1{,}5\ k N_0 = 1$ keV. This gives the approximate estimation of the increase in the neutron output by:

$$N_{L+F} \approx N_F (\eta)^{2,8} \simeq N_F (1{,}5)^{2,8} \simeq 3 \cdot N_F$$

where:

$$\eta = \frac{T_0 + \Delta T}{T_0} = 1{,}5$$

EXPERIMENTAL SYSTEM AND RESULTS

A diagram of the F-L system and the basic diagnostic apparatus is shown in Fig.1. The CO_2 laser beam is introduced from behind the Focus chamber through a NaCl lens and an 8 mm orifice in the central electrode along the Focus axis. Controlling the two systems is done by means of a current pulse generator with a time-delay units. The synchronization was verified by comparing the position on the oscilloscope screen of the laser pulse in relation to the X-ray pulse or the current singularity /with a time jitter of $\pm$ 10 $\div$ 20 nsec/. For registration of laser radiation a semiconductor CdHgTe detector was used supplied from a 30 V pulsed supply unit. The neutron yield was registered by means of a set of G-M silver counters and a fast scintilation detector located at a distance of 7 m from the focal point. A soft X-ray double scintilation counter was utilized for determining the electron temperature. The X-ray photographs of the focus were taken by means of a pinhole camera.

The most important experimental results are plotted in Fig.2. This diagram shows that the Focus discharges without the laser were performed alternatively with those with the laser pulse. Information on the synchronization and the laser energy has been given for each shot. The results presented in Fig.2 indicate a two- or threefold increase in neutron yields. The agreement with the simple theory is quite satisfactory.

To the best of our knowledge, the result obtained in our laboratory is the first one, in which a significant increase in the neutron yield in a combined Focus-Laser system has been achieved. Further work on this experiment is in progress.

REFERENCES

1. S.Kaliski - Laser compression and fusion of plasma in: Third Workshop on "Laser interaction and related plasma phenomena". New York 1973 Rensselaer Pol.Inst.Troy.
2. N.G.Basov, W.A.Gribkov et al-VIII Intern.Conf. on Laser Plasma Fusion, Warsaw, Poland, May 1975.
3. S.Kaliski - Proc.Vibr.Probl. 3, 13, 1972.
4. S.Kaliski - Bull.Acad.Polon.Sci.,Ser.Sci.Techn. 6, 20, 1972.
5. S.Kaliski - Journal of Techn.Physics 3, 16, 1975.

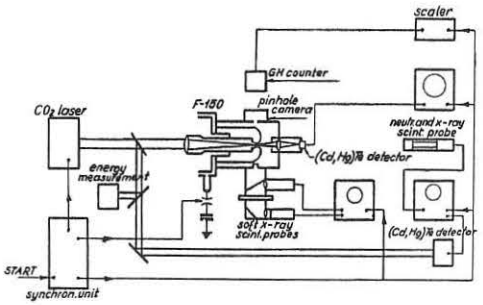

Fig.1. Set-up of the "F+L" experiment.

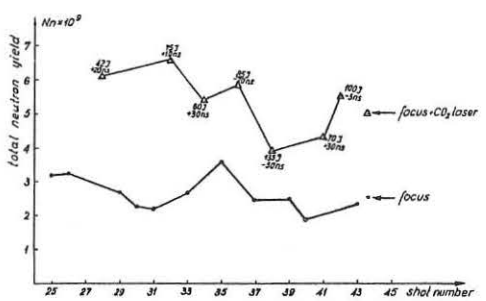

Fig.2. Neutron yield enhancement from CO_2 laser-plasma focus interactions.

189 PARAMETRIC EXCITATION OF ION FLUCTUATIONS IN THE RELATIVISTIC BEAM-PLASMA INTERACTION

H. Schamel*, Y. C. Lee, and C. Morales,
University of California, Los Angeles, USA.

The temporal evolution of a beam-plasma system is investigated numerically and analytically. A cold relativistic beam permeating an infinite and uniform plasma drives through the hydrodynamic two-stream instability a monochromatic beam mode. Saturation occurs by beam trapping. At this stage the amplitude of the wave is large enough to drive parametric instabilities involving ion fluctuations. Various aspects of this general problem have been investigated by Thode and Sudan[1] in computer simulations. Our numerical approach is of mixed type. We follow the beam particles individually by solving the relativistic equation of motion whereas the background particles and waves are treated analytically by using the linear dielectric function.

The total high frequency electric field E considered here consists of three modes

$$E(x,t) = A_+(\tau)e^{i(k_+x-\omega_p t)} + A_-(\tau)e^{i(k_-x-\omega_p t)} + A_o(\tau)e^{i(k_o x-\omega_p t)} + c.c.$$

where A_o is the amplitude of the fastest growing beam mode, $A_\pm$ refers to the amplitude of the parametrically excited stokes and anti-stokes modes, $k_\pm = k_o \pm k$ and k is the wavenumber of the ion density fluctuation. The normalized amplitudes of the high frequency modes are slowly varying quantities ($\tau = \varepsilon t$) and are determined by

$$\dot{A}_+(\tau) = -i A_o C$$

$$\dot{A}_-(\tau) = -i A_o C^*$$

$$\dot{A}_o(\tau) = -i(A_+ C^* + A_- C - F)$$

where the amplitude of the ion density fluctuation $C \propto \frac{\delta n}{n_o}$ is determined by

$$\ddot{C} + \Delta C = -p(A_+ A_o^* + A_-^* A_o)$$

The free parameters Δ and p depend on k, the initial beam velocity v_o, and on the smallness parameter $\varepsilon = \left(\frac{n_b}{2n_o}\right)^{1/3}\gamma_o^{-1}$ where $\gamma_o = (1 - v_o^2/c^2)^{-1/2}$ and n_b is the beam density. Through $F = N^{-1}\sum_{j=1}^{N} \exp(-ik_o x_j(t))$, the Fourier transformed beam charge density, the N beam particles enter into the coupled wave system. The position of the j-th particle $x_j(t)$ is obtained by solving the relativistic equations of motion. In the nonrelativistic limit and for $C \to 0$ the system reduces to the single wave model of O'Neil et al[2].

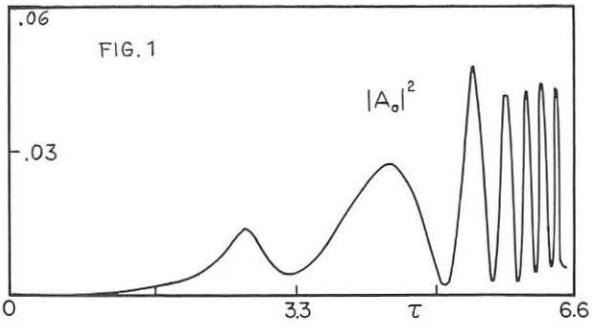

Fig. 1 shows the time evolution of $|A_o|^2$ for $\varepsilon = 1/38$, $\Delta = .04$, p = 644. We can distinguish two different phases. The first stage, $0 < \tau < 4.9$, is dominated by the relativistic dynamics of beam trapping as in the single mode model of Lampe & Sprangle[3]. The appearance of a second maximum where all beam particles are trapped being due to the velocity dependence of the trapped particles. In the second stage, $4.9 < \tau$, the parametric process dominates. The beam mode triggers the growth of ion fluctuations which feed back on the pump-wave to generate the fast oscillations seen in fig. 1. Since the beam particles cannot respond to this faster time scale, the particle dynamics is simply shut-off. What remains is a pure wave coupling problem. The decoupling of the beam can also be seen from fig. 2, where the time evolution of the fractional energy lost by the beam $\left[\sum_j \gamma_j(\tau) - \gamma_o\right](N\gamma_o)^{-1}$ is plotted.

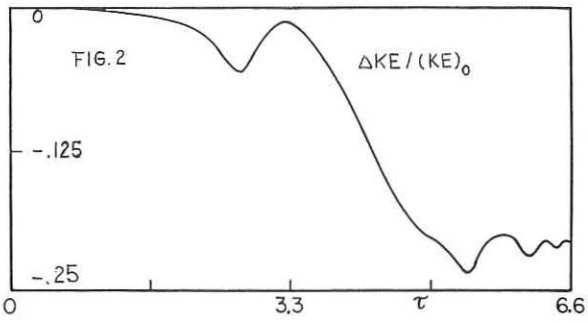

In this example the beam has lost 21 percent of its initial energy. The energy is at first fed into the high frequency oscillations, and then because damping has been neglected transferred to the ion fluctuation. The growth of the ion mode which is an absolutely growing mode is algebraic ($\propto \tau^n$) rather than exponential. Fig. 3 shows $|C(\tau)|$ together with the stokes mode.

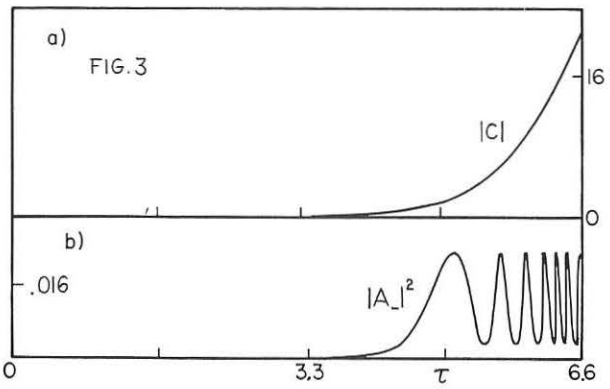

The onset of the parametric stage, and with it the energy extracted from the beam can be changed by changing p. Maximum energy is transferred to the plasma when the parametric process sets in right after the second maximum of $|A_o|$. Then the energy loss of the beam in the hydrodynamic stage can be as high as 23 % independent of the Thode-Sudan-parameter $S = (\gamma_o^2 - 1)\varepsilon$ provided $S > 2.5$.

*Permanent address: Ruhr-Universität Bochum, Theoretische Physik I, 4630 Bochum, W.-Germany

(1) L. E. Thode and R. N. Sudan, to appear in Phys. Fluids, (1975).
(2) T. M. O'Neil, J. H. Winfrey, and J. H. Malmberg, Phys. Fluids 14, 1204 (1971).
(3) M. Lampe and P. Sprangle, Phys. Fluids 18, 475 (1975).

PRELIMINARY EQUILIBRIUM STUDY ON ERASMUS, AN ASPECT RATIO TWO TOKAMAK WITH NO COPPER SHELL.

V.P. BHATNAGAR, G. BOSIA+, A.M. MESSIAEN, P.E. VANDENPLAS, R.R. WEYNANTS

Laboratoire de Physique des Plasmas - Laboratorium voor Plasmafysica

Association "Euratom-Etat belge" - Associatie "Euratom-Belgische Staat"

Ecole Royale Militaire - 1040 Brussels - Koninklijke Militaire School

and

R.J. TAYLOR, B. COPPI

Massachusetts Institute of Technology, Cambridge, Massachusetts 02139 U.S.A.

Abstract. Preliminary experiments on ERASMUS, the aspect ratio two tokamak of the Ecole Royale Militaire, demonstrate the attainment of equilibrium at very low aspect ratios. Flat top tokamak discharge current pulses of 40 kA and 3.5 ms duration have been obtained with a toroidal magnetic field of 4 kG on axis.

ERASMUS is the tokamak of the Ecole Royale Militaire / Koninklijke Militaire School characterized (see fig. 1) by an aspect ratio of 2, a large vessel volume ($\sim 0.8\ m^3$) and no copper shell. Its design is similar in many respects to the VERSATOR and RECTOR tokamaks of M.I.T. [1]. There are 3 x 8 ports of dimensions 32 x 5 cm^2 at eight locations around the machine. Pyrex glass windows on several of these ports provide 100 % visibility of the inside surface of ERASMUS. This unusually large access to the tokamak will be an asset in carrying out planned RF heating experiments on ERASMUS. The machine pumped by a turbomolecular pump attained a base pressure of 4×10^{-7} Torr.

The toroidal field coils are wound on the vacuum chamber itself. Neither a copper shell nor a limiter is used but the vertical and horizontal fields are provided by external coils placed outside the vacuum chamber (see fig.1). An air-core transformer is used for ohmic heating. The configuration of the machine enables a quick and simple assembly/disassembly operation.

Initial testing of ERASMUS was carried out at M.I.T. with the energizing supplies of the RECTOR machine. These supplies were insufficient to fully energize ERASMUS ; nevertheless, we were able to obtain flat top plasma currents of 40 kA for a few milliseconds. Final installation and operation of ERASMUS will be carried out in Brussels.

Before the tokamak plasma operation, the machine was subjected to "discharge cleaning". In this operation a 5 kHz, 25 kW power oscillator is fed to the OH transformer and a plasma is produced in a mixture of 50 % argon and 50 % hydrogen in the presence of a small dc toroidal field ($\sim$ 100 Gauss). Plasma particles bombard and heat the inside surface of the tokamak. One could visually watch and observe the gradual disappearance of "thin film rainbow patterns" on the inner surface of the machine during several days of discharge cleaning indicating that the latter is very effective.

Results. For the preliminary testing, only the magnetic diagnostics including the in/out and up/down position sensing loops were used. Typical oscillograms obtained after a few hundred shots of operation and with densities of $1 - 2 \times 10^{13} cm^{-3}$ (4 mm interferometer) are shown in figs. 2 and 3 and the following observations are made :

1) In fig. 2, a slow increase of plasma current in the flat top region confirms that the equilibrium has been obtained. Negative spikes in the loop voltage at the end of the pulse indicate the destruction of the equilibrium. Moreover, in/out and up/down traces show only a minor displacement of plasma position in the flat top region.
2) During the experiment, in/out and up/down traces have been found to respond correctly to the programming of vertical and horizontal fields provided by the external coils.
3) In fig. 3, the third trace shows the light (photodiode) output decreasing as a function of time and then peaking up again at the end of the discharge when the plasma hits the walls giving rise to a large neutral flux.
4) In fig. 3, the fourth trace shows that the level of hard x-rays is insignificant during the pulse when equilibrium conditions are attained.
5) In figs. 2 and 3, the high value of loop voltage tends to indicate that the machine still needs cleaning.

In conclusion, equilibrium has been obtained in an aspect ratio 2 tokamak with no copper shell and no limiter. This appears to be the first demonstration of equilibrium at very low aspect ratios. Tokamak plasma discharge current of 40 kA, 3.5 ms duration have been obtained for a toroidal field of $\sim$ 4 kG on the axis of the plasma resulting in a $q \sim 6$. We hope to get better values of q as the operation continues and as a result of the cleaning of the machine. Moreover, adequate energizing supplies are being installed in Brussels to increase the current magnitude as well as the length of pulse. The vertical field will be programmed and a feedback system on the horizontal field will be provided.

References.

[1] U. Ascoli-Bartoli, G. Bosia, G. Boxman, P. Brossier, B. Coppi, L. De Kock, B. Meddens, B. Montgomery, A. Oomens, L. Ornstein, R. Parker, L. Pieroni, S. Segre, R. Taylor, P. Van Der Laan, R. Van Heyningen, Proc. V IAEA Conference on Plasma Physics and Contr. Nuclear Fusion, Tokyo 1974, Vol.I, p. 191.

+ On leave of absence from Torino University, Italy.

Acknowledgements. It is a pleasure to acknowledge the skilled scientific help of Messrs S. Fairfax and F. Martin of M.I.T. The helpful discussions with Prof. R.R. Parker are gratefully acknowledged. The technical help of Mr P. Dandridge of Atomic Ltd, Cambridge in the fabrication of the machine is appreciated. The preliminary tests at M.I.T. were partially supported by the US - Energy Research and Development Administration under contract No. AT (11-1) - 3070.

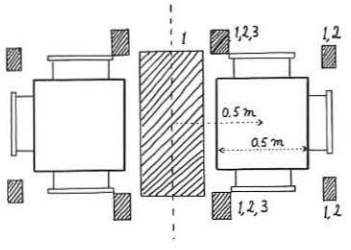

Fig. 1. Schematic drawing of ERASMUS. 1 : OH winding, 2 : vertical field winding, 3 : horizontal field winding.

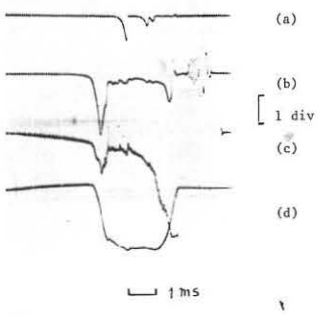

Fig. 2. Oscillogram of a typical plasma shot. (a) I_p (20 kA/div), (b) V_{loop} (20 V/div), (c) in/out (d) up/down. Horizontal scale 1 msec/div.

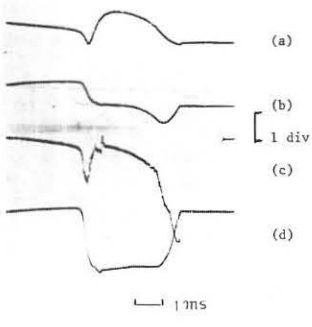

Fig. 3. Oscillogram of a typical plasma shot. (a) and (b) same as in fig. 2. (c) photodiode light output (d) hard x-ray.

EXPRESSIONS FOR IMPURITY IONIZATION IN TOROIDAL MAGNETIC CONFIGURATIONS

G. TONON

ASSOCIATION EURATOM-CEA
Département de Physique du Plasma et de la Fusion Contrôlée
Service IGn - Centre d'Etudes Nucléaires
B.P.85 - Centre de Tri - 38041
GRENOBLE CEDEX (France)

ABSTRACT : Analytic expressions are given for the mean charge of the impurity ions, the mean charge of the plasma and the effective charge when coronal equilibrium is assumed.

In order to find the distribution of charge states Z in toroidal discharges we can use coronal equilibrium /1/ :

$$\frac{n_{i,z+1}}{n_{i,z}} = \frac{S(z,T_e)}{\alpha(z+1,T_e)} \qquad (1)$$

where we balance collisional ionization by radiative recombination. The collisional ionization-rate coefficient $S(z,T_e)$ and the radiative recombination-rate coefficient $\alpha(z,T_e)$ chosen, are given respectively by /2/, /3/ :

$$S(z,T_e) = 9\ x10^{-6}\ \frac{\lambda^{-1/2} \sum_z \exp(-\lambda)}{(\chi_z^{z+1})^{3/2}\ (4{,}88 + \lambda^{-1})} \quad (cm^3\ s^{-1})$$

$$\alpha(z+1,\ T_e) = 5.2\ 10^{-14}\ \lambda^{1/2}\ Z\ (0.429 + \tfrac{1}{2}\ \mathrm{Log}\ \lambda + 0.469\ \lambda^{-1/2}) \quad (cm^{-3}s^{-1}) \qquad (2)$$

$$\lambda = \frac{\chi_z^{z+1}}{T_e}$$

In these formulas χ_z^{z+1} (eV) denotes the ionization potential /4/ and $\sum_z$ is the number of electrons in the outermost layer corresponding to the state of charge Z.

For a two component plasma with hydrogen or deuterium and the impurity concentration C_i :

$$C_i = \frac{n_i}{n_p} = \frac{\sum_z n_{i,z}}{n_o + \sum_z n_{i,z}} \qquad (3)$$

where subscripts i,o and p denotes impurity,fuel and total plasma ions, we have calculated from relation (1) the following plasma parameters :

1°) The mean charge $\overline{Z}_i$ of the impurity ions :

$$\overline{Z}_i = \frac{\sum_z n_{i,z} Z^2}{\sum_z n_{i,z} Z} \qquad (4)$$

In the figure 1, $\overline{Z}_i$ is plotted as a fonction of the electronic temperature T_e for various impurities. We see that light impurities (carbon, nitrogen and oxygen) are completely stripped when T_e exceeds 500 eV and we have :

$$\overline{Z}_i \simeq \frac{1}{5}\ M\ T_{e(eV)}^{1/6} \quad \text{for} \quad T_e < 500\ eV \qquad (5)$$

when M denotes the atomic mass number (for example M = 16 for oxygen). For heavy elements $\overline{Z}_i$ = 24, 35 and 50 for iron, molybdenum and tungsten respectively, at T_e = 3 keV. For these elements the following relations hold :

$$\overline{Z}_i \simeq \frac{1}{2}\ M^{1/4}\ T_{e(eV)}^{1/2} \quad \text{for } T_e < .15\ keV$$

$$\overline{Z}_i \simeq \frac{1}{3}\ M^{1/2}\ T_{e(eV)}^{1/3} \quad \text{for } .15 < T_e < 1.5\ keV \qquad (6)$$

$$Z_i \simeq \frac{1}{2}\ M^{2/3}\ T_{e(eV)}^{1/7} \quad \text{for } 1.5 < T_e < 10\ keV$$

as we see on the figure 2.

2°) The average charge $\overline{Z}_p$ of the plasma :

$$\overline{Z}_p = \frac{n_e}{n_p} = \frac{n_o + \sum_i n_i \overline{Z}_i}{n_o + \sum_i n_i} \qquad (7)$$

For small impurity concentration ($n_i \ll n_p$) we have :

$$\overline{Z}_p \simeq 1 + \sum_i C_i \overline{Z}_i \qquad (8)$$

For example when $.15 < T_e < 1.5$ keV, we get from relations (6) :

$$\overline{Z}_p \simeq 1 + \frac{1}{3}\ T_e^{1/3} \sum_i M^{1/2} C_i \qquad (9)$$

3°) The effective ionic charge Z_{eff} given by :

$$Z_{eff} = \frac{\sum_{i,z} n_{i,z} Z^2}{\sum_{i,z} n_{i,z} Z} = \frac{n_o + n_i \overline{Z}_i^2}{n_o + n_i \overline{Z}_i} = \frac{1 + \overline{Z}_i(\overline{Z}_p - 1)}{\overline{Z}_p} \qquad (10)$$

and from (8) :

$$Z_{eff} \simeq \frac{1 + C_i \overline{Z}_i^2}{\overline{Z}_p} \qquad (11)$$

In figure 3 the effective ionic charge Z_{eff}, calculated from relation (10), is plotted as a fonction of the average plasma charge $\overline{Z}_p$ for molybdnum impurities. In this figure, temperature and concentration influence are shown by solid and dotted line respectively.

The question remains whether an ionization equilibrium state is reached in toroidam discharges like a Tokamak. In order to answer roughly this question, we have determined $\overline{Z}_i$ values so that the ionization time τ_z (or $n_e\tau_z$) calculated from a method proposed by HINNOV /5/ is equal to the ion confinement time τ_p (or $n_e\tau_p$). In the figure 4, the $\overline{Z}_i$ values obtained for $n_e\tau_p = 10^{11}$ and $10^{12}\ cm^{-3}.s$, are compared, to the equilibrium values given for iron in the figure 1. We see that for $n_e\tau_p \geq 10^{12}\ cm^{-3}.s$ (typical values for S.T or T.F.R. machines) ionization equilibrium is reached.

I would like to thank Dr. P. BLANC for numerical evaluation of the coronal equilibrium.

REFERENCES. /1/ - G. ELWERT, Z. Naturforsch 7a, 6 (1951), p. 432-439.
/2/ - R.W.P. Mc. WHIRTER, Chapter 5 "Spectral Intensities" Plasma Diagnostic Techniques. Ed. Academic Press (1965).
/3/ - M.J. SEATON, Montly Notices Ray.Astron. Soc. 119, (1959), 81.
/4/ - T.A. CARLSON, C.W. NESTOR, N. WASSERMAN, J.D. Mc. DOWELL, O.R.N.L. 4562 - VC 34 (1970).
/5/ - E. HINNOV, Princeton Plasma Physics Laboratory, MATT.777 (1970).

Fig. 1 - Mean impurity charge $\overline{Z}_i$ versus plasma electronic temperature T_e for various elements (carbon, nitrogen, oxygen, iron, molybdenum and tungsten).

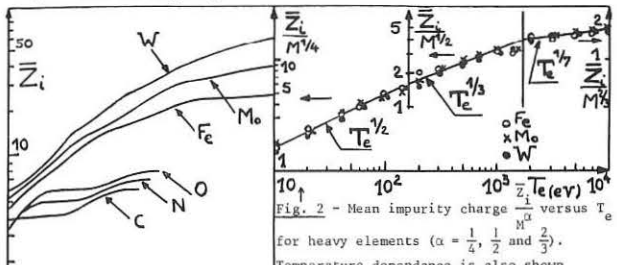

Fig. 2 - Mean impurity charge $\frac{\overline{Z}_i}{M^{\alpha}}$ versus T_e for heavy elements ($\alpha = \frac{1}{4}, \frac{1}{2}$ and $\frac{2}{3}$). Temperature dependance is also shown.

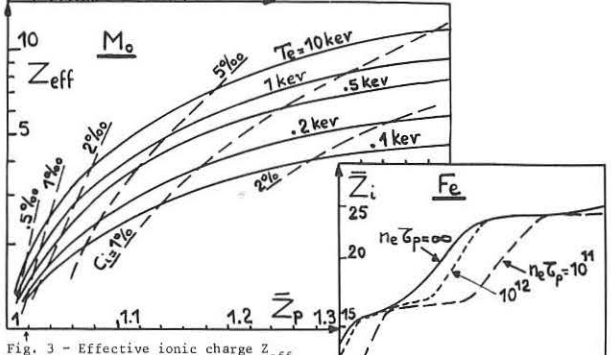

Fig. 3 - Effective ionic charge Z_{eff} versus average plasma $\overline{Z}_p$ for molybdenum impurities. Solid and dashed lines represent temperature T_e and concentration C_i influence respectively.

Fig. 4 - Mean iron charge $\overline{Z}_i$ versus T_e for various values of $n_e\tau_p$ (10^{11} - 10^{12} and ∞).

SELF-GENERATED MAGNETIC FIELDS IN LASER PLASMAS*

J. J. Thomson, C. E. Max, and D. T. Attwood

University of California, Lawrence Livermore Laboratory

Livermore, California, USA

ABSTRACT

Megagauss-level magnetic fields have been predicted theoretically and observed experimentally. We discuss the field generation due to resonance absorption of laser light and thermoelectric currents. We describe our experiment to measure these fields by Faraday rotation of light (2660Å)

Recently experimental and theoretical investigations have shown the possibility of megagauss magnetic fields internally generated in laser plasmas.[1,2] Fields of this magnitude can substantially affect plasma transport properties. There is possible evidence for reduced thermal conductivity in the plasma in the experimentally observed fast ions and abnormally high hard x-ray production. Reduction of thermal transport has serious consequences for laser fusion, and thus we have begun to study internally generated fields both theoretically and experimentally. We discuss here two kinds of magnetic fields: one due to thermal currents and the other due to resonance absorption of laser light.

If laser momentum is transferred to plasma electrons, currents may be set up, providing a source for magnetic fields. Let us assume the ions are immobile for simplicity. The electron momentum equation is

$$\left(\frac{\partial}{\partial t} + \nu\right) n\underset{\sim}{V} + \underset{\sim}{\nabla} \cdot (n\underset{\sim}{V}\underset{\sim}{V}) + \underset{\sim}{\nabla} \cdot \left[\int \underset{\sim}{v}\underset{\sim}{v} f d^3v - n\underset{\sim}{V}\underset{\sim}{V}\right] = -\frac{en_o}{m_e}\underset{\sim}{E} + \frac{1}{m_e}\left(\rho\underset{\sim}{E} + \frac{1}{c}\underset{\sim}{J}\times\underset{\sim}{B}\right), \tag{1}$$

where $n = \int f dv$, $n\underset{\sim}{V} = \int \underset{\sim}{v} f dv$, ν is an effective collision frequency, and $\rho = -e(n-n_o)$, the charge density. We are interested in quasi-steady fields, so we time-average over the laser light period. Using Maxwell's equations, we may derive an equation for $\langle\underset{\sim}{B}\rangle$:[1,2]

$$\frac{\partial}{\partial t}\langle\underset{\sim}{B}\rangle = \frac{m_e c^2 \nu}{4\pi e}\underset{\sim}{\nabla} \times \left(\frac{1}{n_o}\underset{\sim}{\nabla}\times\langle\underset{\sim}{B}\rangle\right) + \frac{cm_e}{e}\underset{\sim}{\nabla} \times \frac{1}{n_o}\underset{\sim}{\nabla} \cdot (\underset{\approx}{P}_e + \underset{\approx}{P}_r) \tag{2}$$

where $\underset{\approx}{P}_e$ is the fluid pressure tensor and $\underset{\approx}{P}_r$ is the radiation pressure tensor:

$$\underset{\approx}{P}_r = \frac{1}{en_o}\left[\frac{1}{8\pi}\langle E^2+B^2\rangle \underset{\approx}{I} - \frac{1}{4\pi}\langle\epsilon_R \underset{\sim}{E}\underset{\sim}{E} + \underset{\sim}{B}\underset{\sim}{B}\rangle\right] . \tag{3}$$

ϵ_R is the real part of the complex dielectric function. If the pressure is isotropic, $\underset{\approx}{P}_e = n_o T \underset{\approx}{I}$, and the source term due to fluid pressure simply becomes

$$S_1 = -\frac{cm_e}{qn}(\underset{\sim}{\nabla} \log n_o) \times \nabla T . \tag{4}$$

If the pressure is anisotropic, other sources are present. Consider a planar target. The density gradient points into the target. Near the center of the laser beam, the temperature gradient points out of the target, and is thus collinear with ∇n. However, at the edge of the beam, the temperature gradient rotates to continue to point at the center of the beam, thus giving rise to a finite $\nabla n \times \nabla T$. For typical scale lengths of 10μ, and temperatures of ∿1 keV, we find $\frac{dB}{dt} \cong 10^{-2}$ megagauss/picosecond. Thus megagauss levels are expected over 100 picosecond laser pulses.

Two-dimensional hydrodynamic calculations using the code LASNEX typically show field strengths of 1-2 megagauss extending over regions 20-40 in diameter. This leads to a significant reduction in thermal transport in the high field region, and may lead to a loss of implosion symmetry in a laser fusion target.

Next we consider the radiation pressure term:

$$S_2 = \frac{cm_e}{q}\underset{\sim}{\nabla} \times \frac{1}{n_o}\underset{\sim}{\nabla} \cdot \underset{\approx}{P}_r \tag{5}$$

Stamper and Tidman have demonstrated that inverse bremstrahllung absorption of laser light will lead to magnetic field generation in underdense plasmas. We have considered the situation in which plane polarized light is incident obliquely upon a plasma, leading to the well-known phenomenon of resonance absorption. The laser light turns at the density $n_c \cos^2\theta$, where n_c is the critical density and θ the angle of incidence. But if a sufficient amount of field leaks to the critical density, plasma waves are excited, which are then damped by the particles.

We have considered this problem for the simple case of a linear density gradient, with scale length L, and find that the source term near the critical density is approximately given by

$$S_2 = \frac{c}{en_c L^2}(\omega/\nu)^2 \frac{E_o^2}{8\pi} \sin\theta \cos\theta \exp\left[-(4/3)n_o L \sin^3\theta - 2k_o L(\nu/\omega)^2\right] \tag{6}$$

where k_o is the free-space wavelength, and ν is the effective collision frequency due to resonance absorption. The field is perpendicular to the laser polarization plane. For typical laser fusion parameters, this term is several orders of magnitude larger than the $\nabla n \times \nabla T$ term of Eq. (4).

We have observed this phenomenon in particle-in-cell plasma simulations. The magnetic field saturates at a level of several megagauss due to convection by particles expelled by the breaking of the resonantly exited plasma waves.

Magnetic fields were measured in plasmas by Stamper et. al.,[1] by finding the Faraday rotation angle of a probe beam. Their probe beam was at double the frequency of their main Nd. laser beam. We have endeavored to improve their experiment in several ways: 1) we use frequency quadrupled light (2660Å) in order to probe higher plasma densities; 2) we look at both polarizations simultaneously to eliminate shot-to-shot variations; 3) we have done extensive hydrodynamic simulations of the exploding target, including ray tracing of the probe light in order to better estimate $\theta \propto \int n_e \underset{\sim}{B} \cdot d\underset{\sim}{\ell}$, the Faraday angle, and 4) we will rotate the polarization vector of the main beam relative to the probe beam, in order to separate polarization-dependent effects.

In our experiment, light from the main beam is split off and frequency quadrupled. There is a peak-to-peak time delay between laser and probe of 150-250 ps. During this time, hydrodynamic expansion has decreased the sharpness of the plasma density gradient, but the magnetic field is still near its peak value. The target is a 150 x 10μ parylene disk. The probe beam passes through a Wollaston calcite polarization beam splitter onto hard film. The rotation angle is inferred from the relative intensities of the two polarization components imaged onto the hard film.

The figure shows a preliminary experiment. The image at the left is taken with the polarization angle aligned with the 2660Å light, while at the right, the polarization angle is 90°. The target is a 250 μ steel ball, struck slightly below center with a .5 joule beam. On the right, one may see a thin filament of rotated light. This experiment is currently being improved to quantitatively determine the magnitude of the magnetic fields.

REFERENCES

1) J. A. Stamper and B. H. Ripin, Phys, Rev. Lett. 34, 138 (1975).

2) J. J. Thomson, C. E. Max, and K. Estabrook, UCRL-76690, to be published in Phys. Rev. Lett.

* Research performed under the auspices of the USERDA.

NONLINEAR EVOLUTION OF TEARING MODES

M. Rosenbluth, B. Waddell, D. Monticello and R. White
Institute for Advanced Study, Princeton
New-Jersey, USA

With the usual Tokamak ordering $\frac{r}{R} \ll 1$, the non-linear evolution of instabilities preserves their initial helical symmetry. Hence the problem reduces to a two-dimensional one (r and kz + mθ) which we treet numerically. Previously we have shown the evolution of ideal MHD kink modes into "bubbles" and the suppression of bubbles by magnetic shear. Here we report on the inclusion of finite resistivity which leads to the tearing mode and the formation of magnetic islands.

When the island size exceeds the very small values at which linear theory breaks down inertia becomes negligible and magnetostatic equilibrium applies i.e.

$$\nabla^2 \psi = j(\psi) \tag{1}$$

Thus the current must be a function of the helical flux $\psi = kr A_\theta + mA_z$. In addition resistive diffusion and plasma convection leads to the equation

$$\left\langle \frac{\partial \psi}{\partial t} \right\rangle = \eta j - \mathcal{E} \tag{2}$$

where the brackets indicates an average over a flux surface, and $\mathcal{E}$ is the applied electric field.

To complete the statement of the problem a transport model must be given for the time evolution of the resistivity $\eta(\psi)$.

Equations (1) and (2) must be iterated simultaneously to obtain numerical stability. We have devised a numerical scheme which is stable for $m \geq 2$, but so far has not converged for the stronger m = 1 modes.

The principal results are as follows:

1) For very small magnetic islands $\frac{\omega}{r} \sim .01$ (where ω is the island width) the growth is found to follow closely the theory of Rutherford, $\frac{d\omega}{dt} = \text{const} \times \Delta' \eta$ where Δ' is the usual discontinuity of logarithmic derivatives of the linear eigenfunction.

2) In the case $\eta = \text{const.}$ the islands grow to very large size, in fact eventually reaching the center.

3) For more realistic transport laws where the resistivity increases outwards we have observed island saturation. For ST parameters the m = 2 island grows to about 10 % of the radius, consistent with experimental observation.

In the Figure we show the flux surfaces in the final state.

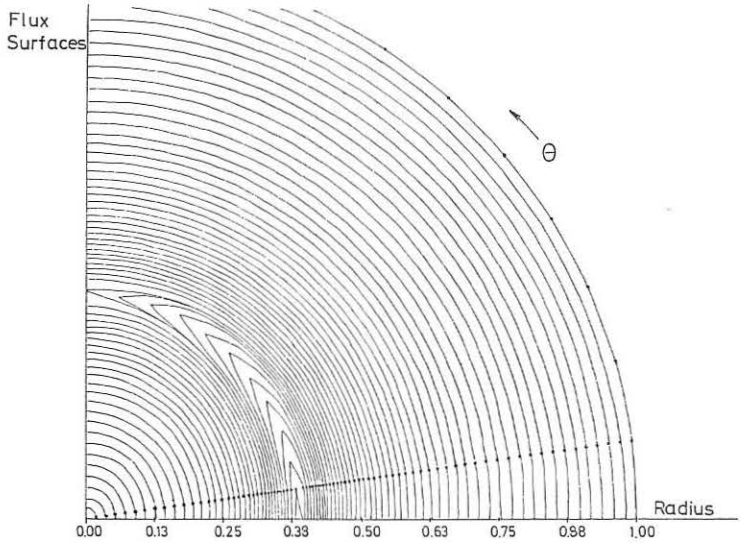

FEEDBACK STABILIZATION OF A SCREW PINCH

R. Keller, A. Pochelon, W. Bachmann

Ecole Polytechnique Fédérale de Lausanne, Switzerland

Centre de Recherches en Physique des Plasmas

Abstract: Results from a stabilization experiment operating on the kink mode of a screw pinch by means of a magnetic feedback loop are presented.

Introduction: The correct behavior of a thermonuclear reactor will require an evolved automatic control system, which allows for the adjustment of a great number of parameters. One of the most important feedback loops will have the task of maintaining plasma equilibrium and suppressing dangerous MHD instabilities. Our aim is to demonstrate the feasibility of stabilizing the fast kink mode of a screw pinch working above the Kruskal-Shafranov limit.

The Pinch Configuration: The θ coil measures 142 cm and has a diameter of 9 cm. The main field reaches 16 kGauss in 3·8 μsec at which time the crowbar is switched on. The quartz discharge tube has an inner diameter of 5 cm. On the discharge tube are mounted the feedback coils and the magnetic dipole probes. The time evolution of the axial J_z current is similar to that of the main B_z field. Two electrodes, 1.2 cm in diameter, are 142 cm apart, and are protected by limiters in order to concentrate the axial current on the front of the electrodes. In this way, precise boundary conditions exist for the pinch. Actually, probe measurements show a pinch with a sinusoidal displacement vanishing at the electrodes [1].

A sharp boundary plasma column experiences an external kink mode where the matter moves as a whole. In order to satisfy the conditions at the end of the column it is necessary [2] to superimpose two modes with different wave numbers. Hence the displacement of the axis is

$$\eta = \frac{y}{2} \exp(-ih_1 z + i\omega t) + \frac{y}{2} \exp(-ih_2 z + i\omega t) \qquad (1)$$

h_1 and h_2 are determined by the necessity of total reflexion at the electrodes (the resulting axial energy transport is zero when both group velocities are equal but opposite in sign).

This statement leads to the following wave form

$$\eta = y \exp(ih_o z + i\omega t) \cdot \cos \frac{\pi z}{L} \qquad (2)$$

with

$$h_o = \frac{\pi q_c}{L \Delta q} \qquad q_c = \frac{1}{2-\beta} \qquad \Delta q = \frac{\pi a}{L} \frac{B_z}{B_\theta} \qquad (3)$$

There are now two q values: $q_1 = q_c + \Delta q$; $q_2 = q_c - \Delta q$. The eigenfrequency of the kink takes the value

$$\omega^2 = \frac{B_\theta^2 q_c}{\mu_o \rho a^2} \left[\left(\frac{\Delta q}{q_c} \right)^2 - 1 \right] \qquad (4)$$

We obtain a new definition of the Kruskal-Shafranov limit: $q = q_c$. The corresponding axial current J_z equals 2020 A for a plasma radius a = 0.8 cm measured from the luminosity profile, and with β = 0.1. The onset of the instability occurs very close to this calculated value.

The feedback coils have a ℓ = 1 configuration. For acting at the m = 1, n = 1 mode in both degrees of freedom, the current distribution should be sinusoidal in θ and z, in the same way as the real and imaginary part of (2). For reason of simplicity we have choosen a short straight coil (h_o = o) built in two halves 30 cm long and 20 cm apart. The 12 turns are equally spaced, covering two 90° sectors. The other two sectors are covered with windings acting on the second degree of freedom. By Fourier analysis we find an efficiency of 45 % for the n = 1 mode and a finite excitation force of the harmonic n = 2. Below twice the Kruskal-Shafranov limit the n = 2 harmonic remains stable.

Magnetic dipole probes are used for detecting the displacement of the plasma in the two orthogonal direction [3]. Their windings are equally spaced and cover 120° sectors. They are placed near the mid-plane, at about 10 cm distance from the two parts of the feedback coils. At this distance the direct coupling between the enforcer coil and the probe is not negligeable and its value is negative. The theory shows that stability is only possible if the coupling is positive and relatively small. We compensate for this inconvenience with a loop connected in series with the probe, and coupled to the feedback current in a correct way.

The feedback loop is similar to the system used in the Scyllac experiment [4]. The probe signal is integrated and preamplified up to ± 20 V. The driver stage reaches a ± 400 V level at very low impedance, necessary to drive the two output triodes Siemens R S 1041 connected in push-pull. The available voltage and current sweep is ± 20 kV and ± 140 A. A ferrite transformer couples the power to the feedback coils. The power amplifier is switched on 5 μsec before the pinch, and a reset opens the preamplifier just when the kink starts growing. Only one feedback loop is installed for stabilizing the degree of freedom in which the kink is growing faster. The amplitude of the other degree of freedom may by held at a small value for an extended duration by feeding the second enforcer coil with a proper step function.

Results: The measurements are performed at 1.8 times the Kruskal-Shafranov limit. To obtain stability the gain of the feedback loop must be set above unity. The stable range is relatively narrow, a gain exceeding 1.4 drives the system overstable.

The stereoscopic streak pictures of Fig. 1 and Fig. 2 show the plasma displacement at 85 μ D_2 filling pressure, without and with stabilization respectively. The upper traces correspond to the degree of freedom which is stabilized. In this case the overall response time of the amplifier is 0.9 μsec and the measured growth rate $\gamma = 0.33 \times 10^6$ sec^{-1}. Fig. 3 and Fig. 4 are similar pictures obtained at 40 μ D_2 filling pressure. The measured growth rate without stabilization is now $\gamma = 0.6 \times 10^6$ sec^{-1}. To achieve stability it was necessary to decrease the response time to 0.6 μsec, by changing the ratio of the output transformer. In both cases the upper degree of freedom continues to be stable when the lower trace already shows wall contact.

References

(1) A. Pochelon, R. Keller: LRP 86/74 (1974) Lausanne.

(2) R. Keller, W. Bachmann, A. Pochelon: LRP 91/75 (1975) Lausanne.

(3) Yu. P. Ladikov and Yu. I. Samoilenko: Soviet Phys. - Techn.Phys. 17, 1644 (1973).

(4) R.F. Gribble, S.C. Barnett, C.R. Harder: Proc. 2nd Topical Conf. on Pulsed High-Beta Plasma, Garching IPP 1/127 (1972).

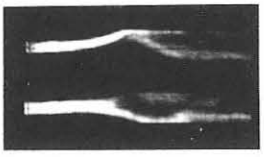

Fig. 1

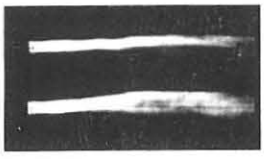

Fig. 2

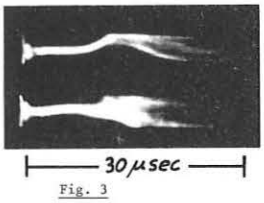

Fig. 3

Fig. 4

SEVENTH EUROPEAN CONFERENCE ON CONTROLLED FUSION AND PLASMA PHYSICS

Lausanne, Switzerland 1 - 5 September 1975

LIST OF PARTICIPANTS

AMATO A.
Cons.Tec.Scient., Roma, Italy

ANDELFINGER C.
IPP, Garching, RFA

APPERT K.
CRPP, EPFL, Lausanne, Switzerland

ASCOLI-BARTOLI U.
CNEN, Frascati, Italy

AUDENAERDE K.
CNEN, Frascati, Italy

AUER G.
Innsbruck Univ., Innsbruck, Austria

AUERBACH T.
ETHZ, Zürich, Switzerland

BABONNEAU D.
CEA, Limeil, France

BABYKIN M.V.
Kourchatov Inst., Moscow, USSR

BACHMANN W.
CRPP, EPFL, Lausanne, Switzerland

BALESCU R.
Univ. Brussels, Belgium

BARBIAN E.P.
FOM, Amsterdam, Netherlands

BARBIERI O. de
CEA, Grenoble, France

BARR H.C.
Uni. Wales, Bangor, UK

BATEMAN R.G.
Oak-Ridge Nat. Lab., USA

BEGG I.M.
Univ. St-Andrews, Scotland

BERGER D.
CRPP, EPFL, Lausanne, Switzerland

BERNARD L.C.
CERN, Geneva, Switzerland

BERS A.
MIT, Cambridge, USA

BHATNAGAR V.
Ecole Royale Militaire, Belgium

BICKERTON R.J.
UKAEA, Culham, UK

BIGHEL L.
CRPP, EPFL, Lausanne, Switzerland

BITTER M.
CRPP, EPFL, Lausanne, Switzerland

BLATTMANN H.
Tagesanzeiger, Zürich, Switzerland

BODIN H.A.B.
UKAEA, Culham, UK

BOGEN P.
IPP, Jülich, RFA

BOOZER, A.H.
PPPL, Princeton, USA

BORIS J.P.
NRL, Washington, USA

BORNATICI M.
Univ. Calabria, Italy

BOSWELL R.W.
ESRO, Noordwijk, Netherlands

BRAAMS C.M.
FOM, Jutphaas, Netherlands

BRAMBILLA M.
CEA, Grenoble, France

BRANDT B.
Euratom, Brussels, Belgium

BROSSIER P.
CEA, Fontenay, France

BROWN D.A.
Royal Holloway Coll., Egham, UK

BURGESS M.D.J.
Oxford Univ., UK

BURKHALTER P.G.
NRL, Washington, USA

BURTSEV V.A.
Inst. Res. Elec., Leningrad, USSR

BUSSAC M.N.
Ec. Polytechnique, Palaiseau, France

BYERS J.
LLL, Livermore, USA

BYRNE R.N.
Science Applications, La Jolla, USA

CANO R.
CEA, Fontenay, France

CANOBBIO E.
CEA, Grenoble, France

CAP F.F.
Innsbruck Univ., Innsbruck, Austria

CHANG C.T.
RISO, Denmark

CHATELIER M.
CEA, Fontenay, France

CHIAN A.C.L.
Univ. Cambridge, UK

CHRISTIANSEN J.P.
UKAEA, Culham, UK

CICCONI G.
Inst. Elettrotec., Genova, Italy

CIMA G.M.
UKAEA, Culham, UK

COFFMAN F.
ERDA, Washington, USA

COHEN H.C.
PPPL, Princeton, USA

COLE H.C.
UKAEA, Culham, UK

CONSOLI T.
CEA, Grenoble, France

COPPI B.
MIT, Cambridge, USA

COQUERAND S.
CRPP, EPFL, Lausanne, Switzerland

COSTA CABRAL J.A. da
Inst. Sup. Tec., Lisboa, Portugal

COSTLEY A.E.
Nat. Phys. Lab., Teddington, UK

CRAXTON R.S.
Imp. College, London, UK

CUPERMAN S.
Tel-Aviv Univ., Israel

DAUTRAY R.
CEA, Limeil, France

DAVIDSON R.C.
Univ. Maryland, USA

DELCROIX J.L.
Univ. Paris, Orsay, France

DENUS S.
Inst. Plasma Phys., Warszawa, Poland

DEVIENNE F.M.
Lab. Phys. Mol., Peymeinade, France

DIETZ J.
IPP, Jülich, RFA

DOLIQUE J.M.
Univ. Grenoble, France

DONALSON T.P.
UKAEA, Culham, UK

DOTE T.
Inst. Phys. Chem., Wako, Japan

DOUCET H.
Ec. Polytechnique, Palaiseau, France

DUECHS D.F.
IPP, Garching, RFA

DUM C.T.
IPP, Garching, RFA

ELSASSER K.
Univ. Bochum, RFA

ENGELHARDT W.
IPP, Garching, RFA

ENGELMANN F.
FOM, Jutphaas, Netherlands

FABRE E.
Ec. Polytechnique, Palaiseau, France

FALTER H.D.
IKVZ, Karlsruhe, RFA

FANCHIOTTI H.
Univ. La Plata, Argentina

FARKAS G.
Central Res. Inst. Phys., Budapest, Hungary

FAULCONER D.W.
Ecole Royale Militaire, Belgium

FENEBERG W.
Munich, RFA

FLEISCHMANN H.
Cornell Univ., USA

FORMAN P.R.
Los-Alamos Lab., USA

FRANKLIN R.N.
Oxford Univ., UK

FRASER A.R.
AWRE, Aldermaston, UK

FREISINGER J.
Giessen Univ., RFA

FUNFER E.
IPP, Garching, RFA

FUTTERMENGER W.
Hannover, RFA

GAUME P.
CEA, Limeil, France

GEKKER I.R.
Lebedev Inst., Moscow, USSR

GIERKE G. von
IPP, Garching, RFA

GILL R.D.
UKAEA, Culham, UK

GIMBLETT C.G.
UKAEA, Culham, UK

GINOT P.
CEA, Fontenay, France

GLOCK E.
IPP, Garching, RFA

GOEDE A.P.H.
FOM, Amsterdam, Netherlands

GOELER S. von
PPPL, Princeton, USA

GOLDNER F.
US Mission EC, Bruxelles, Belgium

GOTO S.
Osaka Univ., Osaka, Japan

GREEN B.J.
JET, Culham, UK

GREEN T.S.
UKAEA, Culham, UK

GREENE J.M.
PPPL, Princeton, USA

GRESILLON D.
Ec. Polytechnique, Palaiseau, France

GRIEGER G.
IPP, Garching, RFA

GRIEM H.
Univ. Maryland, USA

GROSS R.A.
Columbia Univ., New-York, USA

GRUBER O.
IPP, Garching, RFA

GRUBER R.
CRPP, EPFL, Lausanne, Switzerland

GUSCOTT B.
KMS, Ann-Arbor, USA

GUYOT M.
CGE, Marcoussis, France

HAAS R.S. de
FOM, Jutphaas, Netherlands

HAEGI M.
CNEN, Frascati, Italy

HAELG W.
ETHZ, Zürich, Switzerland

HAINES M.G.
Imp. College, London, UK

HALL T.A.
Univ. Essex, Colchester, UK

HALVERSON W.
MIT, Cambridge, USA

HAMBERGER S.M.
UKAEA, Culham, UK

HARTMAN Ch.W.
LLL, Livermore, USA

HARVEY R.J.
Hughes Res. Lab., Malibu, USA

HASTIE R.J.
UKAEA, Culham, UK

HEIJNINGEN van
FOM, Jutphaas, Netherlands

HELLSTEN T.A.K.
Royal Inst. Tech., Stockholm, Sweden

HENDERSON D.B.
Los-Alamos Lab., USA

HENKES W.
IKVZ, Karlsruhe, RFA

HERRNEGGER F.
IPP, Garching, RFA

HEYM A.
CRPP, EPFL, Lausanne, Switzerland

HINES K.C.
Univ. Melbourne, Australia

HIRANO K.
Nagoya Univ., Nagoya, Japan

HIRSCH R.L.
ERDA, Washington, USA

HOEKZEMA J.A.
FOM, Jutphaas, Netherlands

HOFMANN F.
CRPP, EPFL, Lausanne, Switzerland

HOFMANN G.
Hughes Res. Lab., Malibu, USA

HÖRNQVIST N.
Nat. Def. Res. Lab., Stockholm, Sweden

HOSKING R.J.
Univ. Waikato, Hamilton, New-Zealand

HÖTHKER K.
IPP, Jülich, RFA

HUGHES M.H.
UKAEA, Culham, UK

HUGILL J.
UKAEA, Culham, UK

ITO H.
Osaka Univ., Osaka, Japan

JABLON C.
Univ. Paris, Orsay, France

JACQUINOT J.
CEA, Fontenay, France

JEKI L.
Central Res. Inst. Phys., Budapest, Hungary

JENNINGS W.C.
Rensselaer Polytech., New-York, USA

JENSEN V.O.
RISO, Denmark

JOHNSON J.L.
PPPL, Princeton, USA

JOHNSON L.C.
PPPL, Princeton, USA

JOLAS A.
CEA, Limeil, France

JONES I.R.
Flinders Univ., Australia

JUNKER J.
IPP, Garching, RFA

JURGENS B.
FOM, Amsterdam, Netherlands

KAEPPELER H.J.
Univ. Stuttgart, RFA

KALISKI S.
Inst. Plasma Phys., Warszawa, Poland

KALSBEEK H.W.
FOM, Jutphaas, Netherlands

KAMMASH T.
Univ. Michigan, Ann-Arbor, USA

KAPETANAKOS C.A.
NRL, Washington, USA

KARGER F.
IPP, Garching, RFA

KARLSON E.T.
Inst. Tech., Uppsala, Sweden

KELLER R.
CRPP, EPFL, Lausanne, Switzerland

KILKENNY J.D.
Imp. College, London, UK

KILLEEN J.
LLL, Livermore, USA

KLINGELHÖFER R.
IKVZ, Karlsruhe, RFA

KLÜBER O.
IPP, Garching, RFA

KNOEPFEL H.
CNEN, Frascati, Italy

KOCK L.C.J.M.
FOM, Jutphaas, Netherlands

KOJI U.
Kyoto Univ., Uji, Japan

KOPECKY V.
Inst. Plasma Phys., Prague, Czechoslovakia

KÖPPENDÖRFER W.
IPP, Garching, RFA

KORTEN M.
IPP, Jülich, RFA

KOWALSKI S.
Inst. Plasma Phys., Warszawa, Poland

KRALL N.A.
Science Applications, La Jolla, USA

KRITZ A.
CRPP, EPFL, Lausanne, Switzerland

KRUMM P.
Ec. Polytechnique, Palaiseau, France

KUNKEL W.B.
Univ. Calif., Berkeley, USA

KUSNETSOV E.I.
Kourchatov Inst., Moscow, USSR

KUSWA G.W.
ERDA, Washington, USA

LACKNER K.
IPP, Garching, RFA

LALLIA P.
CEA, Grenoble, France

LANGER P.
CEA, Paris, France

LARSSON J.
Umea Univ., Umea, Sweden

LAUNOIS D.P.
CEA, Fontenay, France

LAVRENTIEV O.A.
Inst. Phys. Tech., Kharkov, USSR

LEE S.
Univ. Malaya, Kuala Lumpur, Malaysia

LEES D.J.
UKAEA, Culham, UK

LEGENTIL M.
Univ. Paris, Orsay, France

LEHNERT B.
Royal Inst. Tech., Stockolm, Sweden

LEUTERER F.
IPP, Garching, RFA

LEWKOWICZ I.
Israel AEC, Yavne, Israel

LIETTI A.
CRPP, EPFL, Lausanne, Switzerland

LIGOU J.P.
EIR, Würenlingen, Switzerland

LISTER G.G.
FOM, Jutphaas, Netherlands

LODDER J.J.
FOM, Jutphaas, Netherlands

LOMAS P.J.
Imp. College, London, UK

LORTZ D.
IPP, Garching, RFA

LYON J.F.
Oak-Ridge Nat. Lab., USA

MAANEN-ABELS A.E.P.M. van
FOM, Jutphaas, Netherlands

MACFARLANE J.
Mount Allison Univ., Québec, Canada

MACKINLAY R.R.
UKAEA, Culham, UK

MAIX R.K.
BBC, Oerlikon, Switzerland

MANERO-AMOROS F.
Junta Nucl. En., Madrid, Spain

MARKVOORT J.A.
FOM, Jutphaas, Netherlands

MASCHKE A.W.
Brookhaven Nat. Lab., Upton, USA

MATHIEU J.L.
Ecole Royale Militaire, Belgium

MAYOR J.M.
CRPP, EPFL, Lausanne, Switzerland

MERCIER C.
CEA, Fontenay, France

MERLINI D.
CRPP, EPFL, Lausanne, Switzerland

MESSIAEN A.M.
Ecole Royale Militaire, Belgium

MICHELIS C. de
CEA, Fontenay, France

MICHELSEN P.
RISO, Denmark

MILEY G.H.
Univ. Illinois, Urbana, USA

MILLER B.
ERDA, Washington, USA

MIYOSHI S.
Univ. Tsukuba, Ibaraki-Ken, Japan

MOHRI A.
UKAEA, Culham, UK

MOKHOV A.F.
Kourchatov Inst., Moscow, USSR

MOSER H.O.
Univ. Claude Bernard, Villeurbanne, France

MOSHER D.
NRL, Washington, USA

MOTZ H.
Oxford Univ., UK

MUGGE J.W.
FOM, Jutphaas, Netherlands

MÜLLER G.
Univ. Stuttgart, RFA

NAGAO S.
Tohoku Univ., Sendai, Japan

NALESSO G.F.
CNR, Padova, Italy

NARDI V.
Stevens Inst. Tech., Hoboken, USA

NEUHAUSER J.
IPP, Garching, RFA

NGUYEN The Hung
CRPP, EPFL, Lausanne, Switzerland

NIEDERMEYER H.
IPP, Garching, RFA

NIELSEN M.
RISO, Denmark

NIHEI H.
Univ. Tokyo, Japan

NIKOLAEV F.A.
Lebedev Inst., Moscow, USSR

NISHIDA Y.
Utsonomiya Univ., Utsonomiya, Japan

NOCENTINI A.
FOM, Jutphaas, Netherlands

NOLL P.
JET, Culham, UK

NUCKOLLS J.
LLL, Livermore, USA

NÜHRENBERG J.
IPP, Garching, RFA

OBIKI T.
Kyoto Univ., Uji, Japan

ODA T.
Hiroshima Univ., Japan

OGAWA K.
Agency Sc. Tech., Tanashi, Japan

OHKAWA T.
Gen. Atomic, San Diego, USA

OOMENS A.A.M.
FOM, Jutphaas, Netherlands

OREFICE A.
CNR, Milano, Italy

ORNSTEIN L.
FOM, Jutphaas, Netherlands

PACHER G.W.
IPP, Garching, RFA

PACHER H.
IPP, Garching, RFA

PALUMBO D.
Euratom, Brussels, Belgium

PANARELLA E.
Nat. Res. Council, Ottawa, Canada

PARBHAKAR K.J.
INRS-Energie, Québec, Canada

PAQUETTE G.
Univ. Montreal, Canada

PARIS P.J.
CRPP, EPFL, Lausanne, Switzerland

PARIS R.B.
CEA, Fontenay, France

PARLANGE F.
CEA, Grenoble, France

PEARLMAN J.
Sandia Lab., Albuquerque, USA

PEARLSTEIN L.D.
LLL, Livermore, USA

PEASE R.S.
UKAEA, Culham, UK

PECSELI H.L.
RISO, Denmark

PEIRY J.M.
CRPP, EPFL, Lausanne, Switzerland

PELLEGRINI C.
UKAEA, Culham, UK

PELLETIER G.
Univ. Grenoble, France

PESIC S.
Boris Kidric Inst., Beograd, Yugoslavia

PFIRSCH D.
IPP, Garching, RFA

PHILLIPS J.A.
IAEA, Vienna, Austria

PIETRZYK Z.A.
Univ. Washington, Seattle, USA

PLATZ P.
CEA, Fontenay, France

POCHELON A.
CRPP, EPFL, Lausanne, Switzerland

POPOVICS C.
Ec. Polytechnique, Palaiseau, France

POST R.
LLL, Livermore, USA

PUTNAM S.D.
Phys. International, San Leandro, USA

QUINN W.E.
Los-Alamos lab., USA

RAGER J.P.
CNEN, Frascati, Italy

RASUMOVA K.A.
Kourchatov Inst., Moscow, USSR

RAU F.
IPP, Garching, RFA

RAUCH J.
BBC, Oerlikon, Zürich, Switzerland

REBHAN E.
IPP, Garching, RFA

REISSE J.M.
CEA, Limeil, France

RENNER H.
IPP, Garching, RFA

RIPPER H.
CRPP, EPFL, Lausanne, Switzerland

RIVIERE A.C.
UKAEA, Culham, UK

ROBERTS P.D.
AWRE, Aldermaston, Thatcham, UK

ROBINSON D.C.
UKAEA, Culham, UK

ROGISTER A.
IPP, Jülich, RFA

ROSATELLI C.
Inst. Elettrotec., Genova, Italy

ROSE P.H.
Northwest Inc., Bellevue, USA

ROSENBLUTH M.
Inst. Adv. Studies, Princeton, USA

RUDAKOV V.A.
Inst. Phys. Tech., Kharkov, USSR

RUTKOWSKI H.L.
CRPP, EPFL, Lausanne, Switzerland

RYNN N.
Univ. Calif., Irvine, USA

SADOWSKI M.
Inst. Nucl. Res., Otwock-Swierk, Poland

SAHLIN H.L.
LLL, Livermore, USA

SALAT A.
IPP, Garching, RFA

SALERES A.
CEA, Limeil, France

SALOMAA R.R.E.
Tech. Res. Centre, Helsinki, Finland

SAND F.
Euratom-CNEN, Frascati, Italy

SANMARTIN J.R.
Inst. Nac. Tec. Aeroesp., Madrid, Spain

SANTINI F.
CNEN, Frascati, Italy

SCHAFFER G.
Lausanne, Switzerland

SCHAMEL H.
Ruhr Univ., Bochum, RFA

SCHANDA E.
Univ. Bern, Switzerland

SCHARER J.E.
Univ. Wisconsin, Madison, USA

SCHARFE A.
Inst. Reaktor, Köln, RFA

SCHEP T.J.
FOM, Jutphaas, Netherlands

SCHINDLER H.A.
Res. Lab. Siemens, Erlangen, RFA

SCHMIDT H.
Univ. Stuttgart, RFA

SCHNEIDER R.T.
Off. Naval Res., London, UK

SCHÜLLER F.C.
FOM, Jutphaas, Netherlands

SCHUMAKER K.H.
EOARD, London, UK

SEIFRITZ W.
EIR, Würenlingen, Switzerland

SEKA W.
Univ. Bern, Switzerland

SEKIGUCHI T.
Univ. Tokyo, Japan

SESNIC S.
IPP, Garching, RFA

SHANNY R.
Science Applications, La Jolla, USA

SHARP L.E.
UKAEA, Culham, UK

SHATZ M.
Israel AEC, Yavne, Israel

SHEFFIELD J.
UKAEA, Culham, UK

SHERWELL D.
Univ. St.Andrews, UK

SHIINA S.
Nihon Univ., Tokyo, Japan

SHIMOMURA Y.
Atomic En. Res. Inst., Tokai, Ibaraki, Japan

SHOHET J.L.
Univ. Wisconsin, Madison, USA

SHUKLA P.K.
Univ. Bochum, RFA

SIAMBIS J.
NRL, Washington, USA

SIGMAR D.J.
MIT, Cambridge, USA

SIMIK A.
CRPP, EPFL, Lausanne, Switzerland

SKOVORTSOV Y.V.
Kourchatov Inst., Moscow, USSR

SLOAN M.L.
Austin Res. Ass., Austin, USA

SMEULDERS P.
IPP, Garching, RFA

SOULE J.L.
CEA, Fontenay, France

STAIB P.
IPP, Garching, RFA

STAUDENMAIER G.
IPP, Garching, RFA

STENZ C.
Ec. Polytechnique, Palaiseau, France

STRACHAN J.D.
Australian Nat. Univ., Canberra, Australia

STUART G.W.
Science Applications, La Jolla, USA

SUDAN R.N.
Cornell Univ., Washington, USA

SURDO C. lo
CNEN, Frascati, Italy

SWEETMAN D.R.
UKAEA, Culham, UK

SYKES A.
UKAEA, Culham, UK

SZICHMAN H.
Israel AEC, Yavne, Israel

TAILLET J.
ONERA, Chatillon, France

TAKAMURA S.
CEA, Grenoble, France

TAKEDA S.
Nagoya Univ., Nagoya, Japan

TARONI A.
CNEN, Bologna, Italy

TATARONIS J.A.
New-York Univ., New-York, USA

TAYLOR J.B.
UKAEA, Culham, UK

TENNFORS E.
Roayal Inst. Tech., Stockholm, Sweden

THOMSON J.J.
LLL, Livermore, USA

TOMIMURA A.
Imp. College, London, UK

TOMLINSON R.
United Tech. Res. Center, East Hartford, USA

TRAN M.Q.
CRPP, EPFL, Lausanne, Switzerland

TRENCHARD H.A.
Westinghouse, Hyattsville, USA

TROYON F.
CRPP, EPFL, Lausanne, Switzerland

TRULSEN J.
Univ. Tromsø, Norway

TWERSKY D.
IAEA, Vienna, Austria

UCHIDA T.
Univ. Tokyo, Japan

VANDENPLAS P.E.
Ec. Royale Militaire, Belgium

VARMA R.K.
Phys. Res. Lab., Ahmedabad, India

VELIKHOV E.P.
Kourchatov Inst. Moscow, USSR

VERETENNICOFF M.
Univ. Brussels, Belgium

VERHEEST F.
Rijsuniversiteit, Gent, Belgium

VIREMONT J.
Ec. Polytechnique, Palaiseau, France

WANIEK R.W.
Adv. Kin. Inc., Costa Mesa, USA

WATSON-MUNRO C.N.
Univ. Sydney, Australia

WEGROWE J.G.
IPP, Garching, RFA

WEIBEL E.S.
CRPP, EPFL, Lausanne, Switzerland

WERSINGER J.M.
CRPP, EPFL, Lausanne, Switzerland

WESSON J.A.
UKAEA, Culham, UK

WEYNANTS R.R.
Ec. Royale Militaire, Belgium

WHITE M.S.
Imp. College, London, UK

WIDNER M.M.
Sandia Lab., Albuquerque, USA

WIENECKE M.
IPP, Garching, RFA

WILHEIM R.
IPP, Garching, RFA

WILLIS J.W.
ERDA, Washington, USA

WIMMEL H.K.
IPP, Garching, RFA

WITKOWSKI S.
IPP, Garching, RFA

WOBIG H.
IPP, Garching, RFA

WOLF G.
IPP, Jülich, RFA

WOOTTON A.J.
UKAEA, Culham, UK

WRIGHT R.J.
Imp. College, London, UK

YAMAMOTO K.
Atomic En. Re., Tokyo, Japan

YATSU K.
Univ. Tsukuba, Ibaraki-Ken, Japan

YONAS G.
Sandia Lab., Albuquerque, Japan

ZWICKER H.
Univ. Stuttgart, RFA